# INCEPTION REPORT

MARCH 2025

Presented to

SUGESE Superintendencia General de Seguros

Global Risk Modelling Alliance

InsuResilience Solutions Fund

Presented by

Ingeniar Risk Intelligence

CIMNE

# Consultant

INGENIAR CAD/CAE Ltda.
Carrera 19A # 84-14 OF 504
Edificio Torrenova
Bogotá, D.C., Colombia
www.ingeniar-risk.com

Centro Internacional de Métodos
Numéricos en Ingeniería
Edifici C1 Campus Nord UPC
C/ Gran Capità, S/N 08034
Barcelona, España
www.cimne.com

**Product number: INGENIAR-CIMNE-GRMA-01-v2**

**Cite as:** Cardona, O.D., Bernal, G., Villegas, C., Rincón, D., Gonzalez, D., Grajales, S., Herrera, S., Molina, J. F., Acosta, M., Carreño, M.L., Marulanda, M.C., Marulanda, P., Brenes, A (2025). Inception Report– Risk Assessment and Capacity Building in Costa Rica. Global Risk Modelling Alliance – SUGESE.

CONTENT

# 1 INTRODUCTION

The Global Risk Modelling Alliance (GRMA) program, sponsored by the InsuResilience Solutions Fund (ISF), aims to strengthen the capacities of countries and cities in climate and disaster risk analysis related to finance. This initiative seeks to address critical gaps in models and data, improving climate and disaster risk assessments at both national and subnational levels. To achieve this, GRMA identifies and co-defines, in collaboration with local partners, the specific needs of each country, offering open tools for risk management, data, and access to operational expertise in risk financing.

In the context of Costa Rica, GRMA has established a collaboration with the government – through its institutions, led by SUGESE – to strengthen its capacities in climate risk management. This alliance will provide relevant models and tools that will inform national strategies for risk financing and mitigation. The program is implemented in phases, beginning with the identification of specific needs and culminating in the integration of advanced risk modeling tools into the public policies of the country. This project is funded by KfW of Germany and managed by Frankfurt School on behalf of GRMA.

The INGENIAR-CIMNE consortium was selected to provide risk modeling services under the collaboration between GRMA and the Government of Costa Rica, through an application focused on 4 risk assessment projects:

- Strategic Project: Demonstration of risk assessment methods for critical infrastructure in Heredia.
- Operational Project 1: Disaster and climate risk assessment for road infrastructure – National Route 2 Pan-American Highway (RN2).
- Operational Project 2: Flood and drought risk assessment for small and medium-sized agricultural producers.
- Operational Project 3: Exposure and risk assessment for small and medium-sized hotels and hostels in the Fu-turismo program.

The implementation will be carried out using the CAPRA-ROBOT modeling platform, developed by INGENIAR, which will also be used as an educational tool in the Training Program conducted throughout the entire duration of the consultancy.

This report corresponds to Deliverable 1 – Inception Report, which includes the work plan for activities, including quality assessment, control procedures, and the dates on which deliverables will be presented; information on hazards and risk in Costa Rica, as well as a review of the state of knowledge on hazards, risk, and risk management at the national and regional levels; a review of relevant existing data for risk assessment, its sources, scale, and accessibility, as well as a description of existing initiatives in the region, particularly CCRIF and GRAF, seeking complementarity with potentially available models and data; and finally, a detailed technical description of the methodologies to be applied in the different activities that make up the projects.

This report is structured into different sections as described below:

Section 1.Introduction
Section 2.The workplan, including activities and schedule for each project.

Section 3. Summary of the current state of knowledge on hazard and risk assessment and management in Costa Rica.
Section 4. Description of the state of available information for the development of risk models.
Section 5. Basic theoretical and methodological aspects of probabilistic risk modeling.
Section 6. Methodologies for modeling meteorological forcing, incorporating climate change, and assessing hydrometeorological hazards.
Section 7. Methodologies to be used in the assessment of geological hazards included in this study.
Section 8. Required characteristics for the exposure models of the different sectors considered.
Section 9. Summary of different vulnerability models to be applied in this study.

# 2 WORKPLAN

The workplan presented below has been designed to comply with all the requirements established in the Termos of Reference of the GRMA – Costa Rica Project, as well as those outlined in the technical proposal submitted by INGENIAR-CIMNE. All activities are developed in coordination with Work Technical Group (WTG), which consists of various interested Costa Rican institutions and is coordinated by SUGESE.

## 2.1 Strategic Project: Demonstration of Risk Assessment Methods for Critical Infrastructure in Heredia.

The objective of this strategic project is to conduct modeling across multiple infrastructure sectors in the Heredia canton. This Project involves seismic and flood risk assessment for the portfolio of buildings and infrastructure in Heredia, based on the available information provided by the canton. The Project is carried out through the activities outlined Table 1. The corresponding Schedule is presented in Figure 1. All added values included were agreed directly with the Technical Working Group of this project.

Table 1. Strategic Project tasks

| Activity | Description | Task in ToR | Deliverable in ToR |
|---|---|---|---|
| Climate Model | Modeling of meteorological forcing and the incorporation of climate change projections. | T2.1<br>**T2.2** | D2.1a-f<br>**D2.2a-e** |
| Flood hazard model for the Pirro river | A detailed flood model of Pirro river will be developed to be used as a hazard input for the Heredia canton. | T2.1 | D2.1a-f |
| Seismic hazard model | The available information will be consulted in order to obtain the best available national seismic hazard model, which can be directly applied in catastrophe modeling, both for this Project and for other projects involving seismic risk. | T3.3 | D3.3a-b |
| Site effects Heredia | A site effects information layer will be generated in order to consider, in an approximate way, the response of soils within the canton, aiming to obtain better results in the seismic risk assessment. | Added value | |
| Landslide Hazard Model | A susceptibility and landslide hazard model will be developed at the scale of the Heredia canton. | Added value | |
| Buildings exposure Heredia | An exposure layer will be built at the individual building level within the canton, characterized by height, use, socio-economic level, structural system, replacement cost, among other relevant features. | T5.1,<br>T5.2 | D5a |
| Infrastructure exposure | An infrastructure exposure database will be built across multiple sectors (such as roads, water and sanitation, energy; according to the available information) at individual elements level or through distributed models, as required. | T5.1,<br>T5.2 | D5a |
| Buildings vulnerability | It refers to the definition of vulnerability curves for buildings of Heredia. | T4.1,<br>T5.3 | D4a-d |
| Infrastructure vulnerability | It refers to the construction of vulnerability curves using a model of archetypes of infrastructure elements. | T4.1,<br>T5.3 | D4a-d |
| Risk assessment | Application of the methodologies presented here to assess risk through actuarial metrics of catastrophe modeling | T5.4 | D5b-c |
| Calibration of results | The analytically calculated loss exceedance curve from the model will be compared with one constructed from historical event data to establish its correspondence. | T5.4 | D5b-c |

| Activity | Description | Task in ToR | Deliverable in ToR |
|---|---|---|---|
| Climate Model | Modeling of meteorological forcing and the incorporation of climate change projections. | T2.1<br>**T2.2** | D2.1a-f<br>**D2.2a-e** |
| Investment curve | As an added value, a collection of risk management actions will be evaluated to determine the optimal combination that reduces risk for fixed and increasing investment amounts. | Added value | |
| Resilience assessment | The resilience of the canton will be evaluated by incorporating its capacities to absorb, respond, and recover, in order to achieve a resilience metric for its infrastructure. | Added value | |

| Task | 15 Jan 25 | | Month | | | | | | | | | | | | 15 Apr 26 |
|---|---|---|---|---|---|---|---|---|---|---|---|---|---|---|---|
| | 1 | 2 | 3 | 4 | 5 | 6 | 7 | 8 | 9 | 10 | 11 | 12 | 13 | 14 | 15 |
| **Strategic Project: Demonstration of Risk Analysis Methods for Critical Infrastructure** | | | | | | | | | | | | | | | |
| Climate Model | | | | | | | | | | | | | | | |
| Pirro River Flood Model | | | | | | | | | | | | | | | |
| Seismic Hazard Model (ASLAC) | | | | | | | | | | | | | | | |
| Site Effects in Heredia | | | | | | | | | | | | | | | |
| Landslide Hazard Model | | | | | | | | | | | | | | | |
| Building Exposure in Heredia | | | | | | | | | | | | | | | |
| Infrastructure Exposure | | | | | | | | | | | | | | | |
| Building Vulnerability | | | | | | | | | | | | | | | |
| Infrastructure Vulnerability | | | | | | | | | | | | | | | |
| Risk Assessment | | | | | | | | | | | | | | | |
| Result Calibration | | | | | | | | | | | | | | | |
| Investment Curve | | | | | | | | | | | | | | | |
| Resilience Assessment | | | | | | | | | | | | | | | |

Figure 1. Activities Schedule for the strategic Project. (The blue cells indicate execution. The green cells indicate product delivery.)

## 2.2 Operational Project 1: Operational Project 1: Disaster and Climate Risk Assessment for Road Infrastructure – National Route 2 Pan-American Highway (RN2)

This project involves the risk assessment of road infrastructure, specifically National Route 2 (Pan-American Highway), against multiple hazards, including: seismic activity, flooding, volcanic eruptions, and landslides. While the model will be developed for the RN2 road, as an added value, as an added value, INGENIAR will provide support to the Technical Working Group of this project in order to model the risk for another National Route selected by LanammeUCR, and for the flooding, earthquakes, and landslides hazards. The project is carried out through the activities presented in. The corresponding schedule is presented in Figure 2. All added values included were agreed directly with the Technical Working Group of this project.

Table 2. Operational Project 1 Tasks

| Activity | Description | Task in the ToR | Deliverable in the ToR |
|---|---|---|---|
| Climate Model | Modeling of meteorological forcing and the incorporation of climate change projections. | T2.1<br>**T2.2** | D2.1a-f<br>**D2.2a-e** |
| National Flood Hazard model | A flood hazard model will be developed to be applied in the modeling of the RN2. | T2.1 | D2.1a-f |
| Landslides susceptibility model | A landslide susceptibility model will be developed, compatible with risk modeling. | T3.1 | D3.1a-b |
| Volcano hazards model | The available information will be reviewed, and approximate probabilistic volcanic hazard models will be proposed. | T3.2 | D3.2a-b |
| Seismic Hazard Model | Available information will be reviewed in order to obtain the best national seismic hazard model available, allowing for its direct application in catastrophic modeling, both for this project and for other projects involving seismic risk. | T3.3 | D3.3a-b |
| National Road exposure | A database of exposed elements of road sections will be created for risk assessment. | T6.1 | D6a |
| Road network vulnerability model | Road vulnerability models will be built based on archetypes of road segments. | T4.2 | D4a-d |
| Risk assessment | Application of the methodologies presented here to assess risk through actuarial metrics of catastrophe modeling. | T6.2 | D6b-d |
| Deterministic assessment (stress-test) | The results of some large-scale simulated events will be reported to illustrate the state of infrastructure in the face of extreme events. | T6.3 | D6b-d |
| Calibration of results | The analytically calculated loss exceedance curve from the model will be compared with one constructed from historical event data to establish its correspondence. | T6.2 | D6b-d |
| Investment curve | As an added value, a collection of risk management actions will be evaluated to determine the optimal combination that reduces risk for fixed and increasing investment amounts. | Added value | |
| Resilience assessment | The resilience of the road infrastructure will be evaluated by incorporating the country's capacities to absorb, respond, and recover. | Added value | |

| Task | 15 Jan 25 | | Month | | | | | | | | | | | | 15 Apr 26 |
|---|---|---|---|---|---|---|---|---|---|---|---|---|---|---|---|
| | 1 | 2 | 3 | 4 | 5 | 6 | 7 | 8 | 9 | 10 | 11 | 12 | 13 | 14 | 15 |
| **Operational Project 1: Climate and Disaster Risk Estimation of Road Infrastructure: National Route No. 2 Pan-American Highway South (RN2).** | | | | | | | | | | | | | | | |
| Climate Model | | | | | | | | | | | | | | | |
| Flood National Model | | | | | | | | | | | | | | | |
| Landslide Susceptibility Model | | | | | | | | | | | | | | | |
| Seismic Hazard Model | | | | | | | | | | | | | | | |
| Volcanic Hazard Models | | | | | | | | | | | | | | | |
| National Road Network Exposure | | | | | | | | | | | | | | | |
| Road Network Vulnerability | | | | | | | | | | | | | | | |
| Risk Assessment | | | | | | | | | | | | | | | |
| Deterministic Assessment (Stress Test) | | | | | | | | | | | | | | | |
| Result Calibration | | | | | | | | | | | | | | | |
| Investment Curve | | | | | | | | | | | | | | | |
| Resilience Assessment | | | | | | | | | | | | | | | |

Figure 2. Activity Schedule for Operational Project 1 (The blue cells indicate execution. The green cells indicate product delivery.)

## 2.3 Operational Project 2: Flood and Drought Risk for Small and Medium Agricultural Producers

This project involves risk climate assessment, considering flooding, intense rainfall and drought, in the national portfolios of coffee, sugarcane, and extensive livestock farming, primarily focused on small and medium producers, in particular, those implementing NAMA practices. However, as an added value, the entire national portfolio of the mentioned products will be modeled in order to visualize the contrast between NAMA and non-NAMA producers. The project is carried out through the activities presented in Table 3. The corresponding schedule is presented in Figure 3. All added values included were agreed directly with the Technical Working Group of this project.

Table 3. Operational Project 2 tasks

| Activity | Description | Task in the ToR | Deliverable in the ToR |
|---|---|---|---|
| Climate model | It refers to the modeling of meteorological forcing and the incorporation of climate change projections | T2.1, T2.2 | D2.1a-f, D2.2a-e |
| National Flood Hazard Model | A national flood model will be developed to be applied in the modeling of the entire road network portfolio. | T2.1 | D2.1a-f |
| Drought events | Selection of drought events from the simulations conducted, for baseline climate and future climates with climate change. | T2.2 | D2.2b |
| Intense rainfall events | Selection of very high precipitation events based on the simulations carried out, for baseline climate and future climates with climate change. | Added value | |
| Crops exposure | A base of exposure for crops will be created, distributed nationwide in units of cultivated land for each considered product. | T7.1 | D7a |
| Livestock exposure | A base of exposure for extensive livestock farming will be generated, distributed in livestock production units | T7.1 | D7a |
| Crops vulnerability | It refers to the parameterization of response models to water for the included crops. | T4.3 | D4a-d |
| Livestock vulnerability | It refers to the modeling of variations in animal load per production unit based on variations in the dry matter available for feeding. | T4.3 | D4a-d |
| Flood vulnerability (crops and livestock). | It refers to the modeling of soil inundation and its impact on biomass production (of crops or pasture). | T4.3 | D4a-d |
| Risk assessment | Application of the methodologies presented here to assess risk through actuarial metrics of catastrophe modeling. | T7.2 | D7b-d |
| Deterministic assessment (stress-test) | The results of some large-scale simulated events will be reported in order to illustrate the state of the infrastructure in the face of extreme events. | T7.3 | D7b-d |
| Performance calibration | The simulated yields will be compared with those reported in available agricultural surveys or statistical yearbooks to establish their correspondence. | T7.2 | D7b-d |
| Investment curves | As an added value, a collection of risk management actions will be evaluated to determine the optimal combination that allows for risk reduction with fixed and increasing investment amounts. | Added value | |
| Design of agricultural insurance | An exercise to size an agricultural insurance will be carried out in order to demonstrate the use of risk assessment in the design of financial protection instruments. | Added value | |

| Task | 15 Jan 25 | | Month | | | | | | | | | | | | 15 April 26 |
|---|---|---|---|---|---|---|---|---|---|---|---|---|---|---|---|
| | 1 | 2 | 3 | 4 | 5 | 6 | 7 | 8 | 9 | 10 | 11 | 12 | 13 | 14 | 15 |
| **Operational Project 2: Flood and Drought Risk to MSME Agricultural Producers** | | | | | | | | | | | | | | | |
| Climate Model | | | | | | | | | | | | | | | |
| Flood Hazard National Model | | | | | | | | | | | | | | | |
| Drought Events | | | | | | | | | | | | | | | |
| Crop Exposure | | | | | | | | | | | | | | | |
| Livestock Exposure | | | | | | | | | | | | | | | |
| Crop Vulnerability | | | | | | | | | | | | | | | |
| Livestock Vulnerability | | | | | | | | | | | | | | | |
| Flood vulnerability (crop and livestock) | | | | | | | | | | | | | | | |
| Risk Assessment | | | | | | | | | | | | | | | |
| Deterministic Assessment (Stress Test) | | | | | | | | | | | | | | | |
| Yield Calibration | | | | | | | | | | | | | | | |
| Investment Curve | | | | | | | | | | | | | | | |
| Design of an Agricultural Insurance Scheme | | | | | | | | | | | | | | | |

Figure 3. Timeline of activities for Operational Project 2. (The blue cells indicate execution. The green cells indicate product delivery.)

## 2.4 Operational Project 3: Evaluation of Exposure and Risk for Small and Medium Hotels and Hostels in the Fu-turismo Program.

Tourism is one of the main drivers of the Costa Rican economy, contributing significantly to economic production and job generation. This project aims to assess the disaster risk for this sector, focusing primarily on small and medium-sized hotel businesses[1], in relation to river and coastal flooding, as well as earthquakes and tsunamis. The project is carried out through the activities presented in Table 4. The corresponding schedule is shown in Figure 4. All added values included were agreed directly with the Technical Working Group of this project.

Table 4. Operational Project 3 Tasks

| Activity | Description | Task in the ToR | Deliverable in the ToR |
|---|---|---|---|
| Sea level rise model (Climate Change) | Sea level rise projections will be incorporated for greenhouse gas emission scenarios compatible with the future meteorological forcing considered. | T2.1, T8.2 | D2.1a-f |
| Tropical cyclones hazard model (storm surge and rain) | The influence of tropical cyclones on coastal flooding will be modeled. | T2.1, T8.2 | D2.1a-f |
| Tsunami hazard model | The influence of tsunamis on coastal flooding will be modeled. | Added value | |
| Hotels exposure | A database of hotel buildings will be created, primarily for small and medium-sized business owners. | T8.1, T8.3 | D8a-b |
| Hotels vulnerability | Vulnerability functions for hotel buildings will be established, considering losses in the property, contents, and income, as long as the information allows it. | T4.4 | D4a-d |

[1] However, it was agreed with the TWG of this project to include the entire hotel portfolio as an added value.

| | | | |
|---|---|---|---|
| Risk assessment | Application of the methodologies presented here to assess risk through actuarial metrics of catastrophic modeling | T8.4 | D8c-d |
| Risk indicators | Two risk indicators will be created: one for individual hotel facilities, and another for the tourism sector (at the canton level), to be published on the Fu-turismo portal. | Added value | |
| Results callibration | The analytical loss exceedance curve calculated with the model will be compared with one constructed from historical event data to establish its correspondence | T8.4 | D8c-d |
| Investment curve | As an added value, a collection of risk management actions will be evaluated in order to determine the optimal combination that allows for risk reduction with fixed and increasing investment amounts | Added value | |

| Task | 15 Jan 25 | | Month | | | | | | | | | | | | 15 April 26 |
|---|---|---|---|---|---|---|---|---|---|---|---|---|---|---|---|
| | 1 | 2 | 3 | 4 | 5 | 6 | 7 | 8 | 9 | 10 | 11 | 12 | 13 | 14 | 15 |
| **Operational Project 3: Fu-turismo MSME Hotels and Hostels Exposure and Risk Assessment** | | | | | | | | | | | | | | | |
| Climate Model | | | | | | | | | | | | | | | |
| National Flood Hazard Model | | | | | | | | | | | | | | | |
| Sea Level Rise Model Climate Change | | | | | | | | | | | | | | | |
| Cyclone Model (Storm Surge) | | | | | | | | | | | | | | | |
| Tsunami Model | | | | | | | | | | | | | | | |
| Hotel Exposure | | | | | | | | | | | | | | | |
| Hotel Vulnerability | | | | | | | | | | | | | | | |
| Risk Assessment | | | | | | | | | | | | | | | |
| Result Calibration | | | | | | | | | | | | | | | |
| Risk Indicators | | | | | | | | | | | | | | | |
| Investment Curve | | | | | | | | | | | | | | | |

Figure 4. Activity schedule for Operational Project 3. (Blue cells indicate execution. Green cells indicate product delivery.)

## 2.5 Capacity Building Program

A comprehensive capacity-building program will be developed, making the most of the modeling work from the four projects described above, while transferring essential knowledge and skills. This capacity building program includes the following groups of activities:

### 2.5.1 Workshops and meetings

The *socialization workshops* are in-person sessions aimed at sharing the progress of the work and the partial or final results of the project through plenary sessions. A total of 4 socialization workshops will be held.

- Workshop 1: This is a kickoff workshop for the activities of the training program. The general work plan and the specific plans for the projects are presented, as well as the launch of the training program and the asynchronous virtual course. The formation of the Technical Working Groups for each project is consolidated.
- Workshop 2: In this workshop, the overall progress of the project is presented to all stakeholders, as well as the progress of each of the four individual projects to the respective members of the Technical Working Groups and other stakeholders interested in the follow-up. This workshop

focuses on the intermediate results of hazard, exposure, and vulnerability modeling. A hands-on exercise in modeling the climate component is also carried out.

- Workshop 3: In this workshop, the progress of the risk assessment activities is shared, and the modeling results for each of the individual projects are presented to the respective members of the Technical Working Groups and other stakeholders interested in the follow-up. A hands-on exercise on the evaluation and interpretation of risk metrics is also conducted.
- Workshop 4: This is the final closing workshop. A general review of the activities of all projects is carried out, and the conclusions and recommendations from the evaluation are presented. The workshop focuses on the uses of the modeling and the potential future applications of the results beyond the scope of the consultancy. It also addresses the strategies to be defined jointly with the Technical Working Group for the sustainability, replicability, and transfer of the modeling processes to other territorial entities, regions, or sectors in Costa Rica.

On the other hand, the *working meetings* are in-person or virtual spaces (to be defined according to convenience) between the Consultant and the GTT, aimed at facilitating collaboration on specific tasks and transferring knowledge on practical aspects of data collection, management, and processing, as well as on the scientific aspects of climate and risk modeling.

Work meetings are scheduled individually with each Technical Working Group (TWG) according to the availability of the interested participants and, therefore, do not take place simultaneously with the different TWGs, but rather in a sequence or round of meetings over a period of one to two weeks. The specific focus of each meeting will depend on the progress made in each assessment; however, the following focus is anticipated for each round of meetings:

- Round 1 of meetings: These are the initial meetings with the TWGs of the projects. The project scope is shared once again, and necessary agreements are established regarding specific details related to the scope or added-value elements to be carried out for the benefit of the project. These agreements aim to promote ownership of the results, co-development, and the future sustainability of the modeling processes.
- Round 2 of meetings: In this second round of meetings, the progress of the projects is reviewed, and questions regarding specific details of the hazard, exposure, and vulnerability modeling are addressed. Additionally, training sessions on the models used in each specific project are conducted, complementing the content of the asynchronous virtual course.
- Round 3 of meetings: In this third round of meetings, the preliminary results of the risk assessment are reviewed with the TWGs, and final adjustments to the models are jointly agreed upon in order to consolidate the results. Additionally, training sessions on the models used in each specific project are conducted, complementing the content of the asynchronous virtual course.
- Round 4 of meetings: In the final round of meetings, strategies for the future of modeling, after the completion of the consultancy, are jointly defined with the TWGs in order to ensure the long-term sustainability of the modeling processes and their replicability in other regions or sectors. These strategies will be outlined in terms of a strategic work plan and medium-term needs."

Figure 5 shows the planned schedule for Workshops and Working Meetings. This schedule is indicative, as it depends on the availability of facilities and the GTT members who participate in these activities.

| Task | 15 Jan 25 | | Month | | | | | | | | | | | | 15 April 26 |
|---|---|---|---|---|---|---|---|---|---|---|---|---|---|---|---|
| | 1 | 2 | 3 | 4 | 5 | 6 | 7 | 8 | 9 | 10 | 11 | 12 | 13 | 14 | 15 |
| **Capacity Development in Multi-Hazard Risk Modeling and Management** | | | | | | | | | | | | | | | |
| Workshop 1 | | | | | | | | | | | | | | | |
| Workshop 2 | | | | | | | | | | | | | | | |
| Workshop 3 | | | | | | | | | | | | | | | |
| Workshop 4 | | | | | | | | | | | | | | | |
| Working meeting with TWG 1 | | | | | | | | | | | | | | | |
| Working meeting with TWG 2 | | | | | | | | | | | | | | | |
| Working meeting with TWG 3 | | | | | | | | | | | | | | | |
| Working meeting with TWG 4 | | | | | | | | | | | | | | | |

Figure 5. Schedule of Workshops and Working Meetings

### 2.5.2 Capacity Building Course in Risk Modeling

A capacity building course on climate and disaster risk modeling will be developed in a virtual and asynchronous format to facilitate the transfer of knowledge on the scientific foundations necessary for the implementation and understanding of the model and its results. The program is designed to provide capacity building on the theoretical aspects of risk modeling, focusing on the physical and mathematical foundations involved.

The main objective of this course is to provide participants with the scientific foundations necessary to carry out and understand risk modeling and its results. Participants will be capable of conducting disaster risk assessments for various natural hazards using advanced tools from the CAPRA ROBOT system.

This course is intended for professionals, specialists, and researchers involved in the Technical Working Group of each project, as well as officials from other interested local entities, with backgrounds in disciplines related to earth sciences, engineering, mathematics, physics, econometrics, or financial/actuarial analysis. It is recommended that participants have prior university-level training in probability and statistics.

The course has an approximate duration of 24 weeks, with an estimated commitment of 2 hours per week. However, the actual duration will depend on the personal dedication to the course. Figure 6 presents the corresponding curriculum.

## MODULE 1

| Unit | Content |
|---|---|
| 1 | Introduction |
| 2 | Conceptual framework for probabilistic risk assessment |
| 3 | Point metrics and retrospective assessment |
| 4 | Analytical CAT risk modeling |
| 5 | Modeling of exposed elements |

## MODULE 2

| Unit | Content | | | | | |
|---|---|---|---|---|---|---|
| | Earthquake | Volcano | Tropical Cyclones | Landslides | Floods | Drought |
| 1 | Seismology basics | Volcanology basics | Basic concepts of climate change | | | |
| 2 | Strong motion | Collapse regime of eruptive columnns | Downscaling and incorporation of climate change projections into hazard modeling | | | |
| 3 | Probabilistic assessment of seismic hazard | Modeling of volcanic products | Cyclones: structure, formation and effects | Mass removal processes | Hydrological modeling | |
| 4 | Site effects | Probabilistic assessment of volcanic hazard | Probabilistic assessment of tropycal cyclone hazard | Landslide susceptibility | Hydraulic modeling | Drought and drought indicators |
| 5 | Damage models: Vulnerability and fragility functions | | | | | Crop yield response to water |
| 6 | Seismic vulnerability | Vulnerability to gravitational flows and debris | Wind and storm surge vulnerability | Modeling susceptibility and hazard due to landslides | Flood vulnerability | Livestock load assessment |

## MODULE 3

| Unit | Content |
|---|---|
| 1 | Modeling resilience of dynamical structures |
| 2 | Holilstic risk assessment |
| 3 | Decision making under deep uncertainty: Robust decision making |
| 4 | Decision making under deep uncertainty: Risk control engineering |
| 5 | Introduction to catastrophe financial protection |

#### 2.5.2.1 *Module 1 – Foundations*

Module 1 covers the general foundations of probabilistic risk assessment. This module consists of five units, which include pre-recorded videos with theoretical content and a practical exercise to reinforce learning. The course is designed to progress asynchronously, at a pace of one unit per week, allowing each participant to complete it at their own rhythm, according to their personal availability.

This first module introduces the course approach through the analysis of natural disaster occurrence and the fundamentals of risk management. It also presents the theoretical concepts of probabilistic risk assessment, including ruin theory and metrics such as the loss exceedance curve, probable maximum loss, and expected annual loss. Retrospective and analytical approaches to risk assessment are also addressed. Finally, the methodology for constructing inventories of exposed elements is introduced, based on various sources of information that allow for their description, characterization, and valuation. The table provides a detailed overview of the topics covered in each unit.

Module 1 Syllabus

| Unit | Title | Topics |
|---|---|---|
| **1** | Introduction to Disasters and Risk Management | • Definition of risk<br>• Extensive and intensive risk<br>• Climate change adaptation<br>• Risk management processes<br>• Concepts of risk assessment |
| **2** | Conceptual Framework of Risk Assessment | • Uncertainty in risk assessment<br>• Loss occurrence process<br>• Ruin theory<br>• Loss exceedance curve |
| **3** | Point Metrics and Retrospective Assessment | • Interpretation of exceedance rates<br>• PML curve<br>• Probability of ruin<br>• Expected annual loss<br>• Portfolio and location-based losses<br>• Retrospective estimation of exceedance rates<br>• Estimator distribution<br>• Uncertainty in retrospective estimation |
| **4** | Analytical Assessment | • Probabilistic representation of hazard<br>• Representation of exposure and vulnerability<br>• Analytical evaluation of the loss exceedance curve |
| **5** | Exposed Elements | • Types of exposure<br>• Representation for risk assessment<br>• Exposure scales |

#### 2.5.2.2 *Module 2 – Components of risk modeling*

Once Module 1 has been successfully completed, participants may continue with Module 2, which focuses on the modeling of natural hazards and the assessment of the vulnerability of exposed elements. In this module, each participant can select the hazard of interest from those considered in the GRMA project.

That is, the module provides material related to hazard modeling and vulnerability assessment for all the phenomena included in the GRMA project.

Below is a summary of the scope and content of the modules related to the natural hazards covered in this phase of the course.

*Earthquake*

This module presents the conceptual foundations for the probabilistic assessment of seismic hazard and vulnerability. It covers basic aspects of seismology, the characterization of strong ground motion, seismic hazard assessment methodology, and soil response during a seismic event. In addition, it addresses the analysis of physical vulnerability, which must be evaluated and assigned to each exposed component. The table provides a detailed overview of the topics covered in each unit.

Module 2 Syllabus: Earthquake

| Unit | Title | Topics |
|---|---|---|
| **1** | Basic Aspects of Seismology | • Plate tectonic<br>• Geological faults<br>• Seismic source model<br>• Seismic moment and magnitude<br>• Slip distribution and seismic moment release<br>• Seismic waves<br>• Focal mechanism |
| **2** | Strong Ground Motion | • Accelerograms<br>• Source spectrum<br>• Random vibrations<br>• Attenuation models<br>• Structural response |
| **3** | Probabilistic Seismic Hazard Assessment | • Seismogenic sources<br>• Seismicity<br>• Attenuation<br>• Stochastic catalog<br>• Hazard integration<br>• Deterministic assessment |
| **4** | Site Effects | • Definition of site effects<br>• Estimation techniques<br>• 1D elastic response<br>• 1D nonlinear response<br>• Site effects in regions |
| **5** | Damage Models: Fragility and Vulnerability Functions | • Fragility curves<br>• Vulnerability curves |
| **6** | Seismic Vulnerability | • Structural behavior under cyclic lateral loads<br>• Behavior of structures sensitive to peak ground acceleration<br>• Behavior of structures sensitive to inter-story drift |

Theoretical sessions will be complemented by hands-on practical sessions, in which participants will learn to use specialized software for seismic hazard modeling, including:

**Strong Motion Analyst (SMA):** A program for processing seismological information. It implements methodologies for seismic signal processing, site response analysis, strong motion attenuation, and seismological catalog processing.

**R-CRISIS:** The seismic hazard module of CAPRA-ROBOT, developed primarily by Mario Ordaz (UNAM, Mexico). It is a versatile tool that enables Probabilistic Seismic Hazard Analysis (PSHA) and has been used in projects worldwide, including applications in the nuclear industry, insurance sector, building codes, and seismic microzonation.

**Vulnerability Studio:** A tool that enables modeling the vulnerability of exposed elements through mathematical functions that relate hazard intensity to direct physical impact. It implements various methods for creating vulnerability functions tailored to different types of hazards, allowing for the estimation of loss probability functions for different intensity levels.

**CAPRA ROBOT:** The risk calculation engine. It allows the computation of the Loss Exceedance Curve (LEC) for any exposure database, using the probabilistic CAT risk assessment framework. This module enables aggregation of losses from different hazards, generating multi-hazard risk results. CAPRA ROBOT calculates financial metrics such as the Average Annual Loss (AAL), the Probable Maximum Loss (PML), among others.

Participants will be able to perform probabilistic seismic hazard modeling and risk estimations using these tools, which are aligned with the CAPRA methodology employed in the GRMA project. These capabilities are in line with the objectives of the Strategic Project, as well as Operational Projects 1 and 3, strengthening the integration of technical tools in disaster risk management for the road infrastructure and tourism sectors.

*Tropical cyclones*

This module begins by covering the methods required to incorporate climate change into the assessment of hydrometeorological risk, given that phenomena such as intense rainfall—key triggers for landslides—are significantly affected by this phenomenon.

Next, it addresses key meteorological concepts related to the formation of tropical depressions, storms, and cyclones, their life cycle, wind field and storm surge models, as well as modeling approaches. From an engineering perspective, it also includes topographic effects, gust duration transformations, housing response, and damage models for buildings.

Additionally, the mathematical models necessary for the correct application and understanding of probabilistic risk assessment theory, its results, and associated metrics are presented.

Furthermore, physical vulnerability analysis will be developed for the occurrence of hurricane-force winds and storm surge flooding. The table provides a detailed overview of the topics covered in each unit.

Module 2 Syllabus: Tropical cyclones

| Unit | Title | Topics |
|---|---|---|
| **1** | Basic Concepts of Climate Change | • Earth's climate system<br>• Energy balance<br>• General atmospheric circulation<br>• Radiative forcing<br>• Greenhouse gas emissions<br>• Global circulation models<br>• Global projections |
| **2** | Structure and Formation of Tropical Cyclones | • Structure<br>• Formation conditions<br>• Generation of tropical cyclones<br>• Saffir-Simpson scale<br>• Trajectories and warnings |
| **3** | Effects of Tropical Cyclones | • Gradient wind<br>• Boundary layer<br>• Gust speed<br>• Tide hydrographs<br>• Ekman spiral<br>• Low pressure tide |
| **4** | Probabilistic Assessment of Tropical Cyclone Hazard | • Completeness of trajectories<br>• Trajectory perturbation<br>• Cyclone catalog and hazard integration<br>• Influence of climate change on tropical cyclone formation<br>• Trend in sea level rise |
| **5** | Damage Models: Fragility and Vulnerability Functions | • Fragility curves<br>• Vulnerability curves |
| **6** | Vulnerability to Wind and Flooding | • Effects of wind on structures<br>• Pressure loads on buildings<br>• Cyclic wind loads on tall buildings<br>• Vulnerability to wind field<br>• Vulnerability to debris impact<br>• Vulnerability to storm surge flooding |

The theoretical sessions are complemented by hands-on practical sessions, where you will learn to use specialized software for modeling the tropical cyclone hazard, including:

**Tropical Cyclones Hazard Modeler (TCHM):** TCHM is the CAPRA Robot platform module for tropical cyclone hazard. It implements calculation methodologies for strong winds, storm surge, and accumulated precipitation. TCHM allows the accurate simulation of the strengthening and weakening of tropical cyclones as they move along random tracks, as well as their surface effects in terms of hazard intensity.

**Vulnerability Studio:** This tool allows modeling the vulnerability of exposed elements through mathematical functions that relate hazard intensity to direct physical impact. It implements various methods for creating vulnerability functions adapted to different types of hazards, enabling the estimation of loss probability functions for different intensity levels.

**CAPRA ROBOT:** This is the risk calculation engine. It calculates the Loss Exceedance Curve (LEC) for any exposure database, using the probabilistic CAT-type risk assessment framework. This module allows aggregating losses from different hazards, generating multi-hazard risk results. CAPRA ROBOT calculates financial metrics such as the Annual Average Loss (AAL), Probable Maximum Loss (PML), among others.

Participants will be capable of performing probabilistic modeling of tropical cyclones hazards and risk estimations using these tools, which are aligned with the CAPRA methodology employed in the GRMA project. These capabilities are aligned with the objectives of Operational Project 3, focused on strengthening technical capacities for disaster risk assessment in the tourism sector.

*Landslides*

This module begins by covering the methods required to incorporate climate change into the assessment of hydrometeorological risks, given that phenomena such as intense rainfall—key triggers in the occurrence of landslides—are significantly affected by this factor. Climate change is integrated as a modifier of meteorological forcings, which transforms traditional risk metrics into imprecise probability estimates. To address this deep uncertainty, the theory of random sets is introduced, providing a solid mathematical foundation that allows for a rigorous consideration of climate change effects in risk assessment. Additionally, global climate projections through the year 2100 are used to illustrate the process of simulating meteorological variables indexed to multiple future scenarios.

Subsequently, mass movement processes, landslide classification, and the assessment of susceptibility to their occurrence will be studied. Artificial neural networks will also be introduced as a tool for modeling landslide susceptibility and hazard triggered by rainfall and earthquakes. Furthermore, physical vulnerability analysis will be developed using a binary approach. The table presents in detail the topics covered in each unit.

Module 2 Syllabus: Landslides

| Unit | Title | Topics |
|---|---|---|
| **1** | Basic Concepts of Climate Change | • Earth's climate system<br>• Energy balance<br>• General atmospheric circulation<br>• Radiative forcing<br>• Greenhouse gas emissions<br>• Global circulation models<br>• Global projections |
| **2** | Incorporating Climate Change into Hazard and Risk Modeling | • Downscaling<br>• Stochastic simulation<br>• Scaling rule<br>• All variations model |
| **3** | Mass Movements | • Mass movement processes<br>• Landslide classification<br>• Susceptibility to landslide occurrence<br>• Introduction to neural networks |
| **4** | Landslide Susceptibility | • Slope susceptibility modeling |

| | | |
|---|---|---|
| **5** | Damage Models: Fragility and Vulnerability Functions | • Fragility curves<br>• Vulnerability curves<br>• Binary vulnerability |
| **6** | Landslide Hazard Modeling | • Rainfall–landslide thresholds<br>• Landslides triggered by intense rainfall<br>• Landslides triggered by earthquakes |

The theoretical sessions will be complemented by hands-on sessions in which students will learn to use specialized software for landslide hazard modeling. These include:

**Drought Pro:** An advanced simulation tool that enables stochastic modeling of meteorological forcing—particularly rainfall—as a landslide-triggering phenomenon. The system was initially designed for drought modeling (hence its name) but has evolved into a general climate simulation system. Using a stochastic climate generator, it produces multiple simulations of meteorological variables (such as precipitation and temperature), based on available historical daily series in the territory. Given these capabilities, it is used for modeling various phenomena such as droughts, floods, landslides, or wildfires, by allowing the construction of probabilistic models of meteorological forcing.

**Landslide Hazard Mapper (LHM):** A tool for probabilistic landslide hazard assessment. Landslide susceptibility is evaluated using an artificial intelligence model (Artificial Neural Network – ANN), trained to classify each site as susceptible or not (in terms of its probability of being susceptible) based on its intrinsic characteristics. Triggering factors are defined as a set of seismic or rainfall events, each with associated thresholds for seismic acceleration and rainfall intensity. LHM calculates the probability of exceeding these thresholds for each triggering event and then aggregates, for each site, the total probability of landslide occurrence.

**CAPRA ROBOT:** As previously mentioned, this is the risk calculation engine. It allows the computation of the Loss Exceedance Curve (LEC) for any exposure database, using the CAT-type probabilistic risk assessment framework. This module supports the aggregation of losses from different hazards, generating multi-hazard risk results. CAPRA ROBOT computes financial metrics such as the Average Annual Loss (AAL), the Probable Maximum Loss (PML), among others.

Participants will be able to carry out probabilistic modeling of landslide hazards and risk estimation using these tools, which are aligned with the CAPRA methodology employed in the GRMA project. These capabilities are aligned with the objectives of Operational Project 1, aimed at strengthening technical capacities for disaster risk assessment in the road infrastructure sector.

*Volcanoes*

The module presents the conceptual foundations for the probabilistic assessment of volcanic hazard. Fundamental aspects of volcanology will be studied, as well as the probabilistic modeling of various volcanic products such as ashfall, pyroclastic flows, lahars (or mudflows), and lava flows. The Table provides a detailed overview of the topics to be covered in each unit.

Module 2 Syllabus: Volcanoes

| Unit | Title | Topics |
|---|---|---|
| **1** | Volcanism | • Origin and manifestation of volcanism<br>• Types of volcanoes<br>• Eruptive styles<br>• Volcanic Explosivity Index (VEI)<br>• Main volcanic products |
| **2** | Eruptive Column Collapse Regime | • Eruption magnitude<br>• Forcing mechanisms in eruptive columns<br>• Collapse regime<br>• Distribution of buoyant and collapsed material |
| **3** | Modeling of Volcanic Products | • Lava flows<br>• Pyroclastic Density Currents (PDCs)<br>• Lahars<br>• Ashfall<br>• Ballistic projectiles |
| **4** | Volcanic Hazard | • Probabilistic modeling of eruption occurrence<br>• Recurrence periods vs return periods<br>• Probabilistic integration |
| **5** | Damage Models: Fragility and Vulnerability Functions | • Fragility curves<br>• Vulnerability curves |
| **6** | Vulnerability to Gravity-Driven Flows | • Local high-energy events<br>• Binary vulnerability<br>• Roof resistance to volcanic ash deposits |

The theoretical sessions will be complemented by hands-on practical sessions in which students will learn to use specialized software for volcanic hazard modeling, including:

**VHAST (Volcanic Hazard Analysis and Simulation Tool):** a probabilistic volcanic hazard modeling tool that covers lava flows, pyroclastic flows, ashfall, and lahars. VHAST allows for the definition of probable volcanic product emission sites over a topographic grid, from which volcanic product distribution models are executed, event by event. VHAST incorporates eruptive column collapse models to robustly represent the hazard associated with explosive eruptions of Vulcanian or Plinian-type volcanoes.

**Vulnerability Studio:** a tool that allows the modeling of the vulnerability of exposed elements through mathematical functions that relate hazard intensity to direct physical impact. It implements several methods for creating vulnerability functions tailored to different types of hazards, enabling the estimation of loss probability functions for various intensity levels.

**CAPRA ROBOT:** a risk calculation engine. It enables the computation of Loss Exceedance Curves (LEC) for any exposure database using the probabilistic risk assessment framework of the CAT model type. This module allows the aggregation of losses from different hazards, producing multi-hazard risk results. CAPRA ROBOT calculates financial metrics such as the Average Annual Loss (AAL), the Probable Maximum Loss (PML), among others.

Upon completion, participants will be capable of conducting probabilistic volcanic hazard modeling and risk estimation using these tools, which are aligned with the CAPRA methodology used in the GRMA project. These capabilities align with the objectives of Operational Project 1, aimed at strengthening technical capacities for disaster risk assessment in the road infrastructure sector.

*Floods*

This module begins by covering the methods required to incorporate climate change into the assessment of hydrometeorological hazards, given that events such as intense rainfall can be significantly affected.

It then addresses key aspects of riverine flooding, which occurs when excessive rainfall over a prolonged period causes a river to exceed its capacity, overflow its banks, and inundate nearby areas, depending on the local topography. A climate generator is used to produce precipitation series that follow the same pattern as the historical records in the study area.

The module also covers comprehensive hydrological and hydraulic analyses within the watershed and along the river channel. Additionally, it includes the assessment of physical vulnerability, which must be evaluated and assigned to each exposed component. The topics to be covered in each unit are presented in detail in the Table.

Module 2 Syllabus: Floods

| Unit | Title | Topics |
|---|---|---|
| **1** | Basic Concepts of Climate Change | • Earth climate system<br>• Energy balance<br>• General circulation of the atmosphere<br>• Radiative forcing<br>• Greenhouse gas emissions<br>• Global circulation models<br>• Global projections |
| **2** | Incorporation of Climate Change in Hazard and Risk Modeling for Hydrometeorological Phenomena | • Downscaling<br>• Stochastic simulation<br>• Scaling rule<br>• All-variations model |
| **3** | Hydrological Modeling | • Hydrological cycle<br>• Reynolds transport theorem<br>• Hydrological system: precipitation, evapotranspiration, infiltration, and runoff<br>• Hydrograph of watershed outflow |
| **4** | Hydraulic Modeling | • One-dimensional modeling<br>• Two-dimensional modeling<br>• Coupling with HEC-RAS |
| **5** | Damage Models: Fragility and Vulnerability Functions | • Fragility curves<br>• Vulnerability curves |
| **6** | Vulnerability to Flooding | • Archetype model<br>• Damage functions<br>• Vulnerability functions |

The theoretical sessions are complemented by hands-on practical sessions, where participants will learn to use specialized software for flood hazard modeling. These include:

**Drought Pro:** An advanced simulation tool that enables stochastic modeling of meteorological forcing—particularly rainfall—as a landslide-triggering phenomenon. The system was initially designed for drought modeling (hence its name) but has evolved into a general climate simulation system. Using a stochastic climate generator, it produces multiple simulations of meteorological variables (such as precipitation and temperature), based on available historical daily series in the territory. Given these capabilities, it is used for modeling various phenomena such as droughts, floods, landslides, or wildfires, by allowing the construction of probabilistic models of meteorological forcing.

**Flood Analyst**: a software aimed at evaluating flood hazards. It calculates hazard intensities for extreme rainfall events and riverine floods at multiple locations within the area of interest. Flood Analyst generates stochastic extreme rainfall events and is coupled with the HEC-RAS software (Brunner & Bonner, 1994), which performs hydrological and hydraulic analysis for each event and provides the associated flood footprint.

**Vulnerability Studio:** a tool that allows the modeling of the vulnerability of exposed elements through mathematical functions that relate hazard intensity to direct physical impact. It implements several methods for creating vulnerability functions tailored to different types of hazards, enabling the estimation of loss probability functions for various intensity levels.

**CAPRA ROBOT:** a risk calculation engine. It enables the computation of Loss Exceedance Curves (LEC) for any exposure database using the probabilistic risk assessment framework of the CAT model type. This module allows the aggregation of losses from different hazards, producing multi-hazard risk results. CAPRA ROBOT calculates financial metrics such as the Average Annual Loss (AAL), the Probable Maximum Loss (PML), among others.

By the end of the module, participants will be able to carry out probabilistic flood hazard modeling and risk estimation using these tools, aligned with the CAPRA methodology employed in the GRMA project. These capabilities are in line with the goals of the Strategic Project as well as Operational Projects 1, 2, and 3, strengthening the integration of technical tools for disaster risk management in the Heredia canton, and in the agriculture, road infrastructure, and tourism sectors of the country.

*Drought*

This module begins by covering the methods required to incorporate climate change into the evaluation of hydrometeorological risks, given that phenomena such as intense rainfall are significantly affected by this phenomenon.

Subsequently, it addresses the generation of future climate conditions that combine precipitation deficits with above-average temperatures over a specific period and in a given geographic area. Using information

from future stochastic events, a prospective drought assessment can be conducted for the agricultural sector in order to evaluate crop damage and quantify losses. The total reduction in yield due to water stress can be calculated for the arable lands of a region or the entire country, considering the different stages of crop growth. Likewise, the reduction in livestock production can be quantified based on the decrease in available pasture for animals during drought events.

The following table details the topics that will be covered in each unit.

Module 2 Syllabus: Floods

| Unit | Title | Topics |
|---|---|---|
| **1** | Basic Concepts of Climate Change | • Earth climate system<br>• Energy balance<br>• General circulation of the atmosphere<br>• Radiative forcing<br>• Greenhouse gas emissions<br>• Global circulation models<br>• Global projections |
| **2** | Incorporation of Climate Change in Hazard and Risk Modeling for Hydrometeorological Phenomena | • Downscaling<br>• Stochastic simulation<br>• Scaling rule<br>• All-variations model |
| **3** | Hydrological Modeling | • Hydrological cycle<br>• Reynolds transport theorem<br>• Hydrological system: precipitation, evapotranspiration, infiltration, and runoff<br>• Hydrograph of watershed outflow |
| **4** | Types of Drought and Indicators | • Meteorological drought<br>• Agricultural drought<br>• Hydrological drought<br>• Drought indicators<br>• Standardized indicators |
| **5** | Crop Response to Water | • Exposed elements of the agricultural sector and their characteristics<br>• Soil characteristics required for vulnerability modeling<br>• Crop water response model<br>• Water balance<br>• Crop development<br>• Biomass production<br>• Yield |
| **6** | Livestock Carrying Capacity | • Dry matter estimation<br>• Energy requirements of animals<br>• Carrying capacity |

#### 2.5.2.3 *Module 3 – Advanced Applications*

Once Module 2 has been successfully completed, participants may proceed to Module 3, which focuses on advanced applications in risk management and climate change adaptation. This module represents the final stage of the course and is essential for gaining a comprehensive understanding of the entire process. While it is recommended to complete all three modules for full training, those interested in understanding only the general structure of the risk management process and its strategic relevance may choose to move directly from Module 1 to Module 3.

This module will address key topics for decision-making in contexts of high uncertainty and complex systems, such as resilience modeling in dynamic systems, holistic risk assessment, robust decision-making, risk control engineering, and an introduction to financial protection against disasters. The table details the topics to be covered in each unit. This module is especially useful as it provides advanced tools to integrate technical risk analysis with planning, investment, and public policy processes.

Module 3 Syllabus: Advanced Applications

| Unit | Title | Topics |
|---|---|---|
| **1** | Resilience Modeling of Infrastructure Systems | • Concept of systems<br>• Interdependence of elements<br>• Supply/demand imbalance<br>• Performance curves<br>• Performance simulation |
| **2** | Holistic Risk Assessment | • Definition of contextual conditions<br>• Social fragility and lack of resilience<br>• Aggravating coefficient<br>• Indicator system and membership functions<br>• Disaggregation of holistic indicators |
| **3** | Robust Decision-Making | • Deep uncertainty<br>• Uncertain future states<br>• Theory of random sets<br>• Imprecise risk metrics<br>• Decision-making under deep uncertainty |
| **4** | Risk Control Engineering | • Risk control process<br>• Formulation of intervention actions<br>• Stochastic optimization<br>• Investment curves<br>• Optimal risk management and adaptation plans |
| **5** | Introduction to Financial Protection | • Types of financial instruments<br>• Justification and costs of instruments<br>• Risk retention and transfer structures<br>• Insurance claim modalities<br>• Introduction to CAT Bonds |

Figure 6. Curriculum for the Asynchronous Virtual Course.

## 2.6 Activities for Control and Quality Management

These activities are carried out throughout the development of the consultancy and aim to ensure the expected quality in all processes and products generated. The projects developed by INGENIAR-CIMNE are executed under the specifications of the Project Management Institute (PMI), following the guidelines and standards of the PMBOK (latest edition). All members of the INGENIAR team adopt the best practices and standards recommended by the PMI methodology.

### 2.6.1 Quality assurance plan

Project Quality Management encompasses all the activities necessary to achieve outcomes, meet objectives, and ensure the transfer of knowledge that will contribute to the future evolution of the project. This plan will serve as a guide for project management, containing the necessary tools to provide directions to project teams for its execution.

We understand that quality is a crucial factor for the success of projects and ensures the achievement of the established objectives. Project Quality Management encompasses all the necessary activities to achieve results, meet objectives, and ensure the transfer of knowledge to facilitate its development.

The quality standards that govern the work of INGENIAR-CIMNE include:

- Project Management and Team Leadership: Led by the team leader, who is ultimately responsible for the quality of the services provided.
- Experience: The project team consists of professionals with extensive experience in project management, modeling, risk assessment and management, information systems development, information technology, knowledge transfer, training, and stakeholder management.
- Document Review: All working documents are reviewed by the team leader.
- Regular Internal Follow-up Meetings: Our team holds discussion meetings to review the services provided, identify areas for improvement, and prioritize actions for attention and follow-up.
- Quality Control: Our quality control programs allow us to verify compliance with the quality standards of the Firms in each of our projects.
- Professional Training: All our professionals are trained in the policies and standards mentioned here, as well as those outlined in the terms of reference for this process.

To ensure the completion of the project and the achievement of objectives with high levels of quality, meeting the expectations of stakeholders, INGENIAR-CIMNE will adopt this Quality Assurance Plan, which considers the Planning, Execution, and Control phases, as described below:

- Quality *planning* involves identifying the requirements and standards that the project and its products must meet, as well as the tools to demonstrate compliance. This planning will be carried out in parallel with the overall project planning.

- The *execution* of activities is continuously monitored to assess the team's performance and recommend changes if necessary. Non-conformant results will be recorded and managed, discussed in follow-up meetings, and corrective action plans will be defined, all within an iterative process of continuous improvement.
- Quality *control* involves monitoring the deliverables to validate compliance with quality requirements. This responsibility rests with the team leader.

### 2.6.2 Project Monitoring, Tracking, and Control

To ensure the achievement of project objectives and scope, internal monitoring of activities and contingency management will be implemented. The following project management tools will be used for this purpose:

*Change management*

The change control of the project is based on the monitoring, tracking, and control of activities and deliverables. This will be carried out in supervision sessions. Changes will be documented, and once completed, they will be recorded as permanent changes in the project.

*Project risk management*

Risks that may affect the project are identified to reduce the probability of value loss. The project management team continuously reviews the risks projected at the beginning of the project and updates them as the project evolves.

*Knowledge management*

In this project, knowledge management aims to collect information from experience and systematize it to serve as a foundation for improvement in subsequent phases. Dialogue spaces will be sought to identify information through socialization sessions and follow-up meetings.

*Project Integration Management Plan*

The management of stakeholder integration will occur at all phases of the project:

- In planning: through defining the scope (hazards and sectors per project) with the active participation of all stakeholders.
- In execution: carrying out activities in line with the schedule and budget, adjusting as needed based on reviews and the evolution of the project.
- In monitoring and control: complying with the quality assurance plan and the monitoring and control framework established. Maintaining a record of changes.
- In closure: ensuring the completion of all activities before the approval of deliverables and adequately documenting the process to reach this stage.

*Project documentation*

- Document Structure: Preliminary versions of deliverables will be presented for validation with the GRMA team and counterpart entities, encouraging adjustments in early phases and avoiding rework in the final stages of each activity.
- Identification: A file labeling protocol will be established to identify its content and version.
- Storage: A virtual site will be provided for document storage, and the delivery of products will be made according to the terms of reference requirements.

*Communications Management Plan*

The communication and liaison system will be managed by the team leader, and its compliance will be the responsibility of all parties involved. The communication and liaison tools that will be used during the project execution include:

Table 5. Project communication tools

| **Document** | **Objective** | **Frequency** |
|---|---|---|
| Minutes | Inform the stakeholders about the topics discussed, conclusions, and commitments resulting from the meetings | A set of minutes for each meeting. |
| Information request | Request additional information beyond what was provided at the beginning of the project. | As needed |
| Invitation to meetings | As needed | As needed |
| Products delivery | Deliver reports resulting from the scheduled activities. | According to schedule |

# 3 STATE OF KNOWLEDGE ON HAZARD AND RISK IN COSTA RICA

As part of the literature review and analysis of existing studies required for this project, a description is provided of the current state of knowledge regarding hazard and disaster risk assessment in Costa Rica, with a focus on the phenomena that comprise this assessment. This is a document-based review that includes a description of the most relevant phenomena and historical cases, the evolution of knowledge in Costa Rica in recent years, the current state of policy and tools implementation for risk management, and the research gaps identified for the future.

## 3.1 Climate Change in Costa Rica

Costa Rica, with its diverse tropical climate, has experienced a sustained increase in temperature over recent decades (~0.2–0.3°C per decade since 1970), a lengthening of the dry season, and a higher frequency of hot days (World Bank, 2021). Although rainfall is naturally variable, changes have been observed: more short intense rainfall events, fewer rainy days, and prolonged drought periods (Castro-Vincenzi, 2024). This suggests a more irregular hydrological cycle, with impacts throughout the country (IPCC, 2022).

The country is also more vulnerable to extreme events intensified by global warming, such as droughts, floods, and storms. Although hurricanes were once uncommon, Hurricane Otto (2016) marked a shift in regional hazards (Castro-Vincenzi, 2024). Sea level rise on both coasts worsens erosion, flooding, and the salinization of aquifers (IPCC, 2022). Sensitive ecosystems such as cloud forests and coral reefs show signs of deterioration; an iconic example was the extinction of the golden toad in Monteverde, and the decline of harlequin frogs, linked to diseases and climate anomalies (Pounds et al., 2006; Fernández et al., 2006).

Even before full recognition of anthropogenic climate change, Costa Rica faced extreme events: the 1982–1983 El Niño drought caused agricultural losses and rationing; Storm César (1996) caused severe flooding and landslides.

In the past two decades, impacts have been more intense: Otto (2016) was the first hurricane to directly hit Costa Rica in over a century, causing losses of at least $185 million; Nate (2017) was the costliest disaster, with estimated damages of $562 million (~1% of GDP) (Castro-Vincenzi, 2024). The 2014–2016 drought affected over 500,000 people and caused agricultural losses of 60–80% in some areas. The IPCC (2022) estimates that the 2015 drought left 2.5 million people in Mesoamerica in emergency conditions. Additionally, floods are now almost annual, severely impacting public infrastructure (CNE, 2016; CGR, 2017).

### 3.1.1 History of Climate Change Effects in Costa Rica

Since the 1980s, Costa Rica has gradually built up its scientific capacity to study climate change. During that decade and the 1990s, the National Meteorological Institute (IMN) expanded its observation network, and extreme weather events began to be documented to help distinguish natural variability from possible long-term trends (Fernández et al., 2006). Projects like Mondo (1987) and studies on Hurricane Fifí (Fernández & Vega, 1996) helped lay the methodological groundwork. By the late 1990s, research in

Monteverde was already linking biodiversity loss to rising temperatures (Pounds et al., 2006). In 1994, Costa Rica hosted one of the first regional conferences on global change.

Institutional efforts began with the ratification of the country of the UN Framework Convention on Climate Change in 1994 and the release of its First National Communication to the UNFCCC in 2000, which identified warming trends (about 0.6°C since 1970) and changes in rainfall patterns (MINAE & IMN, 2000). Afterwards, the IMN and universities such as the University of Costa Rica (UCR) and the Costa Rica Institute of Technology (ITCR) expanded their climate research. A key milestone was the report The Climate of Costa Rica (IMN & MINAET, 2008), which became a major reference. The 2009 National Climate Change Strategy promoted applied research, and the creation of the Climate Change Directorate helped strengthen the link between science and public policy. Costa Rica has also contributed to the IPCC's Fifth Assessment Report (AR5) and led regional initiatives such as LatinoAdapta (Morales, 2018).

Costa Rica's approach stands out to be multidisciplinary, context-specific, and closely tied to policymaking. Studies have examined trends in temperature and extreme rainfall (IMN & MINAET, 2008; IPCC, 2022), impacts on ecosystems (Pounds et al., 2006), and effects on crops like coffee, bananas, and sugarcane (Corrales, 2017). The social and economic dimensions of climate change have also been explored, including migration and gender equity (Morales, 2018).

From a methodological perspective, the country uses downscaled regional climate models, risk assessments, and tools like Geographic Information Systems (GIS) to map hazards and vulnerabilities (World Bank, 2021; UNDP, 2021). Hydrological models are also used to project future water availability (IMN & MINAET, 2011), alongside studies on ecosystem-based adaptation solutions. Participatory approaches help include local knowledge in adaptation planning (Morales, 2018).

Today, climate change is visible in rising temperatures—around 1°C above mid-20th-century levels—especially in highland areas, which affects mountain ecosystems and increases pest outbreaks (IPCC, 2022). Although total annual rainfall hasn't changed uniformly, it has become more irregular, with more intense dry seasons and shorter but heavier downpours (Castro-Vincenzi, 2024).

Over the past 15 years, the number of weather-related emergencies has gone up. Around 80% of emergencies in the last decade were caused by such events—mainly floods and landslides (CNE, 2016). Tropical Storm Nate (2017) impacted 76 cantons, caused 14 deaths, and left damages totaling ₡384 billion (Castro-Vincenzi, 2024). Droughts in Guanacaste have also led to serious losses and water rationing (IPCC, 2022). Statistics show a rise in extreme events and their economic costs since 2005 (CGR, 2017). The most vulnerable areas include low-lying coasts, informal settlements, and dry regions.

Risk assessments are based on regional climate modeling (CORDEX), analysis of extreme weather data, and risk maps that combine climate hazards with social and physical data (IPCC, 2022; IMN & MINAET, 2009; CNE, 2016). Sector-specific techniques are also used, including hydrological models (HEC-HMS, WEAP), agroclimatic studies, and participation in international indexes like ND-GAIN and the Global Climate Risk Index (World Bank, 2021). Community-based assessments complement scientific data, and recently, economic cost-benefit analyses have been incorporated to help prioritize investments in adaptation (UNDP, 2021; Morales, 2018).

.

### 3.1.2 Climate Change Adaptation Instruments in Public Policy

Costa Rica has built a robust regulatory framework of public policies to address climate change, aligning international commitments with national policies. It has ratified the UNFCCC (1994), the Kyoto Protocol (2002), and the Paris Agreement (2016), integrating its Nationally Determined Contributions (NDCs) for both mitigation and adaptation (MINAET, 2009). The National Climate Change Strategy (ENCC, 2009) established guidelines for mitigation, adaptation, and monitoring, and led to the creation of the Climate Change Directorate (2014). National legislation includes the Organic Environmental Law (Law 7554/1995) and the Emergency Law (Law 8488/2006), which incorporates climate change as an aggravating factor for natural hazards (CNE, 2016). The National Risk Management Policy (PNGR) 2016–2030 aligns risk management with climate scenarios (CNE, 2016).

In terms of adaptation, the National Climate Change Adaptation Policy (PNACC) 2018–2030 guides the integration of climate risk into key sectors such as water resources, agriculture, health, and infrastructure (MINAE, 2018). The National Adaptation Plan (NAP), launched in 2022, defines priority actions for 2022–2026 in six areas: knowledge, land-use planning, ecosystems, infrastructure, productive sectors, and financing (MINAE, 2022). Although it primarily focuses on mitigation, the National Decarbonization Plan 2018–2050 also brings adaptive co-benefits.

Other instruments include the Environmental Services Payment Program (PSA, 1997) for forest conservation; National Development Plans (e.g., PND 2019–2022) with adaptation goals in water and agriculture (UNDP, 2021); and technical regulations such as resilient construction codes. While Costa Rica lacks a Framework Climate Change Law (La Ruta del Clima, 2021), this gap is partially filled by sectoral environmental laws (Forestry, Biodiversity, Water).

Notable achievements include: More than 98% of electricity from renewable sources, forest cover exceeding 52%, adaptation planning aligned with the UNFCCC and the Sendai Framework (MINAE, 2022; CNE, 2016), submission of three National Communications and two Biennial Reports to the UNFCCC, carbon neutrality goals aligned with the global target of limiting warming to 1.5°C (IPCC, 2022), leadership in international initiatives such as the High Ambition Coalition for Nature (UNDP, 2021).

However, gaps remain. Reports by the Comptroller General's Office (CGR, 2017) show uneven implementation: adaptation has received less attention than mitigation; some instruments like the ENCC were not fully implemented (Morales, 2018); and many institutions have yet to fully integrate climate risk into their mandates. The absence of a framework law has led to institutional fragmentation. At the local level, few municipalities have incorporated adaptation criteria into their plans, largely due to limited technical and financial resources (Morales, 2018). Monitoring and evaluation of policies are limited, and tracking climate finance is difficult (CGR, 2017). Despite this, Costa Rica performs well in the ND-GAIN Index, highlighting its adaptive capacity (World Bank, 2021).

### 3.1.3 Existing Gaps in Knowledge and Governance

Despite progress, gaps persist in knowledge, governance, and implementation of climate change-related activities.

*Scientific gaps* include low spatial resolution of climate data limits land-use planning; future climate scenarios are only available for some regions (Morales, 2018), limited participation in international scientific networks and insufficient technological collaboration, critical sectors are under-researched: public health (e.g., tropical diseases, heat stress) and marine-coastal zones (e.g., acidification, wetland impacts) lack long-term studies, and, although long time-series of climate data exist, a national, integrated, open-access repository is still lacking (World Bank, 2021).

Regarding the *institutional* field, gaps identified are the lack of a framework law which causes overlapping functions and weak coordination among institutions (e.g., MINAE, CNE, MAG, Ministry of Health), the Climate Change Directorate lacks sufficient authority to mandate cross-sectoral action (Morales, 2018), climate finance is fragmented and difficult to track (CGR, 2017), and fewer than 40% of municipalities have updated regulatory land-use plans, and few include climate risk maps.

In *public participation* and *science-policy*, while 90% of the population acknowledges climate change, this awareness has not yet been translated into sustained action (MINAE, 2018), and there is a disconnect between scientific research and public policy: researchers often work in isolation, and decision-makers do not consistently communicate their information needs (Morales, 2018).

In response to the identified gaps and the accelerating manifestations of climate change, Costa Rica has outlined several research and action priorities for the coming years. In the field of research, the priorities are: Improve spatial resolution of climate scenarios, monitor vulnerable ecosystems (e.g., coral reefs, public health), evaluate the effectiveness of adaptation measures using cost-benefit analysis (IPCC, 2022), and develop community resilience indicators and effective communication strategies to promote behavior change (MINAE, 2018).

In the realm of action, the priorities identified are: Strengthen knowledge management and institutional capacity (scientific committees, training, climate services), integrate adaptation into land-use and sectoral planning, update zoning plans, adapt agricultural practices, and redesign urban infrastructure, restore key ecosystems (watersheds, mangroves, coral reefs) as nature-based solutions (MINAE, 2018), develop resilient infrastructure, including appropriate building codes and climate risk assessments in design (MINAE, 2022), ensure sustainable financing**,** including access to international funds, a national climate fund, and parametric insurance mechanisms (CGR, 2017), and promote citizen and private sector participation**,** empowering communities and encouraging sustainable practices such as agroforestry and responsible ecotourism (UNDP, 2021).

## 3.2 Risk from Heavy Rain and Flooding

Extreme rainfall in Costa Rica—defined as daily precipitation exceeding 30 mm—occurs frequently and with high intensity, influenced by phenomena such as the Madden-Julian Oscillation (MJO), hurricanes,

and low-pressure systems (Poleo et al., 2014; Retana, 2012). These events, which account for up to 6% of annual rainfall, trigger floods and landslides in saturated soils or disturbed watersheds, particularly in areas like Guanacaste and the Central Pacific (Retana et al., n.d.; Cruz Roja, 2024a). Events such as La Niña 2010 (with rainfall excesses of 110%) and Tropical Storm Sara (2024) have increased risk for many communities (Brenes & Bonilla, 2012; Cruz Roja, 2024b). Orographic and convective factors further intensify the impact, especially in mountainous regions (CAPRA, n.d.).

Social vulnerability and inadequate land use exacerbate these impacts, leading to erosion, service interruptions, and road damage (Salgado, 2009; Orozco Montoya & Brenes Maykall, 2023). Hurricane Tomas (2010) caused losses totaling 142 billion colones (Retana, 2012). In 2024, with soil saturation levels between 85% and 100%, over 1,900 people were evacuated (Cruz Roja, 2024b). Although cold fronts account for 37% of extreme rainfall events, they contribute only 3% of total precipitation (Retana, 2012). These scenarios demand comprehensive monitoring and adaptation strategies.

Historically, heavy rainfall has caused significant damage: the Reventado River flood (1951), Hurricane Mitch (1998), and Hurricane Tomas (2010) all severely impacted infrastructure and communities (Vallejos Vásquez et al., 2012; CAPRA, n.d.; Brenes & Bonilla, 2012). In 2024, more than 1,900 people were evacuated in Guanacaste, while La Niña (2020–2022) affected 4,879 individuals (Cruz Roja, 2024b; Orozco Montoya & Brenes Maykall, 2023). Climate change and the lack of territorial planning are worsening the frequency and intensity of such events (CAPRA, n.d.; Brenes & Bonilla, 2012). Although response capacity has improved, logistical challenges persist (Cruz Roja, 2024a).).

### 3.2.1 History of the Study of Risk from Intense Rainfall in Costa Rica

The study of extreme rainfall in Costa Rica has evolved significantly—from early records dating back to 1723 to more advanced analyses conducted by the National Meteorological Institute (IMN), especially following the impact of Hurricane Mitch in 1998 (Vallejos Vásquez et al., 2012; Retana et al., n.d.). Over time, the focus shifted from simply tracking climate variability to incorporating the role of social vulnerability in shaping disaster risk (Poleo et al., 2014; Salgado, 2009). Institutions like the IMN and the National Emergency Commission (CNE) led this transformation by applying new technologies and studying key events such as La Niña (2010–2012) (Brenes & Bonilla, 2012).

Organizations such as CORBANA and ECLAC have further enriched this analytical approach by integrating socioeconomic data and future projections (CAPRA, n.d.; Retana, 2012). In the aftermath of Hurricane Tomas (2010), public policy efforts were strengthened. However, the absence of a National Urban Development Plan (PNDU) still limits the effective implementation of these advances (Brenes & Bonilla, 2012).

Today's approach is inherently interdisciplinary, blending meteorology, social sciences, and engineering. It identifies critical areas such as Bagaces and Pérez Zeledón using risk maps and socioeconomic indicators, while emphasizing community participation as a priority (Vallejos Vásquez et al., 2012). Efforts are also underway to promote climate education, territorial planning, and monitoring systems (Cruz Roja, 2024a).

Historical data and predictive models now play a key role in anticipating impacts. Institutions like the CNE and the Costa Rican Red Cross have invested in early warning systems, while watershed-based management is being promoted (Salgado, 2009). Yet, challenges remain—particularly in integrating local knowledge and applying public policy in vulnerable urban zones (Orozco Montoya & Brenes Maykall, 2023).

Between 2020 and 2022, 80% of disasters in the country were hydrometeorological, affecting communities such as Cóbano and Mogote (Cruz Roja, 2024b; Retana et al., n.d.). Analytical tools such as statistical models, time-series analysis, and risk maps are now regularly employed (Poleo et al., 2014; Vallejos Vásquez et al., 2012). The IMN uses climate data alongside unsatisfied basic needs (NBI) indicators, while the CNE relies on hydrological models. Although CAPRA's risk models allow projections dating back to 1861, greater investment in instrumentation and community training is still needed (Orozco Montoya & Brenes Maykall, 2023).

### 3.2.2 Risk Management Instruments for Heavy Rainfall in Public Policy

Costa Rica has strengthened its regulatory framework through Law No. 8488 and the National Risk Management Policy 2016–2030 (Retana et al., n.d.; Orozco Montoya & Brenes Maykall, 2023). The National Emergency Commission (CNE) applies emergency decrees and implements watershed management plans, while the National Adaptation Plan (2022–2026) and the GRAF framework help reinforce institutional resilience (Vallejos Vásquez et al., 2012).

However, regulatory plans and inter-municipal coordination still face limitations, particularly in vulnerable areas (Salgado, 2009). The effectiveness of emergency declarations largely depends on infrastructure investment and proper planning (Cruz Roja, 2024b).

Thanks to Law No. 8488, response mechanisms such as the deployment of 570 volunteers in 2024 have been possible. Still, the law faces resource constraints, and community training remains insufficient, with logistical challenges continuing to hinder efficient response (Cruz Roja, 2024a). Despite progress, greater local investment and international partnerships are necessary (Retana et al., n.d.).

### 3.2.3 Gaps in Knowledge and Risk Governance

Gaps persist in rainfall prediction, the integration of local knowledge, and municipal coordination (Poleo et al., 2014; Retana et al., n.d.; CAPRA, n.d.). Deficiencies in infrastructure and high levels of social vulnerability continue to hinder effective responses (Cruz Roja, 2024a).

The lack of a National Urban Development Plan (PNDU) increases urban exposure, while community education and psychosocial support remain limited (Brenes & Bonilla, 2012; Cruz Roja, 2024b). There is also a need for more research on emerging trends such as the increasing frequency of hurricanes, and greater resources for early warning systems (Vallejos Vásquez et al., 2012).

Key priorities include Improving predictive models, strengthening climate monitoring, developing vulnerability-based adaptation strategies, promoting community participation, and preventing construction in high-risk areas (Salgado, 2009).

Additional efforts must focus on improving infrastructure, enhancing inter-agency coordination, and addressing structural causes of risk such as poverty (Brenes & Bonilla, 2012). Investments in technology, climate education, and participatory planning are crucial to reducing vulnerability to extreme rainfall (CAPRA, n.d.; Retana et al., n.d.).

### 3.2.4 Coastal Flooding in Costa Rica

Costa Rica's coastlines face an increasing flooding hazard, a phenomenon that manifests with distinct characteristics along both the Caribbean and Pacific shores. These flood events are not isolated occurrences but rather the result of a complex interaction of oceanographic and atmospheric processes, intensified by global environmental changes (Lizano, 2014). There has been a notable rise in the frequency and intensity of these events, impacting vulnerable communities, critical infrastructure, and sensitive ecosystems. For instance, projections indicate that by 2030, sea levels in Puntarenas could rise by up to 20 centimeters, reaching 30 centimeters by 2050, which would inundate approximately 1,325 hectares in this province alone (Chacón Soto, 2023). These figures highlight the urgent need to understand and address the factors driving Costa Rica's coastal vulnerability, which is further exacerbated by expanding urban development and often inadequate territorial planning (Quesada-Román et al., 2024).

The processes driving coastal flooding are multifaceted. Rising mean sea levels—driven by thermal expansion of seawater and melting polar ice caps (Lizano, 2014; Nicholls and Cazenave, 2010)—are a fundamental cause. This is compounded by the intensification of storm surges and increased wave height and energy, phenomena linked to more frequent or stronger tropical storms and cyclones (Alfaro, 2007; Lizano, 2013). Coastal erosion is another closely related process, with estimates suggesting that 70% of the world's sandy beaches are retreating (Gornitz, 1995, cited in Lizano, 2014). In Costa Rica, erosion threatens the stability of shorelines, diminishes natural buffering capacity, and facilitates deeper inland penetration of seawater during high tides and storms (Lizano and Gutiérrez, 2011).

The impacts of these floods span multiple sectors. Infrastructure such as roads and ports, exemplified by Caldera, is particularly vulnerable, with waves already surpassing breakwaters and threatening commercial activities (Chacón Soto, 2023). The tourism sector—a cornerstone of Costa Rica's economy—faces significant risks from beach loss and damage to facilities in areas like Guanacaste (Lizano Araya et al., 2023). Coastal communities, many with high social vulnerability, suffer housing losses, livelihood disruptions, and increased exposure to health hazards (Villalobos-Sequeira et al., 2024). Coastal ecosystems, including mangroves in the Térraba-Sierpe National Wetland, are also affected, losing protective functions and biodiversity (Lizano, 2014b). The direct and indirect economic losses associated with these events are substantial, impacting agriculture and fluvial infrastructure as well (Quesada-Román et al., 2024).

Despite advances in understanding these phenomena, significant gaps remain in their study and management. Greater investment is needed in continuous, high-resolution monitoring systems for sea level, wave activity, and coastal topography to improve predictive models and early warning systems (World Bank, 2021). While localized flood scenario studies exist (Lizano Araya et al., 2023), it is critical to develop integrated national-scale risk and vulnerability assessments that incorporate updated projections and account for multiple interacting hazards. Coastal land-use planning must be strengthened and rigorously enforced to limit development in high-risk zones (Quesada-Román et al., 2024). Finally,

improving interinstitutional coordination and resource allocation is essential to implement effective adaptation measures that blend nature-based solutions with resilient grey infrastructure, while actively involving local communities in decision-making processes (Watson et al., 2022).

## 3.3 Drought Risk

Drought in Costa Rica is defined through three interrelated categories: meteorological (rainfall deficit), agricultural (lack of soil moisture), and hydrological (low streamflows) (Soto, 2013). Although drought is a natural climatic phenomenon, it becomes a hazard when precipitation shortages persist, leading to water scarcity (Soto, 2013). The most drought-prone areas are on the Pacific slope, particularly Guanacaste and regions bordering Nicaragua, where the dry season is longer and more intense (Soto, 2013; Quesada-Hernández et al., 2020). The El Niño–Southern Oscillation (ENSO), especially its El Niño phase, significantly reduces rainfall in the Pacific region and accounts for up to 90% of historical droughts (Soto, 2013; Bonilla, 2014).

Drought patterns in Costa Rica result from the interaction between regional and local climatic drivers. ENSO dominates annual variability and causes recurrent droughts in Guanacaste, while in the Central Valley and Central Pacific regions, these events are less frequent (Waylen et al., 1996; Hidalgo & Alfaro, 2012). In contrast, the Caribbean slope rarely experiences meteorological droughts (Birkel, 2006). Overall, Costa Rica's drought pattern is marked by its concentration in the Pacific and its impact across multiple scales.

Since the 1970s, El Niño-related droughts have significantly affected agriculture and water availability. The 1997–1998 event caused major losses in crop production and livestock (van der Zee et al., 2013; Calvo-Solano et al., 2018). Similar impacts were reported during the 2001 and 2009–2010 droughts (Soto, 2013). The 2014–2016 drought, considered the most severe in 75 years, amplified these effects, leading to millions in economic losses and water rationing in Guanacaste (Astorga, 2019).

Between 2005 and 2011, agricultural losses were estimated at $168 million (Soto, 2013). The droughts also affected electricity generation, as hydropower reservoirs declined. Rural communities faced food insecurity, which prompted both state assistance and international cooperation (WFP, 2015).

### 3.3.1 History of Drought Risk Research in Costa Rica

Since the mid-20th century, drought research in Costa Rica has evolved from basic climatic descriptions to more comprehensive investigations. In the 1990s, the concept of the Central American Dry Corridor was defined, and quantitative methods—such as duration indices and streamflow analysis—began to be used (van der Zee et al., 2012; Birkel, 2006).

By the 2000s, drought was increasingly framed within the context of climate change, with contributions to IPCC reports and studies supported by the CNE and IMN (CNE, 2016; Soto, 2013). Since 2010, interdisciplinary approaches combining climatology, hydrology, and social sciences have strengthened understanding of drought-related risk (Quesada-Hernández et al., 2020).

The Standardized Precipitation Index (SPI) has become the most widely used drought indicator, particularly the 6- and 12-month versions (Quesada-Hernández et al., 2020). Other tools include trend analysis (Mann-

Kendall) and climate modeling to explore causal mechanisms such as the Central American Jet Stream (Bonilla, 2014).

Recent studies increasingly incorporate socioeconomic and geospatial variables, identifying high-risk areas using frequency and vulnerability maps (Soto, 2013). Satellite imagery, GIS tools, and participatory research with local communities have also become common practice (Calvo-Solano et al., 2018).

Recent droughts in 2019, 2020, and 2023 suggest a trend toward intensification. In 2015, rainfall in some areas was 50% below average, affecting more than 500,000 people (Astorga, 2019; Rodríguez, 2019). Drought events have triggered food insecurity, drinking water crises, and environmental degradation, highlighting their destructive potential (UNOCHA, 2015).

To assess drought risk, researchers use regional climate models (CMIP6), historical recurrence analysis, and real-time satellite monitoring (Hidalgo & Alfaro, 2015; WMO, 2023). Multicriteria methodologies are also used, combining layers of hazard, vulnerability, and exposure (CNE, 2016). Tools like DesInventar help analyze historical impacts and project future scenarios (Quesada-Hernández et al., 2020).

### 3.3.2 Drought Risk Management Instruments in Public Policy

Costa Rica's institutional framework includes Law No. 8488 and the National Risk Management Policy (2016–2030), which recognize climate change as a drought intensifier (CNE, 2016). In the water sector, key instruments include the PIAAG and the National Drinking Water Policy (2017–2030) (Rodríguez, 2019).

In agriculture, the Ministry of Agriculture and Livestock (MAG) has implemented early warning systems and preventive assistance since 2015. These policies combine infrastructure projects (reservoirs, irrigation), water-use efficiency, and community support. Adaptation is also integrated into the National Adaptation Plan (2022–2026), which prioritizes water resources and agriculture (MINAE, 2022).

Costa Rica has included drought-related actions in its Nationally Determined Contributions (NDCs) and participates in regional platforms like the CCAD and the Sendai Framework (UNISDR, 2015). Drought management has improved thanks to initiatives like the Los Ángeles reservoir and the strengthening of ASADAS (rural water associations). However, challenges remain due to the lack of an updated Water Law (Rodríguez, 2019).

While the country complies with international standards (NAP, Paris Agreement), issues such as institutional weakness and limited funding threaten the long-term sustainability of these advances (Lancet Countdown, 2022). International cooperation has facilitated access to climate funds and technical assistance, supporting the implementation of local adaptation measures (GWP, 2020).

### 3.3.3 Existing Gaps in Knowledge and Governance

Significant gaps remain in local knowledge of the drought phenomenon. There is a lack of study on microclimates and specific regions, as well as inconsistent historical data (Birkel, 2006; Hidalgo & Alfaro, 2015). There are also limitations in attributing recent events directly to climate change (IPCC, 2022), and little research on the ecological, health, and internal migration impacts of drought (UNOCHA, 2015).

On the governance side, the absence of modern Water Law hinders integrated water resource management. Disconnects between scientific research and local action limit the use of early warning systems, and adaptation investment remains insufficient (Rodríguez, 2019). The inclusion of Indigenous and rural territories in policies is still partial, and planning efforts often fail to account for compound risks such as drought–flood interactions.

Current priorities include Refining local climate projections, studying aquifer behavior, developing composite drought indicators, evaluating the effectiveness of adaptation measures (Quesada-Hernández et al., 2020; Castellanos et al., 2022). There is also a pressing need to improve water governance, strengthen early warning systems, empower local communities, and secure sustainable financing (NAP Global Network, 2023; FAO, 2014).

## 3.4 Risk from Landslides

Landslides in Costa Rica are triggered by natural factors such as earthquakes and intense rainfall, as well as by human activities like deforestation and urban expansion. They are classified based on movement speed and material type, including translational, rotational, and debris flows (Pérez Arrieta, 2013; CNE, n.d.; Salazar et al., 2019). In the Virilla River basin, volcanic slopes are highly unstable, while in Irazú, hydrothermal activity contributes to large-scale events (Sequeira-Arguedas, 2021; Alvarado Induni et al., 2020). Annual rainfall exceeding 4,000 mm and slopes steeper than 25° significantly increase the likelihood of events such as the San Blas landslide, which involved 60 million m³ of material (Quesada-Román, 2020). At Barva Volcano, rainfall- or earthquake-induced lahars can reach speeds of 37 m/s (Salazar et al., 2019).

Slope instability is worsened by soil saturation and cohesion loss, threatening infrastructure and human settlements (Umaña González & Blanco Picado, 2016). In areas like Orosí and San José, poor land use intensifies risk (Consultores en Riesgos y Desastres, n.d.). Events such as the 2009 Cinchona earthquake demonstrate the potential severity of landslide hazards. Currently, there are over 145 active landslides in Puriscal and Turrialba, and recent incidents such as the Irazú Towers landslide (2020) highlight the urgent need for preventive action (CNE, 2023).

### 3.4.1 History of Landslide Risk Research in Costa Rica

Formal landslide research in Costa Rica began with the 1772 event at Barva Volcano, evolving in the 1960s with studies by ICE and geomorphological analyses (Salazar et al., 2019). In the 2000s, advanced methodologies such as the Mora-Vahrson approach were adopted, and technologies like Lidar, GPS, and digital models were applied in areas such as San José, Irazú, and Orosí (Umaña González & Blanco Picado, 2016; Alvarado Induni et al., 2020).

Recent research in Orosí and the Upper General River basin integrates geomorphology, probabilistic analysis, and international collaboration (Quesada-Román, 2020). While monitoring and mapping efforts have expanded, some regions—such as Barva Volcano—still lack sufficient documentation (Salazar et al., 2019).

Landslide risk assessment now combines slope stability analysis, fragility curves, and susceptibility maps with GIS tools to identify critical zones. The inclusion of social and physical factors has enhanced land-use planning and improved risk management strategies.

### 3.4.2 Landslide Risk Management Instruments in Public Policy

Costa Rica has legal instruments such as Law No. 3459 (1964) and Decree 22384 (1994), which regulate construction in hazard-prone areas. The CNE promotes actions including population relocation, reforestation, and retaining wall construction (CNE, n.d.). In Orosí and the Upper General River basin, hazard maps are used to guide territorial planning (Quesada-Román, 2020).

However, implementation of these measures remains uneven, and in many areas, their effectiveness has not been documented. Regions like Irazú and Barva still lack specific regulations. Informal urban development in San José and other locations continues to challenge risk governance (Umaña González & Blanco Picado, 2016).

Although early warning systems and emergency drills have been introduced, their impact assessments are limited. The absence of consistent monitoring and limited community education hinder effective protection.

### 3.4.3 Gaps in Knowledge and Governance

Several critical gaps persist. There is a lack of studies on the effectiveness of risk reduction measures in areas such as Jucó de Orosí and Puriscal and limited geological information on Irazú and Barva Volcano (Salazar et al., 2019; Alvarado Induni et al., 2020). In San José and Orosí, the absence of detailed soil data and weak urban policies increase vulnerability.

Shortcomings also exist in digital modeling, community participation, and preventive education, particularly in urban areas. Current priorities include developing risk maps, creating evacuation plans, conducting geotechnical studies, relocating critical infrastructure

In regions like Cartago and the Upper General River basin, it is essential to strengthen land-use planning and inter-institutional collaboration. Integrating risk planning into both urban and rural policies, with international support, is key to reducing growing vulnerabilities.

## 3.5 Seismic Risk

Costa Rica lies within a complex tectonic zone, where the Cocos, Caribbean, and Panama microplates interact. The subduction of the Cocos Plate beneath the Caribbean Plate occurs at rates of up to 89 mm/year, generating frequent and high-magnitude seismicity (DeMets et al., 2010). This tectonic activity produces interplate, intraplate, and crustal earthquakes, such as those observed in the Central Costa Rica and Panama Deformed Belts (Marshall et al., 2000). The most active seismic zones include the Nicoya and Osa peninsulas and the Central Valley (Hidalgo-Leiva et al., 2023). While the Caribbean side is less seismically active, it is still capable of producing destructive events, such as the 1991 Limón earthquake (Mw 7.7).

Historic earthquakes like the 1910 Cartago quake, which caused 700 deaths, and the 1991 Limón earthquake, with 48 fatalities and 7,000 people affected, underscore the country's high seismic hazard (Montero, 1989; Gutiérrez, 2012). More recently, the Cinchona earthquake (2009, Mw 6.2) and the Nicoya earthquake (2012, Mw 7.6) caused significant damage but fewer human losses, reflecting improved building codes and preparedness (Linkimer et al., 2018). Nevertheless, exposure remains high, with expected ground accelerations of up to 0.6g in areas such as Nicoya and Osa (Kerwa, 2022).

### 3.5.1 History of Seismic Risk Research in Costa Rica

Formal research into seismic risk began after the 1972 Managua earthquake, prompting the creation of the National Seismological Network (RSN) in 1983. Since then, ICE and the University of Costa Rica (UCR) have recorded over 120,000 seismic events, significantly improving detection and location accuracy (Kerwa, 2020). In parallel, OVSICORI-UNA has strengthened nationwide seismic monitoring. GPS networks have played a key role in monitoring tectonic deformation, particularly in Nicoya, where the 2012 earthquake was successfully anticipated (Protti et al., 2014).

Costa Rica employs both deterministic and probabilistic approaches for hazard assessment. Probabilistic Seismic Hazard Analysis (PSHA) began in 1977 and has since been refined with new seismic sources and site-specific attenuation functions (Kerwa, 2022). This approach has enabled the development of seismic zonation maps and improvements in structural design practices.

In the past 25 years, Costa Rica has experienced several major earthquakes (Mw ≥ 6.0). Human casualties have been reduced due to modern building regulations, though annual losses from earthquakes are still estimated at $45 million, and 57% of the country is classified as having high or very high seismic hazard (Kerwa, 2022). Reducing seismic risk remains a national priority.

### 3.5.2 Seismic Risk Management Instruments in Public Policy

The Costa Rican Seismic Code, in effect since 1974 and last updated in 2010, regulates earthquake-resistant design based on hazard zones and international standards (CFIA, 2014; EIRD, 2021). Specific regulations exist for critical infrastructure such as bridges and dams. Law No. 8488 (2005) created the National Risk Management System, coordinated by the CNE, and the National Risk Management Policy 2016–2030 aligns these actions with the Sendai Framework (UNDRR, 2022).

Compliance with the seismic code has improved structural resilience, as seen after the 2012 Nicoya earthquake. However, challenges remain in informal construction and rural areas. At the municipal level, only 60% of local governments have incorporated seismic prevention plans (REPOSITORIO CONARE, 2022), and implementation is often limited by financial and oversight constraints.

### 3.5.3 Existing Gaps in Knowledge and Governance

Important knowledge gaps persist regarding active fault systems, especially in Guanacaste, Talamanca, and the Central Valley. Many faults lack data on recurrence intervals, and paleoseismology is

underdeveloped (Kerwa, 2022). There is also no instrumentation in the offshore subduction zone, limiting the accuracy of hazard models. Slow-slip events along the subduction interface are still not fully incorporated into hazard assessments (Protti et al., 2014).

From a governance standpoint, thousands of older buildings—particularly schools and health centers—do not comply with current standards. Enforcement in informal settlements is weak, and only half of the municipalities have implemented building restrictions in high-hazard areas (CNE, 2021). Insurance coverage is low, and unlike countries such as Mexico or Japan, Costa Rica does not yet have an early warning seismic system (Kerwa, 2022).

Key priorities include reinforcing critical infrastructure, expanding monitoring networks, integrating risk management into all levels of urban development, advancing seismic education and community preparedness.

## 3.6 Tsunami Risk

Tsunamis in Costa Rica are infrequent but documented events on both coasts of the country (Chacón-Barrantes et al., 2021a; Fernández et al., 2000). Since the mid-18th century, around 40 tsunamis have been recorded, most of them of moderate magnitude and extent (Soloviev & Go, 1984). On the Pacific coast, they are usually caused by subduction earthquakes along the Middle America Trench, while in the Caribbean, they originate from seismic activity in the Panama Deformed Belt (Lindholm et al., 2017; O'Loughlin & Lander, 2003). Some distant-source tsunamis, such as those from Chile or Japan, have reached Costa Rican shores with wave amplitudes under one meter (NOAA/NCEI, 2021; Angove et al., 2019). Overall, Costa Rica faces a moderate tsunami hazard (Brizuela et al., 2014).

Local tsunamis typically have short arrival times (15–30 minutes) and moderate wave heights, yet enough to inundate low-lying coastal areas (Nishenko et al., 2021; Chacón-Barrantes & Arozarena-Llopis, 2021). Runups of 2–7 meters have been recorded, as in the Gulf of Nicoya (1950) and Guanacaste following the 1992 Nicaragua tsunami (Geist, 2002). In the Caribbean, reefs and co-seismic uplift have helped attenuate impacts. However, slow-rupture earthquakes can produce disproportionately large waves, as also seen in 1992. Given the historically low population density along the coasts, larger past tsunamis may have gone undocumented (Thiel & Hoffmann, 2011).

Although no megatsunami has affected Costa Rica in modern times, several events have caused significant local impacts. In 1854, a tsunami destroyed the settlement of Villa Golfo Dulce (Lindholm et al., 2017). The 1906 Colombia earthquake triggered minor flooding in the southern Pacific. The 1991 Limón earthquake (Mw 7.7) generated a tsunami that penetrated up to 100 meters inland, causing at least two fatalities (Nishenko et al., 2021). In 1992, a regional tsunami affected the northern Pacific with runups reaching 7 meters, though without casualties (Chacón-Barrantes & Arozarena-Llopis, 2021).

### 3.6.1 History of Tsunami Risk Research in Costa Rica

Throughout the 20th century, tsunamis received less attention than other geological hazards (Fernández et al., 2000). Systematic documentation began in the late 20th century with historical catalogs (Chacón-Barrantes et al., 2021a). After the 1992 Nicaragua tsunami, Costa Rica intensified its efforts, and in the

2000s, the first numerical simulations were developed (Ortiz et al., 2001). Geologists also began investigating paleotsunami evidence (Camacho et al., 1994; Thiel & Hoffmann, 2011).

Following the 2004 and 2011 global tsunamis, international cooperation was strengthened (IOC-UNESCO, 2018). In 2013, Costa Rica established SINAMOT at the Universidad Nacional, in coordination with the CNE, to focus on monitoring, capacity-building, and research (Chacón-Barrantes & Murillo-Gutiérrez, 2022). The country joined the Pacific Tsunami Warning System and the CARIBE-EWS, producing updated catalogs, modeling studies, and hazard assessments (Chacón-Barrantes, 2018; Brizuela et al., 2014).

The approach has been comprehensive, spanning historical reconstruction (1539–present) to numerical modeling using tools like MOST/ComMIT (NOAA). Deterministic scenarios with credible maximum earthquakes and regional probabilistic analyses have helped identify critical zones and generate hazard maps and evacuation routes using GIS, though uncertainty remains high.

Disciplines such as geophysics, oceanography, and GIS are integrated. Numerical models have successfully replicated recent events like the 2017 Mexico tsunami. However, gaps remain, especially regarding tsunamis triggered by landslides or volcanic eruptions (von Huene et al., 2004).

In 2012, the Nicoya earthquake (Mw 7.6) generated a small tsunami that was detected instrumentally. The 2010 Chile and 2011 Japan earthquakes triggered preventive evacuations. In 2022, the Hunga Tonga eruption caused an atmospheric tsunami observed on both coasts, with no damage but notable institutional response (Rivera-Cerdas et al., 2023).

Today, tsunami risk in Costa Rica is considered moderate—low probability, but potentially high impact in vulnerable coastal communities (UNISDR, 2015; World Bank, 2016). Tourism development has increased exposure, but also improved preparedness through real-time monitoring, local evacuation plans, and public education campaigns. Exercises like Caribe Wave and PacWave, along with beach signage, demonstrate progress (IOC-UNESCO, 2018). Still, a submarine earthquake of magnitude ~7.8 could generate meter-scale waves, especially in densely populated areas like Puntarenas (Chacón-Barrantes & Arozarena-Llopis, 2021). Climate change and sea level rise may further expand in inundation zones (IPCC, 2019).

### 3.6.2 Risk Management Instruments in Public Policy

Costa Rica has a robust legal and institutional framework aimed at comprehensive disaster risk management, within which efforts to mitigate tsunami hazards are integrated. Law No. 8488 on Emergencies established the National Risk Management System, assigning roles to the CNE and other institutions to prevent and respond to disasters, including tsunamis (Costa Rica, 2006). The National Risk Management Policy 2016–2030 promotes a multisectoral and preventive approach (World Bank, 2016). While it does not specifically mention tsunamis, it does include coastal hazards and climate change in territorial planning.

The CNE and SINAMOT have developed alert and evacuation protocols, updated after recent events (IOC-UNESCO, 2018). Costa Rica is also a signatory to the Sendai Framework for Disaster Risk Reduction (2015–2030), committing to early warning systems and community education (UNISDR, 2015).

### 3.6.3 Gaps in Tsunami Knowledge and Governance

Despite the progress made, significant gaps remain in the knowledge and management of tsunami hazards in Costa Rica, which could undermine the effectiveness of risk reduction efforts. Historical and paleotsunami records remain limited, complicating the estimation of recurrence intervals and maximum magnitudes (Thiel & Hoffmann, 2011). Studies on non-seismic tsunami sources, such as submarine landslides or volcanic eruptions, are also lacking (von Huene et al., 2004). Additionally, bathymetric and LIDAR topographic data are incomplete, reducing the accuracy of tsunami models (Chacón-Barrantes & Murillo-Gutiérrez, 2022).

On the operational side, Costa Rica still lacks adequate tide gauges and DART sensors on the seafloor (Angove et al., 2019). Although SINAMOT has installed some equipment, real-time monitoring is still unavailable along many sections of the coast. Community preparedness is uneven, and tsunami risk has yet to be fully integrated into land-use planning in many coastal areas (World Bank, 2016). Moreover, coordination between technical experts and decision-makers needs improvement to translate data into effective action.

Institutional sustainability also depends on continued investment and capacity-building. Much of the equipment maintenance and research funding still relies on international cooperation or academic initiatives (Chacón-Barrantes & Murillo-Gutiérrez, 2022). Strengthening the geological record, diversifying hazard scenarios, and ensuring progress reaches all at-risk coastal communities remain key priorities.

## 3.7 Volcanic Risk

Costa Rica is home to at least 112 identified volcanic centers, of which 7 are considered active (Alvarado, 2012). Volcanic activity is concentrated along the Central Volcanic Range and the Guanacaste Volcanic Range, associated with the subduction of the Cocos Plate beneath the Caribbean Plate (Barquero, 2020). The most active volcanoes include Turrialba, Poás, Irazú, and Rincón de la Vieja, which pose hazards such as phreatic and explosive eruptions, gas emissions, pyroclastic flows, and lahars. These hazards can affect populated areas, infrastructure, and productive activities (Alvarado et al., 2017).

The Turrialba Volcano has exhibited intermittent eruptive activity since 2010, with significant events in 2014, 2015, and 2016, impacting the Central Valley with ash and gas emissions (OVSICORI, 2021). Poás also experienced major eruptions in 2017 and 2019, leading to park closures and evacuations. At Rincón de la Vieja, over 1,300 eruptions were recorded between 2011 and 2021, many triggering secondary lahars (Barquero et al., 2021). While Irazú has been less active in recent years, it remains under constant monitoring due to its eruptive history.

The risk varies depending on the type of volcano and its surrounding environment. For example, Poás has an acidic crater lake that can trigger sudden phreatic eruptions, while Turrialba, due to its location and prevailing winds, can disperse ash over distant regions (Alvarado et al., 2017). Lahars, or volcanic mudflows, pose serious risk in places like Upala and Bagaces, where past events from Rincón de la Vieja have already caused damage (Barquero et al., 2021).

Urban and tourism growth near active volcanoes has increased exposure. Although monitoring has improved, land-use planning remains limited, and many communities are not prepared for a major

eruption. This highlights the need for volcanic risk management that integrates scientific monitoring, community education, and updated emergency plans.

### 3.7.1 History of Volcanic Risk Research in Costa Rica

The study of volcanism in Costa Rica dates to the 19th century, with early accounts from naturalists and explorers documenting eruptions. In the 1960s, the Costa Rican Electricity Institute (ICE) and the University of Costa Rica began conducting systematic studies. A milestone came with the creation of OVSICORI-UNA in 1984, which now operates a network of seismic stations, thermal cameras, and gas sensors monitoring the country's active volcanoes.

These studies have helped document historical eruption cycles and behavioral patterns, such as Irazú's prolonged 1963–1965 eruption, and more recent activity at Turrialba and Poás (Alvarado, 2012). Techniques such as InSAR and GPS-based deformation analysis, geochemical monitoring, and ash dispersion modeling are now used to anticipate eruptions.

More recently, research has begun to integrate volcanic hazards with social vulnerability**.** For example, studies around Rincón de la Vieja have assessed community preparedness and exposure to lahars and gas emissions. Hazard maps developed by CNE and OVSICORI have significantly improved land-use planning and emergency response**.**

In recent years, remote monitoring and drone use have increased, allowing safer observation of active craters. These scientific advances have improved the country's ability to respond to volcanic events, although challenges remain in risk communication and local preparedness**.**

### 3.7.2 Volcanic Risk Management Instruments in Public Policy

Costa Rica has legal frameworks such as Law No. 8488 on Emergencies and Risk Prevention and policies like the National Risk Management Strategy 2016–2030, which include volcanic risk. The CNE coordinates emergency management efforts, supported by OVSICORI and ICE, which maintain volcano surveillance systems.

Volcanic hazard maps are essential tools for planning, and have been updated for Poás, Turrialba, and Rincón de la Vieja. In high-risk areas, evacuation protocols, exclusion zones, and community drills have been implemented (CNE, 2023). The National Volcanic Emergency System (SINAMEV) manages official information during crises, working with media outlets and local networks.

In the tourism sector, measures have been adopted to restrict access during active periods. National parks, such as Poás, now have safety protocols, gas sensors, and trained guides. However, in rural areas, emergency response plans remain limited, and greater education and community participation are needed.

Costa Rica also engages in regional networks like REDLAVA and collaborates with international centers such as the USGS, which have facilitated technical support, equipment, and funding. Despite progress, uneven implementation of plans across the country limits the effectiveness of volcanic risk governance.

### 3.7.2 Gaps in Volcanic Risk Knowledge and Management

Significant challenges persist in the management of volcanic risk in Costa Rica. One of the most pressing concerns is the limited level of preparedness among communities living near active volcanoes. While emergency plans have been developed, many of them are outdated or have not been tested through simulation exercises, reducing their effectiveness in real scenarios (CNE, 2023). On the scientific front, there is a lack of data on the recurrence intervals of eruptions for less active volcanoes such as Tenorio and Miravalles, and the absence of real-time monitoring systems on volcanoes classified as low risk represents an additional vulnerability. Moreover, the integration of scientific knowledge into local decision-making remains insufficient. Alert systems are not always accompanied by clear and accessible information for the general public, which hinders timely and informed responses.

Further gaps include inadequate infrastructure for temporary shelters in high-risk areas, insufficient investment in preventive education, and weak enforcement of land-use regulations in volcanic zones. In many communities, evacuation routes are poorly marked or in disrepair, limiting their utility during emergencies. To address these issues, it is crucial to strengthen community-based education initiatives, expand monitoring networks to include lower-risk volcanoes, and ensure that emergency plans are both current and actionable. At the same time, improving critical infrastructure in exposed areas, enhancing coordination among institutions, and securing stable funding for research and risk reduction efforts are essential to building long-term resilience.

# 4 CURRENT STATE OF AVAILABLE INFORMATION

Relevant databases, documents, and information have been identified to carry out risk assessments for the four sub-projects in Costa Rica. The information sources and associated data are presented below.

For specific hazards, existing studies on national and local flooding, particularly for the Pirro River, will also be utilized. To evaluate landslide hazards, LiDAR data and local catalogs will be leveraged, whereas volcanic hazard assessments will rely on information derived from the CAPRA model. Internationally recognized models such as RESIS II, CAPRA, and ASLAC will be employed for seismic risk assessment. Available sector-specific information related to infrastructure, agriculture, and hotels is considered adequate. Lastly, existing vulnerability models, primarily CAPRA and GAR, provide a solid foundation for initiating assessments.

## 4.1 Climate

The National Meteorological Institute (IMN) of Costa Rica is the entity responsible for observing, studying, and recording the country's climate. Founded in 1952, its mission is to provide high-quality meteorological, climatological, and seismic information to contribute to the well-being and safety of the population.

The IMN operates a network of automatic weather stations strategically distributed across the national territory. These stations enable the real-time collection of essential meteorological data, such as temperature, relative humidity, atmospheric pressure, wind speed and direction, and precipitation. The collected information is crucial for issuing forecasts and alerts, as well as for studying climate phenomena.

Data from these stations is available at the following link: https://www.imn.ac.cr/web/imn/estaciones-automaticas. This site allows real-time monitoring of the stations, providing continuously updated data and enabling accurate tracking of current weather conditions.

The station network covers various regions, including the North Pacific, Central Pacific, South Pacific, Northern Zone, Central Valley, Northern Caribbean, and Southern Caribbean.

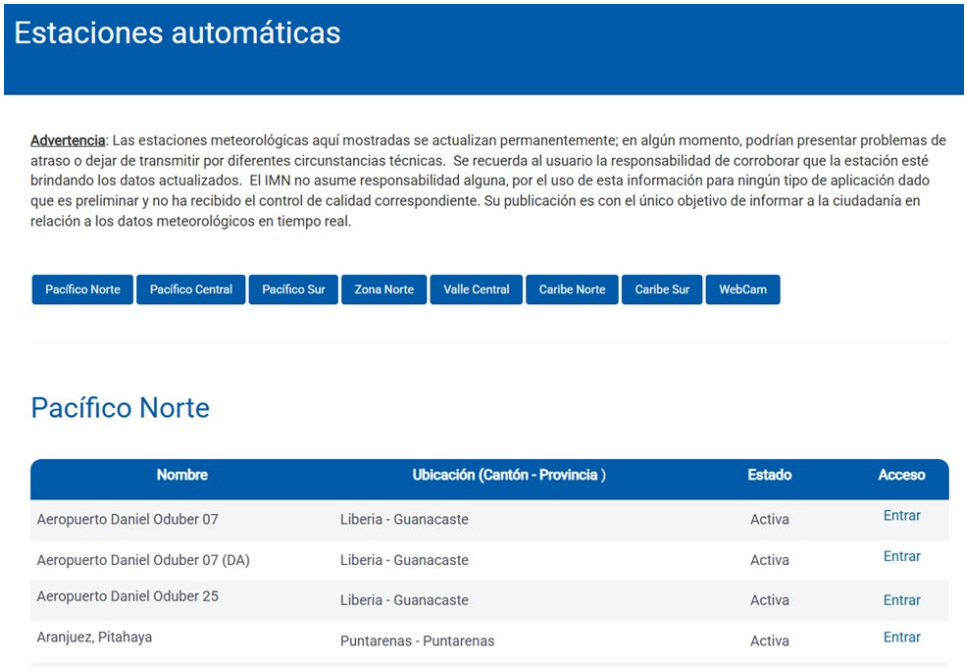


Figure 7. Weather station viewer of Costa Rica

An interactive map is also available on the IMN website:

https://www.imn.ac.cr/web/imn/mapa#c29tZUhhc2hUaGF0RG9lc250RXhpc3Q. This map allows users to view monthly average information for variables such as precipitation, temperature, and wind.

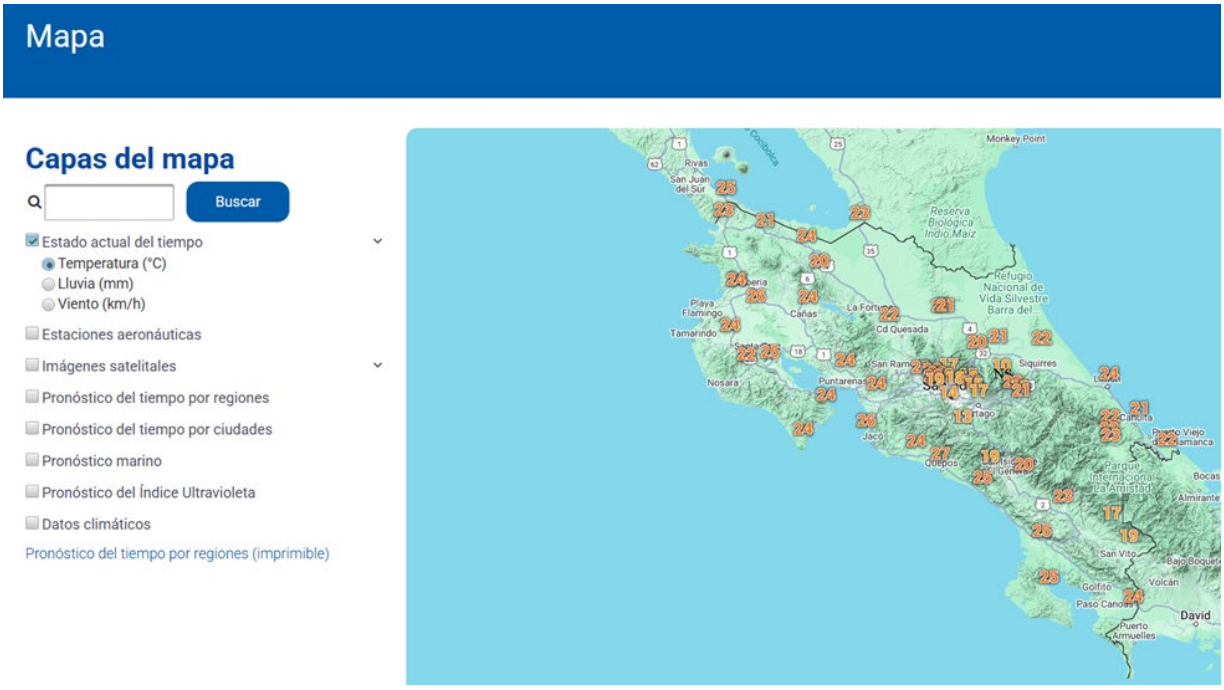


Figure 8. Interactive map of meteorological stations

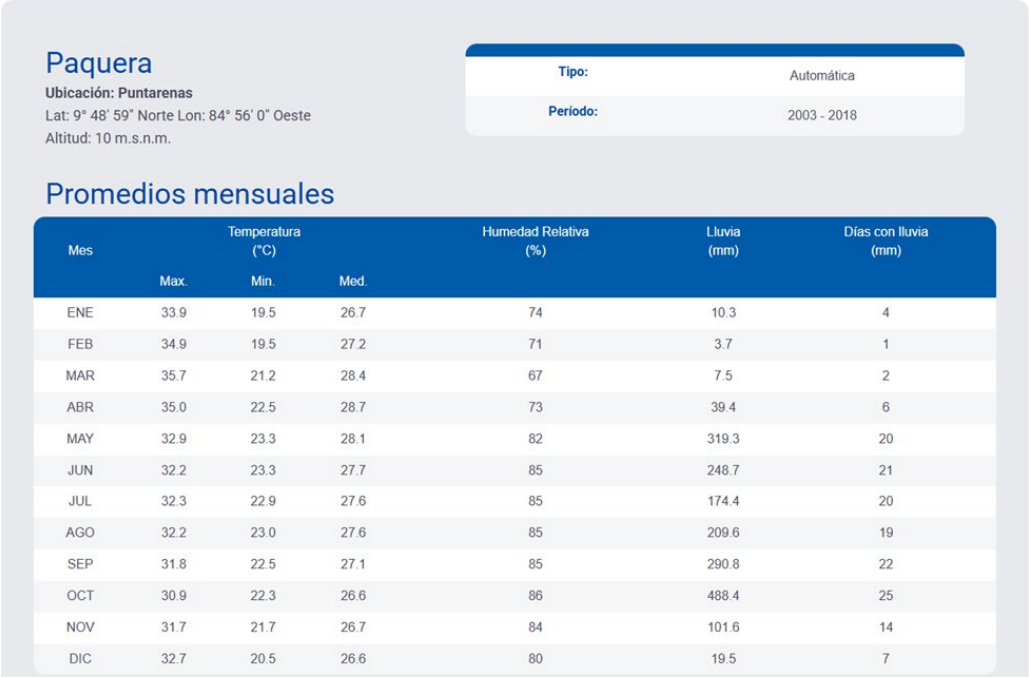

## Paquera

**Ubicación: Puntarenas**
Lat: 9° 48' 59" Norte Lon: 84° 56' 0" Oeste
Altitud: 10 m.s.n.m.

| | |
|---|---|
| **Tipo:** | Automática |
| **Período:** | 2003 - 2018 |

## Promedios mensuales

| Mes | Temperatura (°C) | | | Humedad Relativa (%) | Lluvia (mm) | Días con lluvia (mm) |
|---|---|---|---|---|---|---|
| | Max. | Min. | Med. | | | |
| ENE | 33.9 | 19.5 | 26.7 | 74 | 10.3 | 4 |
| FEB | 34.9 | 19.5 | 27.2 | 71 | 3.7 | 1 |
| MAR | 35.7 | 21.2 | 28.4 | 67 | 7.5 | 2 |
| ABR | 35.0 | 22.5 | 28.7 | 73 | 39.4 | 6 |
| MAY | 32.9 | 23.3 | 28.1 | 82 | 319.3 | 20 |
| JUN | 32.2 | 23.3 | 27.7 | 85 | 248.7 | 21 |
| JUL | 32.3 | 22.9 | 27.6 | 85 | 174.4 | 20 |
| AGO | 32.2 | 23.0 | 27.6 | 85 | 209.6 | 19 |
| SEP | 31.8 | 22.5 | 27.1 | 85 | 290.8 | 22 |
| OCT | 30.9 | 22.3 | 26.6 | 86 | 488.4 | 25 |
| NOV | 31.7 | 21.7 | 26.7 | 84 | 101.6 | 14 |
| DIC | 32.7 | 20.5 | 26.6 | 80 | 19.5 | 7 |

Figure 9. Monthly averages viewer.

In addition to data collected from ground-based stations, satellite-based sources such as CHIRPS and Copernicus also provide valuable information.

### 4.1.1 CHIRPS

The CHIRPS database (Climate Hazards Group InfraRed Precipitation with Station data) is globally recognized as a reliable source for precipitation analysis. It covers a broad geographic range, spanning from 50°S to 50°N across all longitudes, and offers daily precipitation records from 1981 to the present. By combining satellite imagery with ground-based meteorological observations, CHIRPS generates high-accuracy time series that support climate trend analysis and seasonal drought monitoring.

One of CHIRPS's most notable strengths is its ability to integrate satellite data within situ measurements, significantly enhancing the precision and reliability of its records. This makes it an invaluable tool for researchers and professionals involved in climate analysis, water resource management, and risk assessment related to hydroclimatic events.

Daily global datasets, available in version 2.0, can be freely downloaded from the official website: https://www.chc.ucsb.edu/data/chirps. Files are provided in raster format (.tiff) with a spatial resolution of 0.05° x 0.05°, enabling detailed national and regional analyses and the identification of spatial and temporal precipitation patterns with high precision.

### 4.1.2 ERA5 – Copernicus Climate Change Service

The Copernicus Climate Change Service provides a comprehensive global meteorological dataset designed for climate modeling and monitoring. These data are produced through reanalysis processes conducted by the European Centre for Medium-Range Weather Forecasts (ECMWF), a world leader in weather prediction.

The Copernicus database offers both historical and near real-time information, with records dating back to 1940 and updates available with a minimal delay of only five days from the present date. Additionally, data are available on an hourly basis, enabling detailed analyses of climatic variations over both short and long-time scales.

Copernicus data can be downloaded free of charge from their official portal: https://cds.climate.copernicus.eu. Available formats include raster grid files and NetCDF, which are widely used in environmental modeling and spatial analysis applications. These formats facilitate seamless integration into Geographic Information Systems (GIS) and climate analysis tools.

Of particular note is the ERA5 dataset, the fifth generation of climate reanalysis developed by ECMWF, renowned for its high spatial and temporal resolution. ERA5 provides a range of key meteorological variables including precipitation, temperature (mean, minimum, and maximum), solar radiation, specific humidity, surface air pressure, and wind speed.

A significant advantage of ERA5 is that its variables are elevation-adjusted, enhancing accuracy in regions with complex topography.

## 4.2 Climate Change

The National Meteorological Institute (IMN) of Costa Rica, through its portal http://cglobal.imn.ac.cr/, provides detailed information on climate change scenarios for the country. These scenarios are essential for anticipating and planning potential future changes in climate conditions, enabling better preparedness and adaptation to the challenges posed by climate change.

Costa Rica's Fourth National Communication to the United Nations Framework Convention on Climate Change (UNFCCC), published in 2021, is available on the IMN's website. This report presents an assessment of the country's greenhouse gas emissions, outlines the mitigation and adaptation policies and measures implemented, and addresses the financial and technological support needs to fulfill its international climate commitments.

Regarding climate projections, the report analyzes two greenhouse gas concentration pathways (RCPs): RCP2.6 and RCP8.5. These projections cover three climate periods: 2010–2039, 2040–2069, and 2070–2099, offering a detailed view of possible climate variations in the country under different emission scenarios.

In addition to this information, the Coupled Model Intercomparison Project (CMIP) models—currently in its sixth phase (CMIP6)—contribute to the Intergovernmental Panel on Climate Change's (IPCC) Sixth

Assessment Report (AR6). These models can be downloaded from the Copernicus database: https://cds.climate.copernicus.eu/datasets/projections-cmip6?tab=download.

These climate models are fundamental tools for understanding and projecting the impacts of climate change. The platform provides daily and monthly global climate projection data, covering a wide range of experiments, models, and time periods.

Key variables available through these models include precipitation, temperature, wind speed and direction, evapotranspiration, humidity, and sea level.

## 4.3 Flood Hazard at National Level

The National Territorial Information System (SNIT) offers the Water and Sanitation Layers Viewer for Costa Rica, providing access to data from the National Information System for Integrated Water Resource Management (SINIGIRH) related to the water sector, including information on river basins. This data is valuable both for modeling flood hazards at the national level and for detailed analysis of the Pirro River basin.

The data can be accessed and visualized through the following link: https://www.arcgis.com/apps/dashboards/71b40ee586b6439ba343ad1af1ebee1c.


Figure 10. Wathersheds.

Additionally, the SNIT portal provides a vector layer of the waterways, which includes the country's primary and secondary drainage lines.

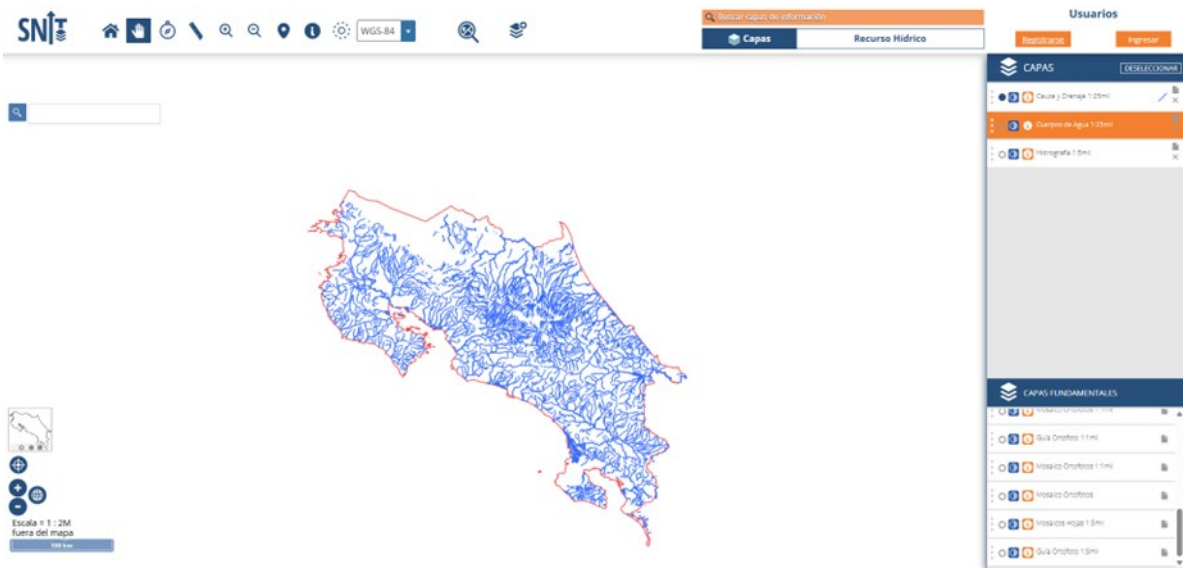


Figure 11. Watercourse and drainage lines.

Based on this information, combined with climate data, the digital elevation model, the soil layer, and the vegetation cover layer (presented later), the corresponding modeling is carried out.

## 4.4 Flood Hazard of the Virilla River (Heredia Canton)[2]

As part of the Strategic Project, a flood risk assessment will be conducted in Heredia canton. To support this, the following sources of information have been identified to complement the hazard model.

### 4.4.1 River Channel

The main channel of the Virilla River is a fundamental component for both the hydrological and hydrodynamic models. The vector layer of the main channel was obtained from the National Territorial Information System (SNIT). Figure 12 shows the water body.

[2] Since the Pirro River is a tributary of the Virilla River, the available information for the Virilla River is useful for the flood risk assessment in the canton of Heredia.

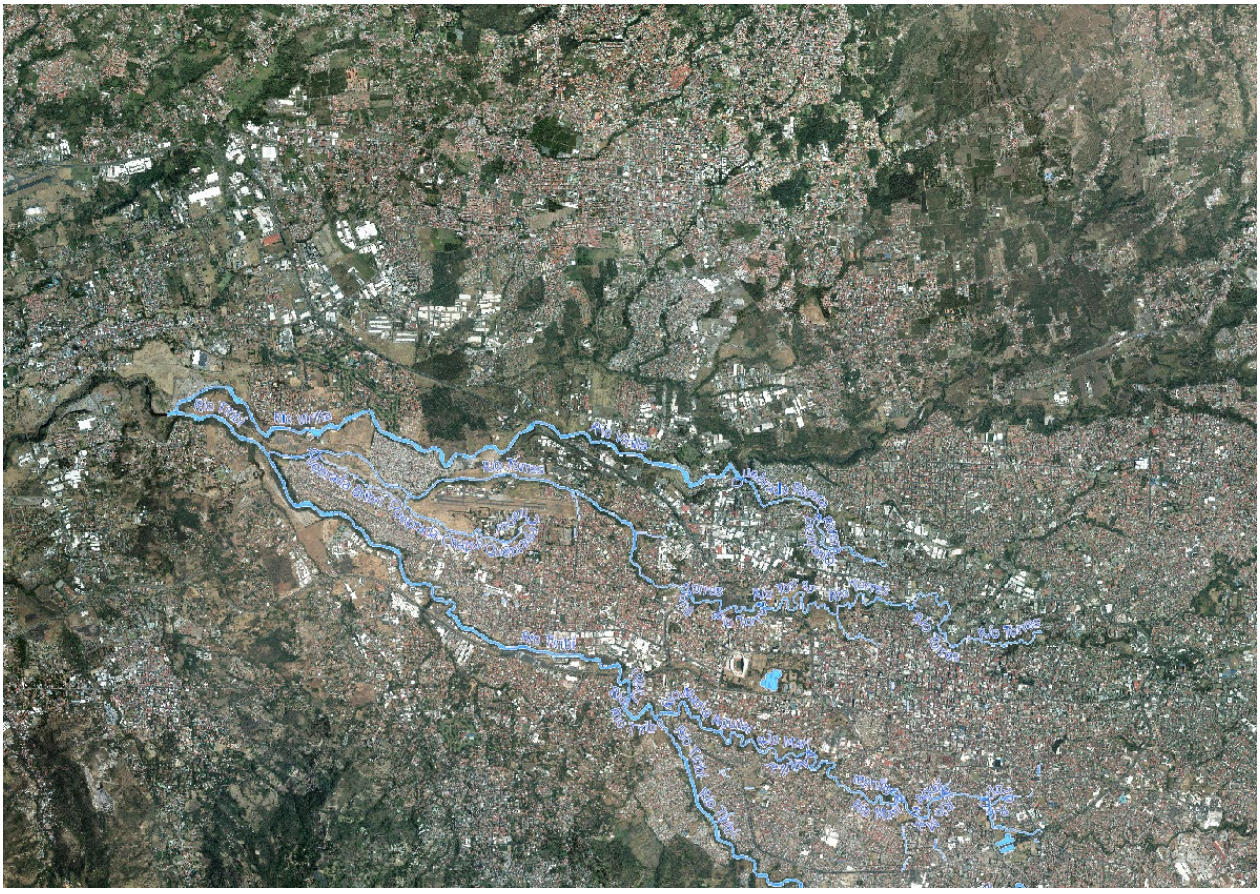

Figure 12. Water Body – San José, Virilla River Shape

### 4.4.2 Topography

In the local flood model, it is essential to have the topography of the watershed feeding the river or channel under study, both for the hydrological and hydrodynamic models.

Although there are various databases with topographic information, the final selection will depend on the level of detail required for the specific analysis, considering the cost-benefit balance between the level of detail and the computation time, which is related to the available computational capacity. Table 6 provides a summary of commonly used sources for downloading digital elevation models.

Table 6. Sources for downloading digital elevation models.

| Source | Name | Resolution | Download Link |
|---|---|---|---|
| GTOPO 30 | Regional Low Resolution Elevation Data | 30 arc-sec (1 km) | https://earthexplorer.usgs.gov/ |
| SRTM | Shuttle Radar Topography Mission | 3 arc-sec (90 m) | https://search.earthdata.nasa.gov/ |
| ASTER | Advanced Spaceborne Thermal Emission and Reflection | 1 arc-sec (30 m) | https://search.earthdata.nasa.gov/ |
| ALOS-PALSAR | Advanced Land Observing Satellite-1 | 12.5 m | https://search.asf.alaska.edu/#/ |

Figure 13 shows, as a reference, the topography of the area through which the Virilla River flows.


Figure 13. Topographic map of the Virilla River. Source: https://es-co.topographic-map.com/map-c74ccz/R%C3%ADo-Virilla/?center=9.89919%2C-84.03168&zoom=11&base=4

Along with climate information on precipitation, the data presented in this section, as well as the information on land cover and soils detailed later in this document, complete the datasets required for the flood model of the Pirro River.

## 4.5 Seismic Hazard

Within the framework of the project, it is not necessary to perform additional seismic hazard modeling; instead, existing information from previous efforts will be used. Below are the most relevant and comprehensive studies identified.

### 4.5.1 RESIS II Model

The Central America Seismic Hazard Assessment Project RESIS II (NORSAR et al., 2008) was a regional initiative aimed at evaluating seismic hazard across Central American countries, including Costa Rica. This project was carried out in collaboration with local institutions such as the National Seismological Network, the Central American School of Geology at the University of Costa Rica, the Costa Rican Institute of Electricity, and international experts in seismology and geotechnics from the Polytechnic University of Madrid, Central America, and Europe.

In Costa Rica, the study focused on the probabilistic seismic hazard assessment, taking into account the country's historical and recent seismicity. A seismic catalog of significant events was compiled and analyzed to identify and characterize the main seismogenic sources. Additionally, regionally appropriate attenuation models were used to estimate expected seismic acceleration at various locations.

The results of RESIS II produced seismic hazard maps, such as the one shown in Figure 14, which have been fundamental in developing earthquake-resistant building codes and territorial planning in Costa Rica. These maps indicate zones with varying levels of seismic hazard, enabling authorities and the general population to take appropriate preventive and mitigation measures.

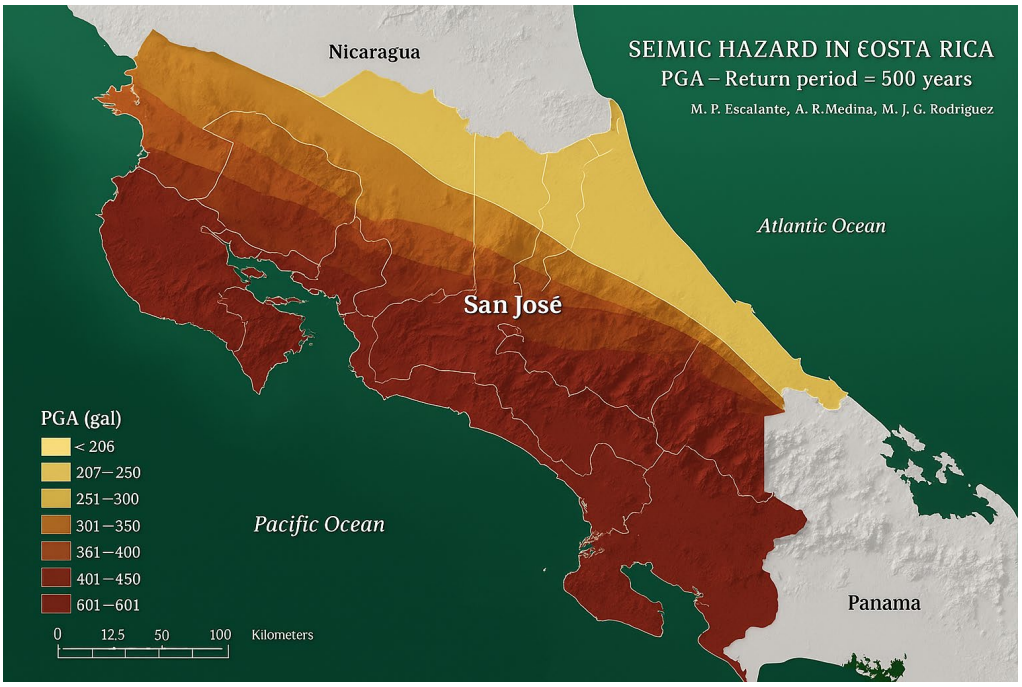


Figure 14. Seismic hazard map in terms of PGA for a 500-year return period. (Source: NORSAR et al., 2008)

It is important to highlight that, since the completion of RESIS II, additional efforts have been undertaken to update and improve the seismic hazard assessment in Costa Rica.

### 4.5.2 CAPRA

The CAPRA (Comprehensive Approach to Probabilistic Risk Assessment) initiative was a platform developed in Central America for probabilistic risk assessment, supported by the World Bank, the Inter-American Development Bank (IDB), and other international institutions. Its objective was to provide tools for comprehensive risk assessment and management related to natural hazards, using a probabilistic approach to estimate potential losses and support disaster risk reduction decision-making.

As part of this initiative, a seismic risk assessment was conducted for the city of San José (ERN-AL, 2009). The seismic hazard analysis was based on the advances presented in the regional RESIS II project (NORSAR et al., 2008), which at the time represented the most advanced study on seismic hazard evaluation in Central America.

Figure 15 shows the seismic hazard map for Costa Rica, expressed in terms of peak ground acceleration (PGA) for a 500-year return period.

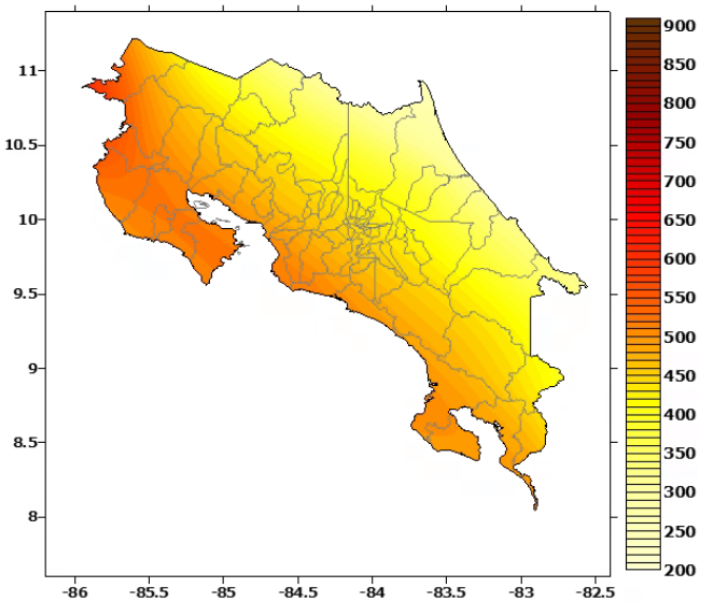


Figure 15. Seismic hazard map in terms of Peak Ground Acceleration (PGA) for a 500-year return period (Source: ERN, 2009).

### 4.5.3 Modelo ASLAC

The ASLAC model (Salgado-Gálvez et al., 2018) is the first harmonized Probabilistic Seismic Hazard Assessment (PSHA) model that comprehensively, continuously, and homogeneously covers the Latin America and Caribbean (LAC) region, with sufficiently high national-level resolution.

For its development, an updated seismic catalog was assembled using local, regional, and international data sources, complemented by a review of historical events to improve accuracy in magnitude and location. Strong ground motion attenuation models were selected based on the seismotectonic characteristics of the region, and hybrid approaches were used to assign combinations of attenuation models to various seismogenic sources.

Seismic hazard assessment was conducted using the CRISIS2015 software (Ordaz et al., 2015), a globally recognized tool that produces exceedance probability curves, uniform hazard spectra, and hazard maps for various structural periods and return intervals.

ASLAC is currently regarded as the most advanced and up-to-date seismic hazard model for Latin America and the Caribbean. It is used in catastrophe risk models for loss estimation in the insurance sector, for example, by CCRIF. It has also been certified by the Colombian insurance regulator (Superintendencia Financiera de Colombia) for use by Colombian insurance companies in solvency assessments and pricing.

Figure 16 presents the seismic hazard maps produced by the ASLAC model. The map on the left shows hazard for a 500-year return period, while the map on the right shows hazard for a 2,500-year return period, both in terms of Peak Ground Acceleration (PGA).

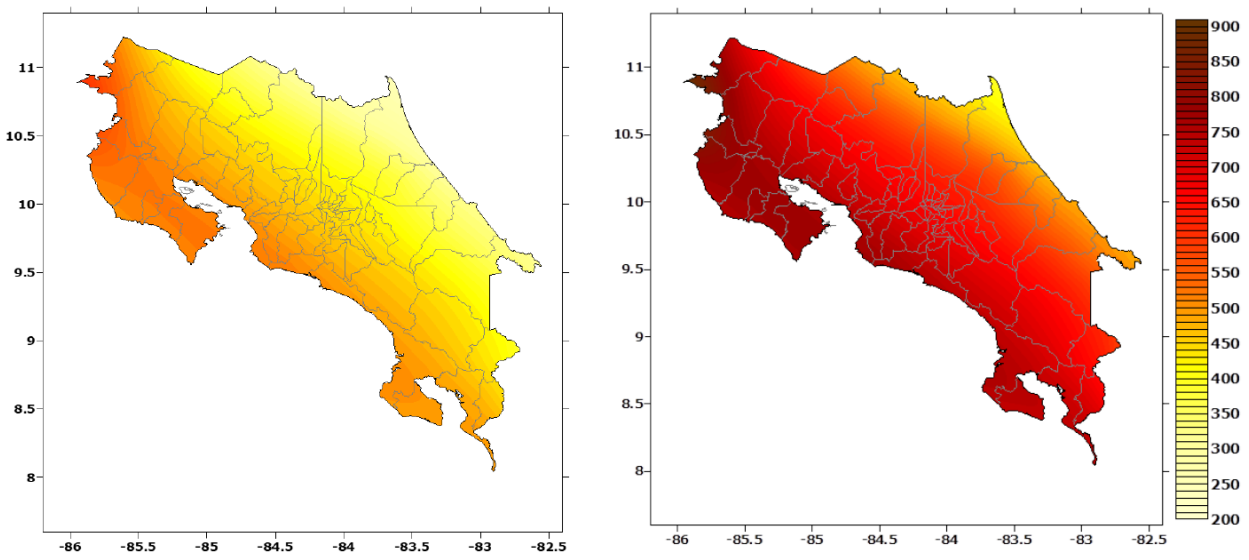


Figure 16.. Seismic hazard maps for Costa Rica Left: PGA for a 500-year return period Right: PGA for a 2,500-year return period. Calculated by INGENIAR using CAPRA-ROBOT. Units in cm/s².

### 4.5.4 Seismic Hazard Model of Costa Rica

This model, developed by Hidalgo Leiva et al. (2022), represents the most recent probabilistic seismic hazard assessment for Costa Rica. It was calculated using the most comprehensive and up-to-date earthquake database, compiled by Arroyo-Solórzano and Linkimer (2021), which includes data from the Seismic Engineering Laboratory and the National Seismological Network at the University of Costa Rica, as well as seismological agencies in Panama and Nicaragua.

In this study, seismicity parameters were updated for tectonic domains including the upper plate, the interplate subduction zone, and the intraslab zone. The upper plate zones were further characterized by the percentage of fault types present, and ground motion models were selected and weighed for each tectonic domain.

According to the study, the resulting peak ground acceleration (PGA) maps (Figure 17), for return periods of 475 and 2,475 years, as well as spectral accelerations, exhibit geographical trends that allow the country to be classified into four seismic hazard levels:

1. Extremely high: Covering the Nicoya, Osa, and Burica peninsulas, which lie directly above the interplate subduction zone.
2. Very high: For most of the Guanacaste province.
3. High: For a large portion of the country (~41%), including central Costa Rica and the capital, San José.
4. Moderate: For the Talamanca Mountain Range and northern Costa Rica.

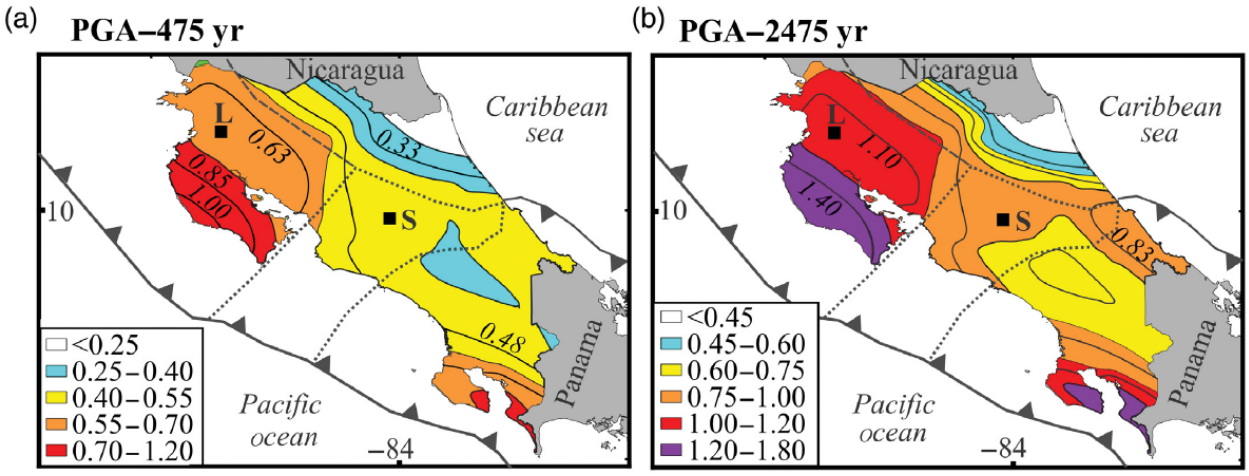


Figure 17. Results from the seismic hazard model for Costa Rica showing selected intensity measures of peak ground acceleration (PGA) for return periods of (a) 475 years and (b) 2,475 years. (Source: Hidalgo Leiva et al., 2022)

### 4.5.5 Seismic Microzonation for the San José Metropolitan Area

Given that site effects are critically important for seismic risk in urban areas, a site effects model will be developed for Heredia as a value-added component of this project. This model will be based on the seismic microzonation study of the San José Metropolitan Area (Schmidt et al., 2005) and the seismic risk modeling work by Arroyo-Solórzano (2023).

The study by Schmidt et al. (2005) was based on the dynamic response of the city's soft soils (up to 50 m deep), characterized through geophysical measurements and the best available data at the time.

Meanwhile, Arroyo-Solórzano (2023) developed a microzonation of Costa Rica's Greater Metropolitan Area (GAM) using geological, geotechnical, and geophysical data, including shear-wave velocity (Vs30) measurements at 42 locations. For the canton of San José and surrounding areas, the microzonation was conducted at a higher resolution.

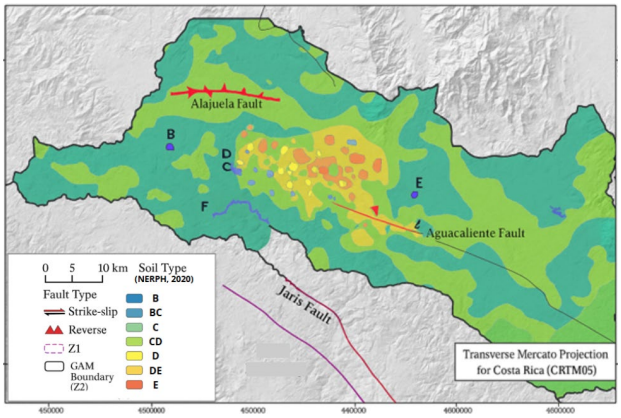


Figure 18. Soil types in the San José Metropolitan Area for assessing earthquake site effects. (Source: Arroyo-Solórzano, 2023)

## 4.6 Landslide Hazard

Although the Terms of Reference specify that no new landslide hazard modeling is required, we aim to complement and enhance the currently available landslide model for Costa Rica. This model is based on local research and expertise, partially employing the method developed by Sergio Mora (University of Costa Rica) and Vahrson (1994) for assessing landslide susceptibility.

Building on this foundation, we propose to increase the model's level of detail by incorporating new and updated layers of susceptibility factors, with the goal of improving the accuracy of landslide susceptibility quantification.

Below, the most relevant and comprehensive studies and data sources identified are described.

### 4.6.1 Landslide Inventory

The landslide inventory is a comprehensive record of historical events that includes information on the types of mass removal processes, their spatial distribution, process classification, and specific characteristics. Two vector layers containing georeferenced data on landslides that have occurred within Costa Rica were identified on the National Territorial Information System (SNIT) portal, under the natural hazard domain managed by the National Commission for Risk Prevention and Emergency Response (CNE).

In https://www.snitcr.go.cr/ico_servicios_ogc_info?k=bm9kbzo6NDU=&nombre=CNE these layers are available for download and in https://www.snitcr.go.cr/Visor/visor they can also be viewed through the SNIT Map Viewer.

The "Landslides" layer, shown in Figure 19, contains 1,126 records corresponding to hydrometeorological and seismic events that have triggered slope instability and landslide impacts. Besides the event locations, this layer provides data on the affected area and perimeter for most records. However, it does not differentiate between types of mass removal processes nor include detailed event-specific characteristics. According to the layer metadata, it is used to update the country's hazard zones, identify areas most prone to landslides, and support decision-making within the National Risk Management System.

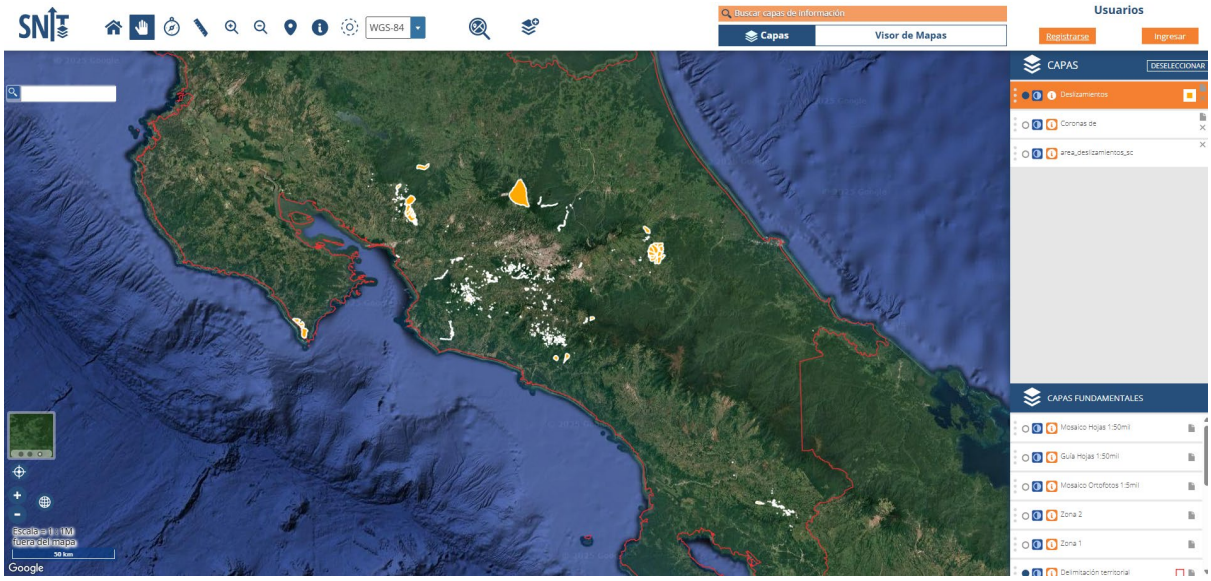


Figure 19. Visualization of the landslides layer in the SNIT map viewer

The *landslide head scarps* layer, shown in Figure 20, contains information on hydrometeorological and seismological events that may trigger landslides and associated impacts. It highlights areas with potential susceptibility to landslides.

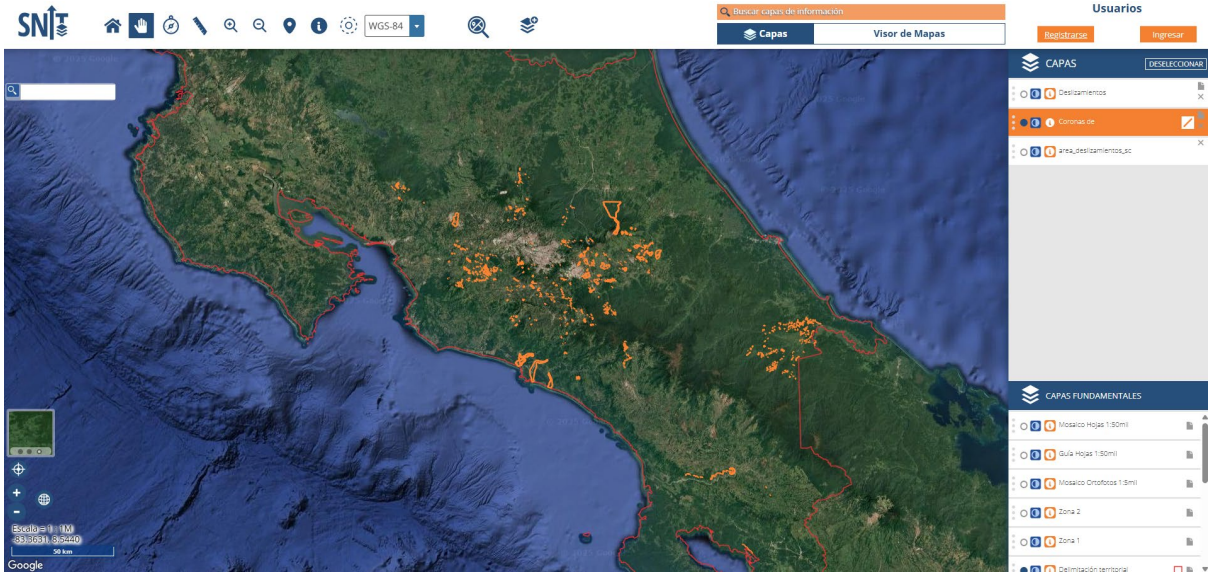


Figure 20. Visualization of the "landslide head scarps" layer in the SNIT map viewer

### 4.6.2 Project by the Central American School of Geology at UCR

A project titled *"Landslide Hazard in Costa Rica"* was identified within the Information and Project Management System of the University of Costa Rica (UCR). This initiative was led by the Central American School of Geology at UCR and carried out between 1996 and 2003. Its main objectives were to produce

landslide hazard maps for a large portion of Costa Rican territory, to develop a regional database on landslides, and to monitor critical events impacting nearby communities.

However, despite identifying the existence of the project, access to its outputs or final reports has not yet been achieved.

### 4.6.3 RECLAIMM/CEPREDENAC-Norway Project

The RECLAIMM Project (*Strengthening Capacities for Landslide Risk Management in Central American Countries*) was a joint initiative between the *Centro de Coordinación para la Prevención de los Desastres en América Central* (CEPREDENAC) and the Government of Norway (Norwegian Geotechnical Institute). Its primary objective was to enhance the capacity of Central American countries to manage and mitigate landslides risk.

In Costa Rica, the project focused on the development of landslide susceptibility maps, taking into account factors such as geology, slope, land use, and precipitation patterns. The methodology used was based on the collection and analysis of geospatial data, which enabled accurate representation of vulnerable areas.

Although the RECLAIMM project was implemented in several countries across the region, specific information regarding its execution in Costa Rica is limited, and access to outputs such as the generated susceptibility maps has not yet been achieved. Nonetheless, this type of initiative has made a significant contribution to strengthening national capacities for landslide risk management.

### 4.6.4 CNE Hazard Maps

The *Comisión Nacional de Prevención de Riesgos y Atención de Emergencias* (CNE) has developed preliminary hazard maps for the entire country. These maps, available at the cantonal level, provide an initial inventory of natural hazard sources across the territory. They identify landslide-prone areas that could be incorporated into the landslide catalog to be used in hazard modeling.

The maps are accessible at: https://www.cne.go.cr/reduccion_riesgo/mapas_amenzas/.

### 4.6.5 Landslide Susceptibility Map Based on LiDAR Imagery

The study by Ruiz Cubillo and Soto (2014) used LiDAR imagery to produce landslide susceptibility maps for selected cantons in the Cerros de Escazú, Costa Rica. The analysis considered factors such as geology, slope, and seismicity. The researchers created geomorphological, geological, and landslide maps, identifying zones of high susceptibility and proposing monitoring strategies. This detailed information on slope susceptibility—accounting for both seismic and meteorological triggers—can greatly enhance a national landslide hazard model and support more effective risk planning and management in vulnerable areas.

### 4.6.6 CDRI-GIRI Model

As part of the *Global Infrastructure Resilience Index* (GIRI), a fully probabilistic landslide hazard model was developed. This model generates stochastic scenarios of landslide events triggered by earthquakes or precipitation—accounting for climate change—for each country and territory worldwide.

In the case of Costa Rica, the model has been implemented, and Figure 21 presents the resulting landslide susceptibility map.

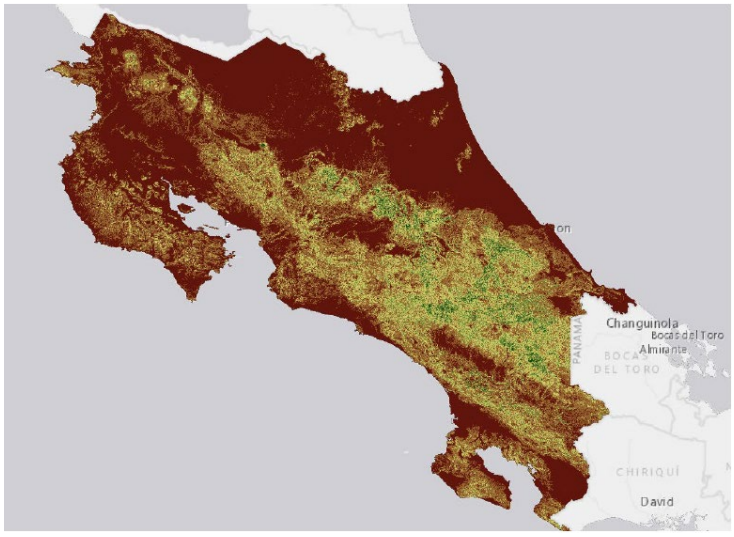


Figure 21. Landslide susceptibility map of Costa Rica from the CDRI-GIRI project led by INGENIAR

## 4.7 Volcanic Hazard

Costa Rica is home to more than ten major volcanic structures, five of which exhibit significant activity. Volcanic hazards could impact certain segments of the RN2 highway and other key transportation infrastructure in the country, posing risk to both infrastructure and mobility. Below are the identified studies that will serve as the foundation for modeling volcanic phenomena in the areas of interest, taking into account parameters such as eruptive dynamics, ashfall, and pyroclastic flows.

### 4.7.1 CAPRA

As part of the CAPRA project, volcanic hazard assessments were conducted for nine active volcanoes in Costa Rica. At the time, a deterministic model was used (ERN-AL, 2009) due to the lack of sufficient data in most cases to support proper probabilistic modeling. Each volcano was characterized based on its eruptive history and general volcanological features to model the most representative hazard scenarios. The models included ashfall, lahars, and pyroclastic flows.

These models have since been updated by INGENIAR. Figure 22 shows maps of pyroclastic flow hazards at Poás Volcano and ashfall at Irazú Volcano, calculated for long return periods using CAPRA-ROBOT.

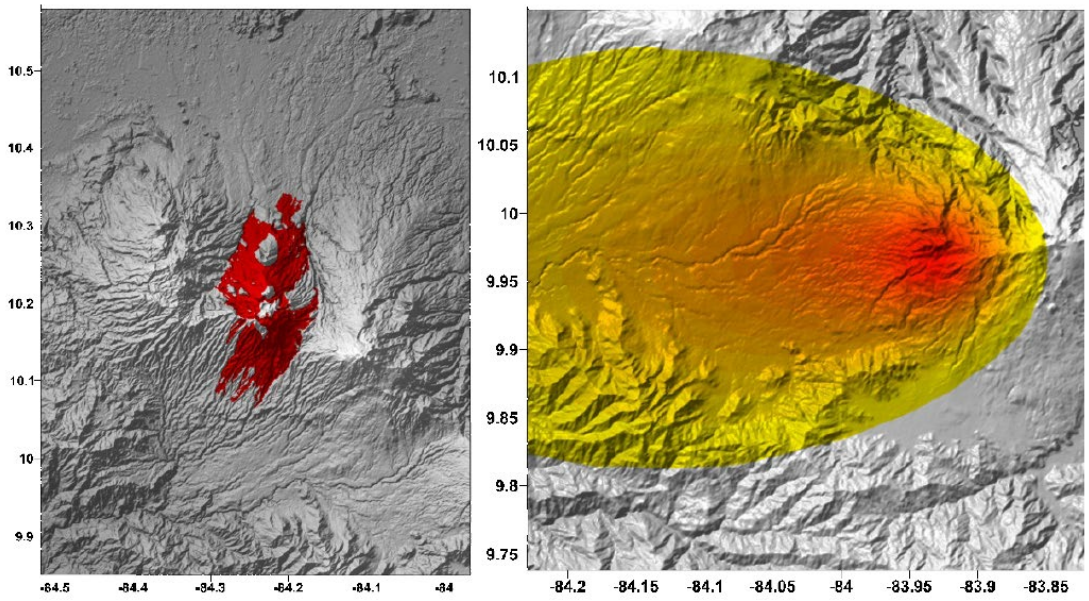


Figure 22. On the left, pyroclastic flow hazard map for Poás Volcano; on the right, ashfall hazard map for Irazú Volcano.

### 4.7.2 National Volcanic Hazard Studies

Several studies focusing on volcanic hazards have been identified for the Poás, Turrialba, Irazú, Arenal, and Rincón de la Vieja volcanoes. These projects, led by the Unidad de Investigación y Análisis del Riesgo of the Comisión Nacional de Prevención de Riesgos y Atención de Emergencias (CNE), aim to update and integrate existing research by incorporating newly available information. Below is a summary of some of the key studies reviewed

#### *4.7.2.1 Update of the Volcanic Hazard at Poás*

The Poás Volcano, being the third most visited national park in Costa Rica, and its recent eruptive activity in 2017 and 2019, prompted authorities to refocus risk management in tourism and to update and integrate existing volcanic hazard studies. This study (Alvarado et al., 2020a) incorporated a larger number of radiocarbons dating (up to 50,000 years) to meet international standards and re-evaluated and updated the volcanic hazards with greater resolution.

#### *4.7.2.2 Volcanic Hazard of Turrialba*

The study (Alvarado et al., 2020b) highlights that, as Turrialba is one of Costa Rica's five historically active volcanoes and due to its recorded activity from 2010 to 2020 (at the time of the study), it was deemed important to conduct a focused risk management evaluation. This study integrates previous research, includes updated information such as new radiocarbon dating, and has been validated by national expert institutions responsible for volcanic hazard management.

#### *4.7.2.3 Volcanic Hazards of Irazú*

Irazú Volcano, the highest volcano in Costa Rica, was responsible for the country's first national volcanic emergency between 1963 and 1965, resulting in over 20 deaths, 300 injuries, and significant economic

losses. This study (Alvarado et al., 2021) updates previous volcanic hazard assessments, emphasizing risk management in the event of a potential reactivation, with special attention to lahars. It also incorporates new and relevant data to strengthen the hazard model, validated by the competent national institutions.

#### *4.7.2.4 Update of the Volcanic Hazard Analysis for Arenal*

This study (Alvarado et al., 2023) was the product of a collaborative effort between several national institutions, including ICE, CNE, and UNA. Its goal was to provide a comprehensive risk management approach to support decision-makers and authorities in planning infrastructure development and settlements, taking into account the risk associated with Arenal Volcano, which exhibited intense activity between 1962 and 2010.

#### *4.7.2.5 Volcanic Hazard Analysis of Rincón de la Vieja*

The study by Alvarado et al. (2022) integrates previous research and incorporates a risk management approach to support the implementation of a land-use planning strategy. This plan aims to assess and mitigate volcanic hazards while promoting responsible tourism development in this high-potential region.

## 4.8 Drought Hazard

In Costa Rica, approximately 90% of meteorological drought cases are linked to the El Niño phenomenon. The areas at greatest risk are located in the North Pacific and the Northern Zone near the Nicaraguan border, extending along the Pacific slope and into the southern part of the Central Region. Figure 23 shows a map highlighting the areas most affected by this phenomenon (Soto, 2013).

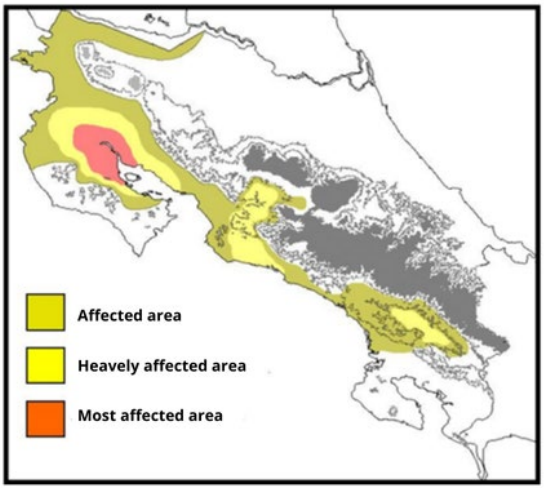


Figure 23. Areas affected by the El Niño phenomenon (Soto, 2013).

Based on the maps showing affected areas and the vulnerability of cantons to extreme dry events (Figure 24), the spatial distribution of risk from extreme dry events is presented in Figure 25. This distribution identifies three main risk zones, described as follows (Soto, 2013):

- Zone 1: Includes the cantons of La Cruz and Pacífico Norte, Upala, Los Chiles, and Guatuso in the Northern Zone; Parrita and Turrubares in the Central Pacific; and Buenos Aires and Pérez Zeledón in the Southern Zone. The frequency of drought occurrences increased during the 2000s.

- Zone 2: Comprises cantons in the Central Region of the country: Mora, San José, Desamparados, Alajuelita, Cartago, and the central canton of Puntarenas. Droughts in this zone are intense, widespread, and frequent.
- Zone 3: Encompasses all cantons of the Guanacaste province, except La Cruz. This zone experiences droughts of the greatest magnitude and frequency.

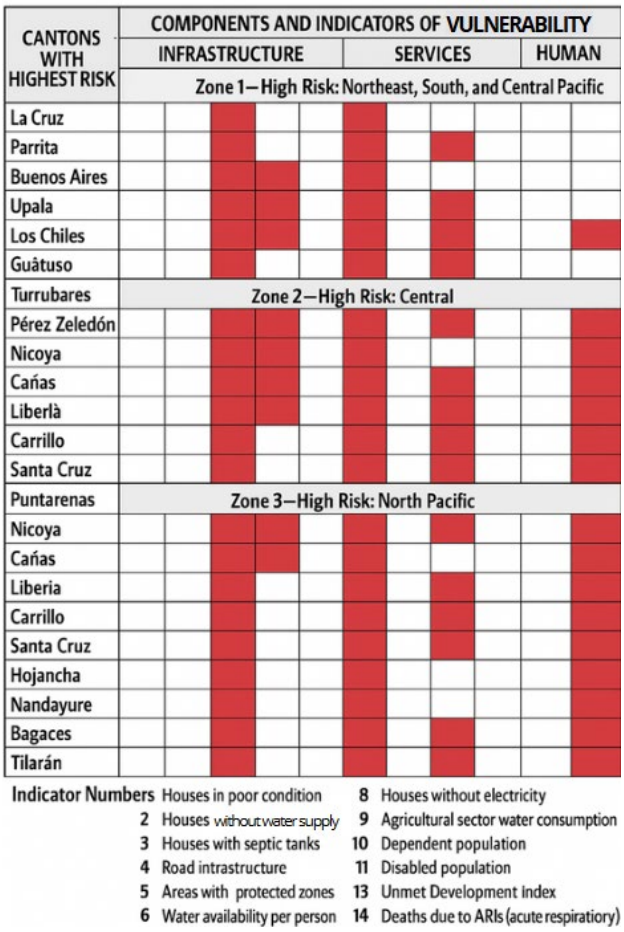


Figure 24. Vulnerability indicators in the cantons with the highest risk (Soto, 2013).

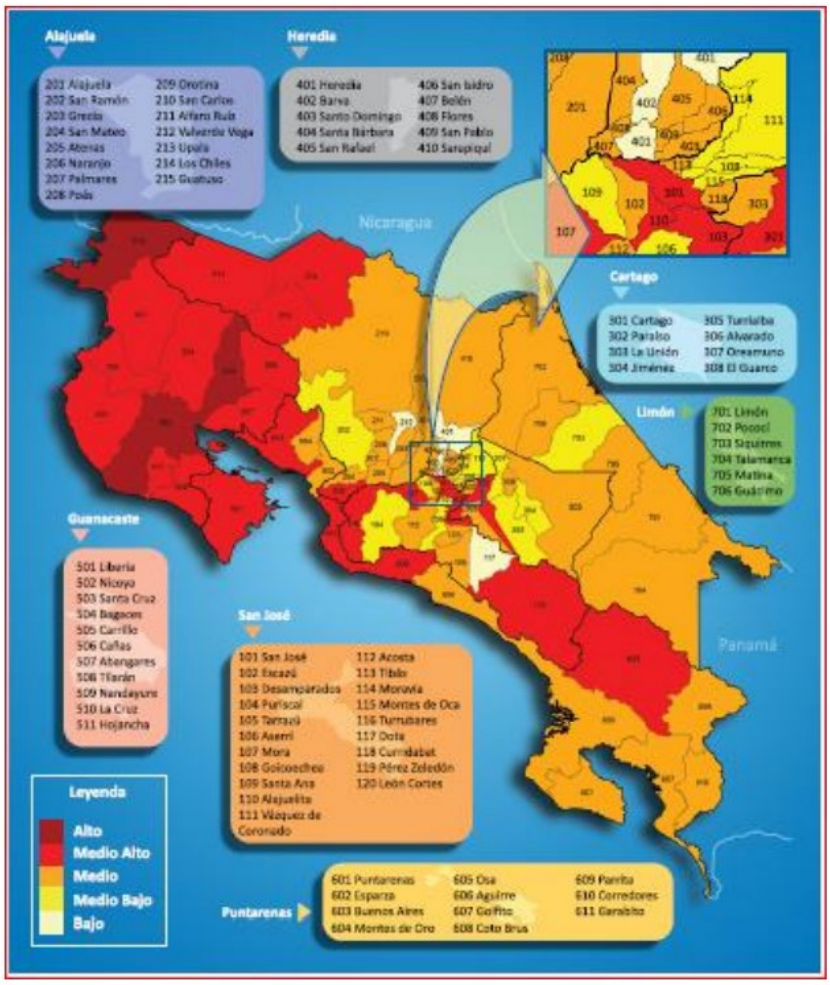


Figure 25. Spatial distribution of risk from extreme dry events (Soto, 2013).

The report "Drought Patterns in Central America" provides insights into the spatial and temporal distribution of drought across the region (Figure 26). For Costa Rica, drought events are concentrated primarily in the northern zone of the country, with the most severe points located along the strip near Nicaragua's Pacific coast.

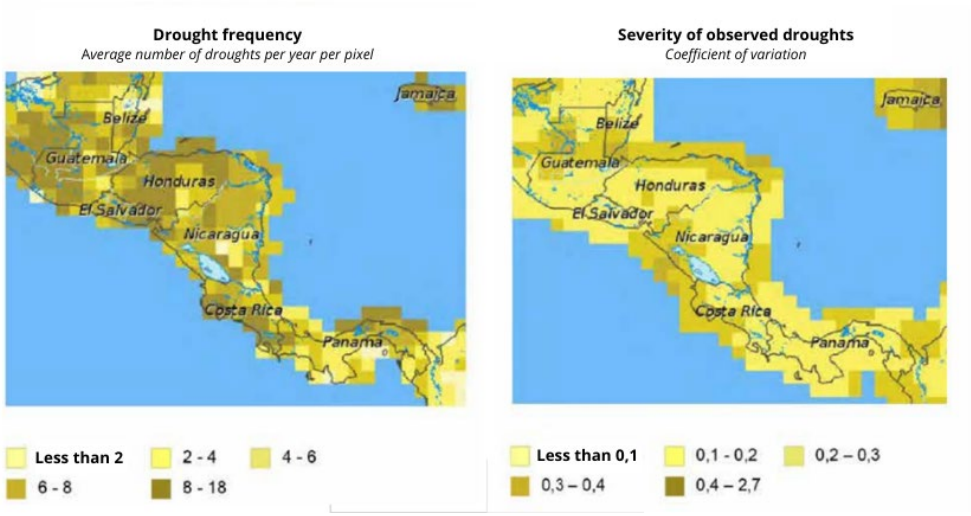


Figure 26. Frequency and severity of droughts (Bonilla Vargas, 2014)

NASA has provided evidence that the El Niño phenomenon had a significant impact on Costa Rican vegetation due to the widespread regional drought in 2018. High levels of plant stress were recorded by the International Space Station, which measures plant temperature as they heat up from water loss. Figure 27 shows the province of Guanacaste, which experienced the most intense drought conditions that year (JPL NASA, 2019).

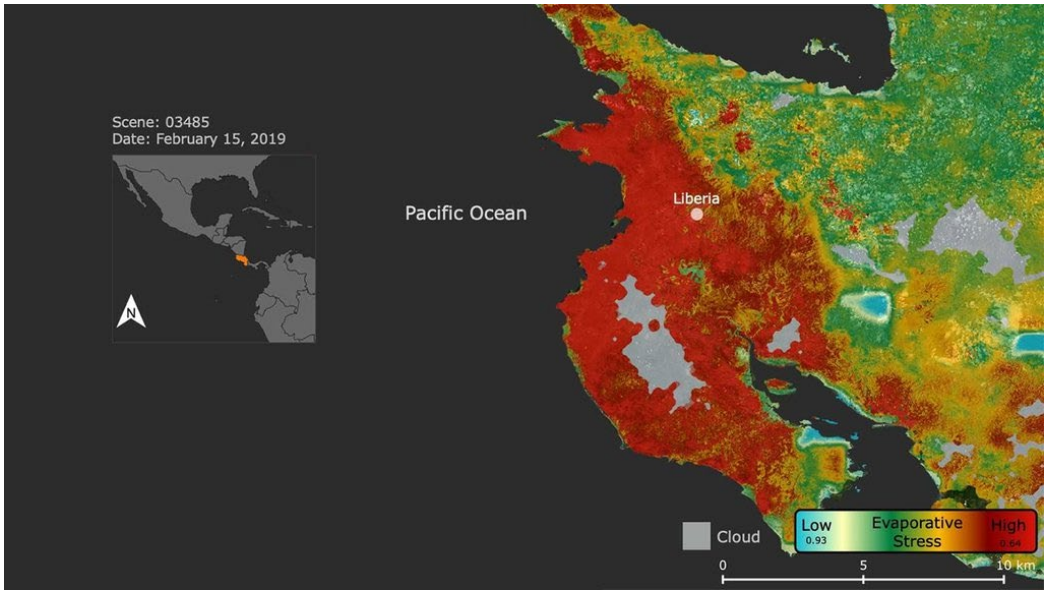


Figure 27. Vegetation stress in the Guanacaste region (JPL NASA, 2019).

To monitor this type of hazard, Costa Rica has established a "Drought Observatory," consisting of a network of 37 meteorological stations that record climatic variables every 30 minutes (including rainfall, temperature, relative humidity, solar radiation, and wind), as well as soil moisture and temperature monitoring (OACG, 2025). Figure 28 shows the viewer interface for these stations.


Figure 28. Viewer of the Drought Observatory stations (OACG, 2025).

### 4.8.1 Drought Indicators

Quesada-Hernández et al. (2020) conducted a comparative study of various drought indices to assess socio-productive impacts in the North Pacific region of Costa Rica. They utilized drought indices such as the Standardized Precipitation Index (SPI), Modified Rainfall Anomaly Index (mRAI), Palmer Drought Severity Index (PDSI), Palmer Hydrological Drought Index (PHDI), Palmer Z Drought Index (Z-index), and the Reconnaissance Drought Index (RDI). The values obtained from these indices were classified according to Table 7:

Table 7. Classification for Evaluating Different Drought Indices (Quesada-Hernández, 2020).

| Category | SPI, RDI, mRAI | PDSI, PHDI, and Z-index |
|---|---|---|
| Extremely wet | ≥ 2 | ≥ 3 |
| Severely wet | 1.5 to 1.99 | 2 to 3 |
| Moderately wet | 1 to 1.49 | 1 to 1.99 |
| Slightly wet | 0.5 to 0.99 | 0.5 to -0.99 |
| Normal | 0.49 to -0.49 | 0.49 to -0.49 |
| Slightly dry | -0.5 to -0.99 | -0.5 to -0.99 |
| Moderately dry | -1 to -1.49 | -1 to -1.99 |
| Severely dry | -1.5 to -1.99 | -2 to -3 |
| Extremely dry | ≤ -2 | ≤ -3 |

Each of these indices is designed to analyze different types of droughts: mRAI, RDI, and PDSI focus on meteorological droughts; the Z-index and SPI at 6 months target agricultural droughts; and SPI at 12 months along with PHDI are used for hydrological droughts. Among these, the SPI is the most commonly applied index in various studies conducted in Costa Rica (Bonilla Vargas, 2014; GWPCAM, 2014; Rodríguez, 2018).

### 4.8.2 Soil Maps

#### *4.8.2.1 SNIT*

The Sistema Nacional de Información Territorial (SNIT) holds cartographic data related to soils for certain cantons or provinces in Costa Rica. Available maps include information on exchangeable acidity, land use, soil carbon, soil families, soil fertility, chemical fertility, organic matter, pH, hydrogen potential, soil salinity, saturation, soil subgroups, soil taxonomy, coffee zoning, and pasture zoning. However, the information on this portal does not cover the entire country (SNIT, 2025).

#### *4.8.2.2 FAO Soil Map*

The FAO and UNESCO organizations developed a World Soil Map at a scale of 1:5,000,000, providing a global overview of soil resources. Figure 30 shows the soil map of Central America (FAO & UNESCO, 2025).

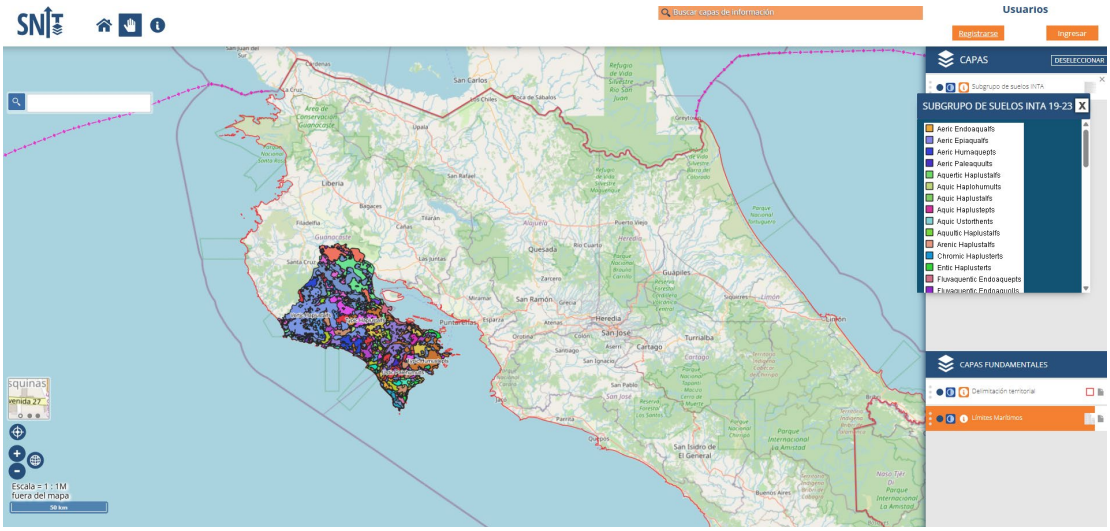


Figure 29. SNIT Map Viewer

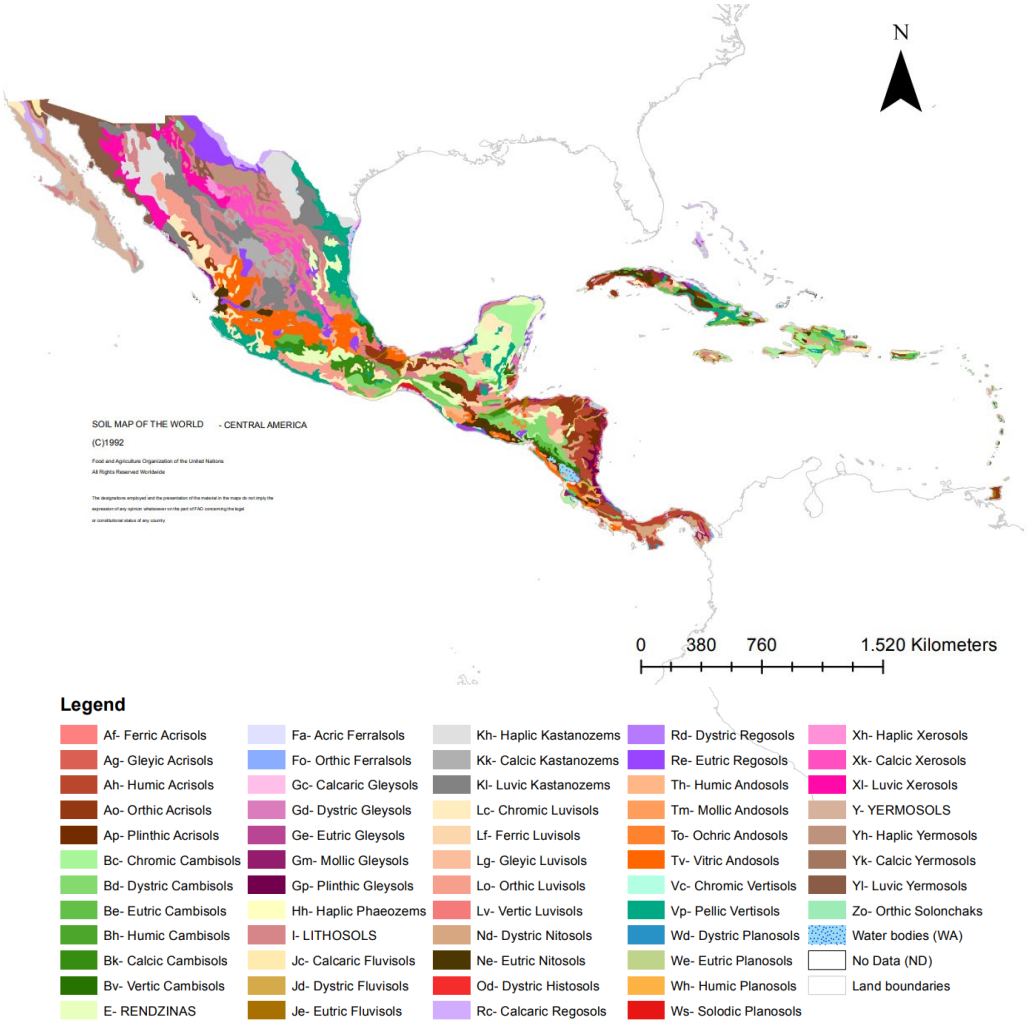


Figure 30. FAO Soil Map of Central America

### *4.8.2.3 FAO Soil Texture Map*

Version 2.0 of the Harmonized World Soil Database (HWSD v2.0) is a global tool that provides detailed information on soil morphological, chemical, and physical properties at a 1 km resolution. Developed in 2008 by the International Institute for Applied Systems Analysis (IIASA) and the Food and Agriculture Organization of the United Nations (FAO), the HWSD was updated in 2013 and 2023. It can be accessed via the following link: https://www.fao.org/soils-portal/data-hub/soil-maps-and-databases/harmonized-world-soil-database-v20/en/

This database integrates data from various national sources, offering detailed attributes for seven soil layers and adopting a unified reference system combining FAO1990 standards with the World Reference Base for Soil Resources (WRB).

HWSD v2.0 includes a raster GIS image file linked to a soil attribute database, providing access to information on the composition of soils in nearly 30,000 mapping units. Each unit has its specific characteristics, including soil texture, as illustrated in Figure 31.

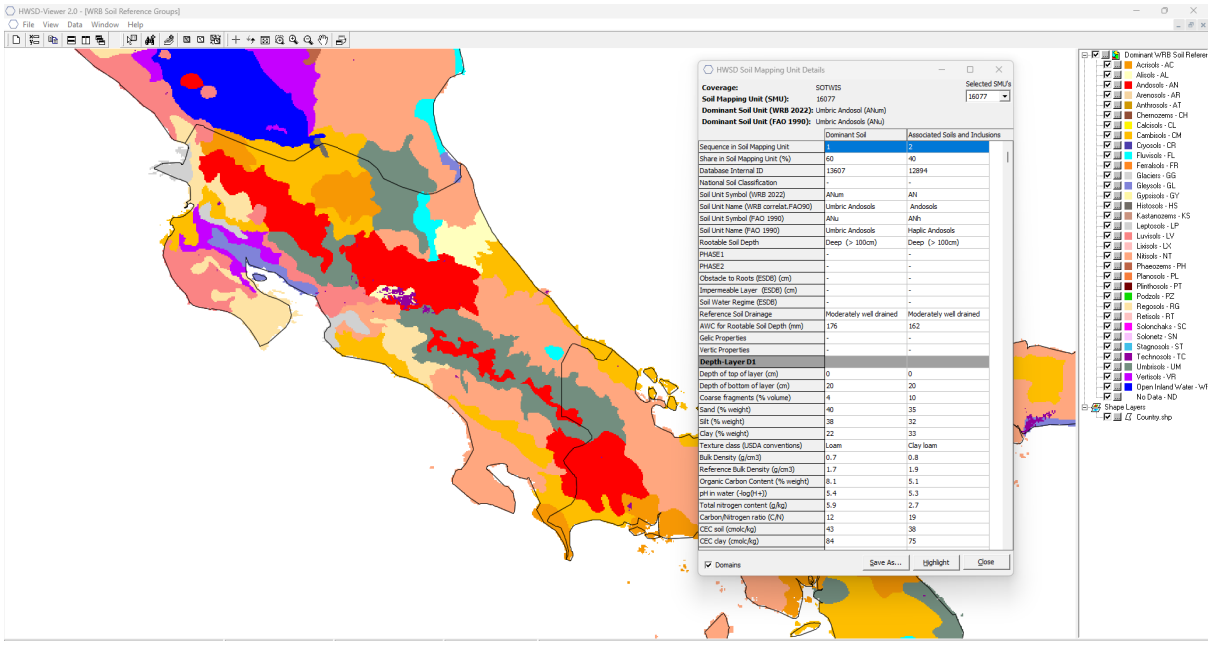


Figure 31. FAO Harmonized World Soil Database.

### 4.8.3 Contingency Plans

Costa Rica has developed a General Emergency Plan for Drought, which outlines actions to address the socioeconomic impacts on affected producers, promote the recovery of various sectors, ensure adequate water supply for consumption, address health and environmental implications, and prevent a potential increase in the incidence of forest fires (Comisión Nacional de Emergencia, 2014).

Additionally, the country has a National Adaptation Plan to Climate Change, which establishes the background, scope, goals, management framework and model, as well as financing for implementing actions aimed at addressing the effects of climate change (Dirección de Cambio Climático & Ministerio de Ambiente y Energía, 2022).

### 4.8.4 NAMA Measures

Costa Rica has implemented a series of NAMAs (Nationally Appropriate Mitigation Actions) targeting the livestock and agriculture sectors—particularly coffee and sugarcane production. These initiatives aim to reduce greenhouse gas emissions and adapt production systems to enhance resilience against climate change.

## 4.9 Tropical Cyclones Hazard (Storm Surge, Rainfall, and Flooding)

To assess the hazard posed by tropical cyclones, a methodological approach based on hurricane track simulations will be employed. Developing the hazard model requires various datasets, including cyclone trajectory information, topography, and bathymetry. The identified data sources are described below.

### 4.9.1 Historical Tracks

The International Best Track Archive for Climate Stewardship (IBTrACS), developed by the National Oceanic and Atmospheric Administration (NOAA), is the most comprehensive and widely recognized global archive of tropical cyclone tracks and characteristics (Knapp et al., 2010).

Each track is composed of advisories issued every six hours, which include: the date and time of the advisory, the geographic location of the cyclone's center, central pressure, and 1-minute sustained wind speed at 10 meters above sea level.

In the following link https://www.ncei.noaa.gov/products/international-best-track-archive the information can be accessed.

### 4.9.2 Simulated Tracks for Future Climate Scenarios

The tropical cyclone catalog used for future climate hazard assessment will be composed of historical records obtained from IBTrACS, complemented by a representative sample from the STORM dataset developed by Bloemendaal et al. (2020). This dataset provides 10,000 years of simulated cyclone tracks, generated using a stochastic model designed to replicate the key characteristics influencing tropical cyclone behavior, including central pressure, forward speed and direction, genesis location, sea surface temperature, and mean sea-level pressure, among others.

Additional stochastic simulations will be conducted to generate new tracks that encompass a wide range of potential events, spanning various frequencies and intensities, ensuring robust and comprehensive hazard modeling.

### 4.9.3 Bathymetry

The 2024 version of the GEBCO (General Bathymetric Chart of the Oceans) bathymetry is a continuous global bathymetric model with a spatial resolution of 15 arc-seconds—approximately 500 meters at the equator—making it one of the highest-resolution global bathymetric models available.

Incorporating this layer into the updated tsunami hazard model would allow for a higher level of detail compared to previously developed models.

The raster layer is available for viewing and download at: https://download.gebco.net/

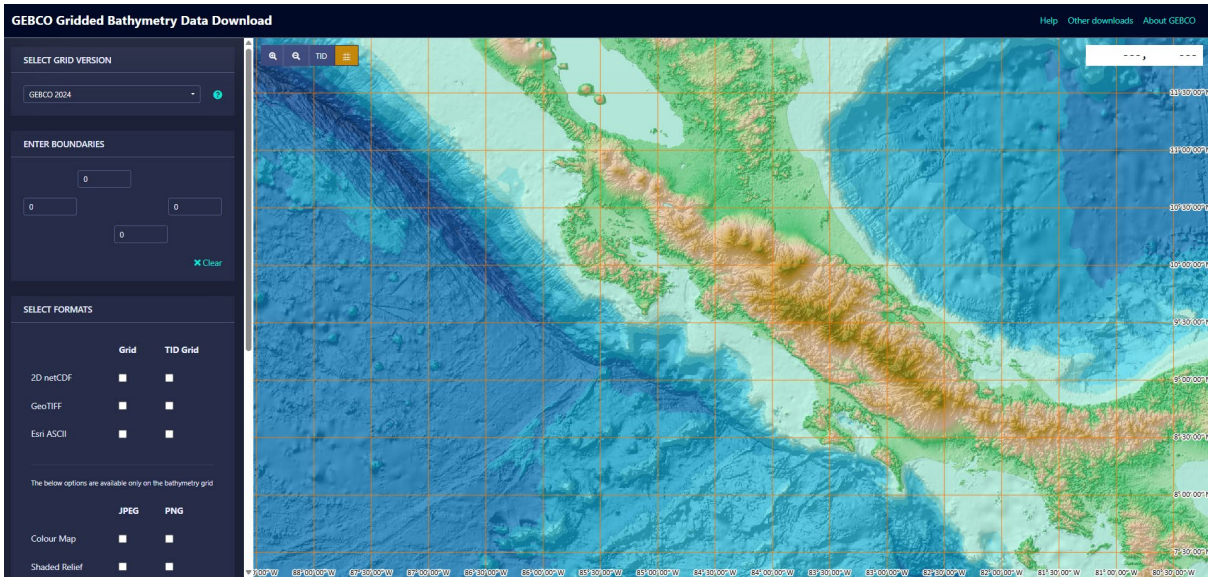


Figure 32. Visualization of bathymetry on the GEBCO portal

### 4.9.4 Topography

The various topographic data sources available are detailed in Section 4.4.2 of this document.

### 4.9.5 Precipitation

The data collected and discussed in Section 4.1 of this document will also be used in the flood and cyclone rainfall modeling. For further details, please refer to that section.

## 4.10 Tsunami Hazard

Although not included in the Terms of Reference, a tsunami risk assessment for the tourism sector along the Pacific coast of Costa Rica will be provided as added value to the project. The data sources described below have been identified and will serve as a basis for updating the tsunami hazard model within the framework of this project.

### 4.10.1 CAPRA

As part of the CAPRA initiative, a tsunami risk assessment was conducted along Costa Rica's Pacific coast (ERN-AL, 2009). The tsunami hazard was evaluated in two main stages:

1. Definition of generation conditions, based on the occurrence rates of large-magnitude earthquakes in the subduction zone. Only earthquakes that cause significant uplift of the ocean floor are considered capable of generating a tsunami.
2. Analysis of tsunami propagation and arrival, which involves the movement of gravity waves across the ocean and the modification of their impact characteristics depending on local bathymetric conditions.

The model included enough number of both historical and simulated earthquakes—generated using CAPRA's seismic hazard module—to realistically represent the conditions necessary for tsunami generation and propagation. To characterize how wave amplitude would be amplified based on local impact conditions, a combined digital elevation model (DEM) incorporating both bathymetry and topography was used, with a resolution of 2 arc-minutes (approximately 3.6 kilometers per pixel). The data were sourced from the ETOPO2v2 database (2006), developed by NOAA.

Figure 33 illustrates the modeled flood height along the Pacific coast for a 100-year return period.

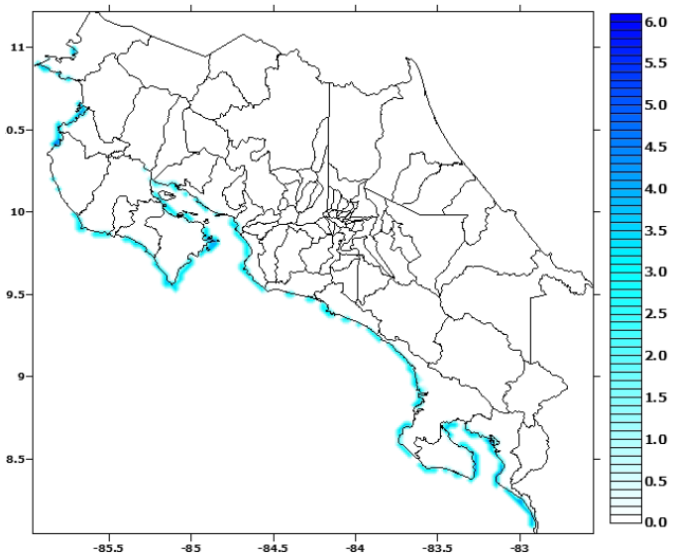


Figure 33. Flood height distribution map for a 100-year return period, in meters.
(Source: ERN, 2009)

### 4.10.2 GAR-GIRI Model

The *Global Assessment Report on Disaster Risk Reduction 2015 (GAR15)*, prepared by the United Nations Office for Disaster Risk Reduction (UNDRR), is a comprehensive global report that analyzes the state of disaster risk worldwide and assesses progress in risk reduction efforts.

As part of the Global Risk Model developed for GAR15 (INGENIAR, 2014), the Norwegian Geotechnical Institute (NGI) modeled tsunami hazard using a global model that considers the occurrence rate of earthquakes along major submarine seismic sources. Detailed methodology for the Probabilistic Tsunami Hazard Assessment (PTHA) is available in Løvholt et al. (2014).

NGI defined hazard scenarios for all tsunami-prone regions globally and created a set of georeferenced raster grids that allow for a probabilistic representation of tsunami intensity values. The hazard is expressed as a suite of scenarios, each characterized by an annual frequency of occurrence, with intensities defined in terms of expected value and standard deviation.

This same hazard model was also used in the development of the *Global Infrastructure Resilience Index (GIRI)*, in which this consulting firm participated.

Figure 34 shows the tsunami wave height hazard for a return period of 475 years.

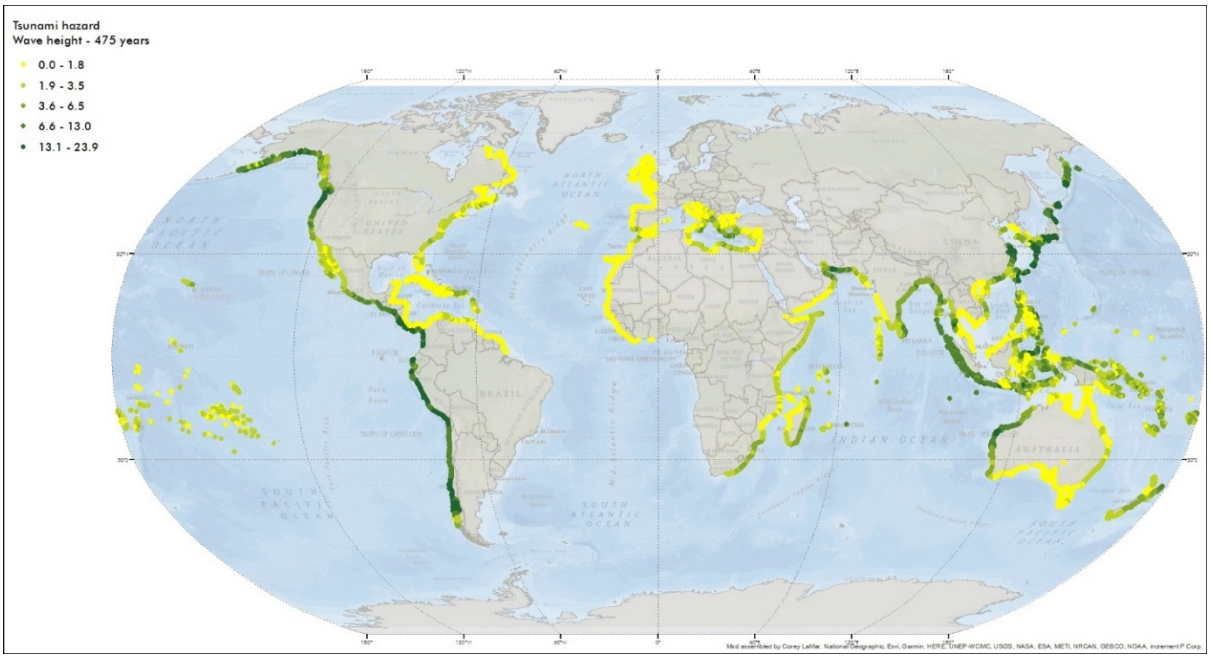


Figure 34. Global tsunami hazard map showing inundation height for a 475-year return period.

### 4.10.3 Bathymetry

The 2024 version of the GEBCO (General Bathymetric Chart of the Oceans) bathymetry dataset will also be used in this context. For more detailed information, refer to section 4.9.3 of this document.

## 4.11 Sea Level Rise Hazard

To analyze sea level rise, the 2024 study titled *"Estudios y proyecciones de aumento en el nivel del mar y erosión costera para las dos costas de Costa Rica"* (Studies and projections of sea level rise and coastal erosion for both coasts of Costa Rica) is considered. This study focuses on assessing the impacts of sea level rise and coastal erosion along the country's shorelines. It includes scenario development for regions such as Caldera on the Pacific coast and various locations on the Caribbean coast, with the aim of evaluating risks and proposing adaptation strategies.

In addition, the study provides a methodological guide that offers a practical framework for conducting assessments related to sea level rise and coastal erosion in Costa Rica.

Complementing this, as mentioned earlier in the document, data from the Coupled Model Intercomparison Project (CMIP), specifically its sixth phase (CMIP6), is available. This initiative contributes to the Sixth Assessment Report (AR6) of the Intergovernmental Panel on Climate Change (IPCC). The CMIP6 datasets, accessible through the Copernicus platform https://cds.climate.copernicus.eu/datasets/projections-cmip6?tab=download, include sea level variables under various Representative Concentration Pathways (RCPs), which are useful for modeling future scenarios.

## 4.12 Exposed Elements – Buildings

The exposure of buildings is modeled using georeferenced data layers, where each portfolio element is represented spatially with geometric features and characterized by specific attributes. The minimum necessary information to describe exposed buildings includes:

- Geographic location
- Replacement or compensation value
- Vulnerability code or classification

When these attributes are not specifically available, it is necessary to gather complementary information to properly characterize each element. This allows for associating an appropriate vulnerability model and estimating a suitable replacement value. For buildings, relevant variables include:

- Number of floors
- Usage sector
- Structural system
- Indicators of people at risk

Below, the sources of information consulted to characterize building exposure in the Heredia canton are described, organized according to each of the attributes mentioned.

### 4.12.1 Geographic Location

To determine a geometric representation of each building in space, the following sources of information are available:

#### *4.12.1.1 Cadastral Map*

In the web-based geographic information system UBICA, managed by the Municipality of Heredia, geographic data for the canton can be accessed. Among these data is the cadastral map of Heredia canton, which includes parcel boundaries and associated information such as location, identification, and land use.

It is important to note that while the cadastral map provides the location and boundaries of parcels or lots, it does not include data on the built-up area of the buildings within those parcels, as illustrated in Figure 35.

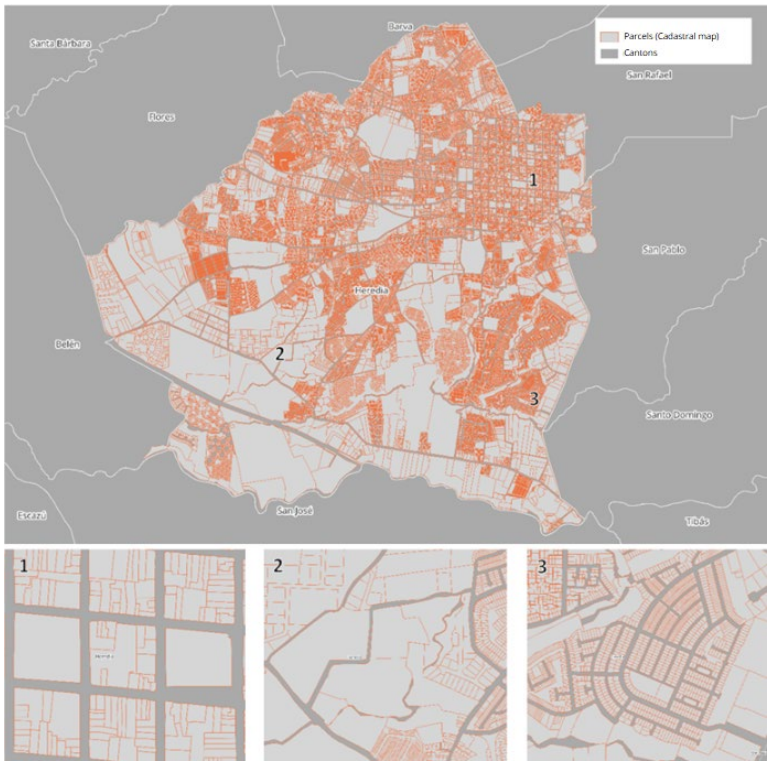


Figure 35. Cadastral map of Heredia canton

#### 4.12.1.2 *Cartography – Buildings*

Among the cartographic data from the Instituto Geográfico Nacional consulted through the Sistema Nacional de Información Territorial (SNIT) is the building and construction coverage for the entire country, derived from orthoimages taken between 2015 and 2018. As shown in Figure 36, this coverage represents contiguous blocks of buildings that may include multiple structures with different owners, number of floors, usage sectors, structural systems, and more within the same block.

Therefore, to accurately obtain the location and boundaries of individual buildings, it is necessary to combine the building coverage geometry—which accounts for constructed areas excluding land area—with the cadastral map geometry, which provides variables to independently characterize each building.

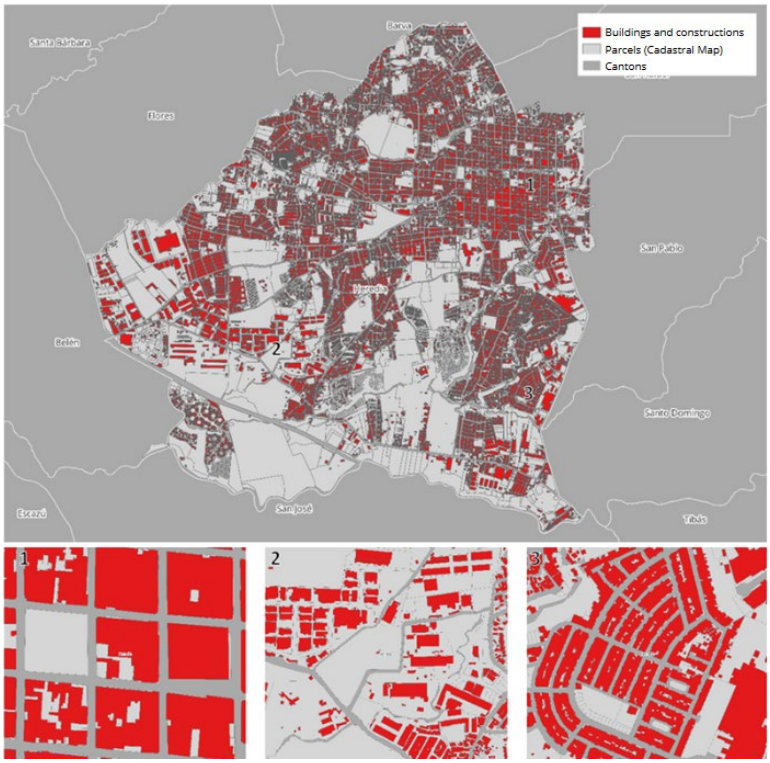


Figure 36. Building coverage

#### *4.12.1.3 Global Risk Assessment Framework (GRAF)*

The Global Risk Assessment Framework (GRAF) is an initiative by the United Nations Office for Disaster Risk Reduction (UNDRR) aimed at strengthening countries' capacities to access and utilize risk-related data to guide decision-making.

As part of the first GRAF pilot implementation in Costa Rica, carried out in coordination with the Comisión Nacional de Prevención de Riesgos y Atención de Emergencias (CNE), exposure models were developed for various sectors, including the housing sector, as shown in Figure 37. This housing exposure database was built using information provided by the Instituto Nacional de Estadística y Censos (INEC) and will serve as a guide and data source for characterizing buildings in the Heredia canton.

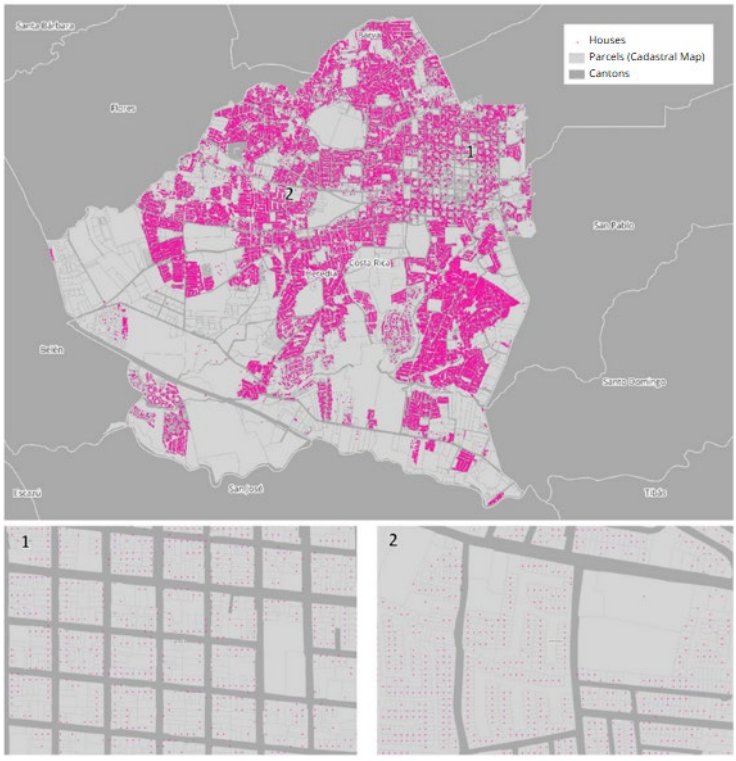


Figure 37. Housing exposure database from the GRAF project

### 4.12.2 Replacement or Compensation Value

#### *4.12.2.1 Homogeneous Zones Value Map*

Within the UBICA web geographic information system, there is a Homogeneous Zones Value Map that shows the value per square meter of a specific area within the canton of Heredia. This map was published by the Ministry of Finance in 2012. Figure 38 displays the Homogeneous Zones Value Map.

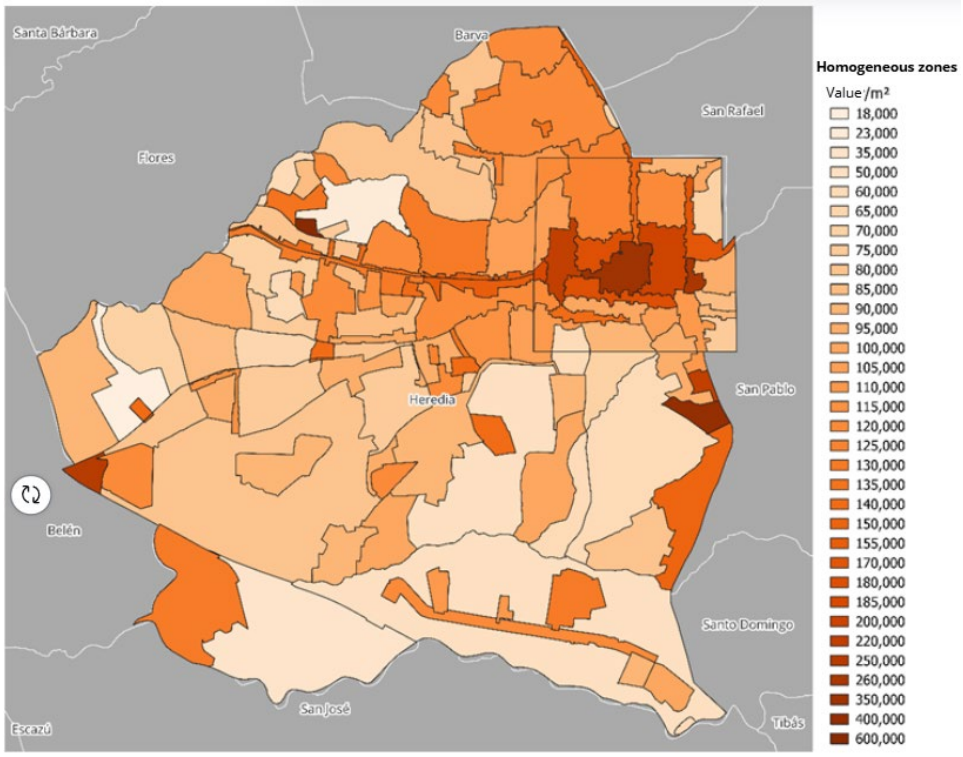


Figure 38. Homogeneous zones value map per m²

#### 4.12.2.2 *Manual of Unit Base Values by Construction Typology*

The Ministry of Finance of Costa Rica develops the Manual of Unit Base Values by Construction Typology as a mandatory tool to determine the replacement cost of buildings for tax auditing purposes.

Unit values by typology are reported for buildings and housing, as well as for different usage sectors, including residential, commercial, lodging, offices, among others. This information can serve as a baseline guide for determining the valuation of buildings.

### 4.12.3 Number of Floors

#### 4.12.3.1 *Vertical Condominiums in 3D*

The UBICA web platform allows users to access information about vertical condominiums within the canton. Among the associated attributes is the building level, which helps estimate the height or number of floors of the structures. Figure 39 shows a query example of a building in the 3D vertical condominiums available on the platform.


Figure 39. 3D Vertical Condominiums. Source: https://ubica.heredia.go.cr/

#### 4.12.3.2 *Copernicus GHSL – Global Human Settlements Layer*

Copernicus is the European Union's Earth observation program, providing open and free global spatial information services. This data is derived from satellite Earth observations combined with in-situ measurements to describe human presence across the planet.

Among the available datasets is the raster spatial dataset GHS-BUILT-H (Pesaresi, M.; Politis, P., 2023), which represents the spatial distribution of building heights. This dataset is generated by combining and filtering global digital elevation models (DEMs) with satellite imagery through linear regression techniques.

Figure 40 shows the building height distribution for the canton of Heredia, which will be used as a complementary source alongside the Vertical Condominiums previously mentioned to accurately determine the height of individual buildings.

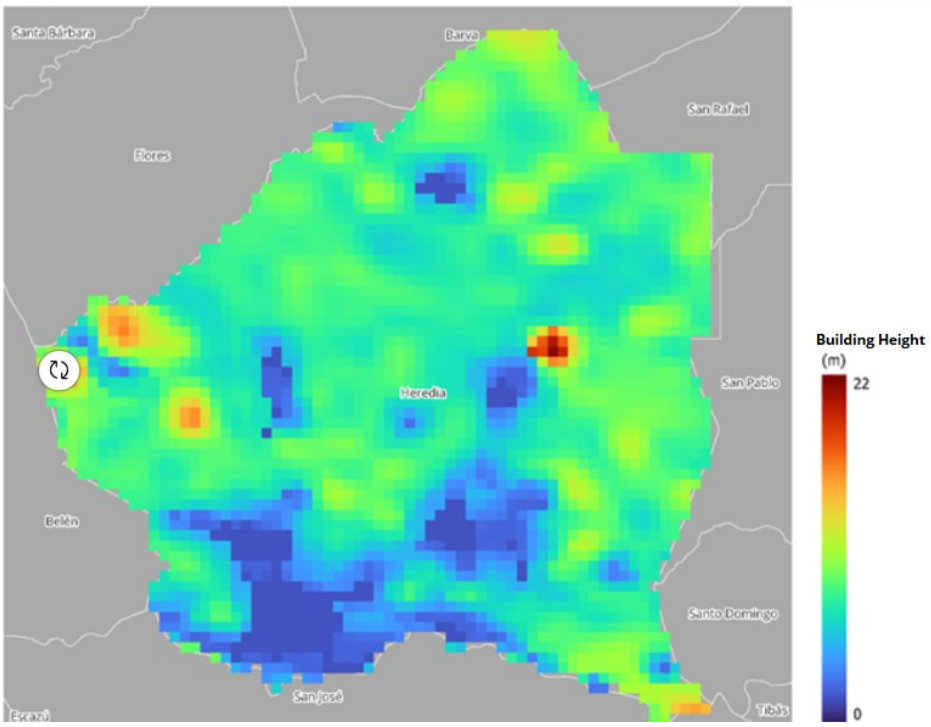


Figure 40. Building height (GHS-BUILT-H).

### 4.12.4 Land Use Sector

#### *4.12.4.1 Cadastral Map*

One of the attributes in the cadastral map is the “Use” variable, which specifies the land use category assigned to each parcel. Figure 41 illustrates the classification of these land use sectors and their spatial distribution within the canton.

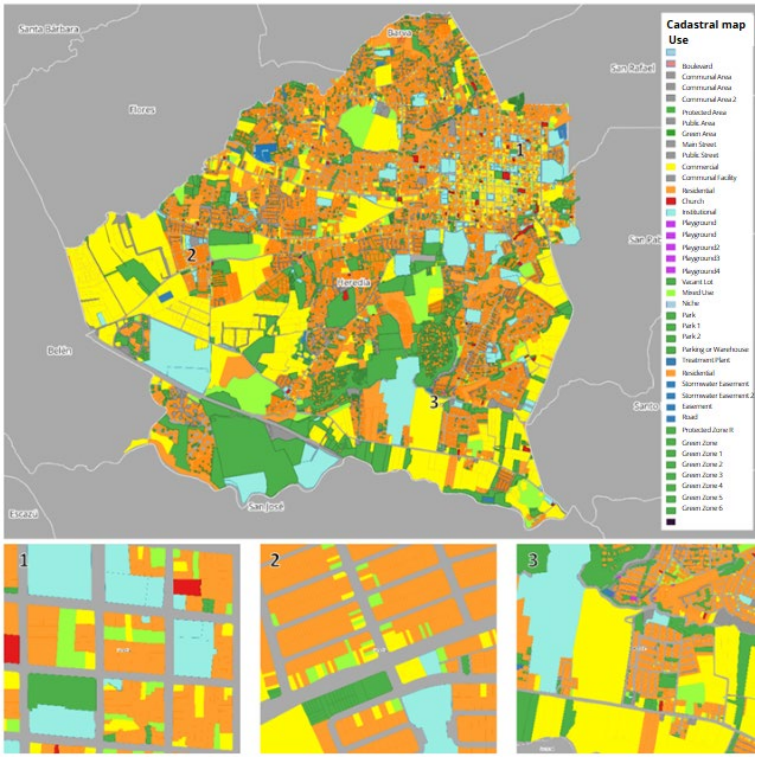


Figure 41. Land use sector

### 4.12.4.2 *Cartography – Buildings*

Within the building coverage, there is a variable called Category, which also indicates the land use sector to which the building belongs, as shown in Figure 42.

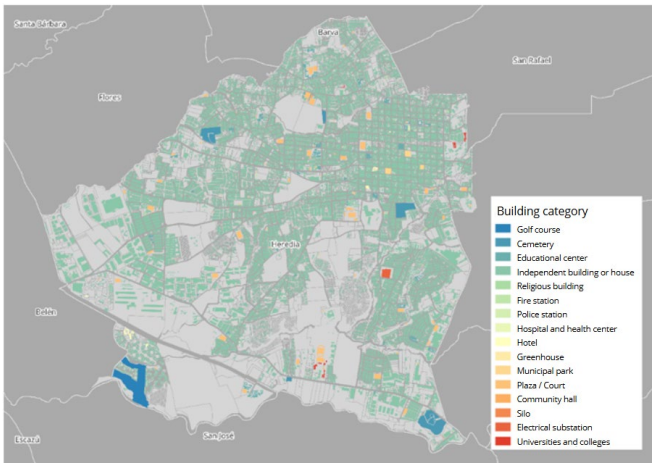


Figure 42. Use category

### 4.12.4.3 *Health Sector*

As part of the implementation of Costa Rica's first GRAF pilot, exposure models were developed for various sectors, including the health sector, as shown in Figure 43. This health sector exposure database was

created using information provided by the Costa Rican Social Security Fund (Caja Costarricense de Seguro Social) and will serve as a guide and information source for characterizing buildings in the Heredia canton.

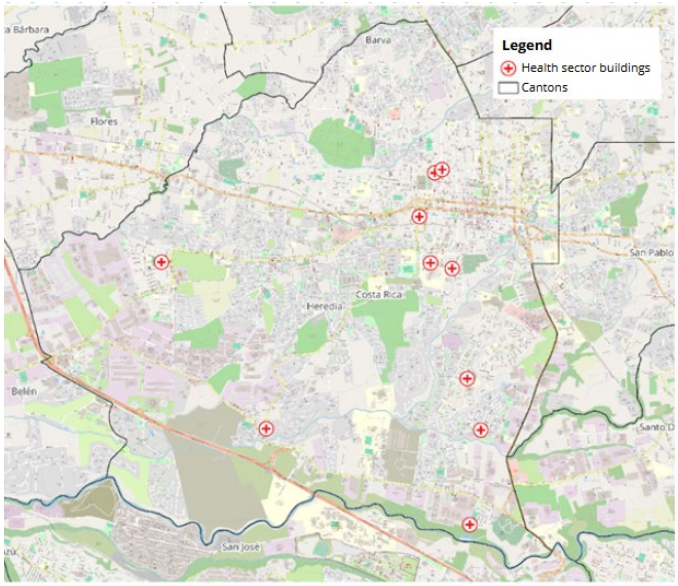


Figure 43. Health sector buildings

#### 4.12.4.4 *Educational Centers*

The UBICA platform provides information about the locations of educational centers in the Heredia canton, as shown in Figure 44. The data source is the Ministry of Public Education of Costa Rica.

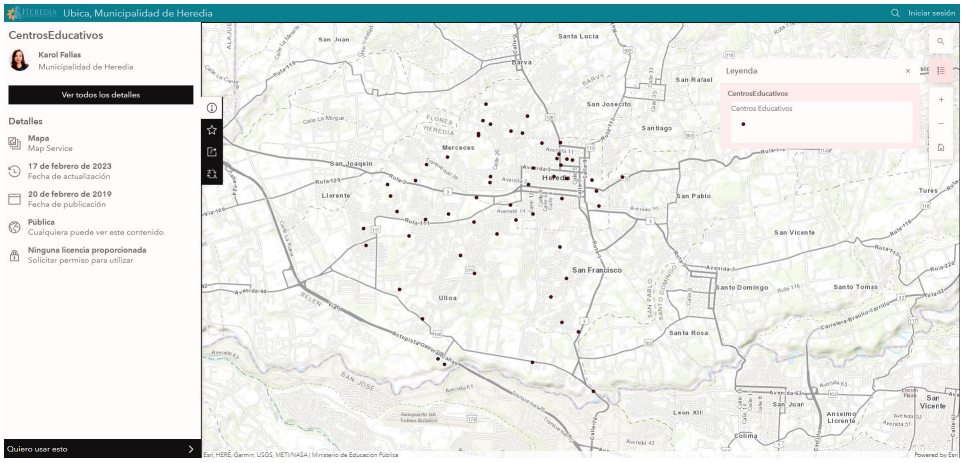


Figure 44. Educational centers. Fuente: Territorial information (https://ubica.heredia.go.cr/)

#### 4.12.4.5 *Informal Settlements*

Similarly, the UBICA platform provides information on the location of informal settlements in the Heredia canton, as shown in Figure 45.

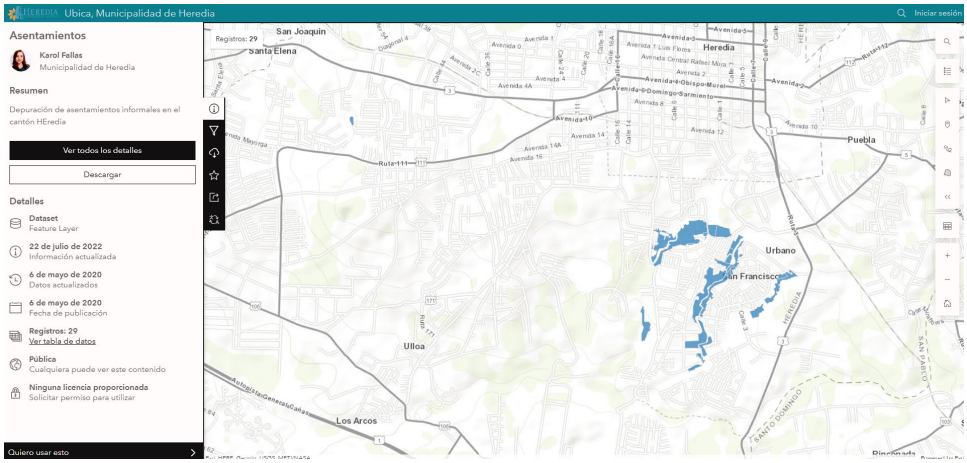


Figure 45. Informal settlements. Source: Territorial information (https://ubica.heredia.go.cr/)

#### *4.12.4.6 Points of Interest*

The UBICA platform provides a layer called Points of Interest, which contains the locations of commercial, residential, and community sites within the Heredia canton. The categorization includes distinct types such as historic tourist sites, historic architecture, local government buildings, public services, and institutional sector buildings like those of the Ministry of Security, Education, Labor, Judicial Power, the National Board, among others. Figure 46 shows the points of interest published by the Municipality of Heredia.

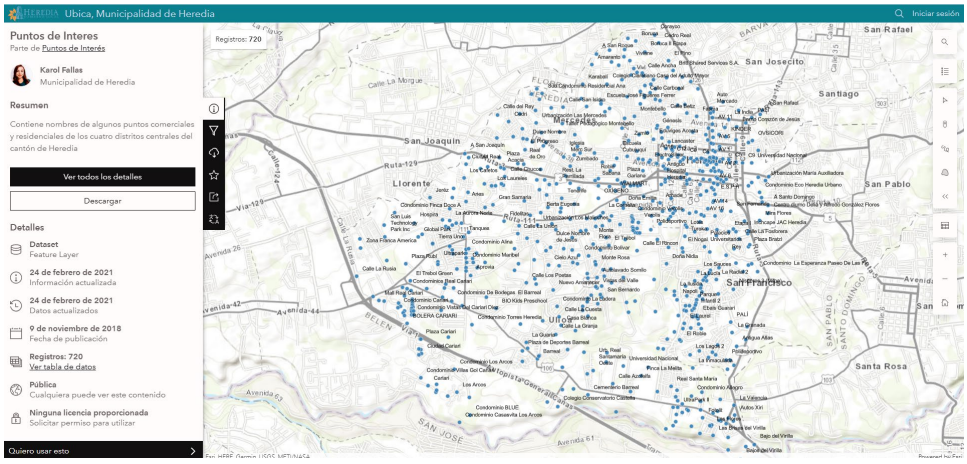


Figure 46. Points of interest. Source: Limits (https://ubica.heredia.go.cr/

#### *4.12.4.7 Public Areas*

The UBICA platform of the Municipality of Heredia provides a map of public areas within the Heredia canton. This map includes properties owned by the Municipality, publicly used lands, properties registered under State institutions, and lands that are potentially occupied illegally. Figure 47 shows a screenshot of the public areas map viewer for the Heredia canton.

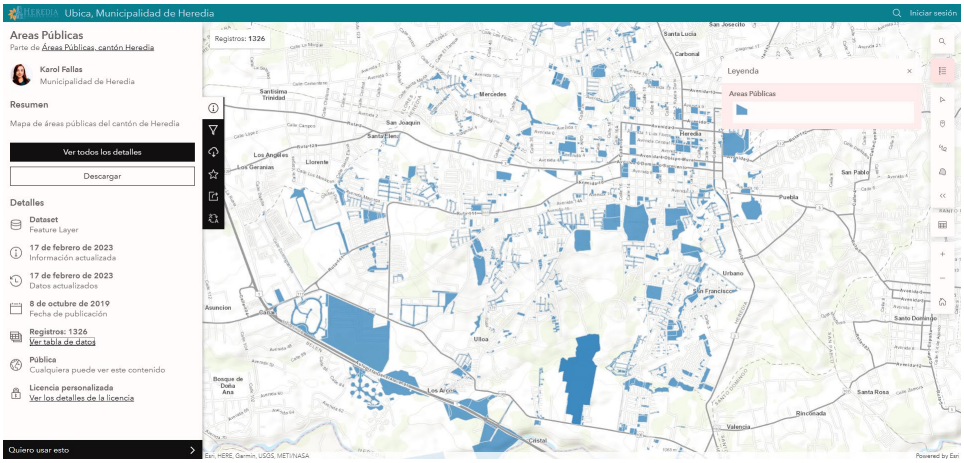


Figure 47. Public areas. Source: Limits (https://ubica.heredia.go.cr/

#### *4.12.4.8 Shelters*

The UBICA platform hosts a map showing the locations of proposed shelters in the event of an emergency within the Heredia canton. This information is provided by the Heredia Municipal Emergency Committee. Figure 48 displays a screenshot of the viewer with the proposed shelter locations.

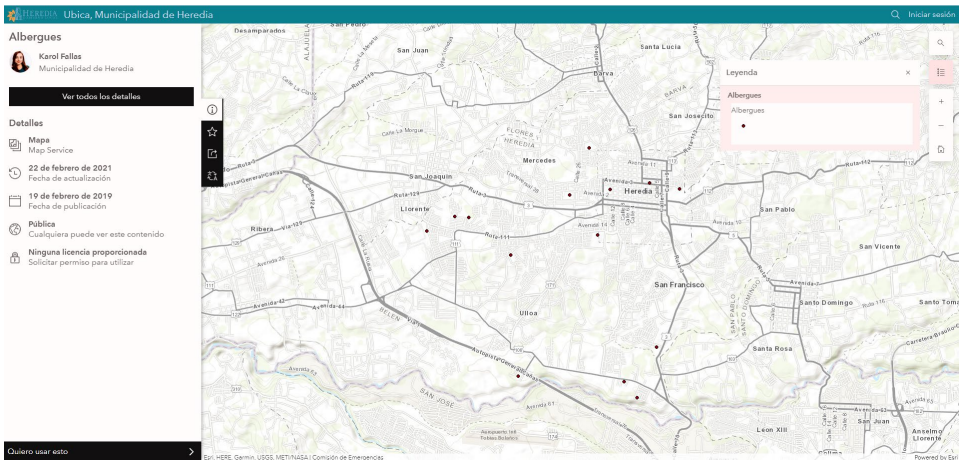


Figure 48. Shelters. Source: Community (https://ubica.heredia.go.cr/)

### 4.12.5 Structural System

Variables such as structural system are typically not available in cadastral records, housing censuses, or other supplementary data sources. One way to approximate this information is through the variable *Predominant Exterior Wall Material* from the National Population and Housing Census. This variable provides insight into the types of construction materials used across the country, their distribution relative to the total housing stock, and their geographic distribution. la Figure 49 presents an overview of the predominant exterior wall materials used in houses within the Heredia canton, based on data from the 2011 Population and Housing Census.

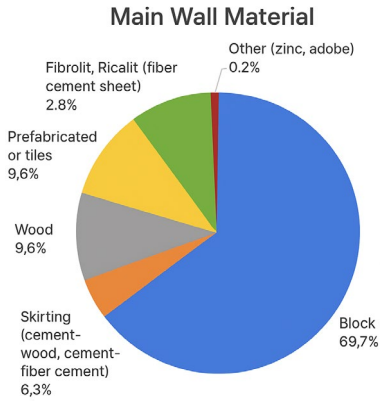


Figure 49. Predominant Exterior Wall Material in Heredia Canton

Based on the predominant exterior wall material and information gathered in previous sections—such as number of floors, usage sector, built area, among other algorithms are developed to assign a structural system to each building. This allows for classification of their vulnerability.

### 4.12.6 Indicators of People at Risk

To identify the population at risk, the UBICA platform provides access to population data and its distribution within the Heredia canton, according to census data published by the National Institute of Statistics and Censuses (INEC) from the 2011 census. Figure 50 shows how population information is displayed on the UBICA platform.

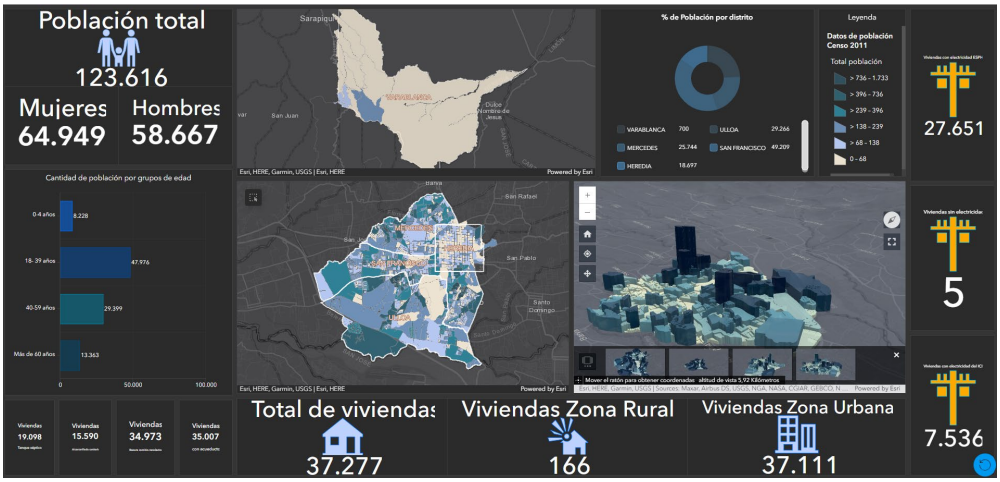


Figure 50. Population data. Source: https://ubica.heredia.go.cr/

## 4.13 Exposed Elements of the Tourism Sector – Buildings

To develop the exposure model for buildings in the tourism sector, the following sources of information are available:

### 4.13.1 Cartography – Buildings

The National Territorial Information System (SNIT) provides nationwide coverage of buildings and constructions. This dataset includes a descriptive attribute for building category, which specifies buildings corresponding to hotels, as shown in Figure 51.

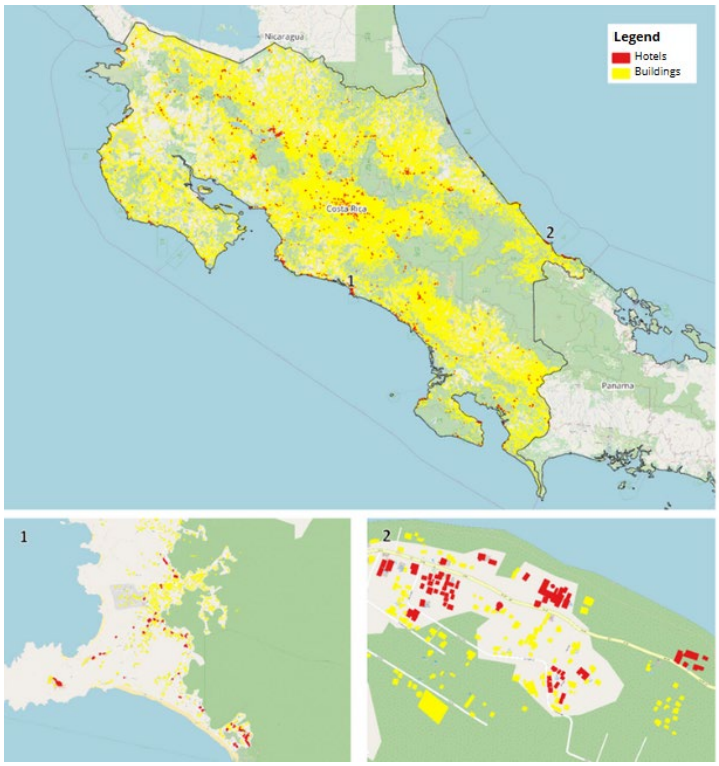


Figure 51. Hotels categorized in the building cartography

### 4.13.2 OpenStreetMap

To complement the official data, open data sources such as OpenStreetMap (OSM) are consulted. OSM is a collaborative, open geographic database that includes infrastructure and other aspects of the built environment, points of interest, land use, and land cover classifications. Figure 52 shows the locations of open data on lodging facilities and hotels in Costa Rica from OpenStreetMap.

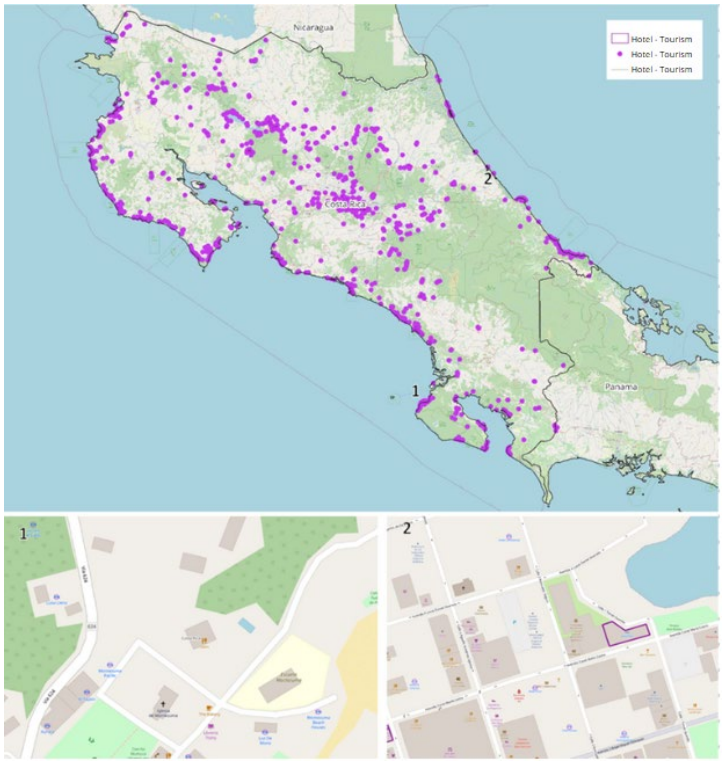


Figure 52. Open data on hotels in OpenStreetMap

### 4.13.3 Unit Base Value Manual by Construction Typology

The Unit Base Value Manual by Construction Typology, developed by the Ministry of Finance of Costa Rica, includes value classifications per square meter specifically for the hotel use sector. This information will be used as a foundational guide to determine the valuation of buildings belonging to hotels and hostels.

## 4.14 Exposed Elements of the Infrastructure Sector

Infrastructure portfolios are developed—similarly to building exposure models—using georeferenced information that includes vector geometric representations (point, line, polygon) and attributes that allow characterization. Each portfolio must include, at a minimum, georeferenced geometry, economic replacement value of the element, and a vulnerability classification.

In this project, the sectors considered for the canton of Heredia are road (highway), rail, energy (electric), communications, and water and sewer systems. Each sector is composed of multiple portfolios due to differences in geometric representation or attribute sets among exposed elements.

Five types of information sources were reviewed for the creation of the various infrastructure sector portfolios:

- Official information from the Heredia canton local government, published on their geographic information system called Ubica, as well as data from the Empresa de Servicios Públicos de Heredia S.A.

- Official data from national-level entities in Costa Rica consolidated in the SNIT system, such as the Ministry of Public Works and Transport (MOPT), the National Road Council (CONAVI), the National Power and Light Company (CNFL), the Costa Rican Electricity Institute (ICE), and the Costa Rican Institute of Aqueducts and Sewers (AyA).
- Exposure model information from the Global Assessment of Risk Framework (GRAF) in Costa Rica, which used the previously mentioned data sources as input.
- Data from collaborative community projects such as OpenStreetMap (OSM) and OpenCellID.
- Information from the National Laboratory of Materials and Structural Models of the University of Costa Rica (LanammeUCR).

The inclusion of a data source depends on the accurate representation of exposed elements and the quality of their attributes. Priority is given to official canton data; however, when this is unavailable or insufficient, the other sources will be used. Data sources that do not provide additional value, are redundant, or degrade model quality compared to the official canton data will be excluded.

The following sections list the data sources and provide a basic description of the procedures for creating exposure portfolios for each infrastructure sector.

### 4.14.1 Road Sector

The road sector includes the development of portfolios representing road segments and bridges within the canton of Heredia.

For bridges, the official data published on the UBICA platform (which is not available for download) includes 40 elements but lacks the relevant attributes necessary for proper bridge characterization. Due to this limitation, the data provided by LanammeUCR on the cantonal road network bridges will be used instead. This dataset includes information on the structure's dimensions, the type of beam material, and the type of superstructure. These attributes allow for accurate characterization of the bridges for multi-hazard assessment. Figure 53 presents a view from the GIS viewer of the Cantonal Road Network (RVC) bridges, focusing specifically on the canton of Heredia.

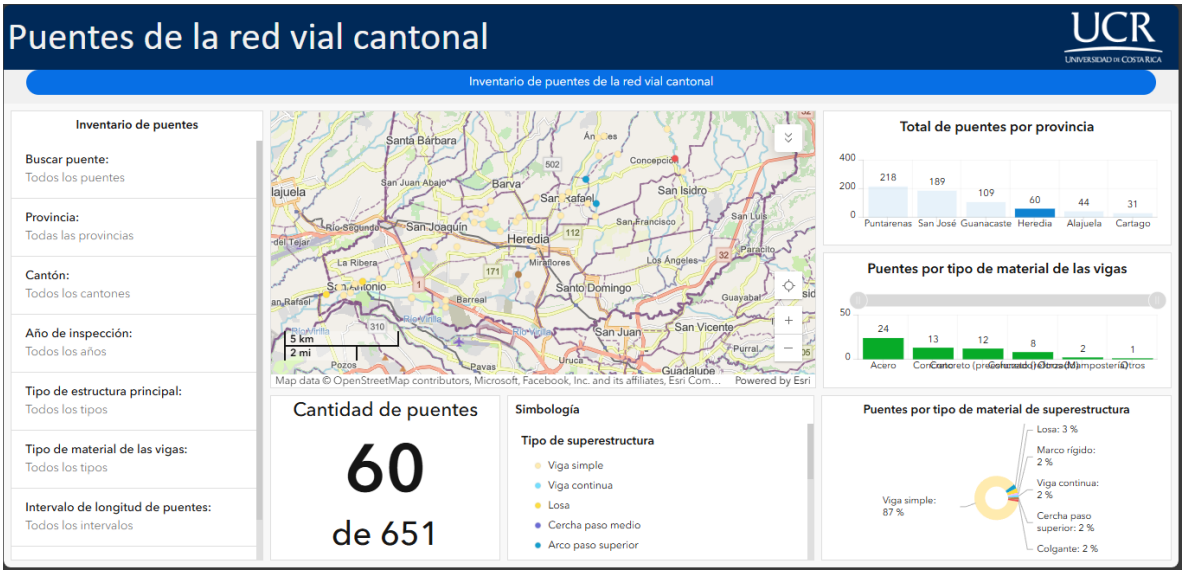


Figure 53. GIS Viewer of Cantonal Road Network (RVC) Bridges from Lanamme, UCR

To ensure that all bridges in the canton of Heredia are included, a cross-reference is conducted between the bridges identified by LanammeUCR and the open data from OpenStreetMap (OSM). If a bridge is found in the OSM database but not listed in the LanammeUCR dataset, it is incorporated into the analysis and assigned specific attributes. Bridge dimensions are determined using satellite imagery, while superstructure and material attributes are gathered through Google Street View.

### 4.14.2 Railway Sector

In this case, the railway sector refers to the San José – Heredia – Alajuela line, which passes through the districts of Heredia, San Francisco, and Mercedes within the canton of Heredia. This segment of the railway spans 4.6 kilometers and includes two passenger stations.

The primary source of information for this portfolio is OpenStreetMap (OSM), chosen due to its geometric alignment with data published by the canton of Heredia on the UBICA platform and by the Ministry of Public Works and Transport (MOPT) on its geoportal. However, these official sources are not available for public download and lack relevant attributes needed to build the exposure model. In contrast, OSM provides valuable data such as the line's length, track width, and elevation relative to the terrain (at grade or on a bridge).

To enhance the characterization of the railway line, aerial imagery from orthophotography will be used to identify superstructure attributes. Through image analysis using artificial intelligence, key features such as the presence of railway ties (yes or no) and the surface material (concrete or ballast) will be evaluated. This approach mirrors the methodology applied for bridge analysis in the road sector.

### 4.14.3 Electric Power Sector

The electric power sector is divided into three subsectors: generation, transmission, and distribution. For each subsector, specific portfolios will be developed to include the relevant elements and their associated attributes.

#### *4.14.3.1 Power Generation*

For the power generation subsector, a portfolio will be created that includes energy generation plants. Although there are no power generation facilities located within the administrative boundaries of the Heredia canton, the systemic nature of the sector makes it essential to consider those external plants that supply electricity directly to the canton. Therefore, these facilities will be included in the analysis.

The main information sources for this portfolio are the GRAF exposure model, which includes datasets provided by CNFL and ESPH, and the OpenStreetMap (OSM) database. Both sources offer point-based geospatial data, the type of energy generation technology (mainly hydroelectric), and the installed capacity of each plant. These attributes will be used to conduct an economic valuation of the plants and to classify them in terms of their vulnerability to natural or human-induced hazards.

#### *4.14.3.2 Electrical Transmission*

For the electrical transmission subsector, the exposure portfolio will include electrical substations (point geometry) and transmission lines (line geometry). As with the generation subsector, the analysis of transmission lines must extend beyond the cantonal boundaries to the provincial level in order to identify the lines and substations that are part of the electricity supply system serving the canton of Heredia.

The information sources for electrical substations include:

- The national substation layer published in the ICE geo-viewer, which only provides location data without additional attributes.
- The GRAF model, which uses datasets from ICE and ESPH and includes data such as input voltage and the predominant construction material of substations (mainly steel).
- OpenStreetMap (OSM), which provides location data only.

The GRAF dataset will serve as the primary source for the portfolio, complemented by the other two sources to enrich the dataset and avoid duplication of elements. As a filtering criterion, only substations located within 2.5 km of a transmission line will be included, as substations not clearly connected to the grid will be considered irrelevant for the analysis.

For transmission lines, the main data source will be the vector layer published by ICE through its geo-viewer, which includes high-voltage lines (138 kV and 230 kV) at the national level. Only those lines that connect the canton of Heredia to energy generation plants will be considered, regardless of whether they fall within the canton's administrative boundaries. Other available sources provide redundant or inconsistent data regarding the exact location of the lines and are therefore not deemed necessary for this component of the exposure model.

Based on the transmission network, the location of the transmission towers supporting the overhead cables will be determined. These towers will be identified based on the vertices of the polylines

representing the transmission lines. Their positions will then be verified and refined using the OSM point cloud for transmission towers, ensuring high spatial accuracy and minimizing geolocation errors.

#### *4.14.3.3 Electrical Distribution*

The electrical distribution subsector involves the development of a portfolio that includes the distribution network, differentiated by type of installation (overhead or underground), as well as the network's utility poles and transformers. Unlike the transmission network, which operates at a regional level to transport electricity, the distribution network functions at a local scale. Therefore, it is considered sufficient to analyze only the data within the canton of Heredia.

The primary data source for the distribution network is the official database provided by EPSH. This dataset includes line geometries and essential attributes for exposure modeling, such as the type of installation (overhead or underground) and line voltage. Figure 54 shows the EPSH distribution network within the canton.

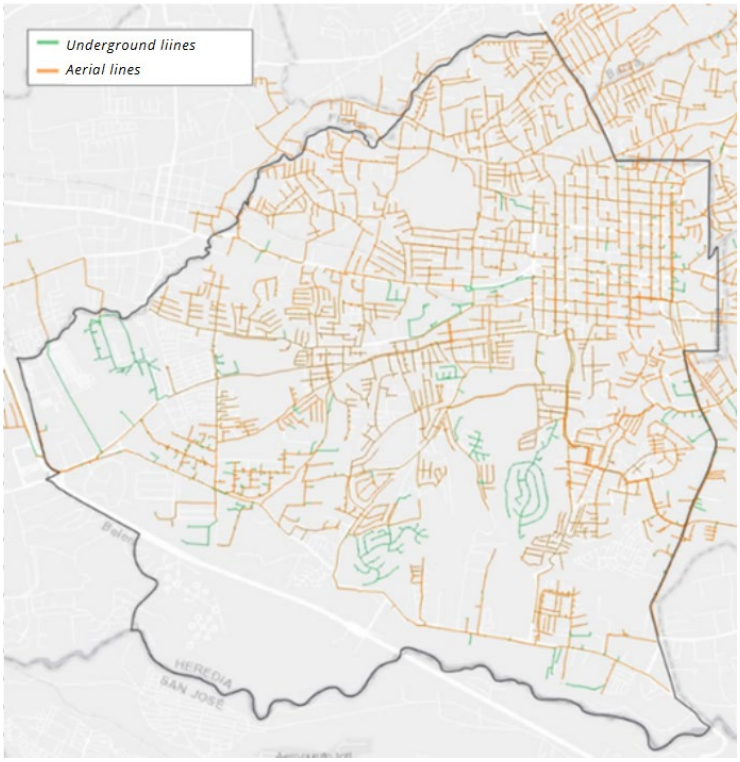


Figure 54. Electrical distribution network of Heredia canton

Additionally, some elements from the GRAF model, based on information from CNFL, can be incorporated. Although its primary coverage lies outside the canton of Heredia, it occasionally includes elements within the canton that are not managed by EPSH. The GRAF data contains the same attributes as the main source, allowing for a suitable complement to the exposure model.

For the utility poles of the overhead distribution network, the main data source is also EPSH, which provides point geometry data along with relevant attributes such as material, height, and year of construction.

Regarding transformers, the primary data source is the GRAF model, which is based on EPSH data (not publicly available). These records include point geometry and essential attributes such as transformer location and type of installation (overhead or pedestal-mounted).

After evaluating all information sources and defining the minimum required attributes for the exposure model, the available data is considered adequate for the economic valuation and vulnerability classification of the electrical distribution network components.

### 4.14.4 Telecommunications Sector

The exposure portfolio for the telecommunications sector is based on representing the infrastructure that provides fixed and mobile services.

For mobile services, the portfolio will consist of telecommunications antennas located within the canton of Heredia. To this end, the database from the collaborative project OpenCellID is utilized, which is the most extensive worldwide source of telecommunications antenna data. Its attributes include the type of network each antenna operates on (GSM, UMTS, LTE), its coverage radius (in meters), and the number of times the antenna has been detected. Figure 55 shows the distribution of antennas within the canton of Heredia.

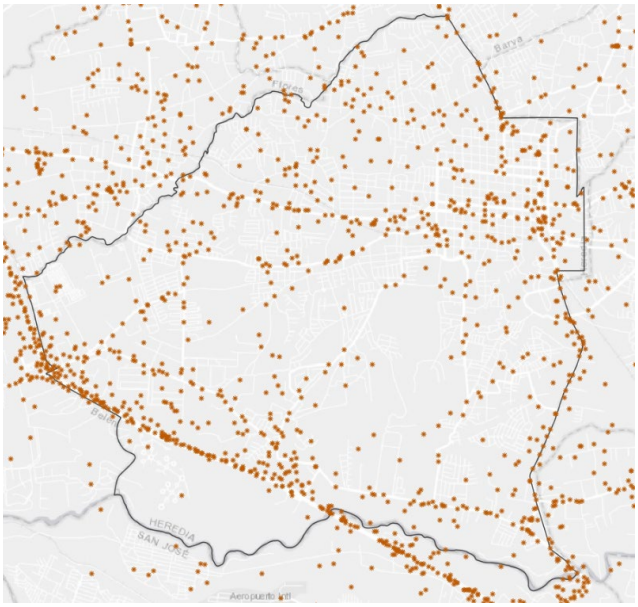

Figure 55. Mobile phone antennas in the canton of Heredia

Based on these attributes, records with few detections will be filtered out, as they may correspond to false positives. A key aspect of the exposure model is determining the relative position of each antenna with respect to the ground—specifically, whether it is at ground level or located on top of a building. To achieve this, building footprints within the canton and population density data will be used to assign a probability that an antenna is at ground level. This information will allow for differentiated vulnerability classifications.

On the other hand, there is no publicly available spatial data on fixed internet and telephone networks in households. However, using certain criteria and conditions, it is possible to structure a portfolio for fixed

communications. In the canton of Heredia, the percentage of homes with internet access according to INEC (2022) ranges between 86.4% and 90.6% across its districts (excluding the Varablanca district). This indicates that a high number of homes and buildings have access to fixed telecommunications services.

Considering this, and the fact that electrical, telecommunications, and road networks typically follow similar distribution patterns, the vector geometry of the road infrastructure will be used as a basis to estimate the possible telecommunications network in the canton. To validate the presence of each network element, criteria such as population density, socioeconomic status, and land use will be applied.

Additionally, the locations of local operator exchanges within the canton will be identified, which will help estimate data flow direction and determine zones with higher data traffic capacity. The final output is expected to be a portfolio containing the road network geometry, representing areas covered by fixed telecommunications services and associating attributes related to data transmission capacity for each network segment.

### 4.14.5 Water Supply and Sewerage Sector

The water supply and sewerage sector is divided into three portfolios: the potable water portfolio corresponding to the water supply system, the fire hydrant system, and the wastewater portfolio corresponding to the sewerage system.

In this sector, it is important to consider not only the infrastructure within the canton of Heredia but also those elements located outside its political-administrative jurisdiction, due to the systemic effect on resource provision. In this case, water capture and conveyance occur in the mountainous region north of the canton's urban area. Therefore, excluding these elements would reduce the accuracy of the risk assessment for the sector.

#### *4.14.5.1 Potable Water*

The potable water subsector includes multiple essential elements for delivering the resource to the population, such as:

- Water intakes
- Water conveyance pipelines
- Potable water treatment plants (PTAP)
- Storage tanks
- Pumping systems
- Conduction and distribution networks

The primary source of information for these elements is the GRAF exposure model, based on data from EPSH. This model includes most of the necessary attributes to characterize the infrastructure. However, in some cases, such as water intakes, there is no information on the captured flow rate, which prevents precise sizing of the structures. In these situations, it is assumed that all elements in the dataset share homogeneous characteristics.

The only element not included in the GRAF exposure model is the distribution network, as EPSH has an updated version of this infrastructure for the year 2024. Key attributes characterizing the distribution network include pipe diameter and material, which are fundamental for its accurate characterization.

Figure 56 shows the distribution network that will be used in the formation of the exposure model.

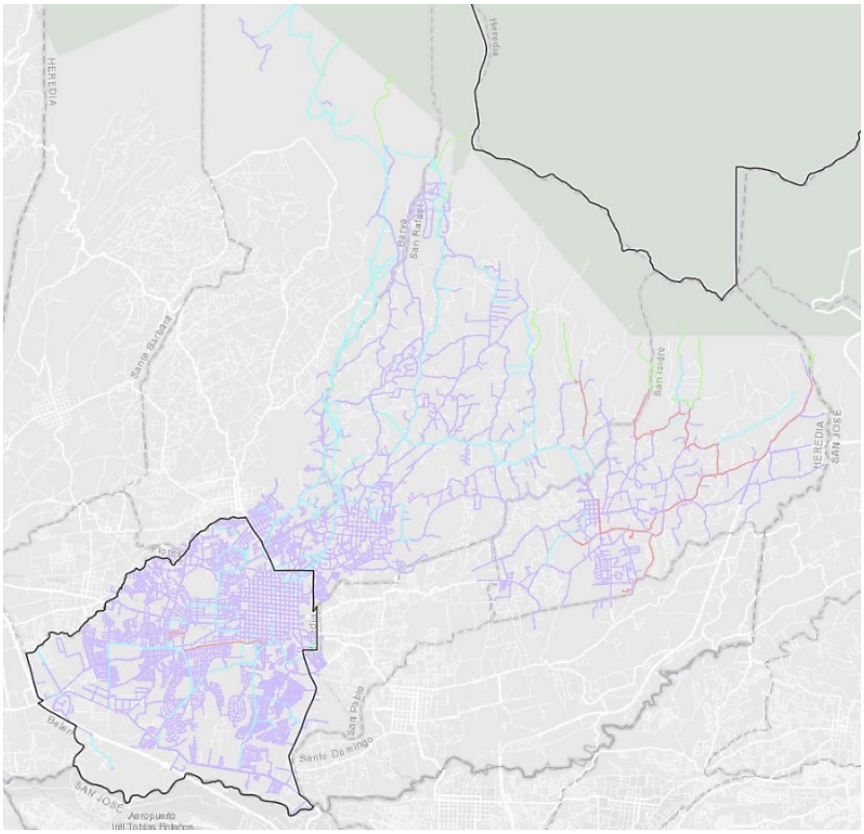


Figure 56. Potable Water Network in the Canton of Heredia

#### *4.14.5.2 Hydrant System*

The hydrant system is a critical component for emergency response, making its inclusion in the risk assessment essential. The data source used to incorporate this system into the exposure model is the EPSH. In this specific case, no distinguishing characteristics were identified among the elements, so all hydrants are considered to have uniform features.

#### *4.14.5.3 Wastewater*

The wastewater subsector includes several key elements necessary for the collection and treatment of wastewater, such as:

- Sanitary sewer network
- Sanitary manholes
- Wastewater treatment plants

The primary data source for these components is the EPSH, whose database is updated to 2024. Figure 55 displays the spatial distribution of the network and sanitary manholes, highlighting the uneven sewer coverage across the canton.

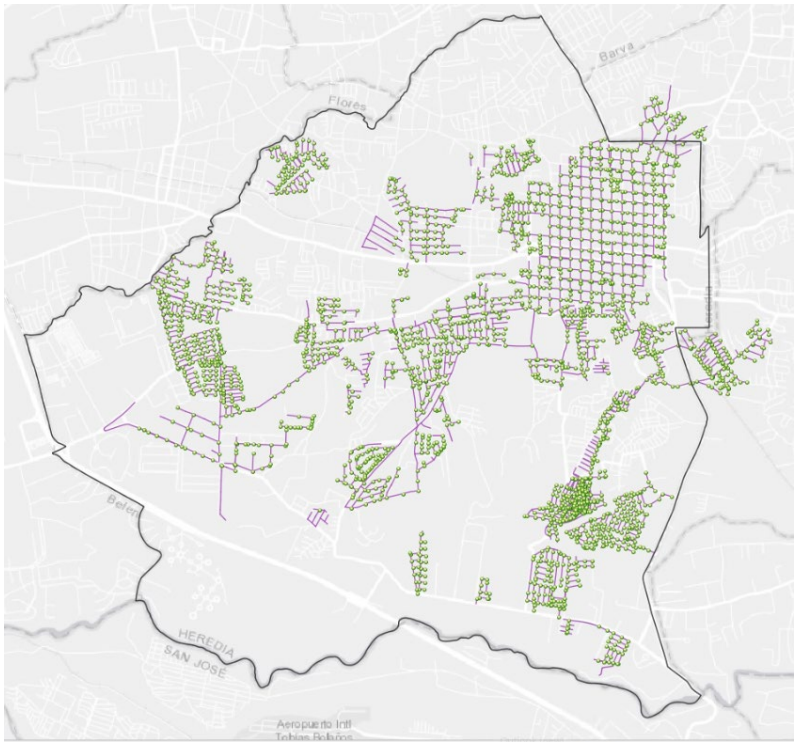


Figure 57. Wastewater Network in the Canton of Heredia

To complement the analysis, spatialized data from the 2011 census by INEC will be used to verify the presence of septic tanks in areas not connected to the sewer network. If zones with access to the sanitary network are identified but lack cartographic representation, the network will be extended following the methodology used for fixed telecommunications services. This includes assigning statistical attributes that align with the existing infrastructure.

For the sanitary sewer network, key available attributes include:

- Pipe diameter and material
- Age of the infrastructure

For sanitary manholes, the dataset provides:

- Dimensions (diameter and depth)
- Construction material
- Physical condition

These attributes will enable a precise vulnerability assessment of the infrastructure.

Regarding wastewater treatment plants, the information includes:

- Treated flow and design flow

- Population served
- Treatment technology used

This data supports accurate sizing and classification of facilities, as well as a more refined economic valuation. Additionally, the treatment plant database will be compared against and, if needed, supplemented by HydroSHEDS data. This approach will consider not only facilities within the Heredia canton, but also those nearby that may be processing wastewater from Heredia's urban area.

## 4.15 Exposed Elements of the Road Network (National Route 2 – RN2)

The exposure portfolio for National Primary Route 2 (RN2) is developed, as in previous sections, using georeferenced vector data (line geometry) and attribute information that enables detailed characterization. The exposure model is constructed by gathering the most comprehensive dataset possible to accurately represent the route in terms of geometry, economic valuation, and vulnerability classification by segment.

To achieve this, several data sources were reviewed:

### 4.15.1 National Laboratory of Materials and Structural Models – University of Costa Rica (LanammeUCR)

LanammeUCR manages a Geographic Information System (GIS) that integrates spatial data on roads, bridges, and geotechnical instability zones along the national road network.

In the case of roads, the system includes attributes that describe the cross-sectional characteristics of Costa Rica's national routes. These attributes include data from pavement tests, such as Falling Weight Deflectometer (FWD) results and the International Roughness Index (IRI), as well as information on pavement materials, geometric features (e.g., road width and number of lanes), and traffic characteristics such as the Average Daily Traffic (ADT). Figure 58 displays a view from the GIS viewer showing the "surface material" attribute of the National Road Network (RVN).

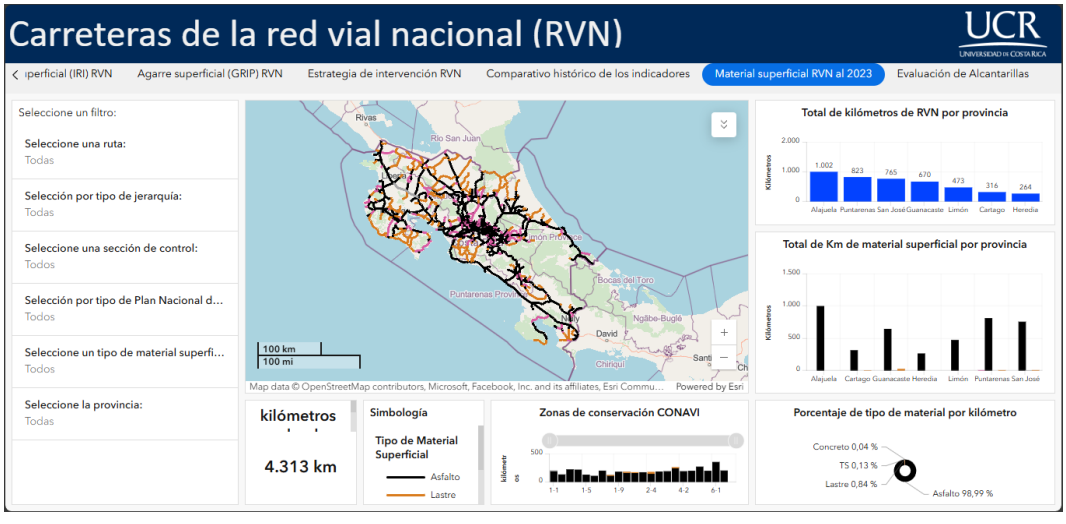


Figure 58. GIS Viewer of the National Road Network (RVN) Roads – LanammeUCR

Regarding bridges, LanammeUCR has compiled detailed information that includes attributes such as dimensions, spans, and superstructure type. This data allows for an accurate representation of bridge elements within the exposure model and supports their classification in the vulnerability model. For instance, Figure 3 presents a view from the GIS viewer displaying the “superstructure type” attribute for bridges in the National Road Network (RVN).


Figure 59. GIS Viewer of bridges of the National Road Network (RVN) Roads – LanammeUCR

### 4.15.2 National-Level Entities (MOPT – CONAVI)

The Ministry of Public Works and Transportation (MOPT) provides spatial data through its geo-viewer (see Figure 60), where the geometric representation corresponds to the road centerline. Relevant attributes for the exposure model include the road hierarchy—classified entirely as primary in this case—and the right of way.

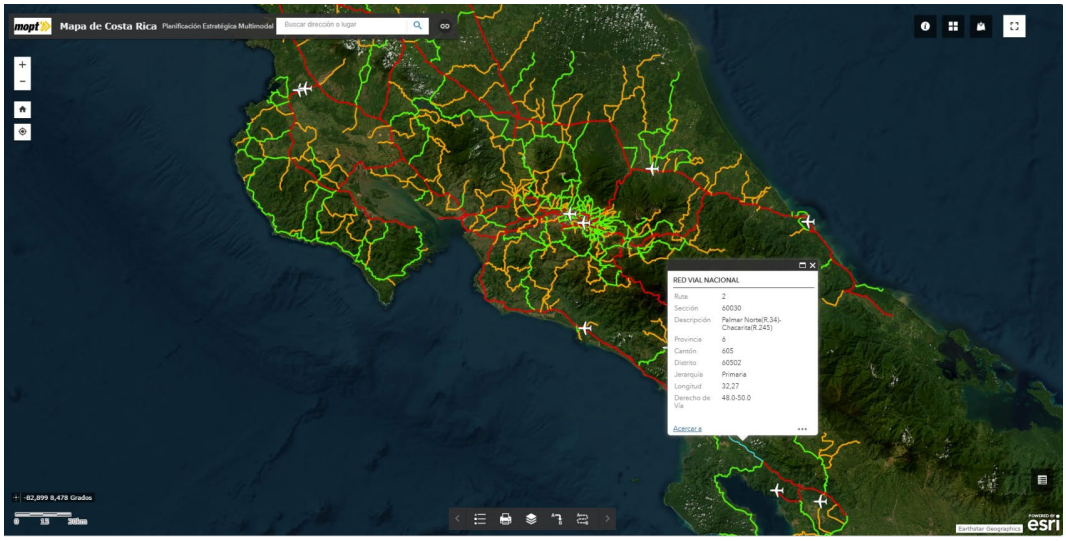


Figure 60. MOPT National Roads Geo-viewer

Additionally, the MOPT has a certification system (see Figure 57) that complements the geo-viewer information with further data about sections of Costa Rica's national roads. Key attributes include terrain classification, surface type, surface description, pavement structure, and composition. These elements are essential for accurately characterizing the road infrastructure of the RN2.

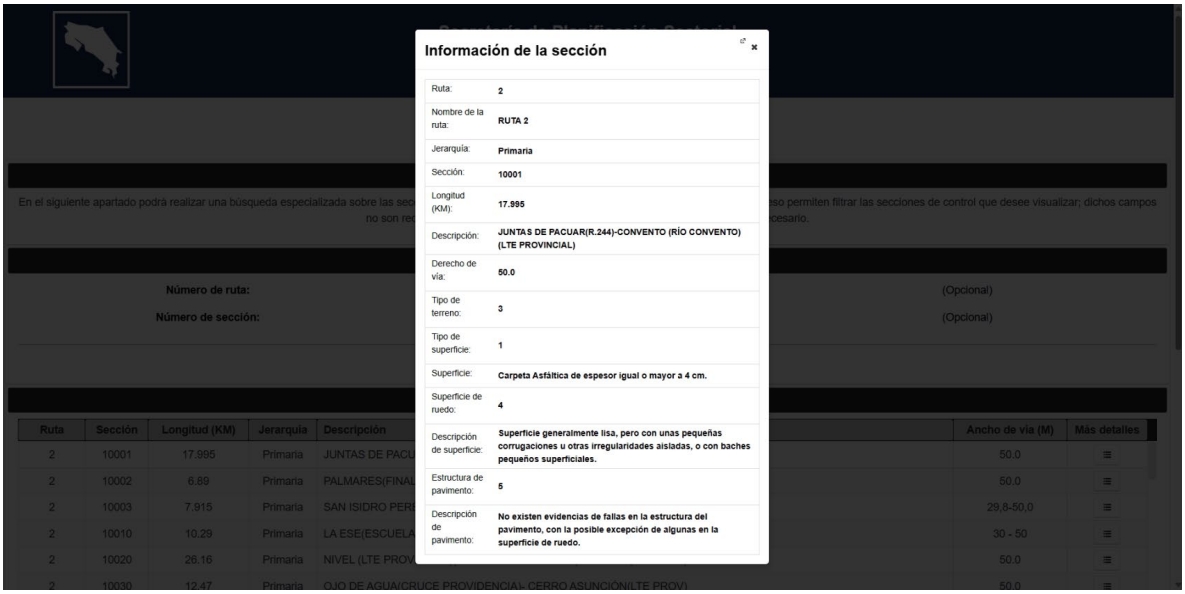


Figure 61. MOPT Road Certification System

On the other hand, the National Road Council (CONAVI) also has a geo-viewer that provides information about the road network; however, in this case, it does not offer additional data beyond what is already presented by the MOPT on its platforms.

### 4.15.3 OpenStreetMap (OSM)

Another valuable source of information is the collaborative community project OpenStreetMap (OSM), which can provide complementary data such as the number of lanes on different road sections and the location of bridges. Identifying bridges is a key step in developing the exposure model for RN2, given their impact on economic valuation and vulnerability assessment.

### 4.15.4 Satellite Imagery – Google Street View

To complete the exposure model of RN2, it is essential to identify supplementary structures that ensure its operability, such as retaining walls, embankments, and drainage ditches. For bridges, attributes like length, approximate width, clearance (gauge), typology, and construction material must be determined, as these factors significantly influence valuation and risk analysis. To achieve this, satellite images and Google Street View are used to extract visual information along various segments of the road. Automated image analysis based on artificial intelligence allows for precise identification and characterization of these elements.

## 4.16 Agricultural Sector Exposure Elements (Crops)

The drought and flood risk assessment for the agricultural sector focuses primarily on coffee and sugarcane crops at the national level. To accurately determine their vulnerability to water deficit or excess events, it is essential to have detailed information about their location, planted and harvested areas, as well as their productive yield (tons per unit area). Additionally, factors such as seasonality and phenological development must be taken into account.

The data utilized comes from various sources, with the most relevant ones—on which the determination of exposure for coffee and sugarcane crops nationwide will be based—discussed below.

### 4.16.1 National Agricultural Survey – ENA (2023)

According to the results of the 2023 National Agricultural Survey (ENA), conducted by the National Institute of Statistics and Census (INEC), detailed and up-to-date information is available on agricultural, livestock, and forestry production in Costa Rica.

Since its inception in 2017, the ENA has been conducted annually as a national-level sample survey. Its purpose is to generate data on planted and harvested areas, production volumes, product destinations, and agronomic practices applied to the crops most significant to the country's economy.

Table 8 illustrates the extent of planted and harvested areas, as well as the production volumes of permanent crops, including coffee and sugarcane. For sugarcane, only the area intended for sugar production is considered, excluding sugarcane used for forage and sweetener production.

Table 8. Planted and Harvested Area (hectares) and Production (metric tons) by Permanent Crop, 2023. (INEC, 2024)

| Crop | Area | | Production |
|---|---|---|---|
| | Planted | Harvested | |
| Avocado | 3 995,8 | 2 869,4 | 13 471,7 |
| Banana | 47 766,1 | 46 320,5 | 2 439 825,2 |
| Coffee | 74 000,2 | 59 175,0 | 416 215,4 |
| Sugarcane | 56 619,6 | 49 533,7 | 3 191 449,4 |
| Chayote | 444,0 | 366,9 | 39 785,5 |
| Mango | 5 637,1 | 3 129,5 | 24 583,7 |
| Orange | 12 847,0 | 7 256,6 | 174 626,0 |
| Oil palm | 69 398,6 | 66 695,7 | 1 109 441,9 |
| Hearth of palm | 3 200,3 | 2 820,5 | 2 883,5 |
| Plantain | 8 774,4 | 5 926,8 | 72 877,5 |

### 4.16.2 Sixth National Agricultural Census (2014)

The Sixth National Agricultural Census is a key resource for this study, providing a detailed overview of the agricultural sector and its development. This large-scale, nationwide statistical survey collected information from all agricultural holdings in the country, capturing their main characteristics and activities during the 2014 agricultural year.

Since no agricultural census had been conducted since 1984, this update is essential for analysis and decision-making within the sector. Moreover, its results serve as the basis for updating sampling

frameworks used in the annual National Agricultural Surveys (ENAs), ensuring more accurate and representative data for future studies.

This report primarily presents information at the national and provincial levels, with some data available at the canton level. Notably, Figure 63 and Figure 64 illustrate the distribution of coffee and sugarcane planted areas by canton. Beyond cultivated areas, the census also reveals the proportion of these crops that have reached production age (Figure 62). This information is crucial for permanent crops like coffee and sugarcane, where productivity depends not only on cultivated areas but also on plant maturity. Such data are fundamental for estimating agricultural production and planning adaptation strategies for the sector.

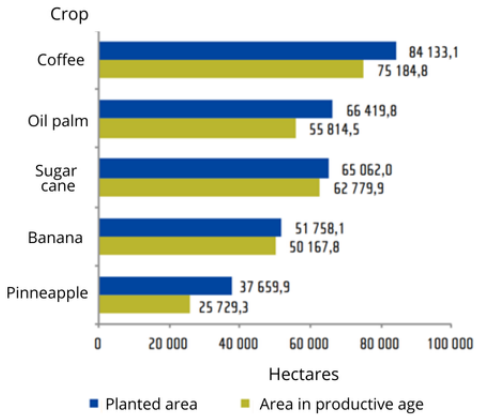


Figure 62. Planted Area and Production-Age Area (hectares) of Major Permanent Crops (INEC, 2015)

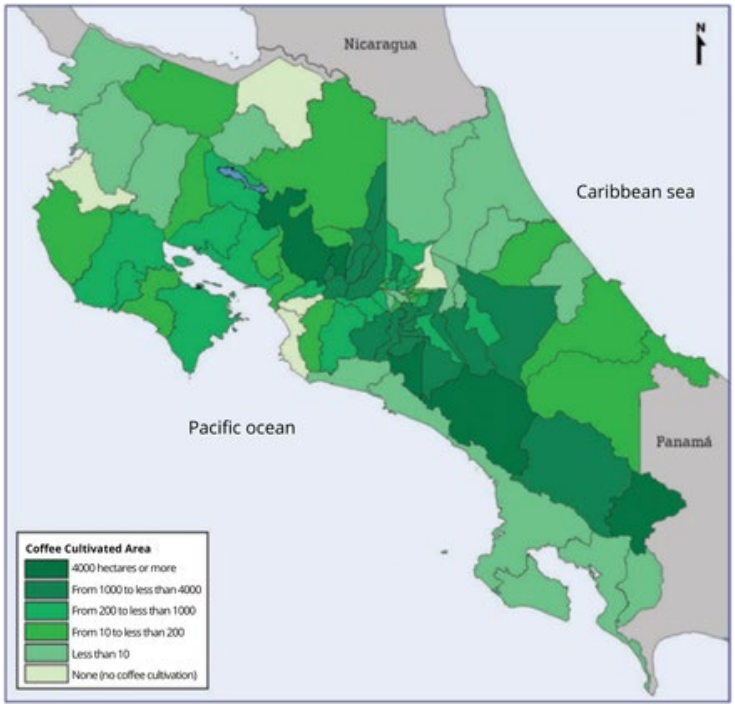


Figure 63. Distribution of Coffee Planted Area by Canton (hectares) (INEC, 2015)

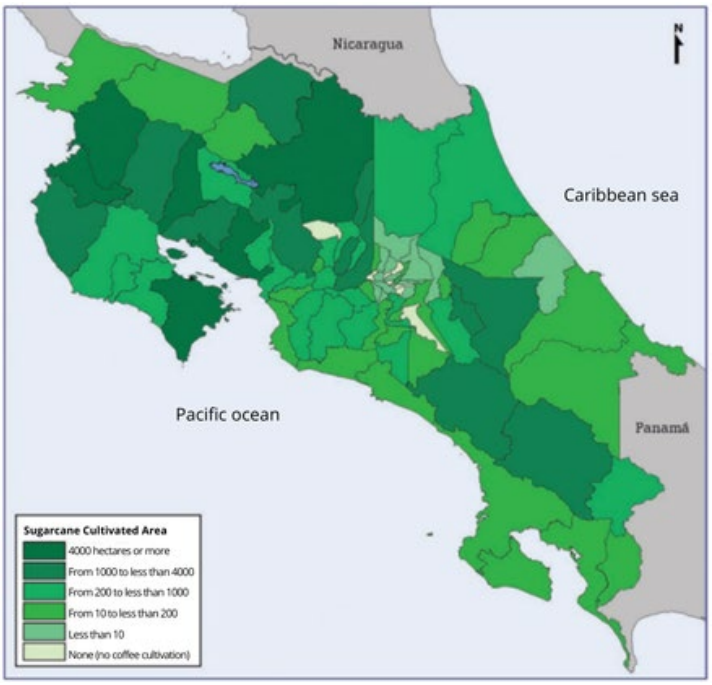


Figure 64. Distribution of Sugarcane Planted Area by Canton (hectares) (INEC, 2015)

At the provincial level, the census provides detailed data on the use of agricultural inputs, specifying types of fertilizers, weed control methods, and the application of pesticides such as insecticides and fungicides. Key aspects of crop management are also analyzed, including the destination of the production, the origin of the seeds used, and the implementation of irrigation systems.

Since this study focuses on micro, small, and medium-sized producers, the number of farms and their distribution by size are examined at both the national and provincial levels, as illustrated in Figure 65. Additionally, this information is broken down by province for both coffee and sugarcane.

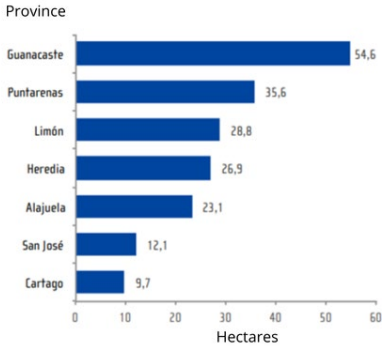


Figure 65. Average Farm Size by Province (hectares) (INEC, 2015)

Figure 66 illustrates the location and distribution of agricultural farms across Costa Rica. Although having this georeferenced information in a digital format would be ideal, it is currently not publicly available online or in open-access databases. Generally, this type of data is protected under data privacy laws, and in many cases, access requires authorization from the responsible entity—in this case, INEC. Nonetheless, Figure

66 provides a more detailed view of the geographic distribution of farms compared to provincial and cantonal scales.

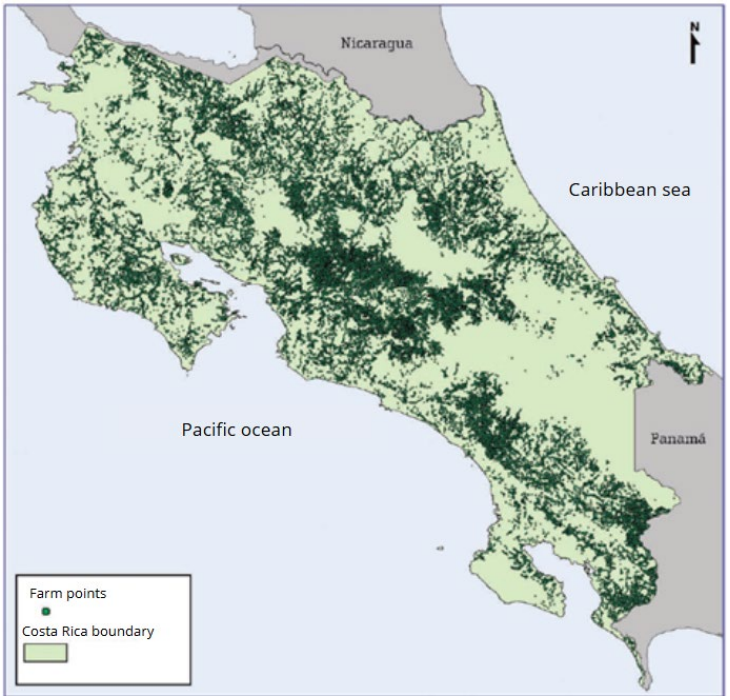


Figure 66. Distribution of Farms Based on Georeferenced Census Points (INEC, 2015)

### 4.16.3 Land Cover and Land Use Map of Costa Rica – REDD+

Land cover and land use maps are effective tools for obtaining spatial information on various types of land cover, such as forests, water bodies, agricultural areas, urban zones, and other land uses. These maps enable detailed landscape analysis, facilitating environmental assessment and management.

The Land Cover and Ecosystems Mapping Diagnostic for Costa Rica (SIMOCUTE, 2019) indicates that there is no clear legal mandate defining the State's role in this area. Although the demand for information is high, the lack of a standardized methodology complicates the comparison of maps over time and has resulted in irregular updates. Efforts have been made to unify criteria, such as the design and validation of the CLC-CR Legend (Corine Land Cover Costa Rica version) by INAT in 2015. However, to date, no map has adopted this legend.

Despite these challenges, the National Territorial Information System (SNIT) maintains a series of land cover and use maps of Costa Rica, updated biennially since 2013 (2013, 2015, 2017, 2019, 2021). Thanks to the application of a consistent methodology, these maps have achieved coherence and continuity over time.

The development of these maps is led by the National Meteorological Institute (IMN), an agency under the Ministry of Environment and Energy (MINAE) responsible for greenhouse gas emissions reports (INGEI). IMN coordinates this process with support from the REDD+ Secretariat, comprised of the National Forestry

Financing Fund (FONAFIFO) and the National System of Conservation Areas (SINAC). Beyond providing territorial information, these maps are a key tool for measuring activity data and calculating greenhouse gas emissions and removals in the AFOLU sector (SNIT, 2024; MINAE, 2015; CDI, 2015).

Figure 67 and Figure 68 illustrate the evolution of Costa Rica's land cover and land use distribution between 2013 and 2021. This information is essential for the spatial analysis of agricultural and livestock land cover, allowing the identification of land use trends and the assessment of changes in permanent crops as well as pasture areas used for livestock.

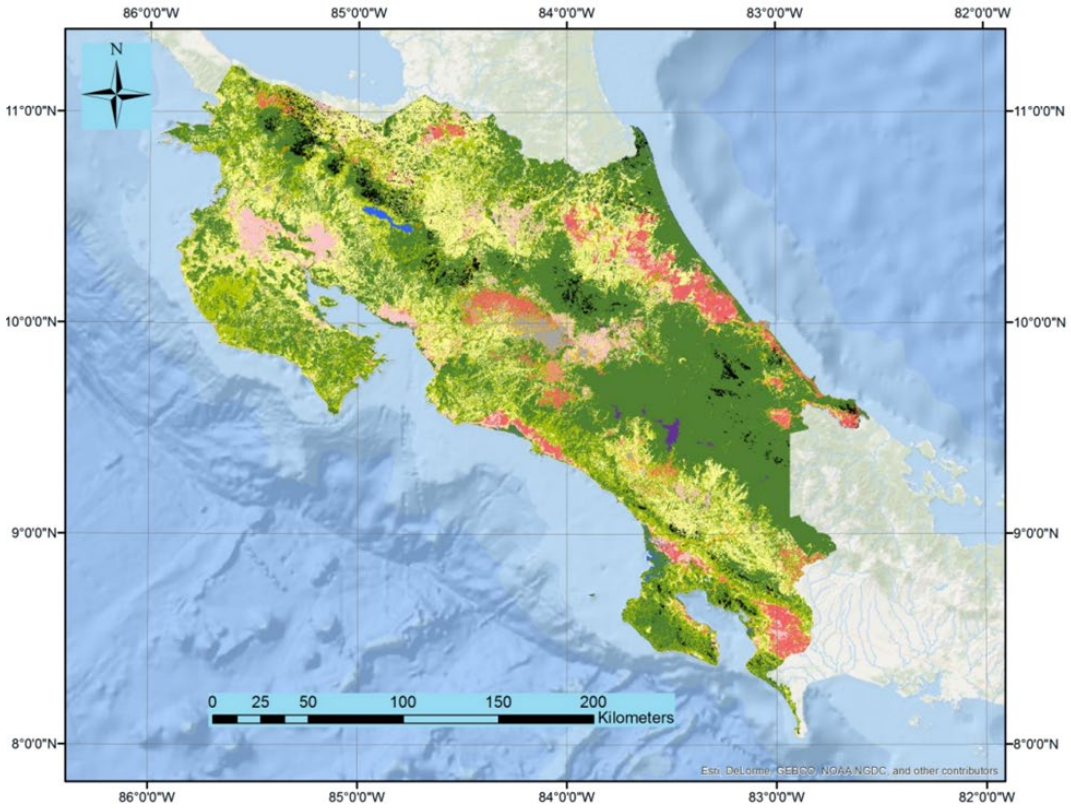


Figure 67. Land Cover and Land Use Map of Costa Rica 2013 (MINAE, 2015; CDI, 2015; SNIT, 2024)

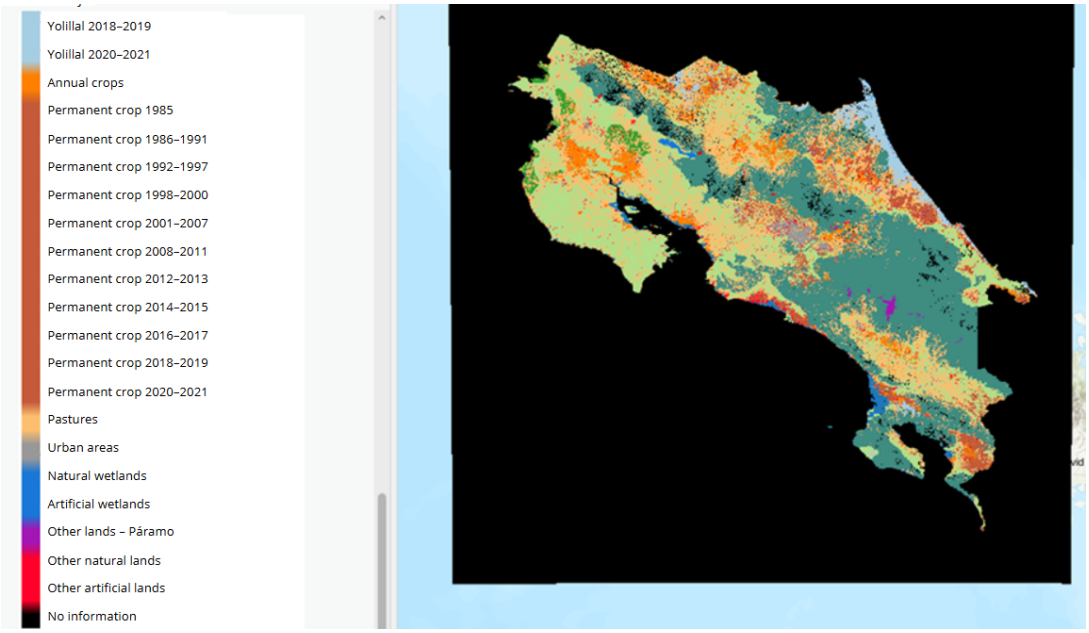


Figure 68. Land Cover and Land Use Map of Costa Rica, 2021 (SNIT, 2024)

### 4.16.4 Study of Effective Practices for the Adaptation of Priority Crops for Insurance in Costa Rica

This study, conducted by the Tropical Agricultural Research and Higher Education Center (CATIE, 2018a, 2018b), identifies agricultural practices aimed at mitigating the impact of climatic and non-climatic events on priority crops such as coffee (CATIE, 2018b) and sugarcane (CATIE, 2018a). It analyzes the production system, the events affecting each stage of the crop cycle, and the mitigation strategies used by experts, including their costs and evaluation under environmental programs. This study has established a reliable technical knowledge base for its application in financial products and agricultural insurance, which is one of the goals of consultancy conducting the present study. Additionally, CATIE's findings support another essential objective of this study: promoting risk management through sustainable practices that enhance the resilience and adaptability of the agricultural sector within the framework of the Ministry of Agriculture and Livestock's (MAG) Nationally Appropriate Mitigation Actions (NAMA).

While all the information from the CATIE project is vital, the specifications of phenological cycle stages by production region stand out as particularly useful. These include details on crop varieties, planting dates, total cycle duration, and the length of each phase.

As an example, Figure 69 illustrates the adjustments made to the timing and duration intervals of each phase in the Brunca production region. The figure shows how the sugarcane cycle is distributed throughout the year, considering the region's climatic conditions. Four main phases are identified, beginning with germination or sprouting (Phase 1) and ending with plant maturation (Phase 4), whose duration is influenced by crop variety and local soil and climate conditions. The rainy season (April to November) notably impacts the first three phases, while the dry season (December to March) favors maturation. This distribution highlights the importance of adapting agronomic management to local climatic conditions to

optimize crop yield. These phases were adapted based on expert consultation and literature review (CATIE, 2018).

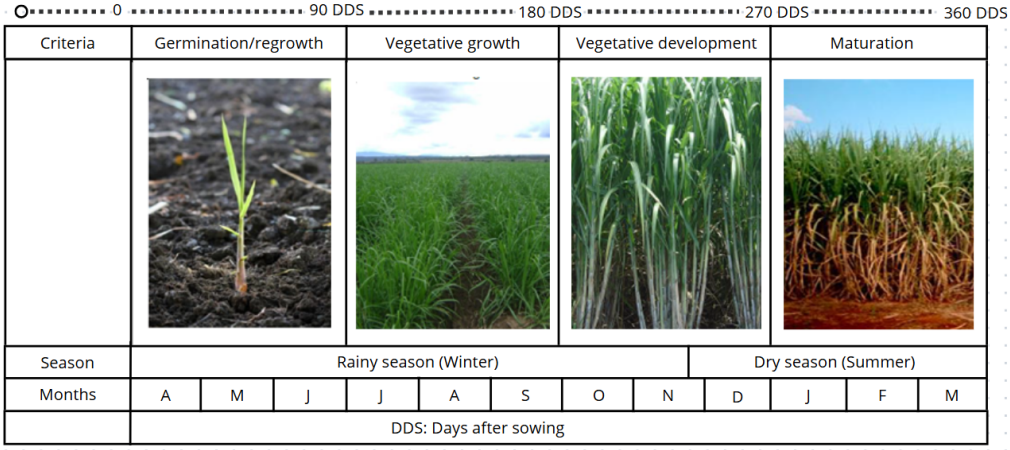


Figure 69. Phenological Cycle Stages of Sugarcane in the Brunca Production Region (Prepared based on expert consultation)

Similarly, the coffee crop exhibits a well-defined phenological cycle, although with a longer duration due to the specificities of its development. As an example, Figure 70 illustrates the adjustment made to the months and duration intervals of each phase in the Turrialba production region. This figure shows how the coffee phenological cycle unfolds over an approximate two-year period, influenced by the region's climatic conditions. The coffee cycle is divided into six main phases, beginning with seed selection and preparation (Phase 0) and concluding with the plant's natural dormancy and leaf shedding (Phase 6). The duration varies depending on the variety and local edaphoclimatic conditions.

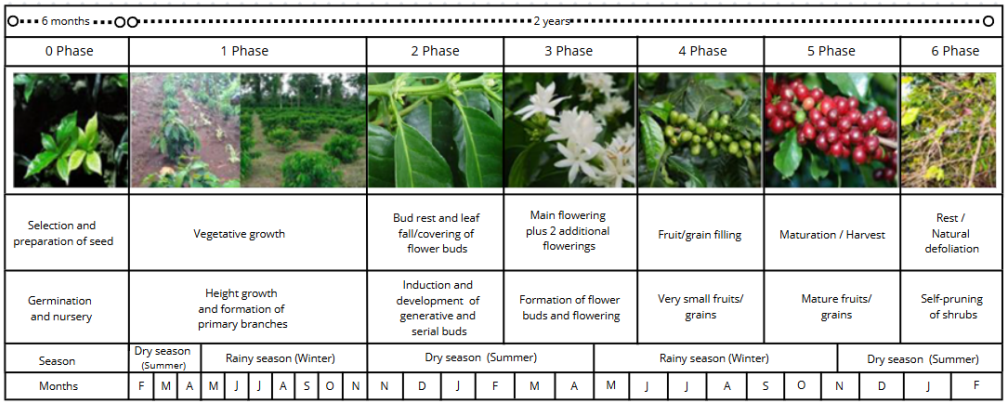


Figure 70. Phenological Cycle Stages of Coffee in the Los Santos Production Region (Prepared based on expert consultation)

Finally, CATIE (2018) conducted a suitability analysis to identify optimal, moderate, and deficient areas for sugarcane and coffee cultivation in Costa Rica. The suitability maps are presented in Figure 71 and Figure 72.

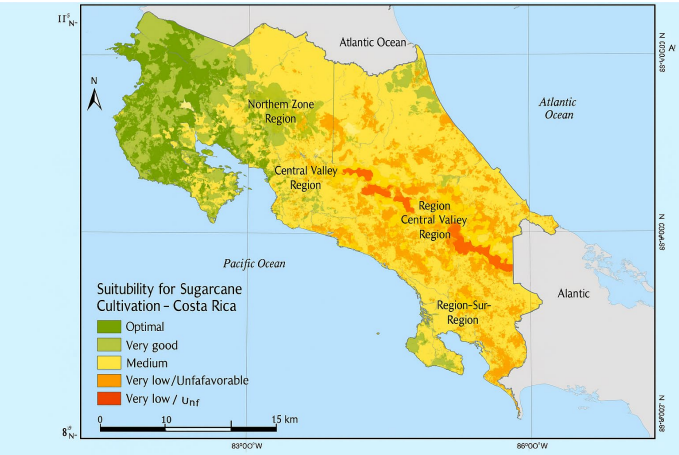


Figure 71. Sugarcane Cultivation Suitability Map in Costa Rica

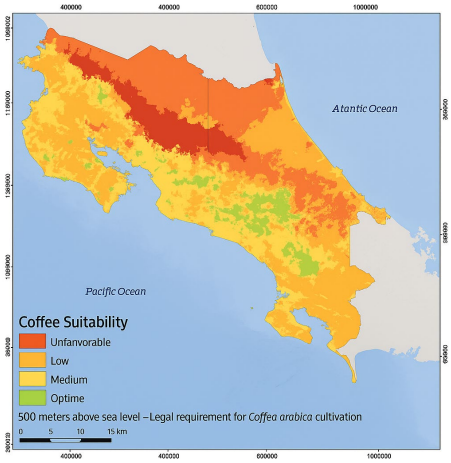


Figure 72. Coffee Cultivation Suitability Map in Costa Rica

## 4.17 Exposure Elements of the Livestock Sector

The drought and flood risk assessment in the livestock sector considers as exposed elements the livestock inventory, including the various types of pastures and the herds of animals dependent on them.

The model's methodology estimates losses in meat production systems based on the reduction of live animal weight following such events. However, it does not account for demographic changes within the herd, such as births, natural deaths, or animal movements between regions in the country.

The information used comes from various sources, with the most relevant ones—on which the determination of the livestock sector's exposure at the national level will be based—detailed below.

### 4.17.1 National Agricultural Survey – ENA (2023)

According to INEC, the 2023 National Agricultural Survey (ENA) provides detailed information on cattle and pig farming, as well as livestock management practices at the national level. This study includes data on the cattle herd, broken down by sex, age, and purpose, as well as records of births and losses by cause, as shown in Table 9. For pig farming, the survey reports the number of animals by purpose and production

stage, along with efficiency indicators such as farrowings per sow, weaning days, and the interval between weaning and pregnancy.

Table 9. Total Cattle Population by Sex and Purpose (INEC, 2024).

| Purpose | Total | Sex | |
|---|---|---|---|
| | | Males | Females |
| **Total** | **1,510,563** | **420,620** | **1,089,943** |
| **Meat** | 901,299 | 325,247 | 576,052 |
| **Milk** | 284,904 | 16,505 | 268,399 |
| **Dual purpose** | 322,599 | 77,107 | 245,492 |
| **Work** [1] | 1,761 | 1,761 | – |

[1] Footnote: likely refers to animals used for labor purposes, such as oxen.

The estimated pig herd indicates that 88.5% is dedicated to meat production, while the remaining 11.5% corresponds to breeding pigs. Figure 73 shows the percentage distribution of meat pigs by production stage, and Figure 74 presents the percentage distribution of breeding pigs by sex.

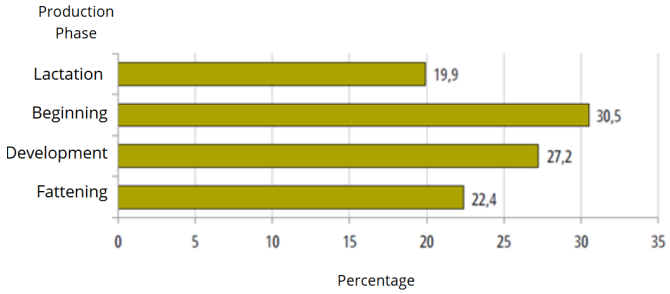


Figure 73. Percentage Distribution of Meat Pigs by Production Stage (INEC, 2024)

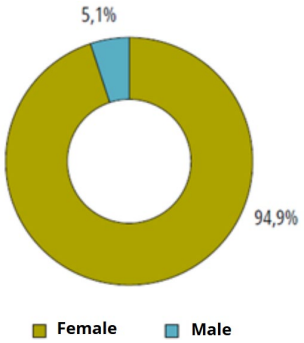


Figure 74. Percentage Distribution of Breeding Swine by Sex (INEC, 2024)

The ENA also provides valuable information on cattle losses in Costa Rica, enabling the identification of the main causes affecting the sector. Table 10 details the total number of cattle lost during 2023, classified by age group and cause of loss. In addition to losses from diseases, theft, and animal attacks, the survey highlights the impact of climatic factors such as floods and droughts, offering a more comprehensive view of the challenges faced by livestock farming.

On the other hand, information on swine livestock is presented according to purpose (meat production or breeding), but it does not specify causes of loss, limiting the analysis of specific factors affecting this sector.

Table 10.Total Cattle Losses by Age Group and Primary Cause of Loss, 2023

| Cause of loss | Total | Age | | |
|---|---|---|---|---|
| | | Under 1 year | 1 to under 2 years | 2 years and older |
| **Total** | **63,640** | **20,519** | **11,913** | **31,208** |
| **Theft, slaughter, robbery** | 11,148 | 582 | 963 | 9,603 |
| **Low rainfall (drought)** | 816 | – | 31 | 785 |
| **Pests and diseases** | 27,648 | 13,962 | 5,671 | 8,015 |
| **Floods** | 38 | 3 | – | 35 |
| **Accidents (fractures, blows)** | 9,482 | 2,039 | 1,564 | 5,879 |
| **Animal attacks (felines, snakes)** | 10,959 | 2,531 | 3,095 | 5,333 |
| **Other** | 3,549 | 1,402 | 589 | 1,558 |

### 4.17.2 VI National Agricultural Census (2014)

In addition to the information presented in section 4.16.2, the 2014 National Agricultural Census provides data on livestock activities in Costa Rica. The census survey covers various types of livestock, including cattle, goats, sheep, pigs, and poultry, among others. The census results, reflecting the number of farms and animal populations, are shown in Figure 75.

| Activity | Total farms | Total animals |
|---|---|---|
| Cattle | 37 171 | 1 278 817 |
| Goats | 2 348 | 12 852 |
| Sheep | 1 792 | 35 800 |
| Pigs | 14 355 | 435 243 |
| Donkeys | 482 | 3 149 |
| Buffalo | 247 | 4 380 |
| Horses | 19 695 | 66 942 |
| Poultry (2)) | 36 752 | 18 589 455 |

1 A single farm may engage in one or more livestock activities, and thus may be counted in several categories.
2 Includes chicks, pullets, roosters, and hens; does not include other poultry such as turkeys, wild turkeys, quail, geese, ducks, or other

Figure 75. Types of Livestock Activities by Total Number of Farms and Animal Population

The document primarily provides information at the national and provincial levels, with some data available on the cantonal scale. For example, Figure 76 display the number of heads of cattle. Additionally, for cattle data includes the total number of farms raising these animals, broken down by herd size and number of animals.

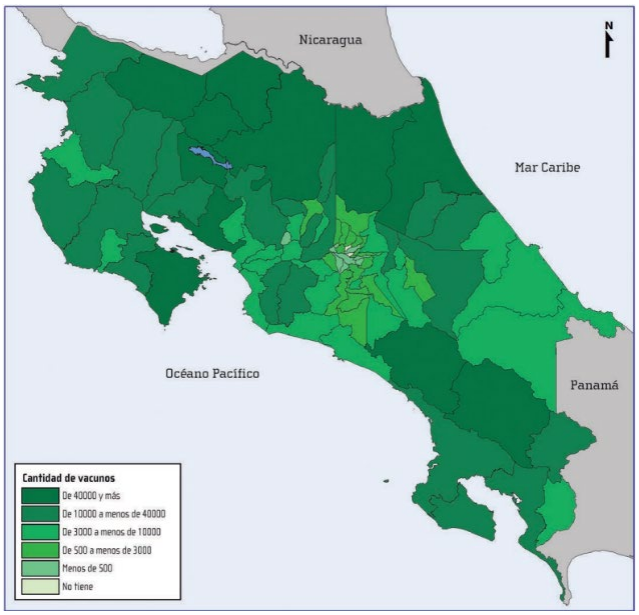


Figure 76. Distribution of Cattle Population by Canton

## 4.18 Physical Vulnerability of Buildings

The vulnerability of exposed elements is defined through mathematical functions that relate hazard intensity to direct physical impact. These functions, known as vulnerability functions, must be estimated and assigned for each type of asset identified in the exposure database. Below are the sources and studies consulted, within which vulnerability functions were studied and developed for various structural systems present in the region and for the hazards analyzed. It is important to highlight that these functions are available either because they were developed by the same consultant or are publicly accessible.

### 4.18.1 CAPRA ROBOT

CAPRA ROBOT includes a library of vulnerability functions specifically generated for typical construction classes in the Latin America and Caribbean region. This library covers vulnerability functions for earthquakes, strong winds, storm surges, and floods. More details can be found in ERN-AL (2009).

Figure 77 shows an example from these vulnerability function libraries developed for different structural systems, in this case for earthquake hazards.

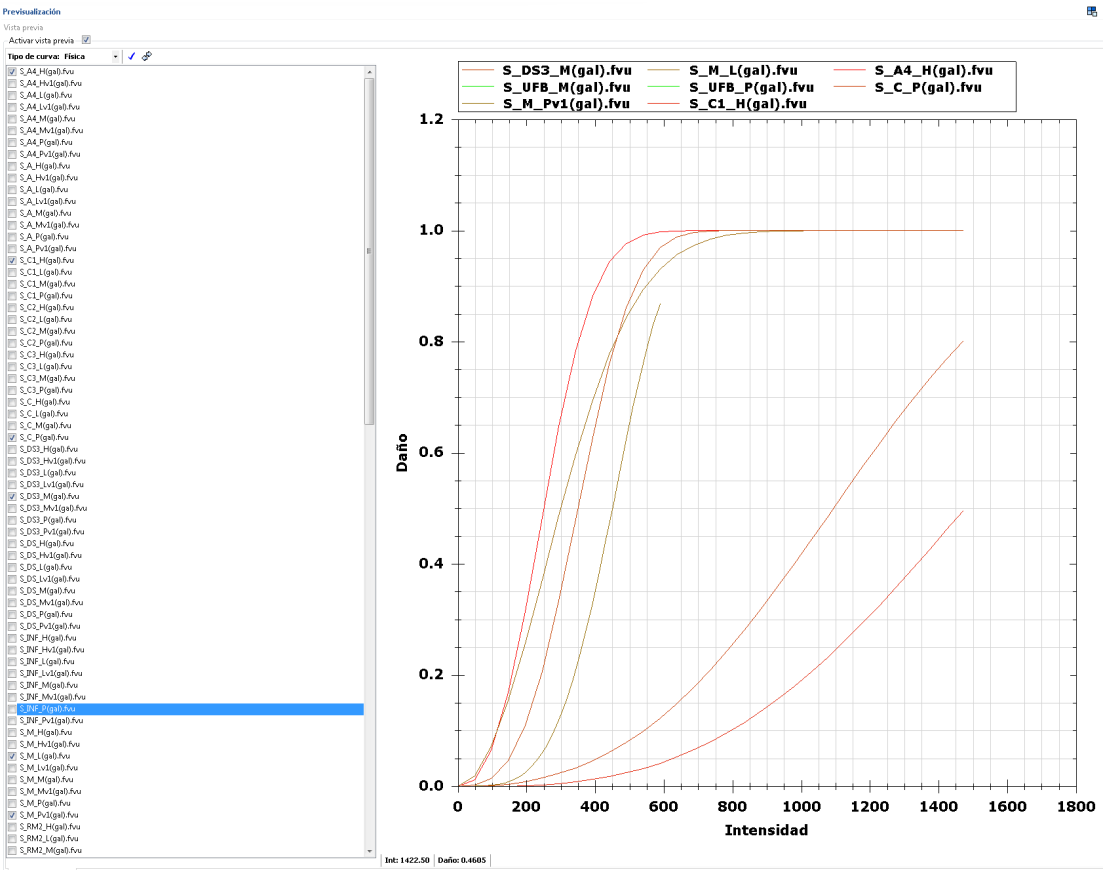


Figure 77. Vulnerability Function Library for Buildings – CAPRA Project

### 4.18.2 GAR15

As part of the GAR15 project, a vulnerability regionalization was carried out to capture the different construction characteristics across world regions, based on available regional studies and data. The outcome includes libraries of vulnerability functions for various hazards, such as the one shown in Figure 78. More details can be found in INGENIAR (2014).

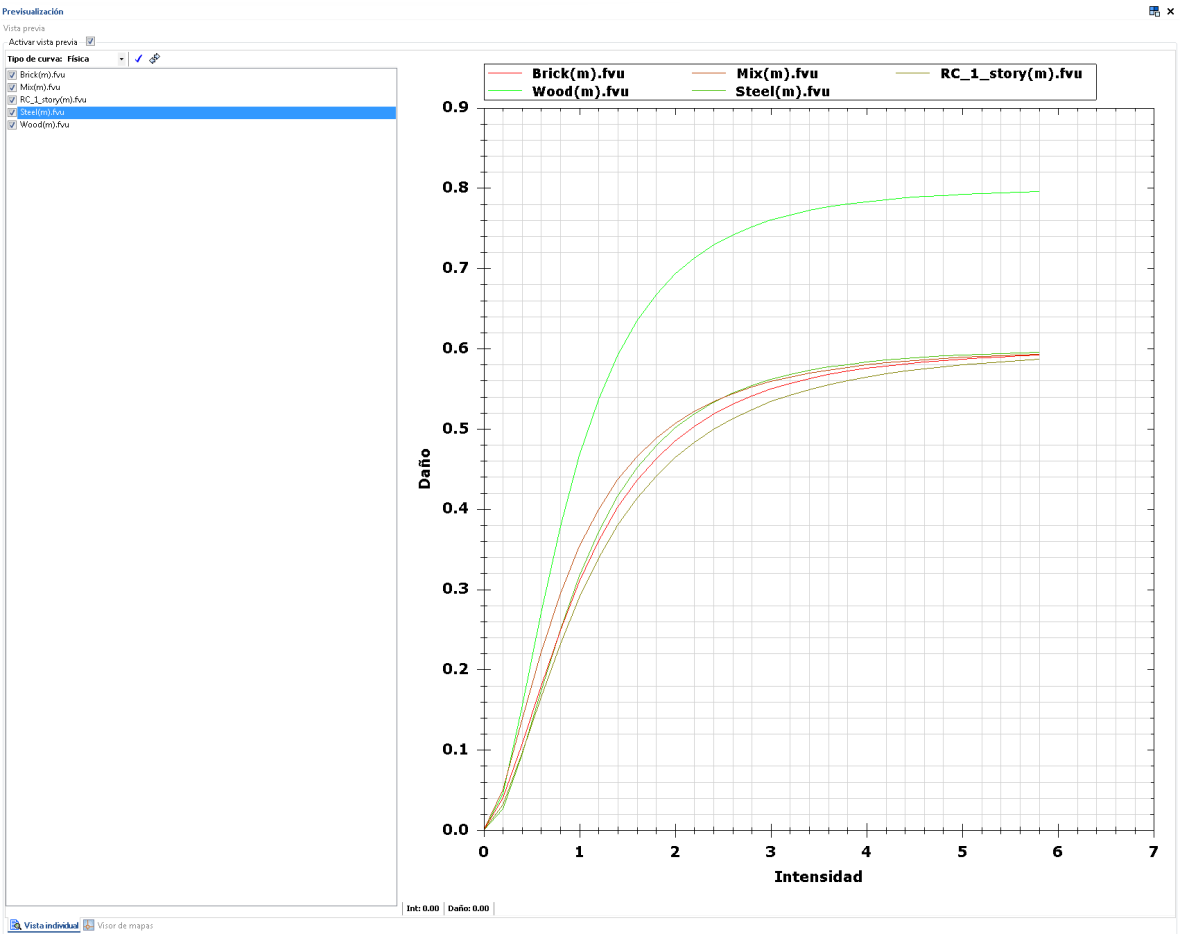


Figure 78. Vulnerability Function Library for Buildings – GAR15 Project

### 4.18.3 Vulnerability to Tsunami Hazards

The primary data source for modeling vulnerability to tsunami hazards is the study by Suppasri et al. (2013). This work defines fragility functions based on data collected from the 2011 Great East Japan Earthquake tsunami. These fragility functions were converted into vulnerability functions using the same methodology applied to the HAZUS earthquake vulnerability functions, as described in CIMNE et al. (2012).

## 4.19 Physical Vulnerability of Infrastructure

For infrastructure elements, vulnerability functions are used to describe damage. These functions are defined based on archetypes—an approach that allows for capturing complexities in elements that cannot be addressed otherwise at this scale of analysis.

Vulnerability archetypes are simplified representations of infrastructure elements, composed of a series of components that collectively account for the element's characteristics and complexity, enabling it to fulfill its intended function. Each component within the archetype is assigned a damage function, according to

its classification based on key characteristics defined within this methodology. These characteristics include:

- Type: Classification based on the element's nature, such as civil construction (different from buildings), building, mechanical equipment, electrical equipment, electromechanical equipment, or furniture.
- Protected: Indicates whether the element is protected against a specific hazard by another element within the archetype.
- Buried: Specifies if the element is located below ground level in the archetype.
- Watertight: Defines whether the element is watertight or not.
- Reference Level: The vertical position of the element within the archetype (corresponding to floor number in buildings).
- Height: The height of the element relative to its reference level within the archetype.
- Foundation: Type of foundation—flexible, shallow, or deep—applicable only to buildings and civil works.
- Structural System / Material: The structural system or material type of element.
- Participation: The cost contribution of the element relative to the total cost of the archetype.

Based on these categories, damage functions are assigned to each element, which are then aggregated according to each element's cost participation to determine the overall vulnerability of the archetype.

## 4.20 Physical Vulnerability of the Road Network

The physical vulnerability of a road can be defined using an archetype-based methodology that segments and classifies roads by vulnerability according to their attributes. A combination of vulnerability classifications can be generated based on the attributes considered in the segmentation; for example, in a portfolio with two road classifications (national and local) and three terrain categories (flat, rolling, steep), six typologies can be created, each with different weightings for their components.

For estimating vulnerability curves, a general segment typology is established, defining participation values for each road element. Figure 79 illustrates the base typology and its components. Table 11 presents the contribution of each component within the archetypes corresponding to road segments.

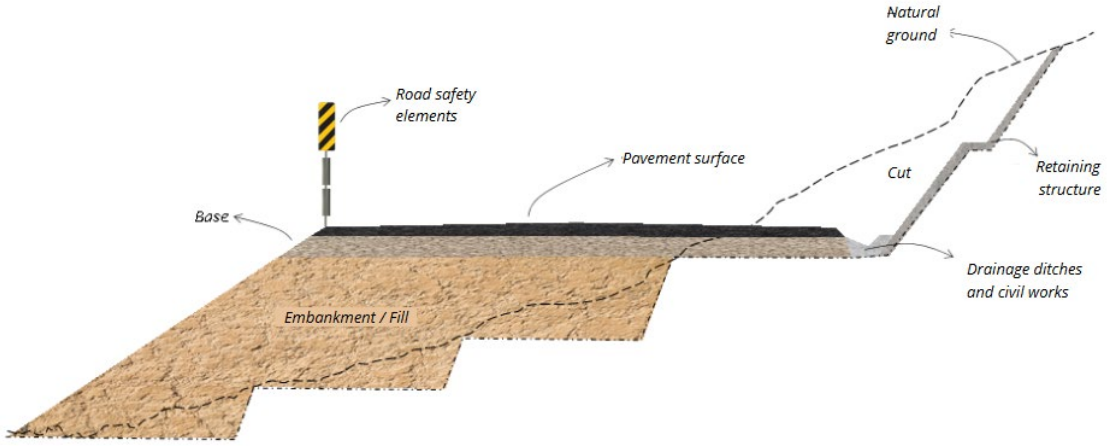


Figure 79. Cross-Sectional View of the Base Road Segment Typology

Table 11. Component Contribution in Base Typology for Road Segment Archetypes

| Element | V1 | V2 | V3 | V4 | V5 | V6 |
|---|---|---|---|---|---|---|
| Pavement | 66% | 46% | 29% | 75% | 54% | 32% |
| Base Layer | 17% | 18% | 11% | 9% | 11% | 6% |
| Embankment | 9% | 17% | 30% | 8% | 14% | 33% |
| Structures | 6% | 7% | 9% | 6% | 7% | 9% |
| Retention Systems | 0% | 9% | 17% | 0% | 11% | 15% |
| Road Safety | 2% | 3% | 4% | 2% | 3% | 5% |

Figure 79 presents the estimated vulnerability functions for flooding events across six archetypal road segments.

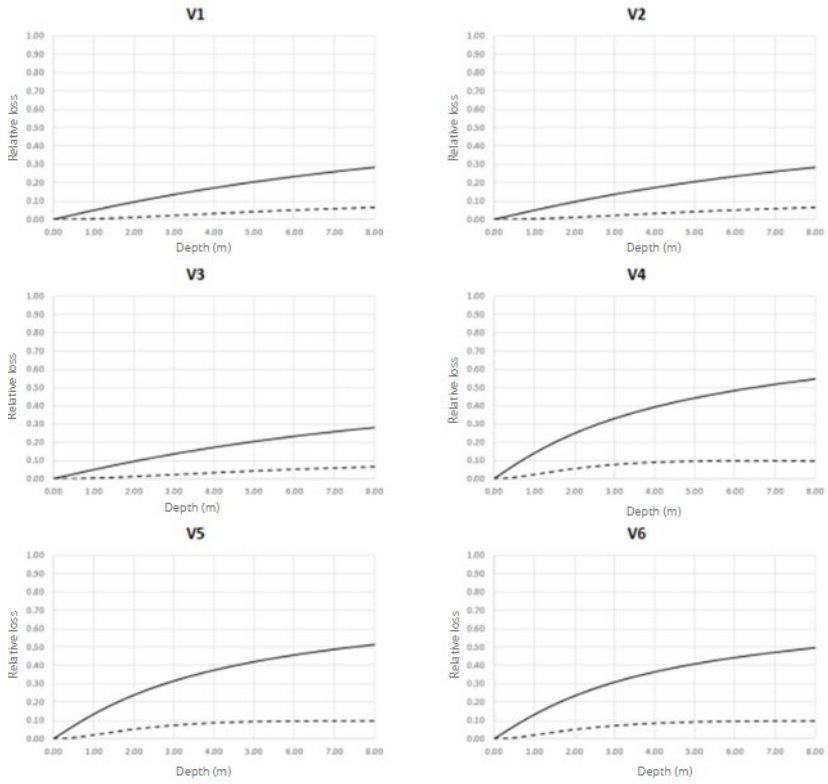


Figure 80. Vulnerability Curves for Six Base Road Segment Typologies

## 4.21 Physical Vulnerability of Crops

In Costa Rica, there are studies and methodologies that assess the vulnerability of crops such as coffee and sugarcane to extreme hydrometeorological events like droughts and floods.

The Manual for Vulnerability Assessment and Adaptation Training in Coffee, published by the Tropical Agricultural Research and Higher Education Center (CATIE, 2018d), provides a practical methodology to evaluate the vulnerability levels of coffee production units in the face of climate change, including aspects related to droughts and floods.

In the documents titled “Effective Practices for Reducing Impacts from Climatic Events” for coffee and sugarcane crops (CATIE, 2018a; 2018b), the Ministry of Agriculture and Livestock (MAG) offers important information about crop characteristics, phenological stages, soil preparation practices, weed control, planting methods, and fertilization. It also includes spatial location and information on crop sensitivity.

According to the report “Drought Conditions and Management Strategies in Costa Rica” (Soto, 2013), the areas that are most at risk of extreme drought events are the North Pacific and the Northern Zone toward Lake Nicaragua. These regions experience below-average surface and groundwater runoff, affecting soil moisture and, consequently, agricultural production.

Additionally, a literature review allowed the generation of crop-specific parameters necessary for modeling crop development using the FAO’s Aquacrop program methodology. These parameters describe various crop variables, including crop cycle duration, crop coefficient (Kc), water use efficiency, and sensitivity to

water stress, all of which influence yield and crop response to available water. Below is a list of the different variables and their descriptions.

Table 12. Crop Model Variables

| Variable | Description | Unit |
|---|---|---|
| CropType | Crop type: '1' - Leafy vegetables, '2' - Root/tuber, '3' - Fruit/grain | [-] |
| CalendarType | Growth cycle determination: '1' - Calendar days, '2' - Growing Degree Days (GDD) accumulated | [-] |
| SwitchGDD | Convert calendar days to GDD ('0': No; '1': Yes) | [-] |
| PlantingDate | Planting date | (dd/mm) |
| HarvestDate | Last harvest day | (dd/mm) |
| Emergence | Time from planting to emergence | days or GDD |
| MaxRooting | Time from planting to maximum root depth | days or GDD |
| Senescence | Time from planting to senescence | days or GDD |
| Maturity | Time from planting to maturity | days or GDD |
| HIstart | Time from planting to start of yield formation | days or GDD |
| Flowering | Duration of flowering (-999 for non-fruit/grain crops) | days or GDD |
| YldForm | Duration of yield formation | days or GDD |
| GDDmethod | Method used for GDD calculation: | [-] |
| | '1': Tavg = (Tx + Tn)/2; | |
| | '2': Tavg = (T*x + Tn*)/2; | |
| | '3': Tavg = (T*x + Tn)/2 | |
| Tbase | Base temperature below which crop development stops | [°C] |
| Tupp | Upper temperature threshold above which crop development stops | [°C] |
| PolHeatStress | Pollination affected by heat stress (0: No; 1: Yes) | [-] |
| Tmax_up | Max air temperature where pollination starts to fail | [°C] |
| Tmax_lo | Max air temperature where pollination fails completely | [°C] |
| PolColdStress | Pollination affected by cold stress (0: No; 1: Yes) | [-] |
| Tmin_up | Max air temperature below which pollination starts to fail | [°C] |
| Tmin_lo | Air temperature below which pollination fails completely | [°C] |
| BioTempStress | Biomass production affected by temperature stress (0: No; 1: Yes) | [-] |
| GDD_up | Minimum GDD required for total biomass production | [°C·days] |
| GDD_lo | GDD at which no biomass production occurs | [°C·days] |
| fshape_b | Shape factor describing biomass reduction due to insufficient GDD | [-] |
| PctZmin | Initial percentage of minimum effective root depth | [%] |
| Zmin | Minimum effective root depth | [m] |
| Zmax | Maximum root depth | [m] |
| fshape_r | Shape factor describing root expansion | [-] |
| fshape_ex | Shape factor describing effects of water stress on root expansion | [-] |
| SxTopQ | Maximum water extraction in upper root zone | [$m^3/m^3$/day] |
| SxBotQ | Maximum water extraction in lower root zone | [$m^3/m^3$/day] |
| a_Tr | Parameter describing effect of canopy decline on transpiration/photosynthesis capacity | [-] |
| SeedSize | Soil surface area covered by a plant at 90% germination | [$cm^2$] |
| PlantPop | Number of plants per hectare | [plants/ha] |
| CCmin | Minimum canopy cover fraction to ensure yield formation | [fraction canopy] |
| CCx | Maximum canopy cover | [fraction soil cover] |
| CDC | Canopy decline coefficient | [fraction/day or GDD] |
| CGC | Canopy growth coefficient | [fraction/day or GDD] |
| Kcb | Crop coefficient when canopy is fully developed but before senescence | [-] |
| fage | Crop decline coefficient due to age | [%/day] |
| WP | Normalized water productivity for ET0 and CO2 | [g/$m^2$] |

| | | |
|---|---|---|
| WPy | Adjustment to normalized water productivity for ET0 and CO2 during yield formation | [% of WP] |
| fsink | CO2 absorption and response capacity factor per crop: | [-] |
| | Cereals (corn, rice, wheat, sunflower, sorghum): 0 to 0.2 | |
| | Legumes (soybean, beans): 0.2 to 0.4 | |
| | Undetermined (tomato, quinoa): 0.4 to 0.6 | |
| | Roots and tubers (potato, beet): 0.6 to 0.8 | |
| bsted | Adjustment of water productivity by CO2 (Steduto et al., 2007) | [-] |
| bface | WP adjustment based on FACE laboratory experiments | [-] |
| HI0 | Reference harvest index | [-] |
| HIini | Initial harvest index | [-] |
| dHI_pre | Possible increase in harvest index due to water stress before flowering | [%] |
| a_HI | Coefficient describing positive impact on harvest index from stomatal closure during yield formation | [-] |
| b_HI | Coefficient describing negative impact on harvest index from stomatal closure during yield formation | [-] |
| dHI0 | Maximum allowed increase of harvest index over reference | [-] |
| Determinant | Crop production associated with flowering ('0': indeterminate, '1': determinate) | [-] |
| exc | Excess potential fruits | [%] |
| MaxFlowPct | Percentage of total flowering period at which flowering peak occurs | [%] |
| p_up1 | Upper soil water depletion threshold for water stress effects on canopy expansion | [0 - 1] |
| p_up2 | Upper soil water depletion threshold for stomatal control of canopy | [0 - 1] |
| p_up3 | Upper soil water depletion threshold for canopy senescence | [0 - 1] |
| p_up4 | Upper soil water depletion threshold for pollination effects on canopy | [0 - 1] |
| p_lo1 | Lower soil water depletion threshold for water stress effects on canopy expansion | [0 - 1] |
| p_lo2 | Lower soil water depletion threshold for stomatal control of canopy | [0 - 1] |
| p_lo3 | Lower soil water depletion threshold for canopy senescence | [0 - 1] |
| p_lo4 | Lower soil water depletion threshold for pollination effects on canopy | [0 - 1] |
| fshape_w1 | Shape factor describing water stress effects on canopy expansion | [-] |
| fshape_w2 | Shape factor describing water stress effects on stomatal control | [-] |
| fshape_w3 | Shape factor describing water stress effects on canopy senescence | [-] |
| fshape_w4 | Shape factor describing water stress effects on pollination | [-] |
| ETadj | Adjustment of water stress threshold depending on daily ET0 (0: No, 1: Yes) | [-] |
| Aer | Volume below saturation where aeration stress begins due to deficit | [%] |
| LagAer | Number of days to consider aeration stress | days |
| beta | Reduction of lower water availability threshold when senescence begins due to water stress | [%] |
| GermThr | Proportion of total available water in root zone required for crop germination | [0 - 1] |

## 4.22 Vulnerability of the Livestock Sector

The vulnerability model used in this study follows methodologies applied in international research for estimating the yield of agricultural and livestock products. In this context, vulnerability is defined as the loss of pasture capacity to sustain the animal load at a given site due to reductions in natural pasture production caused by drought or flooding events.

Since a bioeconomic model of pasture response and animal growth is employed, vulnerability curves or functions are not used. To apply this model effectively, it is essential to understand the characteristics of the forage species commonly used in Costa Rican livestock systems. According to INTA (2022), some of the most common forages include forage cane (*Saccharum* sp.), Cameroon grass (*Pennisetum* sp.), Cuba OM 22 grass (*Pennisetum purpureum* x *Pennisetum glaucum*), and forage maize, among others. Examples of

these forages are illustrated from Figure 80 through Figure 82, while Table 13 summarizes their main properties.

Additionally, the characteristic parameters listed in Table 13 are utilized to simulate pasture growth accurately. This allows for an appropriate estimation of the dry matter content produced per cultivated unit, which in turn determines the feed available for livestock.

Figure 81. Forage grass Cuba OM 22, La Garita, Alajuela. INTA (2022).

Figure 82. Forage cane is used for animal feed. INTA's EELM, Quepos. INTA (2022).

Figure 83. Taiwan grass, Comunidad de Encuentro Farm, Los Reyes, Coto Brus. INTA (2022).

Table 13. Energy sources for humid and dry tropics. Brunca Region (INTA, 2022).

| Source | T/ha/year | CP | DM % | RR |
|---|---|---|---|---|
| Cameroon | 110–150 | 13–15 | 18–20 | 60 |
| Taiwan | 110–130 | 12–14 | 20 | 60 |
| Maralfalfa | 120–130 | 15–16 | 12–16 | 55 |
| Sugarcane | 120–150 | 3–8 | 40–80 | 10–12 (months) |
| Sorghum | 160–200 | 10–12 | 28 | 90 |
| Maize | 80–100 | 8–10 | 25 | 90 |
| Cuba OM 22* | 200–300 | 12–14 | 15–18 | 55 |

### 4.22.1 Map of Forage Grass Distribution

Understanding the geographic distribution of forage grasses in Costa Rica is crucial, especially when considering their vulnerability (see Section 4.22). The Agricultural Census provides data on pasture areas distributed by province and canton (INEC, 2015). Figure 84 illustrates the extent of pastureland by canton. For more detailed information on pasture coverage, refer to Section 4.16.3 on land cover maps.

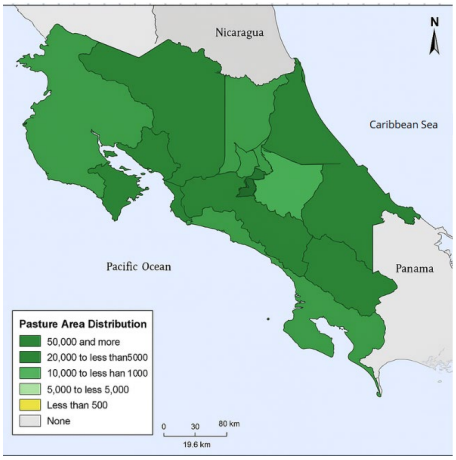


Figure 84. Distribution of pasture area by canton (INEC, 2015).

## 4.23 Summary of Information Sources and Associated Data

The information sources and associated data previously detailed in this section are summarized in the following tables for ease of reference and consolidation.

### 4.23.1 Climate Change

Table 14. Climate Information Sources for Costa Rica

| Source | Name | Description | Download Link |
|---|---|---|---|
| National Meteorological Institute (IMN) | Automatic Weather Stations | Temperature, relative humidity, atmospheric pressure, wind speed and direction, precipitation. | https://www.imn.ac.cr/web/imn/estaciones-automaticas |
| | Interactive Map | Monthly average information on precipitation, temperature, and wind. | https://www.imn.ac.cr/web/imn/mapa#c29tZU |

| | | | |
|---|---|---|---|
| | | | hhc2hUaGF0RG9lc250RXhpc3Q |
| CHIRPS[3] | Satellite-based datasets | Daily precipitation records. High-resolution time series suitable for climate trend analysis and seasonal drought monitoring. Raster format (.tiff), spatial resolution: 0.05° x 0.05°. | Free download: https://www.chc.ucsb.edu/data/chirps |
| ERA5 – Copernicus Climate Change Service | Global meteorological data | Historical and near real-time data with high spatial and temporal resolution. Includes precipitation, temperature (mean, minimum, maximum), solar radiation, specific humidity, surface air pressure, and wind speed. *Variables adjusted for elevation changes. Raster format (grid and NetCDF). | Free download: https://cds.climate.copernicus.eu |

### 4.23.2 Climate Change

Table 15. Climate Change Information Sources for Costa Rica

| Source | Name | Description | Download Link |
|---|---|---|---|
| National Meteorological Institute (IMN) | Climate Change Scenarios | Greenhouse gas concentration pathways (RCP): RCP2.6 and RCP8.5. Three climatic periods: 2010–2039, 2040–2069, 2070–2099. | http://cglobal.imn.ac.cr/ |
| Copernicus Climate Change Service (CMIP Models) | Coupled Model Intercomparison Project (CMIP) | Global climate projection data (daily and monthly). Includes precipitation, temperature, wind speed and direction, evapotranspiration, humidity, and sea level. | https://cds.climate.copernicus.eu/datasets/projections-cmip6?tab=download |

### 4.23.3 Hazard

#### *4.23.3.1 Flood Hazard*

The information available in the sources presented in Table XX is useful for both, flood hazard modeling at national level and the specific analysis in Virilla river watershed.

Table 16. Information on the water sector and watershed Sources for Costa Rica

| Source | Name | Description | Download Link |
|---|---|---|---|
| National Territorial Information System (SNIT) | Water and Sanitation Layers Viewer – National Integrated Water Resource Management Information System (SINIGIRH) | Information on the water sector and watersheds | https://www.arcgis.com/apps/dashboards/71b40ee586b6439ba343ad1af1ebee1c . |
| | Vector layer of river channels | Main and secondary drainage lines nationwide | |

[3] Climate Hazards Group InfraRed Precipitation with Station data

#### 4.23.3.2 *Seismic Hazard*

Within the framework of the project, it is not necessary to carry out additional seismic hazard modeling; instead, the available information from previous efforts will be used. Below are the most relevant and comprehensive studies that have been identified.

Table 17. Seismic hazard studies for Costa Rica

| Name | Source | Description |
|---|---|---|
| RESIS II | NORSAR et al. 2008 | Seismic hazard assessment for Central American countries |
| CAPRA | ERN-AL (2009) | Seismic risk assessment for San José, Costa Rica (hazard based on RESIS II) |
| ASLAC | Salgado-Gálvez et al. (2018) | Advanced seismic hazard model for Latin America and the Caribbean |
| Costa Rica Seismic Hazard Model | Hidalgo Leiva et al. (2022) | Most recent probabilistic seismic hazard assessment for Costa Rica |

#### 4.23.3.3 *Landslide Hazard*

To complement and enhance the landslide model currently available for Costa Rica, developed by INGENIAR. This model draws upon local research and expertise, incorporating elements of the Mora and Vahrson (1994) method for assessing landslide susceptibility, originally developed by Sergio Mora of the University of Costa Rica. Building on this foundation, the proposal aims to increase the model's level of detail by integrating new and updated layers of predisposing factors, thereby strengthening the assessment and quantification of landslide susceptibility to better inform risk management and policy decisions.

Table 18. Datasets and information useful for landslide model updating

| Name | Source | Description | Download Link/viewer |
|---|---|---|---|
| Landslide Catalogue | SNIT | Historical inventory including mass-movement activities, spatial distribution, processes, and characteristics | Download link https://www.snitcr.go.cr/ico_servicios_ogc_info?k=bm9kbzo6NDU=&nombre=CNE |
| Landslide Hazard Viewer | | Interactive map viewer | Map viewer: https://www.snitcr.go.cr/Visor/visor. |
| Landslide hazard in Costa Rica | Central American School of Geology Project, UCR (1996–2003) | Landslide hazard maps covering significant portions of Costa Rica | Not publicly accessible |
| RECLAIMM/CEPREDENAC-Norway Project | CEPREDENAC/Norway | Susceptibility maps considering geology, slope, land use, and precipitation patterns | Limited access |
| Hazard maps | CNE | Landslide-prone areas to include in the hazard modeling | https://www.cne.go.cr/reduccion_r |

| | | | |
|---|---|---|---|
| | | | iesgo/mapas_amenazas/. |
| LiDAR-based susceptibility map | Ruiz Cubillo and Soto (2014) | Detailed geomorphological, geological, and landslide maps for Escazú Hills | |
| CDRI-GIRI Model | Led by INGENIAR | Stochastic scenarios of earthquake- or precipitation-induced landslides (including climate change) | |

#### *4.23.3.4 Volcanic Hazard*

Costa Rica has more than ten major volcanic structures, five of which exhibit significant activity. Volcanic hazards could affect certain segments of Route RN2 and other key transportation infrastructure across the country, posing a risk to both infrastructure and mobility. The following identified studies will serve as a basis for modeling volcanic products in the areas of interest, taking into account parameters such as eruptive dynamics, ashfall, and pyroclastic flows.

Table 19. Information about volcanic hazard in Costa Rica

| Name | Source | Description |
|---|---|---|
| Volcanic hazard for 9 active volcanoes in Costa Rica | CAPRA – ERN-AL, updated by Ingeniar/CAPRA ROBOT | Deterministic modeling of ashfall, lahars, and pyroclastic flows |
| National volcanic hazard studies | Alvarado et al., (2020a, 2021, 2022, 2023), ICE, CNE, UNA | Updated hazard analyses for Poás, Irazú, Arenal, and Rincón de la Vieja volcanoes |

#### *4.23.3.5 Drought Hazard*

The following identified studies will serve as a foundation for drought modeling.

Table 20. Drought information

| Name | Source | Description | Download link |
|---|---|---|---|
| Drought Patterns in Central America | Soto (2013) | Spatial and temporal drought distribution | |
| Drought Monitoring | OACG | Climate variables monitored every 30 minutes | |
| Drought Indicators | Quesada-Hernandez et al. (2020) | Indices for meteorological, agricultural, hydrological drought | |
| Soil Maps | SNIT, FAO/UNESCO, IIASA/FAO | Detailed soil classification, morphological, chemical, and physical properties | https://www.fao.org/soils-portal/data-hub/soil-maps-and-databases/harmonized-world-soil-database-v20/en/ |

#### *4.23.3.6 Tropical Cyclone Hazard*

To assess tropical cyclone hazard, a methodological approach based on hurricane track simulation will be applied. Developing the hazard model requires various datasets containing information on cyclone tracks, topography, and bathymetry. The identified data sources are described below.

Table 21. Data sources for tropical cyclones

| Name | Source | Description | Download Link |
|---|---|---|---|
| Historical trajectories - IBTrACS database | NOAA | Historical cyclone tracks and characteristics | https://www.ncei.noaa.gov/products/international-best-track-archive |
| Simulated future trajectories | Bloemandaal et al. (2020) | STOR dataset providing 10,000 simulated years of cyclone trajectories | |
| Bathymetry | GEBCO | Global continuous bathymetric model | https://download.gebco.net/. |

#### *4.23.3.7 Tsunami Hazard*

To assess tropical cyclone hazard, a methodological approach based on hurricane track simulation will be applied. Developing the hazard model requires various datasets containing information on cyclone tracks, topography, and bathymetry. The identified data sources are described below.

Table 22. Tsunami models

| Name | Source | Description |
|---|---|---|
| Tsunami risk evaluation – Costa Rica's Pacific coast | CAPRA (2009) | Historical and simulated earthquakes |
| GAR-GIRI Model | INGENIAR - NGI | Probabilistic global tsunami hazard model |

#### *4.23.3.8 Sea Level Rise Hazard*

Relevant information for the Sea Level Rise Hazard is described in the table below.

Table 23. Information available for sea level rise hazard modeling

| Name | Source | Description | Download Link |
|---|---|---|---|
| Coastal Erosion Projections | IMN | Scenarios for Pacific and Caribbean coasts | |
| Methodological guide | | Provides a practical framework for conducting studies on sea level rise and coastal erosion in Costa Rica | |
| Copernicus Climate Change Service (CMIP Models) | Coupled Model Intercomparison Project (CMIP) | Global climate projection data (daily and monthly). Includes precipitation, temperature, wind speed and direction, evapotranspiration, humidity, and sea level. | https://cds.climate.copernicus.eu/datasets/projections-cmip6?tab=download |

### 4.23.4 Topography

Within the local flood model, it is essential to have topographic information for the watershed feeding into the river or channel under study, both for the hydrological component and the hydrodynamic model. While various databases containing topographic information are available, the final selection will depend

on the level of detail required for the analysis, taking into account the cost–benefit balance between model resolution and computational time, in relation to available computing capacity.

Table 24. Sources for downloading digital elevation models.

| Source | Name | Resolution | Download Link |
|---|---|---|---|
| GTOPO 30 | Regional Low Resolution Elevation Data | 30 arc-sec (1 km) | https://earthexplorer.usgs.gov/ |
| SRTM | Shuttle Radar Topography Mission | 3 arc-sec (90 m) | https://search.earthdata.nasa.gov/ |
| ASTER | Advanced Spaceborne Thermal Emission and Reflection | 1 arc-sec (30 m) | https://search.earthdata.nasa.gov/ |
| ALOS-PALSAR | Advanced Land Observing Satellite-1 | 12.5 m | https://search.asf.alaska.edu/#/ |

### 4.23.5 Strategic Project: Demonstration of Risk Assessment Methods for Critical Infrastructure in Heredia.

#### *4.23.5.1 Additional Hazard Information*

Additional inputs for hazards considered in the strategic project in the canton of Heredia.

Table 25. Additional hazard related inputs for the canton of Heredia.

| Name | Source | Description |
|---|---|---|
| Virilla River Flood Hazard[4] | SNIT | Main channel of the Virilla River |
| Seismic Microzonation – Greater Metropolitan Area | Based on Schmidt et al. (2005) and Arroyo-Solórzano (2023) | Microzonation for seismic risk modeling in San José Metropolitan Area |

#### *4.23.5.2 Building exposure*

Building exposure is modeled using georeferenced data layers. Each asset in the portfolio has a spatial representation and descriptive attributes. The minimum required information includes geographic location, replacement value, and a vulnerability classification. Other valuable attributes include number of stories, building use type, structural system, and population risk indicators.

Table 26. Exposure related inputs for the canton of Heredia.

| Variable | Name | Source | Description |
|---|---|---|---|
| Location | Cadastral map | UBICA (Heredia Municipality) | Parcel boundaries, location, ID, and land use (*does not include built area*) |
| Building footprints | | SNIT | National-level coverage of building blocks, number of floors, land use, structural system, etc. |

[4] Since the Pirro River is a tributary of the Virilla River, the available information for the Virilla River is useful for the flood risk assessment in the canton of Heredia.

| | | | |
|---|---|---|---|
| Exposure Models | Global Risk Assessment Framework (GRAF) | UNDRR initiative providing sector-specific exposure models, including for housing | |
| Replacement Value | Homogeneous zone value map | UBICA | Unit values per square meter for defined zones |
| Base construction values | Costa Rica Ministry of Finance | Unit values for different construction typologies for fiscal assessment | |
| Number of Floors | 3D vertical condominiums | UBICA | Height or number of stories |
| Human Settlement Height | Copernicus GHSL | Spatial distribution of building heights | |
| Building Use | Land Use Map | UBICA / Municipality of Heredia | Cadastral map with usage data |
| | Points of Interest | | Location of public, institutional, and heritage buildings. |
| | Public areas | | Location of public buildings |
| | Shelters | | Location of shelters |
| Health Sector | GRAF | Includes infrastructure for the health sector (data from the Costa Rican Social Security Fund) | |
| Structural System | National Population and Housing Census | Predominant wall material (*used as proxy for structural type*) | |
| Population at Risk Indicators | — | Population data and spatial distribution | |

#### *4.23.5.3 Infrastructure sectors exposure*

Each infrastructure portfolio should include georeferenced geometry, replacement cost estimates, and a vulnerability classification. The Heredia project considers road, rail, energy, telecommunications, and water and sanitation infrastructure.

*Road sector*

Table 27. Information available for the road sector of Heredia canton.

| Sub-sector | Source | Description |
|---|---|---|
| Roads and Highways | UBICA / Municipality of Heredia | Road segments: geometry and classification |
| | OpenStreetMap | Vector geometry for public and private roads; surface type and number of lanes |
| | CONAVI | National road network viewer (used for validation and attribute checks) |
| Bridges | LanammeUCR | Identification of cantonal bridges: location, dimensions, material, and structural system |
| | OpenStreetMap | Identification of bridge segments within the road network |
| Railways | OpenStreetMap | Length, width, and elevation of rail segments |
| | Orthophotography | Aerial images for identifying superstructure features |

*Energy sector*

The energy sector is divided into three sub-sectors: generation, transmission, and distribution. Each includes diverse elements with specific geometric and attribute requirements.

- **Electricity Generation**: Includes generation plants within and outside the Heredia canton. Even plants outside the area are considered due to systemic interdependencies.
- **Electricity Transmission**: Comprises substations (point geometry) and transmission lines (line geometry). Analysis extends to the provincial level to identify all components relevant to Heredia's supply.
- **Electricity Distribution**: Portfolio includes aerial and underground distribution networks, utility poles, and transformers—limited to infrastructure within Heredia.

Table 28. Information available for the energy sector of Heredia canton and surroundings

| Name | Source | Description |
|---|---|---|
| Electricity Generation | GRAF | Two datasets based on CNFL and ESPH data. Includes point geometry, generation method, and installed capacity |
| | OpenStreetMap | Similar attributes to GRAF, including point geometry and plant specifications |
| Transmission | GRAF | Substations and transmission line data |
| | ICE | National geoportal coverage; includes substations and high-voltage transmission lines (138kV and 230kV) |
| | OpenStreetMap | Substation locations |
| Distribution | EPSH | Official dataset: line geometry, installation type (aerial or underground), voltage level |
| | | Utility Poles:<br>Point geometry; includes material, height, and year of installation |
| | GRAF | Includes same attributes as EPSH |
| | | Transformers:<br>Point geometry; includes location and installation type (aerial or pedestal) |

*Telecommunications sector*

The telecommunications exposure portfolio is based on the representation of infrastructure that supports both fixed and mobile services. Available datasets focus primarily on antenna infrastructure and inferred estimates of network layout.

Table 29. Information available for Telecommunication sector.

| Source | Data Description |
|---|---|
| OpenCellID | Includes network type (GSM, UMTS, LTE), coverage radius (meters), and frequency of identification. Data cleansing methods estimate the relative position of antennas using building footprints and population density. Used to develop differentiated vulnerability classifications. |
| INEC 2022 | No public spatial data is available on internet and landline networks in households. Road network vector geometry is used as a proxy to estimate potential telecom network layout within the canton. |

*Water and Sanitation sector*

This sector is divided into two sub-sectors: potable water and wastewater systems.

- **Potable Water:** Includes water intakes, aqueducts, potable water treatment plants (PTAP), storage tanks, pumping systems, and distribution and conduction networks.
- **Wastewater**: Includes the sanitation network (sewer systems), sanitary wells, and wastewater treatment plants.

It is essential to include infrastructure both within and outside Heredia's administrative boundaries, as external components may play a critical role in service provision.

Table 30. Available Information for the water and sanitation sector of Heredia canton.

| Subsector | Source | Data Description |
|---|---|---|
| Potable Water | GRAF (based on EPSH data) | Includes most attributes required to characterize infrastructure. Assumes homogeneity of elements. Data on intakes and captured flow is missing. |
| | EPSH | Updated (2024) version of the distribution network: pipe diameter and material. |
| Hydrant System | EPSH | Location of hydrants |
| Wastewater | EPSH | Spatial distribution of the sewer network and sanitary wells. |
| | INEC 2011 (spatialized census data) | Sewer network: pipe diameter, material, and age. |
| | | Sanitary wells: diameter, depth, construction material, physical condition. |
| | | Wastewater treatment plants: treatment capacity, design capacity, population served, and technology used. |
| | HydroSHEDS | Database of wastewater treatment plants. |

#### *4.23.5.4 Physical Vulnerabiity of Buildings*

The physical vulnerability of exposed buildings is characterized by using mathematical functions that relate hazard intensity to direct physical damage. These vulnerability functions must be estimated and assigned for each asset type identified in the exposure database. The project relies on well-established and accessible sources of vulnerability functions, many of which were developed by the same consulting team or are publicly available.

Table 31. Information available about physical vulnerability of buildings.

| Name | Source | Description |
|---|---|---|
| CAPRA-ROBOT | ERN-AL (2009) | Library of vulnerability functions for typical construction classes in Latin America and the Caribbean. Includes hazards: earthquakes, strong winds, storm surges, and floods. |
| GAR15 | INGENIAR (2014) | Function libraries cover multiple hazards. |
| Tsunami Vulnerability Functions | CIMNE et al. (2012) | Specific functions for tsunami-related damage estimation. |

*Note: These vulnerability sources also apply to the Tourism Project.*

#### 4.23.5.5 *Physical Vulnerabiity of Infrastructure*

For infrastructure elements, vulnerability is described using functions that estimate damage levels based on hazard intensity. These functions are developed using an archetype-based approach, which allows for incorporating structural complexity that cannot be captured at broader scales. The archetypes are constructed based on exposure data and follow the methodology described in the project's methodological framework.

This approach is essential to appropriately model the vulnerability of diverse infrastructure systems—such as transport, electricity, water, and telecommunications—given their unique configurations and interactions. Each infrastructure type is associated with one or more archetypes that reflect typical structural and functional characteristics relevant to hazard impact simulation.

### 4.23.6 Operational Project 1: Disaster and Climate Risk Assessment for Road Infrastructure – National Route 2 Pan-American Highway (RN2)

#### 4.23.6.1 *Exposure*

The exposure model for National Primary Route 2 (RN2) is developed using georeferenced vector data representing linear features and relevant attributes. The goal is to construct a comprehensive portfolio that accurately represents the road's geometry, economic value, and vulnerability classification along its segments.

Table 32. Information available for the exposure model of the National Route 2 Pan-American Highway

| Source | Data / Information |
|---|---|
| LanammeUCR | Geoportal with information on the national road network: attributes including dimensions, pavement, and traffic<br>Geoportal with information on national bridges: location, dimensions, material, and type of superstructure |
| MOPT | Geoviewerr with geometric representation of the road axis; includes road hierarchy and right-of-way data |
| | Road Certification System: includes terrain classification, pavement surface description, and pavement structure composition |
| CONAVI | Geoportal for the national road network; validation support (no additional attributes beyond MOPT) |
| OpenStreetMap | Number of lanes in various segments, bridge locations |
| Google Street View | Satellite imagery to identify attributes such as retaining walls, embankments, drainage ditches |
| | Bridge characteristics: approximate length, width, clearance, typology, and construction material |

#### 4.23.6.2 *Vulnerability*

The physical vulnerability of the RN2 road network is assessed using the archetype-based methodology previously described. This approach incorporates the variability of structural and functional characteristics observed across different road segments and associated infrastructure elements.

### 4.23.7 Operational Project 2: Flood and Drought Risk for Small and Medium Agricultural Producers

#### *4.23.7.1 Exposure*

This component evaluates the drought and flood risk to the agriculture sector, focusing on coffee and sugarcane crops at the national scale. The assessment considers the geographic distribution, area under cultivation and harvest, yield (tons per unit area), and crop phenology.

The livestock sector exposure includes pasture areas and livestock herds that depend on them. Risk modeling in meat production systems is based on expected live weight losses following hazard events, though it does not yet account for demographic changes (e.g., births, natural deaths, or animal movement).

Table 33. Information available for the exposure model for agriculture and livestock

| Sector | Name | Source | Description |
|---|---|---|---|
| Agriculture | National Agricultural Survey – ENA (2023) | INEC | Detailed, updated data on crop production: area planted/harvested, output, production use, and agronomic practices |
| | VI National Agricultural Census (2014) | | Information on all farms in Costa Rica, including spatial distribution of coffee and sugarcane at the canton level. Also includes production inputs and farming techniques. No georeferenced datasets available (protected under data privacy laws). |
| | Costa Rica Land Cover and Use Map – REDD+ | SIMOCUTE, 2019 | Spatial data on land cover categories such as forests, agriculture, urban zones, and water bodies |
| | Land Cover and Use Map | SNIT | Territorial data used to estimate AFOLU GHG emissions and removals |
| | Effective Practices for Crop Adaptation | CATIE (2018a, b) | Inputs for financial products and agricultural insurance: crop phenology, variety, planting date, duration of growth stages |
| | Suitability Study | CATIE | Maps of optimal, moderate, and poor suitability for coffee and sugarcane cultivation in Costa Rica |
| Livestock | National Agricultural Survey – ENA (2023) | INEC | Disaggregated data on cattle and pigs: herd composition, productivity indicators, loss records |
| | VI National Agricultural Census (2014) | | Data on livestock activities, including species such as bovine, caprine, ovine, porcine, and poultry |

#### *4.23.7.2 Vulnerability*

- **Crop Vulnerability**: The vulnerability of coffee cultivation is evaluated using practical assessment methods tailored to climate change effects, including drought and flood sensitivity.
- **Livestock Vulnerability**: Uses a bioeconomic modeling approach to simulate pasture response and animal growth.

Table 34. Information available for the vulnerability model for agriculture and livestock

| Sector | Name | Source | Description |
|---|---|---|---|
| Agriculture | Vulnerability and Adaptation Manual for Coffee | CATIE (2018d) | Practical guide to assess coffee farming vulnerability to climate change |
| | Effective Practices for Reducing Climate Impacts | CATIE ( 2018a, b), MAG | Includes crop characteristics, soil preparation, planting, fertilization, and vulnerability data |
| | AquaCrop Model | FAO | Generates crop-specific parameters for modeling development and productivity under stress conditions |
| Livestock | Pasture Characteristics in Costa Rica | INTA (2022) | Bioeconomic model of pasture performance and livestock growth |
| | Pasture Location Map | INEC (2015) | Distribution of pasture areas by canton |

### 4.23.8 Operational Project 3: Evaluation of Exposure and Risk for Small and Medium Hotels and Hostels in the Fu-turismo Program.

#### *4.23.8.1 Exposure*

Table 35. Datasets and information available for the tourism sector of Costa Rica.

| Name | Source | Description |
|---|---|---|
| Building Cartography | SNIT | National coverage of buildings and structures, filtered to include hotels only. |
| Infrastructure and Land Use | OpenStreetMap (OSM) | Includes hotel infrastructure, surrounding built environment, points of interest, land use classifications, and land cover types. |
| Base Unit Value Manual for Hotel Typologies | Costa Rica Ministry of Finance | Provides square meter valuation for hotel-use buildings. |

#### *4.23.8.2 Physical Vulnerabiity of buildings*

Vulnerability functions and methodology used for the Heredia Strategic Project (Section 4.5.4) will also apply to the tourism sector, enabling consistency across assessments and leveraging shared resources for building and infrastructure typologies.

## 4.24 Other initiatives

### 4.24.1 CCRIF SPC

The CCRIF SPC (Caribbean Catastrophe Risk Insurance Facility) is an innovative parametric insurance mechanism that provides coverage to Caribbean countries — and more recently to some Central American nations — against natural disasters such as hurricanes, earthquakes, and extreme rainfall events. It was established in 2007 following the devastating impacts of the 2004–2005 hurricane seasons, with support from the World Bank, international donors, and Caribbean governments.

CCRIF has shared with the consulting team the catastrophic risk profiles for Costa Rica related to earthquakes, hurricanes, and excessive rainfall through PDF documents that describe the models and

summarize the results. It is important to clarify that these risk profiles do not correspond to the datasets used for modeling purposes, nor have the models themselves been shared.

It is worth mentioning that CCRIF's seismic model, SPHERA, is based on the ASLAC seismic hazard model developed by ERN of Mexico and INGENIAR. This model has been proposed for use in seismic and landslide risk modeling, as detailed in Deliverable 2 of this consultancy.

### 4.24.2 Global Risk Assessment Framework (GRAF)

The Global Risk Assessment Framework (GRAF) is an initiative of the United Nations Office for Disaster Risk Reduction (UNDRR) aimed at strengthening countries' capacity to access and apply risk-related data to inform decision-making.

As part of the implementation of the first GRAF pilot in Costa Rica, carried out in coordination with the National Commission for Risk Prevention and Emergency Response (CNE), exposure models were developed for several sectors, including the housing sector. The housing exposure database was built using information provided by the National Institute of Statistics and Censuses (INEC), and it will serve as a reference and key source of information for characterizing buildings in the Heredia canton.

For the seismic hazard component, the project will use the ASLAC model, a more recent and detailed hazard model that has been internationally validated and approved, ensuring a higher level of accuracy and relevance for the current analysis.

### 4.24.3 Nationally Appropriate Mitigation Actions (NAMAs)

Costa Rica has developed a series of Nationally Appropriate Mitigation Actions (NAMAs) targeting the agriculture and livestock sectors, particularly for coffee and sugarcane production. These initiatives aim to reduce greenhouse gas (GHG) emissions and promote the adaptation of production systems to increase resilience to climate change.

NAMAs in Costa Rica are part of the country's broader climate strategy, designed to drive technological change and foster low-emission production models. For example, the Coffee NAMA seeks to develop a low-emission coffee supply chain while improving market access for Costa Rican coffee growers. Similarly, the Sugarcane NAMA promotes a transformation of the sugar industry to reduce GHG emissions and enhance market opportunities, and the Livestock NAMA focuses on reducing $CO_2$ emissions and promoting carbon sequestration in the livestock sector.

The implementation of these NAMAs could provide valuable insights for the project, especially in terms of identifying alternative practices that could be included in the risk index. Understanding the processes, modeling approaches, and information used in the development of the Coffee, Sugarcane, and Livestock NAMAs is essential for integrating climate mitigation and adaptation measures into risk assessment tools.

The knowledge generated through these initiatives is key to advancing the objective of informing and enhancing the design of a comprehensive risk index, aligned with national climate policies and sectoral strategies.

## 4.25 Data Gaps Identified

The review revealed a broad array of relevant and sufficient databases, maps, documents, and studies for successful project implementation. However, enhanced spatial resolution of climate data, historical event records, and locally adapted vulnerability models could improve assessments. A major challenge remains the absence of an integrated, open-access national information platform.

It is important to note that, from the beginning of the project, efforts have been made to request and collect available national data. Several datasets have been shared by local institutions and are already integrated into the analysis presented in Section 4. New information requested from the outset may be incorporated, provided it is delivered on time, to be included in upcoming tasks.

There are two main streams in the project: delivering multi-hazard risk assessment metrics and capacity building. Due to the limited timeframe, it is not feasible to generate or co-develop additional data. If no additional information is delivered, the project relies on the information currently referenced, which is considered sufficiently robust and appropriate for the objectives and scope of this initiative.

Importantly, the training course included in this project is designed to empower national institutions and technical personnel with the tools and methodologies needed to strengthen and expand existing data, develop exposure databases, and conduct risk assessments aligned with their specific priorities and decision-making needs in the future.

# 5 CATASTROPHIC RISK MODELING METHODOLOGY

The objective of probabilistic catastrophic risk modeling is to estimate the probability distribution of losses that may occur within a set of exposed elements, following the occurrence of a hazard event (Cardona, 1986a;b;c; 1989; 1990). Probabilistic modeling enables forecasting of future loss levels by accounting for the specific hazards present in the territory and the inherent uncertainties in their estimation, as well as the intrinsic vulnerability of the exposed elements and its respective uncertainty.

## 5.1 Conceptual Approach to Risk Modeling

Probabilistic risk modeling involves estimating the potential consequences that a set of exposed elements may suffer as a result of hazardous events. Robust risk modeling is fundamental for building a sustainable and resilient development process, as it enables the consideration of trade-offs between potential harms and benefits. In other words, such a process can only be effectively guided when supported by a risk model that is sufficiently robust, both in terms of credible impact estimations and in providing a sound technical foundation for decision-making without arbitrariness. A sound risk model should meet the following (non-exhaustive) list of characteristics:

- *Multi-hazard*. This feature is essential, as it is necessary to incorporate models that capture the specific dynamics of different natural hazards and their interactions. This ensures a comprehensive view of risk by considering all possible losses associated with various types of hazards, rather than focusing on just one. Additionally, risk must be expressed in a way that allows for the impacts of different hazards on exposed elements to be comparable and additive.
- *Probabilistic*. The occurrence of hazardous natural phenomena involves a high degree of inherent uncertainty due to the many variables and dynamics at play. Therefore, a conceptual and mathematical framework is needed to incorporate this uncertainty appropriately favoring probability distributions over point estimates. The risk assessment approach used in this study is based on the core principles of Ruin Theory (Embrechts et al., 2012), which allows for the characterization of potential damage and losses through probability distributions. This results in probabilistic metrics that offer integrated, comprehensive, and transparent guidance to decision-makers about the risk they face.
- *Stochastic*. This is not synonymous with the previous point. It means that the model should be based on both the physical nature of natural phenomena and the randomness of their occurrence. Typically, this requires thousands of hazard event simulations to build a reasonably comprehensive set of potential damages or losses to exposed elements, and thus the resulting consequences (Bernal et al., 2019).

*Non-stationary*. Traditional probabilistic disaster risk models are often stationary, meaning they do not allow for significant changes in the frequency of hazard events over time. While this is suitable for non-climatic phenomena such as earthquakes, it is inadequate for hazards influenced by climate change. In these cases, a modeling approach that incorporates underlying trends altering event occurrence rates is required, which implies the use of non-stationary risk models. As a result, risk metrics must be expressed as functions of time (Bernal et al., 2019).

- *Based on Deep uncertainty*. In addition to the above, integrating climate change into the risk model introduces a variable for which no meaningful probability distribution can be assigned—this represents deep uncertainty. Mathematically, the model must be capable of handling certain variables through non-probabilistic uncertainty structures that allow for the simulation of the actual state of uncertainty. This enables the expression of risk metrics in terms of imprecise probabilities (Bernal et al., 2019).
- *Decision-oriented*. Defining a risk assessment and analysis model, particularly for identifying risk and related adaptation measures, must not only rely on physical and mathematical considerations, but also ensure that results can guide decision-making. To achieve this, it is essential to understand the stakeholders involved in risk and adaptation, their needs, and to provide them with relevant information. The risk model must account for the magnitude and likelihood of projected impacts, but most importantly, it must allow for the evaluation of the effectiveness of feasible risk management strategies, based on the local context and the degree of risk aversion.

The general procedure for probabilistic disaster risk modeling—considering climate change—is illustrated in Figure 85.

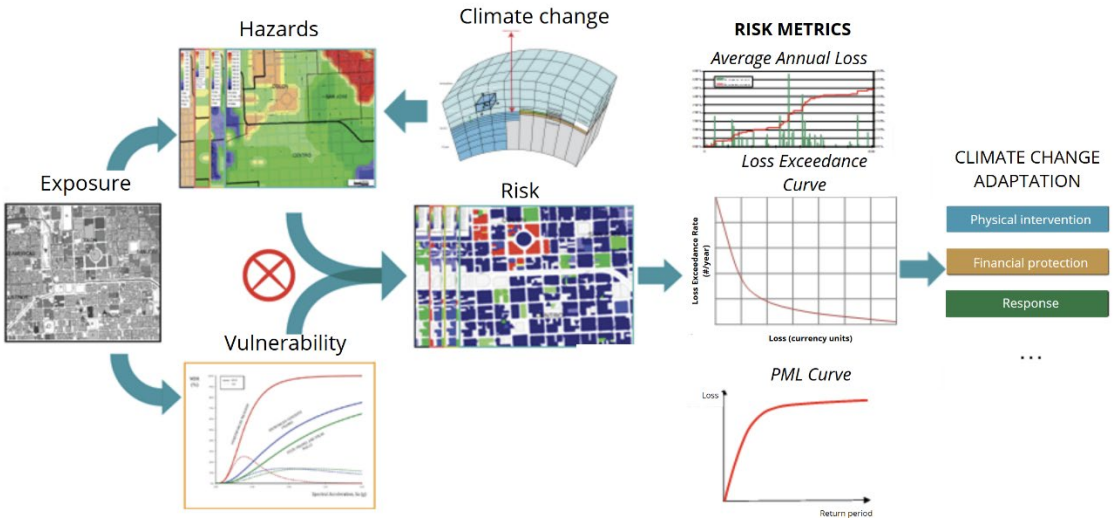


Figure 85. Components of Risk Modeling and Their Interrelation.

As illustrated in Figure 84, once risk has been evaluated using actuarial metrics—such as Expected Annual Loss, the Loss Exceedance Curve, and Probable Maximum Loss—it becomes possible to establish an objective relationship with risk management measures and their effectiveness. This means the model can be used to design intervention strategies composed of multiple measures, each with a quantifiable capacity to reduce risk.

Following this approach, risk in this study is evaluated based on three fundamental factors:

- *Hazard* is defined as a set of stochastically simulated events that are collectively exhaustive and mutually exclusive; that is, they cover all possible ways in which the hazard may manifest,

assuming independent events whose frequencies follow a natural power law (i.e., equivalent to a recurrence curve).

- *Exposed elements* refer to immovable assets, infrastructure, or agricultural production that are subject to hazards and susceptible to damage or disruption.
- *Vulnerability* refers to the propensity or predisposition of exposed elements to be adversely affected. Assessing vulnerability requires a specific model for each type of exposed element and each type of hazard—there is no unified representation. However, the modeling process results in a common impact metric (economic loss), which makes the different models additive and comparable in risk terms.

The first fully probabilistic approach to the risk problem from an actuarial perspective was proposed by Filip Lundberg in 1903 (Lundberg, 1903). In 1930, Harald Cramér formalized Lundberg's theory into what is now known as Ruin Theory (Cramér, 1930). Lundberg defined an income-outcome model in which an insurance company begins operations with a given amount of capital, which increases over time as premiums are collected. Simultaneously, losses (which the company must cover) occur randomly over time. If, due to claim payments, the company's capital falls below zero, it is considered bankrupt. Lundberg was interested in determining the probability of an insurance company's insolvency.

Ruin Theory assumes that the occurrence of claims is not deterministic. Lundberg demonstrated that the occurrence of losses over time can be modeled as a Poisson process. Later, it was shown that any renewal process is valid within the framework of Ruin Theory (Andersen, 1957). A renewal process is a type of continuous-time, discrete-state stochastic process widely used across scientific and engineering disciplines to model the random occurrence of events. In this context, "events" refer to loss occurrences, regardless of their origin. This is why Ruin Theory—or insolvency theory—is well-suited to modeling the impacts associated with any type of phenomenon, whether natural or not, and is applicable to risk management beyond the insurance sector, including social, economic, environmental, and broader development contexts.

A renewal process is defined by a single parameter: its intensity or rate. In risk assessment, this parameter corresponds to the loss exceedance rate, which is the inverse of the average time between events that exceed a given loss threshold p. Therefore, when estimating the risk of a portfolio of exposed elements (i.e., the probability of exceeding a loss amount p within a time window), its exceedance rate v(p) must be calculated based on the probability of occurrence of any hazard event capable of surpassing p. This defines a renewal process that enables estimation of the probability of loss p being exceeded within any given period.

## 5.2 Risk Quantification

From a mathematical standpoint, risk modeling aims to characterize a stochastic process of loss occurrence over time (i.e., a loss process). A loss process has key characteristics that shape the modeling approach adopted in this study, which is commonly used in actuarial catastrophic modeling, safety and reliability engineering, the aerospace industry, and other fields.

Consider a historical loss process as shown in Figure 86. For a given economic loss threshold $p$, one can identify all events in the graph whose losses exceed $p$. The times between events $(T_1, T_2, \dots, T_n)$ are shown

in Figure 86 and are used to estimate the parameter λ of the renewal process that models the occurrence of events exceeding $p$ (i.e., $\lambda = \nu(p)$).

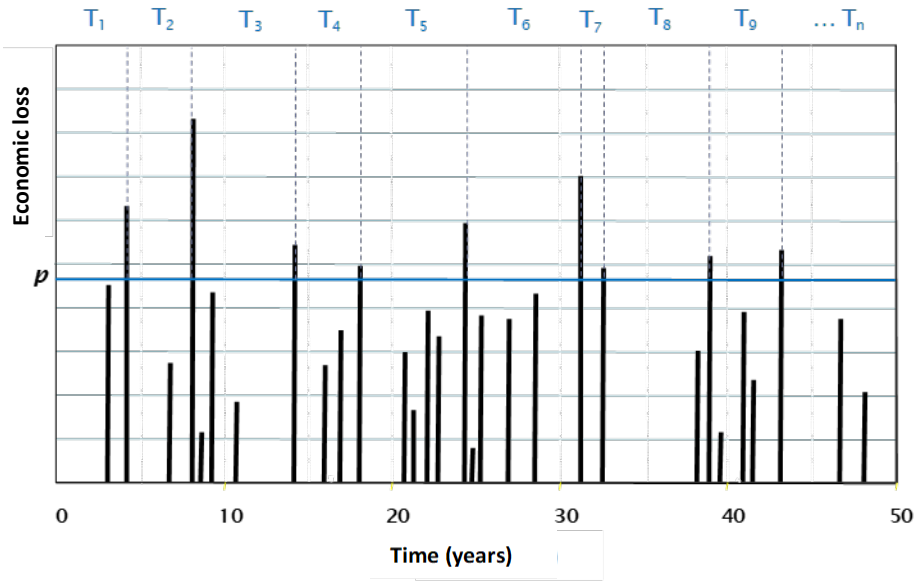


Figure 86. Hypothetical Process

For a given loss $p$, the population exceedance rate ($\lambda$) can be estimated from the sample exceedance rate ($\Lambda$) as follows (Bernal et al., 2021):

$$\lambda \approx \Lambda = \frac{n-1}{\sum_{i=1}^{n} T_i} \qquad \text{Equation 1}$$

where $n$ is the number of events exceeding the loss $p$, and $T_i$ are the observed time intervals. This estimator satisfies the four statistical criteria for estimating parameters of probability distributions: it is unbiased, has minimum variance, and is consistent and sufficient. If we assume a Poisson process (i.e., event times follow an exponential distribution), it can be shown that the estimator $\Lambda$ follows an inverse Gamma distribution with parameters $n$ and $(n-1)\lambda$, from which its coefficient of variation (*CV*) can be calculated as (Bernal et al., 2021):

$$CV = \frac{1}{\sqrt{n-2}} \qquad \text{Equation 2}$$

The coefficient of variation indicates the relationship between the standard deviation and the mean of a random variable. As shown in Equation 2, *CV* decreases as the number of observations ($n$) increases (see Figure 87).

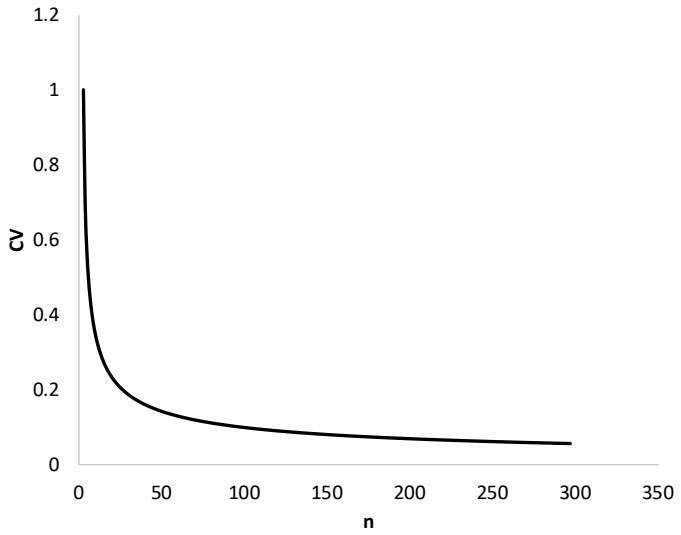


Figure 87. Variation of the exceedance rate's coefficient of variation with sample size

This behavior demonstrates that for large-loss events (i.e., catastrophic events), estimating the exceedance rate from historical data is highly uncertain—there are few events that exceed that loss threshold—regardless of data quality or the number of years recorded. This is why loss simulations are necessary: to model hazard, exposure, and vulnerability and their mathematical relationships to appropriately estimate the loss exceedance rate, since historical data is generally insufficient.

Risk is determined by the convolution of hazard and vulnerability, at the location of the exposed elements and for all such elements. In probabilistic loss modeling, both hazard and vulnerability are represented probabilistically. Hazards are characterized by both temporal and spatial probability distributions. The temporal occurrence of hazard scenarios is modeled as a renewal process, which entails fitting a probability model to the time between two consecutive events.

The uncertainties associated with hazard and vulnerability are defined by their own nature—temporal and spatial for hazard, and intensity-dependent for vulnerability. As such, the primary output of the model is a specific probability distribution of loss for each hazard event. The probability density function of loss for exposed element $j$, conditional on the occurrence of hazard event $i$ (i.e., $f(p_j|E_i)$), is calculated as:

$$f(p_j|E_i) = \int_0^\infty f(p_j|s)f(s|E_i)ds \qquad \text{Equation 3}$$

where the first term of the integral pertains to vulnerability ($f(p_j|s)$, the probability density of loss given an intensity $s$), and the second term relates to hazard ($f(s|E_i)$, the probability density of intensity given the occurrence of event $E_i$).

The total loss from event $i$ is the sum of all individual losses ($p_j$) from the exposed elements. Since these are random variables, proper arithmetic must be used to determine the total event loss. The sum is computed over the probability moments of the variables $p_j$, as follows:

$$E(p|E_i) = \sum_{j=1}^{NE} E(p_j)$$ Equation 4

$$\sigma^2(p|E_i) = \sum_{j=1}^{NE} \sigma^2(p_j) + 2 \sum_{\substack{k=1 \\ k<j}}^{NE-1} \sum_{j=2}^{NE} cov(p_k, p_j)$$ Equation 5

where $E(p|E_i)$is the expected loss of event $i$, $\sigma^2(p|E_i)$is its variance, $NE$ is the total number of exposed elements, $E(p_j)$ is the expected loss for element $j$, $\sigma^2(p_j)$is its variance, and $cov(p_k, p_j)$ is the covariance between losses in two different exposed elements.

Using the probability moments of the total loss from an event, a Beta distribution is fitted, with the following probability density function ($f_P$):

$$f_p = \frac{\Gamma(\alpha+\beta)}{\Gamma(\alpha)\cdot\Gamma(\beta)} \cdot p^{\alpha-1} \cdot (1-p)^{\beta-1}$$ Equation 6

where $\alpha$ and $\beta$ are the parameters of the Beta distribution, and $\Gamma(\cdot)$ is the Gamma function. This defines the loss associated with the occurrence of hazard event *i* in probabilistic terms.

Risk is commonly described using the loss exceedance curve, which specifies the frequencies at which losses exceed a given value. This annual exceedance frequency, which is simply the *exceedance rate* $\nu(p)$, is calculated as:

$$\nu(p) = \sum_{i=1}^{N} Pr(P > p|E_i) \cdot F_A(E_i)$$ Equation 7

where $\nu(p)$ is the exceedance rate for loss $p$, $N$ is the total number of hazard events, $F_A(E_i)$ is the annual frequency of event $i$, and $Pr(P > p|E_i)$ is the probability of exceeding $p$ given that event $i$ occurred. The summation includes all hazard events that can generate losses. The inverse of $\nu(p)$ is the return period of loss $p$ ($Tr$), which is simply the expected time between events that exceed loss $p$.

$$Tr = \frac{1}{\nu(p)}$$ Equation 8

The loss exceedance curve contains all the necessary information to probabilistically characterize the loss occurrence process associated with hazard events. Figure 88 shows an example of a loss exceedance curve.

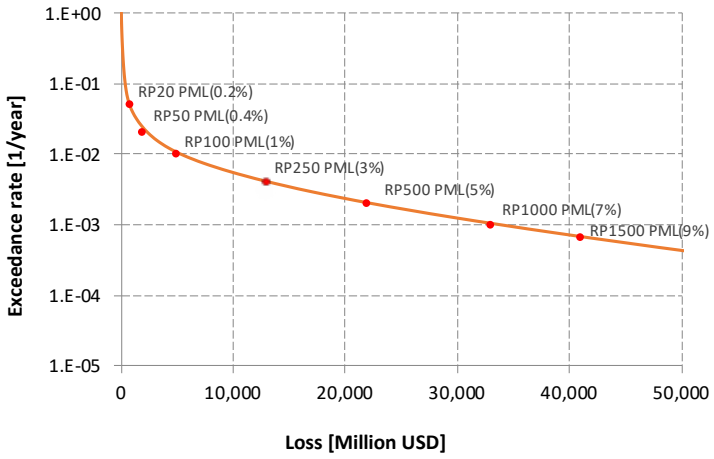


Figure 88. Example of a loss exceedance curve. The vertical axis shows the exceedance rate. The horizontal axis shows the associated loss. (RP = Return Period; PML = Probable Maximum Loss).

The calculation in Equation 7 corresponds to the estimation of the exceedance rate for all loss amounts across all exposed elements, for all events in the hazard model, and for all hazards. As shown in Figure 89, the probabilistic risk assessment can be summarized in the following steps: 1) For each hazard event, the loss for every exposed element is determined (Equation 3); 2) the total event loss is calculated as the sum of individual losses (Equation 4, Equation 5 y Equation 6); 3) once all event losses are quantified, exceedance rates are calculated (Equation 7).

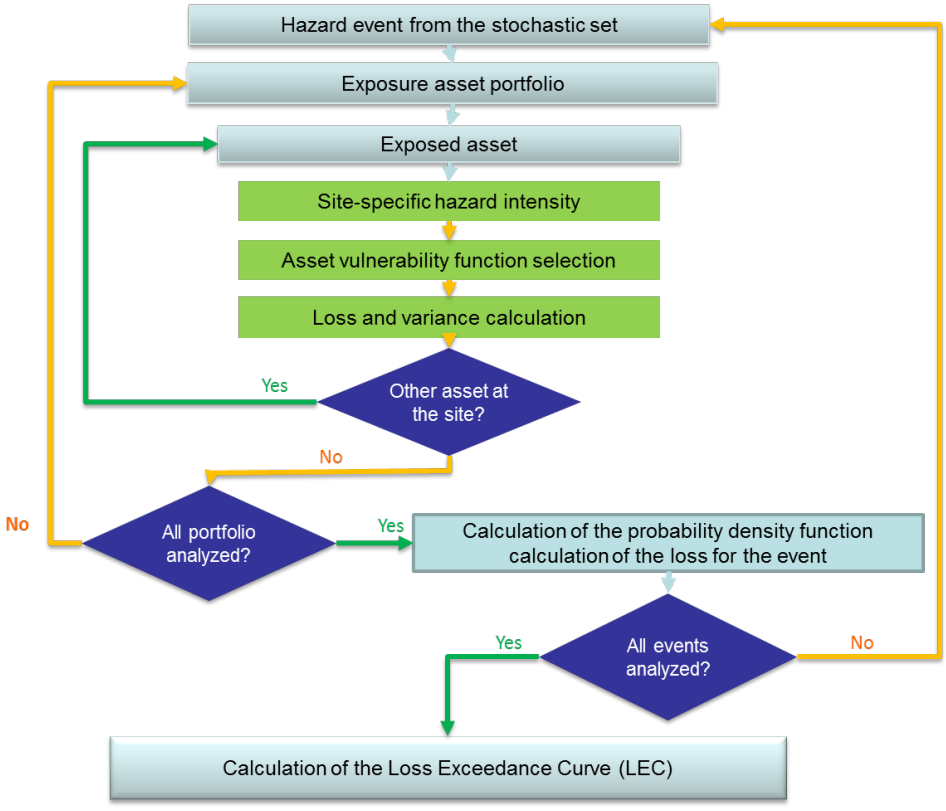


Figure 89. Flow diagram of probabilistic risk assessment

## 5.3 Risk Metrics

From the loss exceedance curve, several risk metrics can be derived, each serving different purposes in decision-making and risk management processes. These metrics offer a comprehensive representation of risk, typically condensed into one or a few indicators, rather than presenting the full set of event-specific losses or the entire exceedance curve.

### 5.3.1 Average Annual Loss (AAL)

The AAL represents the expected value of annual losses. It reflects the average annual amount which, when accumulated over time, would be equivalent to all future losses. Conceptually, the AAL corresponds to the fair pure premium required annually to cover all possible losses. It can be calculated as the area under the loss exceedance curve:

$$PAE = \int_0^\infty v(p)dp \qquad \text{Equation 9}$$

Alternatively, based on event-specific loss data, AAL can also be calculated as:

$$PAE = \sum_{i=1}^{N} E(P|E_i)\, F_A(E_i) \qquad \text{Equation 10}$$

Where $(P|E_i)$ is the expected loss from event *i*, and $F_A(E_i)$ is the annual frequency of occurrence of event *i*. The expected loss given the occurrence of a specific event depends on the vulnerability of the exposed elements.

AAL is a crucial risk indicator because it integrates into a single value the impact of hazardous events on vulnerable exposed elements. It is the most robust risk metric—not only because it summarizes the loss occurrence process in one number, but also because it is relatively insensitive to uncertainty, as it reflects the mathematical expectation of annualized losses.

### 5.3.2 Probable Maximum Loss (PML)

While the loss exceedance curve is the primary output of risk assessment, the PML curve is often preferred, as the concept of a return period is generally easier to interpret. As previously explained, the return period is the expected time between events that exceed a certain loss, and it is mathematically the inverse of the exceedance rate. The loss exceedance curve and the PML curve contain equivalent information.

From the PML curve, loss values can be determined for any selected return period. Choosing a return period to reference a PML value depends entirely on the risk aversion of the decision-maker. Figure 90 shows an example of a PML curve, where a selected return period of 400 years on the horizontal axis corresponds to a loss value on the vertical axis. This indicates that such a loss is expected to be exceeded, on average, once every 400 years.

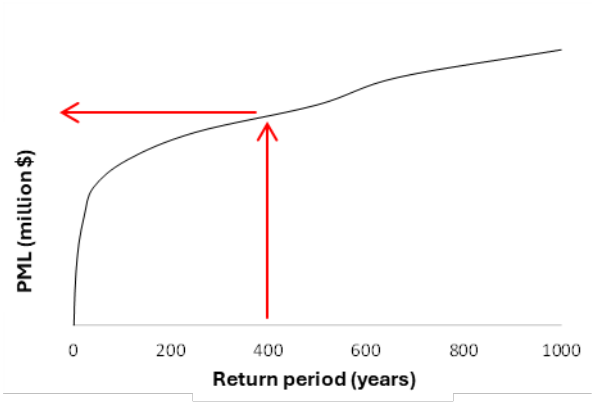


Figure 90. Example of a PML curve

### 5.3.3 Probability of Occurrence Within an Exposure Time

This metric is equivalent to the so-called probability of ruin ($P_Q$), which represents the probability of exceeding a given loss level within a specified exposure time. It derives directly from the renewal process and allows associating the exposure time, typically the period during which the asset at risk is expected to be in use—with the probability of exceeding any loss amount. It is common to present a set of $P_Q$curves defined for various exposure periods (see Figure 91). By selecting a loss amount on the horizontal axis, one can read from the graph the probability that such a loss will be exceeded at least once during the specified exposure time, based on the corresponding curve.

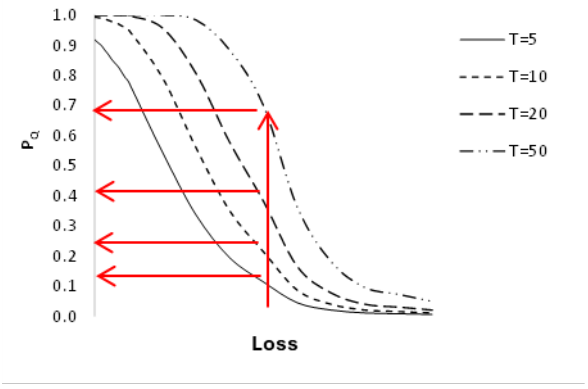


Figure 91. Example of $P_Q$ curves

### 5.3.4 ProbabilityLoss Exceedance in the Next Event

This curve indicates the probability of exceeding a specific loss threshold following the next event—or any randomly selected event. It is not linked to the time between hazardous events. Instead, it represents the likelihood that the losses associated with a given event will surpass a certain amount, regardless of when the event occurs. This metric is particularly useful for emergency preparedness activities, as well as for pricing financial instruments and designing mitigation strategies. Figure 92 presents an example of the probability of exceeding a given loss in the next event.

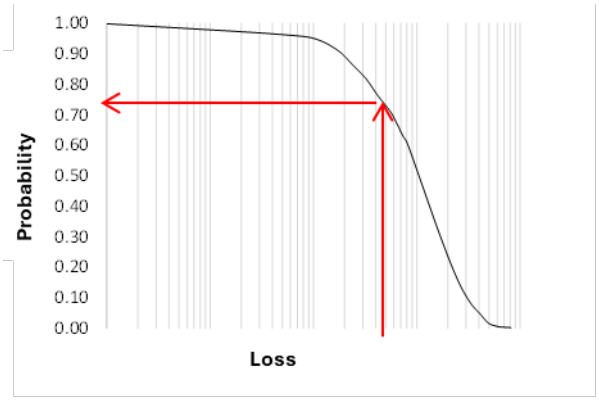


Figure 92. Example of a probability of loss exceedance curve for the next event

## 5.4 Incorporaction of Underlying Trends

The stationarity assumption of a Poisson process implies that its mean rate (i.e., the exceedance rate) remains constant over time. This approximation is widely accepted due to the difficulty of incorporating time-dependent models for hazard, exposure, and vulnerability, as well as the considerable uncertainty that arises when attempting to include them. However, in cases where stationarity is clearly an unrealistic assumption and the future dynamics of the risk components are known or can be reasonably approximated (as is the case with climate change), the model can be extended using non-stationary processes.

Let us consider a loss exceedance curve resulting from a probabilistic risk assessment. This output expresses the exceedance rates of losses based on hazard, exposure, and vulnerability—rates that are assumed to be constant over time. However, if future changes in the model components can be reasonably modeled, it is possible to compute new loss exceedance curves for future time periods. Consequently, exceedance rates become time-dependent, transforming the loss exceedance curve into a *loss exceedance surface* (see Figure 93). The exceedance surface contains all the functions $v(p,t)$ required to define the occurrence over time of losses greater than *p*, modeled as a non-homogeneous Poisson process.

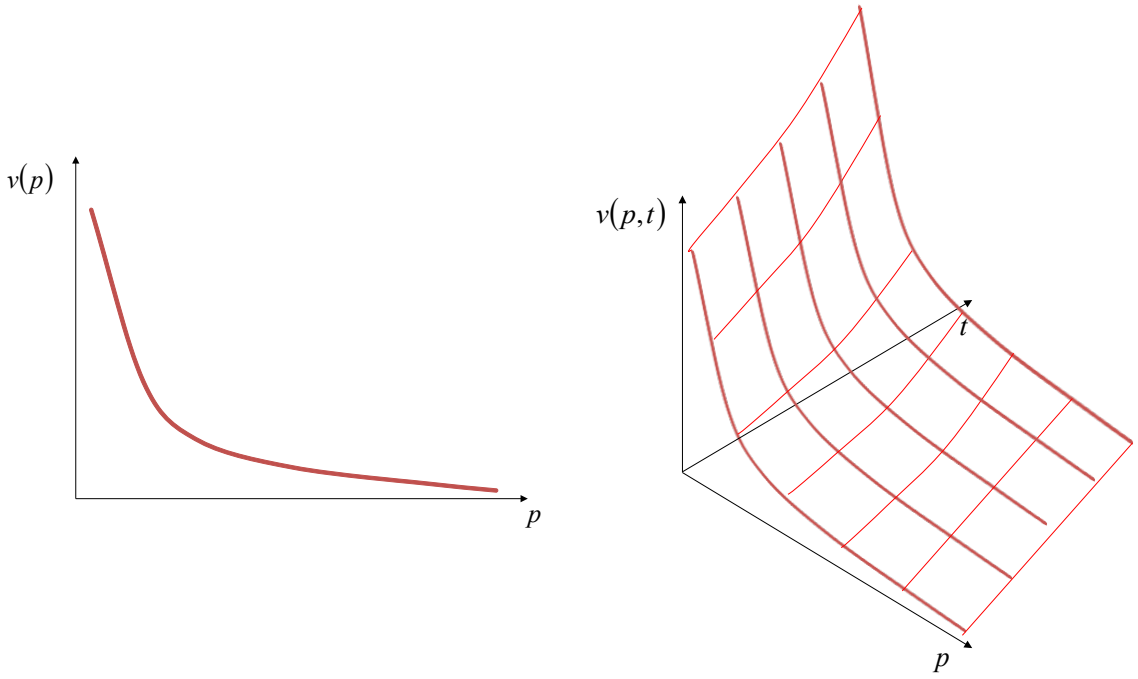


Figure 93. Time dependency added to loss exceedance rates. Left: loss exceedance curve; Right: loss exceedance surface

A non-homogeneous Poisson process satisfies the same fundamental properties as a homogeneous one—that is, it exhibits independent, Poisson-distributed increments. The key difference is that the process rate becomes a function of time, $\lambda(t)$[5]. A risk assessment conducted under this approach has the following properties:

- The loss occurrence process remains stochastic.
- The mean rate of the process changes over time.
- All risk metrics (e.g., AAL, PML) become time-dependent functions.

As a result, point-based metrics such as the Average Annual Loss (AAL) become time-varying. This change implies a loss of some desirable characteristics of these condensed integral indicators. To obtain fixed-point values, a simple time-averaging process is required, involving an arbitrary choice of temporal boundaries.

## 5.5 Incorporating Variables with Deep Uncertainty

Future characteristics of the built environment, the dynamics of sociotechnical systems, or the precise conditions of the future climate—among others—are highly desirable inputs for risk modeling, as they are essential for designing actions and policies aimed at anticipating risk materialization. However, predicting with arbitrary precision how non-stationary natural phenomena, exposed elements, and their vulnerability will change in the distant—or even near—future is virtually impossible. Moreover, assigning any kind of

[5] For a general description of the non-homogeneous Poisson process, the reader is referred to Kirgman (1992).

probability model to such dynamic and complex behavior is extremely difficult without resorting to arbitrary assumptions.

Most variables involved in probabilistic risk assessment fit well within traditional probability models. As previously discussed, it is even possible to incorporate underlying trends into risk calculations while remaining within the bounds of probability theory. But what happens when a new variable is introduced for which no reasonable point assumptions can be made, there are no observed data (or not enough), its behavior cannot be predicted through physical models, and there is no clear consensus about its evolution? This situation constitutes a deep uncertainty problem. Climate change is a clear example of a variable subject to deep uncertainty.

Addressing deep uncertainty in risk assessment requires an expansion of the methodological approach—shifting catastrophic risk modeling from being solely indexed to probability theory to being framed within *random set theory.* Random set theory (Kendall, 1974; Matheron, 1975) is currently considered the most general mathematical theory for dealing with uncertainty. It enables operations with various types of uncertainty structures, including Dempster-Shafer evidence theory, info-gap models, probability boxes, raw intervals, fuzzy sets, and even traditional probability distribution functions.

Let $(\mathcal{L}, \ell)$be the random set that contains all the loss calculation outcomes. Then, $\mathcal{L}$ is the collection of focal loss elements (i.e., intervals $L_j$), and $\ell(L_i)$, for $L_j \in \mathcal{L}$, is the mass assignment—meaning the probability of occurrence of the event that produced the focal loss element. Let $F$ be the event in which the loss $P$ exceeds a given threshold $p$ (i.e., $F = \{P: P \geq p\}$). Then, the *lower* and *upper* loss exceedance rates are obtained as follows:

$$v(p)_L = \sum_{j=1}^{n} I\left[L_j \subseteq F\right] \cdot \ell\left(L_j\right) \qquad \text{Equation 11}$$

$$v(p)_U = \sum_{j=1}^{n} I\left[L_j \cap F \neq \emptyset\right] \cdot \ell\left(L_j\right) \qquad \text{Equation 12}$$

where $n$ is the total number of focal elements in $\mathcal{L}$, and $I[\cdot]$ is the indicator function. Therefore, the inclusion of variables with deep uncertainty—such as climate change—implies that the results must be expressed through an *imprecise loss exceedance curve*, composed of a lower and upper bound. Likewise, all risk metrics are determined as intervals, meaning they are inherently imprecise in nature.

## 5.6 Risk Management Decision-Making and Climate Change Adaptation

Disaster risk management encompasses various types of actions. Beyond the conventional understanding of emergency response and disaster relief, it also includes preparedness for such scenarios. More importantly, it ranges from deepening knowledge—through the monitoring of phenomena, hazard, vulnerability, and risk studies and modeling—to risk reduction from both non-structural and structural perspectives. Non-structural measures involve regulations, guidelines, educational and training processes,

land-use planning, and more. Structural measures include the construction of erosion control works, riverbank and riverbed conditioning, and interventions in buildings and infrastructure.

These knowledge and risk reduction actions are closely connected to climate change adaptation measures. Within the broad spectrum of possibilities for risk reduction, the type of event, the existing risk, environmental, and/or climate change management system, as well as national or local policies—or even expert or public official opinions—can influence measures that can or should be adopted. For instance, in risk scenarios dominated by high-intensity events, relocation processes are often considered. However, this is neither the only option available nor necessarily the optimal one. Determining the best combination of risk reduction alternatives is, in general, extremely difficult without introducing arbitrariness.

Both catastrophic risk and risk management measures are hypothetical states whose exact quantification is impossible. This implies that risk modeling must rigorously quantify uncertainty (as discussed previously); otherwise, it does not qualify as disaster risk analysis. Similarly, the incorporation of risk management measures that intervene in the conditions giving rise to risk must follow an approach that accounts for all possible variations in how such interventions may unfold. This is not only a strongly non-linear problem but also one characterized by *deep uncertainty*.

Confronting deep uncertainty requires innovative approaches that facilitate decision-making beyond the classical deterministic view—which is incomplete and insufficient—where the problem and its solution are assumed to be fully defined. Instead, a shift toward an uncertainty-centered vision is needed, one grounded in the principles of post-normal science, which acknowledges the vast space of possible futures in which the problem may evolve and seeks solutions that perform well across most of these uncertain scenarios.

Recently, several authors have proposed approaches to address deep uncertainty and guide decision-making (see, for example, the compilation in Marcahu et al., 2019). A particularly noteworthy approach is *Robust Decision Making (RDM)* (Lempert, 2019), which follows a methodology known as *XLRM*, where: *X* represents the uncertainties, *L* the possible actions to be considered, *R* the system model, and *M* the success metrics for the actions. According to Lempert (2019), the steps to achieve robust decision-making are: 1) Frame the analysis by defining a model (R) that adequately describes the problem; 2) simulate, considering the uncertainty (X) and the effect of possible actions (L) on the system; 3)Explore the results and quantify the success metrics (M); 4) compare and analyze how well the actions achieve the intended goals; 5) iterate and re-evaluate. In summary, it is recognized that robust decision-making cannot be achieved without accounting for the multiple branches that define the domain of possible futures. This requires a paradigm shift from predictive precision toward adaptability and resilience under uncertainty.

### 5.6.1 Risk Control Engineering (RCE)

Following the metaconcepts of control theory, Bernal et al. (2021) present the principles of *Risk Control Engineering (RCE)* as a methodology for quantifying the various ways in which disaster risk and climate change adaptation measures can be controlled through different types of intervention. RCE is a methodological framework specifically designed to support governments, institutions, and private sector stakeholders in guiding decision-making under deep uncertainty in the context of risk management. The RCE process is summarized in Figure 94. RCE follows guidelines and procedures like those outlined by

Lempert (2019) in the RDM approach, leading to decision-making based on the best possible outcome (optimization) across a wide array of uncertain futures.

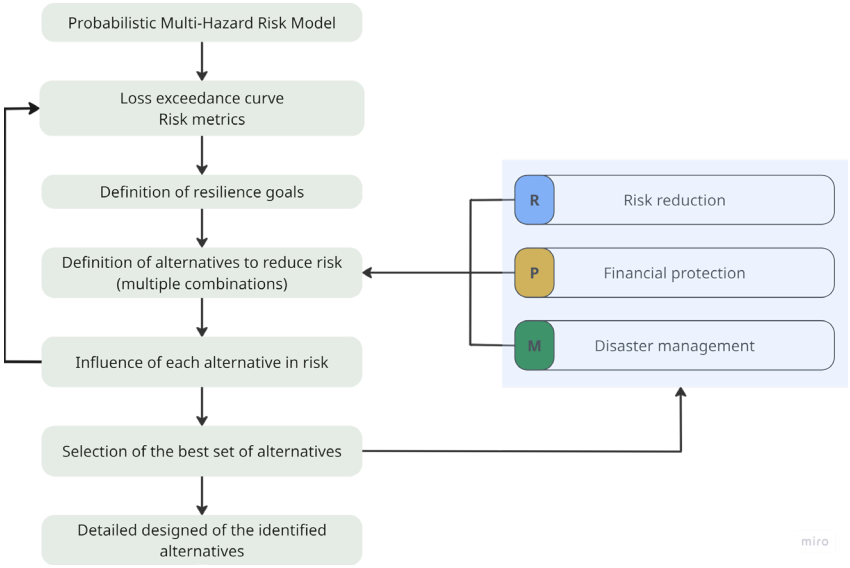


Figure 94. Risk Control Engineering (RCE) process.

RCE is based on measuring the effect of disaster risk reduction and/or climate change adaptation measures to identify optimal strategies at a favorable cost. The primary risk metric used is the loss exceedance curve (LEC). The effectiveness of a measure in reducing risk is rigorously evaluated based on its capacity to reduce the LEC within an interval corresponding to the scope of the measure.

Among its many valuable properties, the LEC can be stratified, allowing for the definition of a set of intervention measures aimed at risk reduction and/or climate change adaptation (see

Figure 95). The concept of risk stratification is associated with the effectiveness of risk reduction measures at different levels. Each risk management measure affects a particular layer or “stratum” of the LEC, rather than the entire loss domain.

Because each risk management measure impacts the LEC differently, a collection or set of measures is required to bring the risk down to acceptable levels. This set of measures constitutes a *disaster risk management strategy*. The risk landscape is altered when a particular strategy is applied. The most effective way to determine whether a strategy is adequate for reducing risk is to repeat the risk assessment while including the effect of all the measures it comprises. If many potential strategy variations are defined—based on the composition and effectiveness of their respective measures—it becomes possible to identify which of the studied strategies is optimal or efficient in reducing risk.

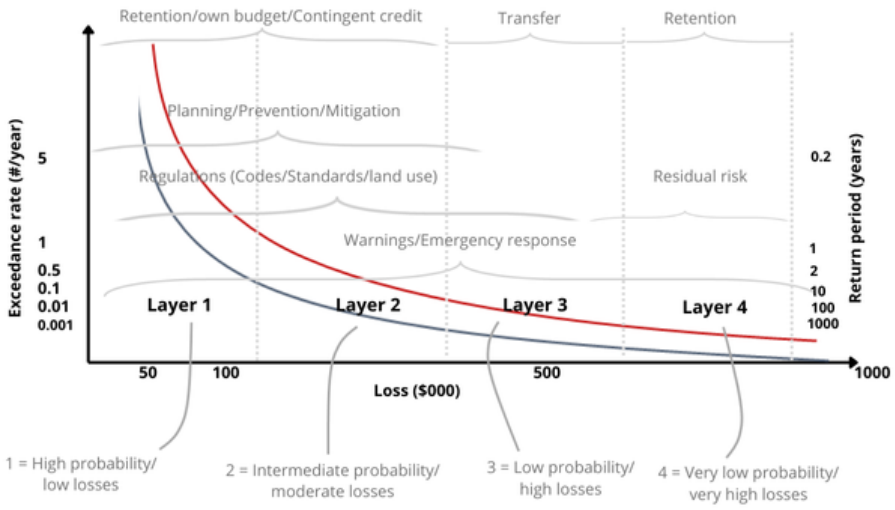


Figure 95. Illustration of LEC stratification in a non-intervened state (red curve) and the risk reduction effect of applying actions by stratum (blue curve)

The RCE methodology considers three types of actions or risk management and/or climate adaptation measures that can be incorporated into modeling to assess their effectiveness:

1. Risk reduction measures, which aim to reduce exposure and vulnerability. These include mitigation, protection, prevention, and planning actions that either correct existing exposure or vulnerability or prevent the emergence of new risk conditions, thereby directly reducing the LEC.

2. Financial protection or risk transfer mechanisms, which aim to provide compensation mechanisms that ensure the availability of resources to cover disaster-related costs and support recovery. These mechanisms typically involve transferring part of the risk to a third party, who agrees—against economic compensation—to cover a portion of the losses with their own resources. While these measures do not directly reduce the gross loss, they do lower the net loss borne by the risk holder.

3. Disaster response measures, which seek to limit total impacts once a disaster occurs. Early warning systems, emergency and contingency plans, as well as immediate response, reconstruction, recovery, and restoration of essential services, must be defined based on the risk model and play a significant role in re-establishing (or not) the pre-existing exposure and vulnerability conditions for future events (Cardona, 1996; 1997).

As previously stated, a risk management and climate adaptation strategy consist of a combination of multiple measures. It can be defined in terms of: i) the set of measures it includes ii) the risk reduction capacity of each measure; and iii) the implementation cost of each measure. Measures are incorporated into the risk model by modifying the parameters they are expected to influence. For example:

- Reducing the vulnerability of exposed buildings and infrastructure, thereby lowering potential losses in hazardous events.

- Relocation processes directly alter exposure, reducing the total value at risk by moving elements to a new location with different exposure and vulnerability profiles.

- Financial protection mechanisms limit the net loss to the risk holder, capping it to retained portions.

Achieving acceptable levels of risk can be accomplished through a vast number of possible combinations of risk management and climate adaptation measures. Identifying the best combination is usually very difficult without arbitrariness. For this reason, RCE stochastically generates multiple possible risk management strategies to test the effectiveness of each within the risk model. Because randomly searching for the optimal combination can be computationally extensive, evolutionary computation is employed to approximate the strategy or combination of measures that most cost-effectively reduce risk.

The genetic optimization algorithm implemented in RCE is summarized as follows:

1. A large number of combinations of risk management measures are randomly generated to form an initial generation of strategies. Each strategy is considered an individual. The genotype of an individual is the set of measures it contains (see Figure 96). Each individual has a different capacity to reduce risk. The one that achieves the highest risk reduction at the lowest cost is considered the *champion* of the first generation.

2. The evolutionary process begins by randomly creating new combinations of alternatives through crossover and mutation from individuals in the previous generation. This process is repeated for a certain number of generations. The *champion* of the final generation holds the optimal combination of risk management measures to be implemented. This combination becomes a strong candidate to serve as the selected management strategy.

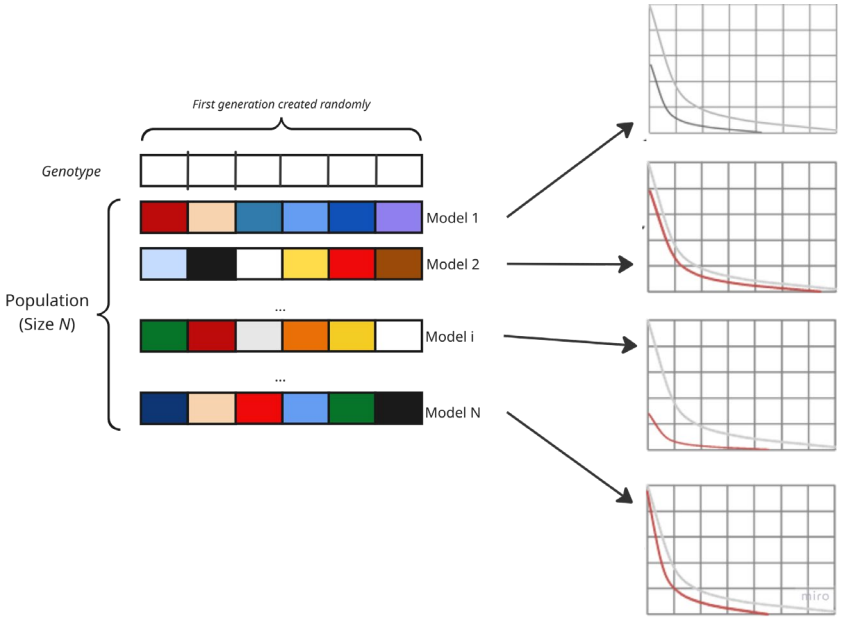


Figure 96. Illustration of the creation of an initial generation of risk management strategies. The colors in the boxes represent different characteristics of each measure.

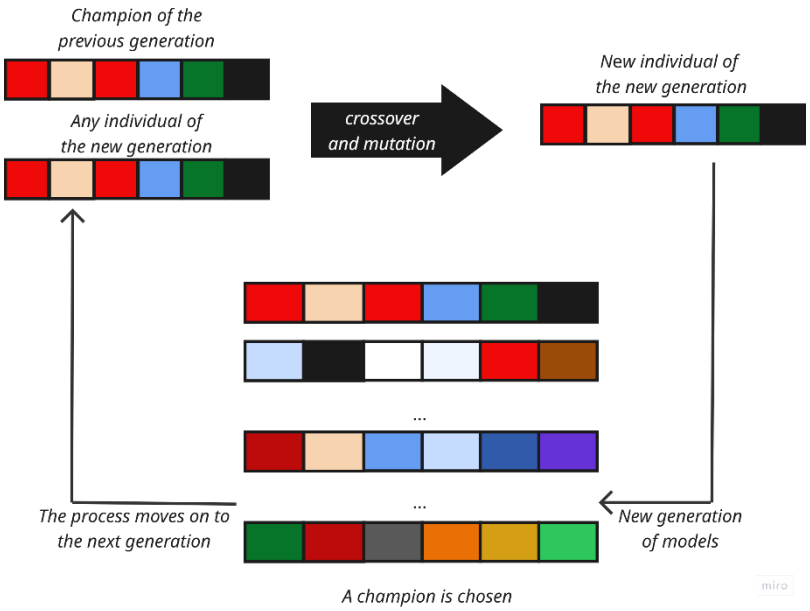


Figure 97. Illustration of the evolutionary process for optimizing the combination of risk reduction measures

As this approach relies on randomized optimization, the strategies resulting from the process may vary with each run. It is therefore possible to define a group of viable strategies that meet the optimization criteria or other constraints (such as a maximum investment budget), in order to present a set of possible strategies to decision-makers. In other words, within a robust decision-making process, optimization serves as a tool for pre-selecting strategies from the vast space of possible options.

# 6 PROBABILISTIC MODELING OF HYDROMETEOROLOGICAL HAZARDS

The first component of risk modeling is the hazard, which must describe all the ways in which natural phenomena may manifest in each territory. Due to the primary influence of climate change on hydrometeorological hazards—as opposed to geological hazards, which are less critically affected—this report presents these two groups of hazards separately. This separation facilitates a clearer connection between the climate component and hydrometeorological phenomena. Nonetheless, it is important to note that some geological hazards can be influenced by climatic, and more specifically, meteorological conditions, such as landslides triggered by excessive rainfall or the transport of volcanic ash by wind.

## 6.1 Meteorological Forcing Modeling

This study adopts a methodology based on the modeling of meteorological forcing, from which hydrometeorological hazards are derived. Using available historical records of precipitation, temperature, and other meteorological variables in the country[6], long-term time series (on the order of thousands of equivalent years) are constructed through a synthetic series simulator. This simulator stochastically generates full years of temporally and spatially correlated data (i.e., based on first- and second-order statistics calculated from historical records). This procedure constitutes a statistical downscaling for the later incorporation of climate change projections.

On the simulated series, it is possible to identify extreme conditions (such as excessive or deficient rainfall and extreme temperatures) that may occur infrequently (i.e., not necessarily observed in historical records). These extreme conditions give rise to hazard events such as droughts, riverine floods, or coastal flooding. The potential impacts of climate change are incorporated by perturbing the stochastic series to reflect projected changes in temperature and precipitation, which are then used to recalculate each hazard.

### 6.1.1 Stochastic Generation of Climate Series

The proposed methodology uses a synthetic climate generator based on parametric probability distributions to define historical climate datasets and estimate the probability of occurrence of specific precipitation or temperature values—even beyond the range of historical observations. The methodology analyzes each day of the year independently and identifies the probability distribution that best fits the historical records. Subsequently, random values for daily precipitation and temperature are generated for a specified number of simulation years using the parameters of the selected distributions.

To evaluate the fit of the probability distributions, the Kolmogorov-Smirnov goodness-of-fit test was used. A significant level of 0.05 was adopted, implying that the probability of incorrectly rejecting the null hypothesis (i.e., the data do follow the proposed distribution) is just 5%. If the *p-value* exceeds the significance level, the null hypothesis cannot be rejected, and one cannot conclude that the data do not fit the assumed distribution.

[6] Variables such as potential evapotranspiration, relative humidity, wind speed and direction, among others.

In the specific case of precipitation, it is necessary to distinguish between rainy and dry days. Therefore, the probability density function is defined as a discrete distribution indicating the probability of rainfall, coupled with a continuous distribution determining its intensity on rainy days (see Figure 98). The probability of a dry day ($P_0$) is defined as the ratio of dry days to the total number of days in the sample.

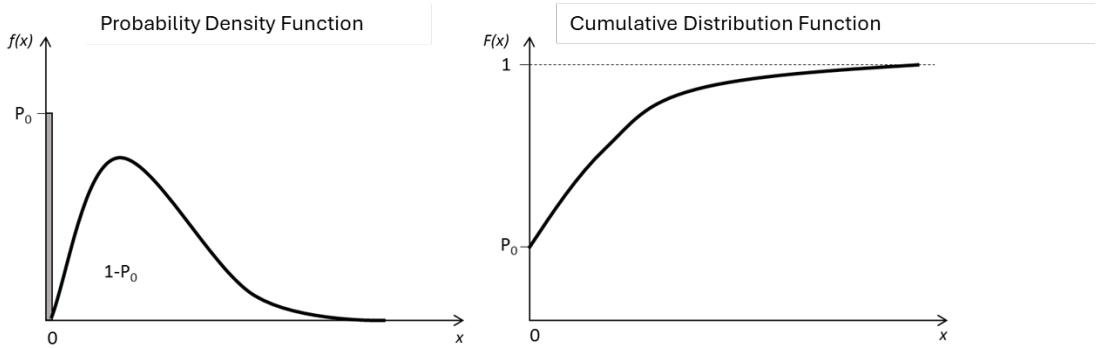


Figure 98. Example of coupled probability density and cumulative probability functions for precipitation

Once the most appropriate probability distributions for precipitation and temperature (mean, maximum, and minimum) are defined for each of the 365 days of the year, random numbers are generated for a specified number of simulation years (typically around 1,000 years). This results in random climate data series for each weather station within Costa Rica.

Next, to include the correlation between precipitation and temperature over successive periods, the autocorrelation matrix is calculated for each synthetic series. Temporal autocorrelation reflects how a variable correlates with its past and future values (Wilks, 2006). Additionally, spatial correlation effects—simultaneous data patterns across multiple stations in the study area—are incorporated by calculating the spatial autocorrelation matrix among stations. This ensures that unrealistic abrupt changes in precipitation, temperature, etc., are avoided.

Figure 99 illustrates one-year synthetic time series of precipitation and temperature simulated for an arbitrary location using the methodology described above. It is important to note that these values do not constitute forecasts; rather, they are randomly generated values that have been temporally and spatially correlated to replicate and represent the climate of the study area. This approach provides additional information (compared to the limited historical data available) about potential future hydrometeorological events that may not have occurred yet.

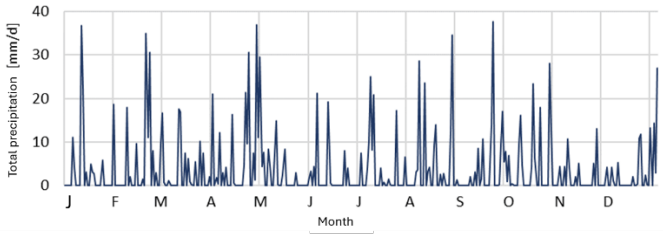

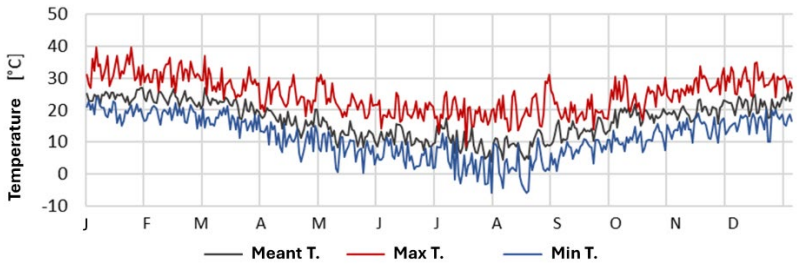


Figure 99. One-year synthetic time series for precipitation and temperature at an arbitrary location.

One advantage of the stochastic generation of climate series is the ability to simulate extreme outliers—precipitation values exceeding historical maxima or temperature values beyond historically recorded ranges. This means that the modeled series includes precipitation and temperature values that have not occurred historically but could occur with low probability in the future. Consequently, climate variability is implicitly incorporated into the generation of these synthetic series, as they are temporally correlated with past and future values and spatially correlated with other stations in the study area. Figure 100 presents a flowchart of the stochastic generation process for meteorological series, specifically for precipitation and temperature.

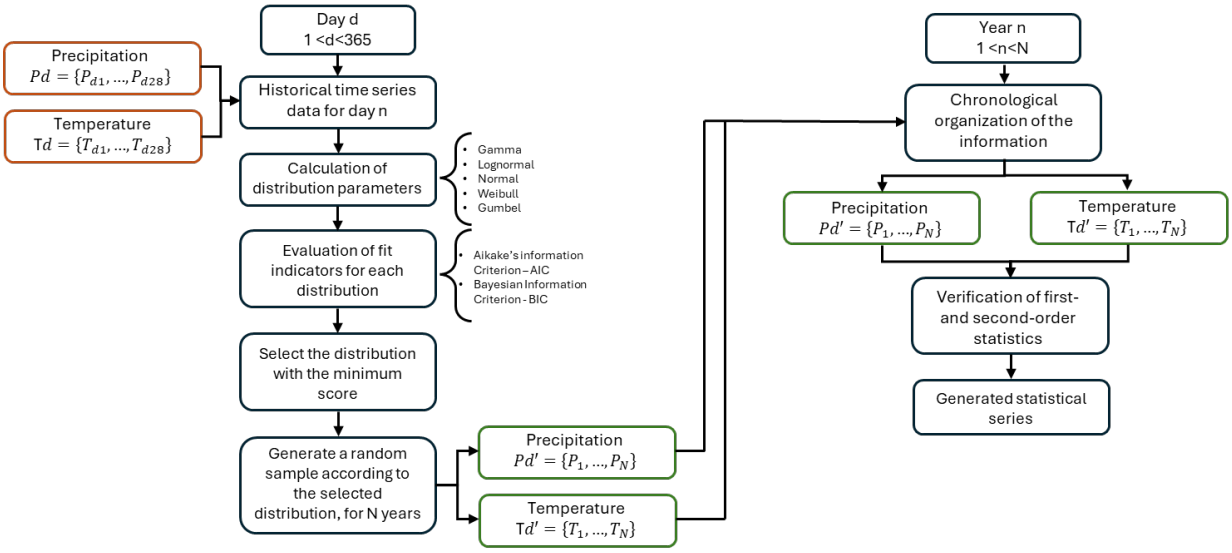


Figure 100. Flowchart of the synthetic series generation process.

### 6.1.2 Incorporating Climate Change into Climate Series Generation

Incorporating climate change into the simulated series constitutes a statistical downscaling procedure based on the stochastic generation of meteorological series. In this approach, the temporal variability and inherent variance of meteorological variables are assumed to be adequately defined by historical climate data. Thus, only the mean values of the simulated series are modified to reflect the variations projected by Global Climate Models (GCMs).

To incorporate climate change into the generation of climate series, all available projections from CMIP6 global circulation models[7] are analyzed for multiple emissions scenarios: SSP1-2.6, SSP2-4.5, SSP3-7.0, SSP4-6.0, and SSP5-8.5, as shown in Figure 101.

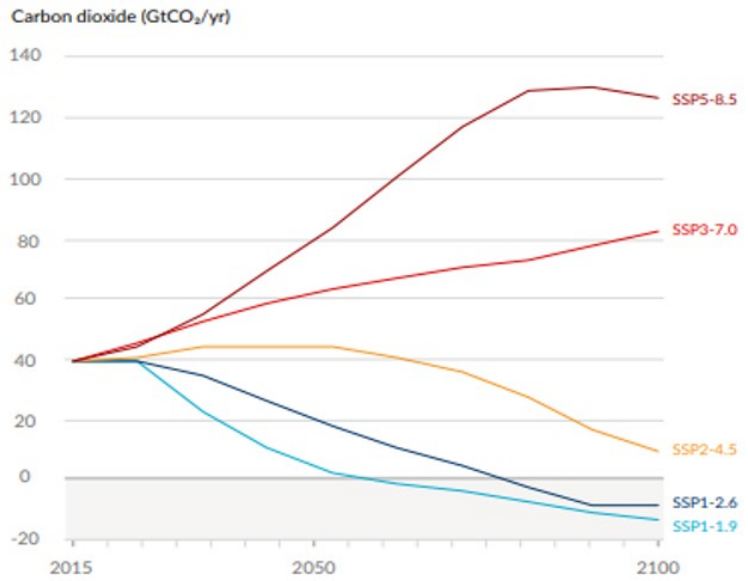


Figure 101. Climate change scenarios according to IPCC – AR6 (2021)

The SSP[8] are narrative-based scenarios of climate change that account for socioeconomic development and the world's capacity for mitigation and adaptation. Each pathway corresponds to a specific emissions trajectory. For example, a scenario like SSP5, characterized by high fossil fuel use and low mitigation efforts, is associated with an average additional radiative forcing of 8.5 W/m² by 2100, while a scenario like SSP2, with moderate mitigation, is linked to a forcing of 4.5 W/m² (Escoto et al., 2017). On the other hand, SSP1, associated with sustainability (low population growth, high economic development,

[7] The following General Circulation Models (GCMs) are used (including multiple versions): Australian Community Climate and Earth System Simulator (ACCESS 1); Beijing Climate Center Climate System Model version 1.1 (BCC-CSM 1.1); Beijing Normal University Earth System Model (BNU-ESM); Canadian Earth System Model (CanESM2); Community Climate System Model (CCSM4); Community Earth System Model Version 1 (CESM1); Centro Euro-Mediterráneo sui Cambiamenti Climatici (CMCC); Centre National de Recherches Météorologiques - Coupled Model 5 (CNRM-CM5); Commonwealth Scientific and Industrial Research Organisation (CSIRO-Mk3-6-0); Flexible Global Ocean-Atmosphere-Land System, Gridpoint version 2 (FGOALS-g2); First Institute of Oceanography-Earth System Model (FIO-ESM); Geophysical Fluid Dynamics Laboratory - Earth System Model 2G (GFDL-ESM2G); Goddard Institute for Space Studies-E2 (GISS-E2); Hadley Centre Coupled Model Version 3 (HadCM3); Hadley Centre Global Environmental Model, version 2 (HadGEM2-ES); Institute for Numerical Mathematics Climate Model 4 (INMCM4); Institut Pierre Simon Laplace Model (IPSL-CM5A); Model for Interdisciplinary Research on Climate 4 (MIROC4h); Model for Interdisciplinary Research on Climate Earth System Model (MIROC-ESM); Max Planck Institut fur Meteorologie Earth System Model (MPI-ESM); Meteorological Research Institute Global Climate Model 3 (MRI-CGCM3); Norwegian Earth System Model (NorESM1).

[8] The Shared Socioeconomic Pathways (SSPs) include five scenarios: SSP1 represents a sustainability-focused world; SSP2 follows a "middle of the road" trajectory; SSP3 reflects a world shaped by regional rivalry; SSP4 is characterized by growing inequality; and SSP5 envisions development driven by fossil fuels.fósiles.

education, global governance, international cooperation, technological advancement, and environmental awareness), corresponds to a forcing of 2.6 W/m².

Figure 102 shows projected changes in mean precipitation and temperature at an arbitrary location. These projections result from combining 53 CMIP6 global circulation models, evaluated for the greenhouse gas emissions scenarios previously described.

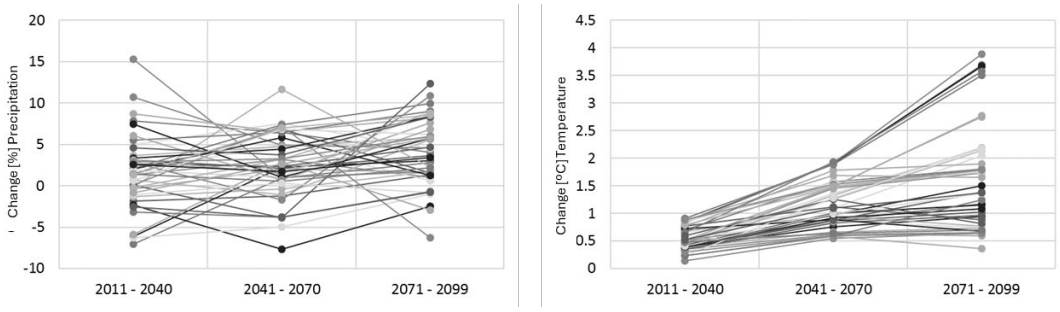


Figure 102. Projected changes in precipitation (left) and temperature (right) according to multiple GCMs and SSPs for an arbitrary location

From the dispersion graphs of global circulation models, the following can be concluded:

- GCMs exhibit high variability, meaning that projections for a single point span a wide range of expected values.
- No single model perfectly fits historical records for a specific point or area.
- It is not advisable to use the maximum or minimum values of GCMs, as they may under- or overestimate historical climate and increase uncertainty in future variability projections.

The scope of this study includes assessing the impact of climate change on variations in precipitation and temperature under the following considerations:

- GCMs consistently provide projections for these two variables; in rare cases, they offer data on other climate parameters (e.g., humidity, radiation, wind speed), which involve complex physical and chemical interactions across coupled atmosphere-ocean-land-ice systems.
- The hazard modeling methodology is limited to stochastic generation of precipitation and temperature series (a statistical climate simulation process based on historical records). Modeling other variables (humidity, radiation, wind speed) require complex atmospheric circulation and earth system interaction models, which are outside the scope of this study.

From the simulated meteorological series, either for current climate conditions or those altered by climate change, the meteorological forcing from which hazard events arise is extracted. These hazard events are then simulated using physics-based models, as described in the following sections.

## 6.2 Drought Hazard

In general terms, for the case of drought, multiple drought indicators are calculated for all weather stations and at different time scales in monthly steps using both historical and synthetic precipitation and

temperature series. Once the time series of the selected indicator is obtained at each station, drought events are identified. These events occur when the indicator takes on a negative value or falls below a critical threshold.

### 6.2.1 Reference Evapotranspiration

The calculation of some drought indicators requires prior estimation of reference evapotranspiration, to assess atmospheric conditions that determine whether there is an excess of water in the atmosphere (low evapotranspiration) or a deficit (high evapotranspiration and little rainfall). Reference evapotranspiration is estimated using the Penman-Monteith method, as detailed in "*Crop Evapotranspiration: Guidelines for Computing Crop Water Requirements*" (Allen, Pereira, Raes, & Smith, 1998), the most widely used method globally.

Reference evapotranspiration is the potential atmospheric evaporation calculated over a uniform vegetative surface without water limitations. The reference surface is a hypothetical crop with an assumed height of 0.12 m, a fixed surface resistance of 70 s/m, and an albedo of 0.23 (Allen et al., 1998). It is independent of crop type, development stage, or management. Since there are no restrictions on water content, soil characteristics do not influence the result. These conditions allow for comparisons across different locations or stations to evaluate the evaporative conditions of the atmosphere, which vary only based on prevailing climatic conditions.

It is important to distinguish reference evapotranspiration ($ET_0$) from the evapotranspiration of a specific crop under standard conditions ($ET_c$)) and that under non-standard conditions ($ET_{c\,aj}$). Standard crop evapotranspiration considers crop-specific traits such as resistance, albedo, leaf anatomy, stomatal characteristics, and aerodynamic properties. Meanwhile, $ET_{c\,aj}$ accounts for crops growing under suboptimal conditions due to soil or water stress, diseases, or fertilization that alter crop yields.

The Penman-Monteith method (see Equation 1) allows for quantifying the simultaneous processes of evaporation (water vaporization from surfaces such as soil or wet vegetation) and transpiration (vaporization from plant tissues). Required parameters include solar radiation, temperature, humidity, wind speed, vapor flux, and aerodynamic resistance.

$$ET_0 = \frac{0.408\Delta(R_n - G) + \gamma \frac{900}{T + 273} u_2 (e_s - e_a)}{\Delta + \gamma(1 + 0.34u_2)} \qquad \text{Equation 1}$$

Where $R_n$ is the net radiation, $G$ is the soil heat flux, $\gamma$ is the psychrometric constant, $T$ is the mean daily temperature, $u_2$ is the wind speed at 2 meters height, $(e_s - e_a)$ represents the vapor pressure deficit and $\Delta$ is the slope of the vapor pressure curve. Applying the Penman-Monteith method requires meteorological data, which may not always be available. Missing parameters are estimated based on expert judgment, regional climate data, and FAO guidelines (Raes, 2009). Further details of the method are provided in Annex 1.

### 6.2.2 Indicators

Meteorological drought indicators are widely used to identify drought events by detecting precipitation below the mean and simultaneous temperature conditions above average. These indicators define the *duration* and *severity* of drought events. Start and end dates delineate the event's duration, during which the indicator remains below a predefined critical level (the lower the value, the more intense the drought). Severity denotes the cumulative deficiency of the indicator below the threshold between these dates. The ratio of severity to duration defines the drought's intensity (Mishra & Singh, 2010). These concepts are illustrated in Figure 103. Each drought event includes the following components:

- *Severity:* Area under the event curve, i.e., the cumulative value of the indicator during the event.
- *Duration:* The time the event lasts.
- *Intensity:* Calculated as severity divided by duration; a unit measure of the event's magnitude.

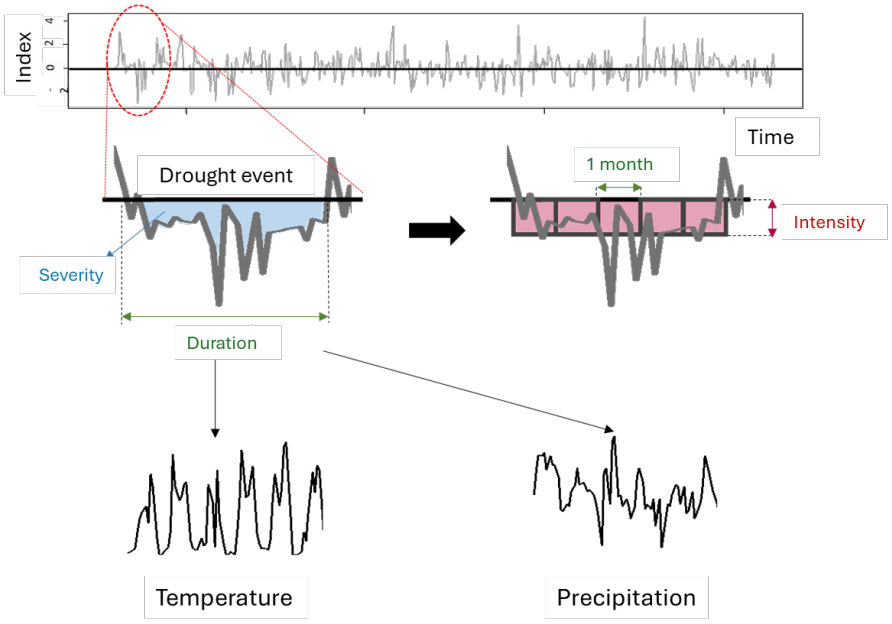


Figure 103. Conceptual diagram of drought indicators, severity, duration, and intensity.

Depending on the drought type being assessed, different parameters may be included in index calculations. Meteorological droughts are linked to precipitation deficiencies in terms of quantity, intensity, and duration, as well as increased evaporation and transpiration due to high temperatures, strong winds, low relative humidity, intense sunlight, and reduced cloud covers. Agricultural droughts are defined by soil water deficiencies causing plant stress and reduced biomass or yield. Hydrological droughts are identified by reduced streamflow, reservoir levels, and wetland areas. This classification—meteorological, agricultural, hydrological, and socio-economic drought—was first proposed by Wilhite and Glantz (1985).

According to Jayanthi (2014), agricultural drought indicators should integrate rainfall and temperature variables along with evapotranspiration for effective monitoring of rainfed crops and pastures. Banimahd

and Khalili (2013) compared commonly used agricultural drought indices such as the Palmer Drought Severity Index (PDSI) (Palmer, 1965), the Standardized Precipitation Index (SPI) (McKee, Doesken, & Kleist, 1993), the Effective Drought Index (EDI) (Byun & Wilhite, 1999), the Reconnaissance Drought Index (RDI) (Tsakiris, Pangalou, & Vangelis, 2007), and the Standardized Precipitation Evapotranspiration Index (SPEI) (Vicente-Serrano, Beguería, & López-Moreno, 2010).

Their findings showed that SPEI and RDI were better at identifying extreme drought severities, highlighting the important role of evapotranspiration. This aligns with Tsakiris et al. (2007), who demonstrated that precipitation alone does not correlate well with crop yield, emphasizing the need to incorporate reference evapotranspiration.

This study does not use indicators that consider soil or crop-specific parameters, such as the Palmer Index. Instead, the drought hazard model evaluates only climatic conditions (precipitation and temperature), classifying droughts independently of their agricultural impacts. Crop and soil-specific parameters are addressed in the vulnerability model (see Section 9.4).

Standardized drought indicators such as RDI and SPEI can be compared across spatial and temporal dimensions. Drought severity using these indicators can be classified according to Table 36:

Table 36. Drought classification based on standardized indicator values.

| Drought Class | Indicator Value |
|---|---|
| No drought | Greater than 0 |
| Mild | Between -1 and 0 |
| Moderate | Between -1.5 and -1 |
| Severe | Less than -1.5 |

In all cases, negative indicator values signify drought conditions, with more negative values indicating more severe droughts. Evaluating scenarios using multiple indicators is advisable, as no single indicator is universally applicable due to the complexity of drought and varying regional climate conditions (Tsakiris et al., 2007). Indicators are calculated for each series (historical or simulated) at every point in the analysis grid. Figure 104 shows an example of a drought indicator over three years of historical data and the threshold line for identifying droughts starting from mild events (threshold = -1). In this example, a four-month drought is observed from late 1981 to early 1982[9].

.

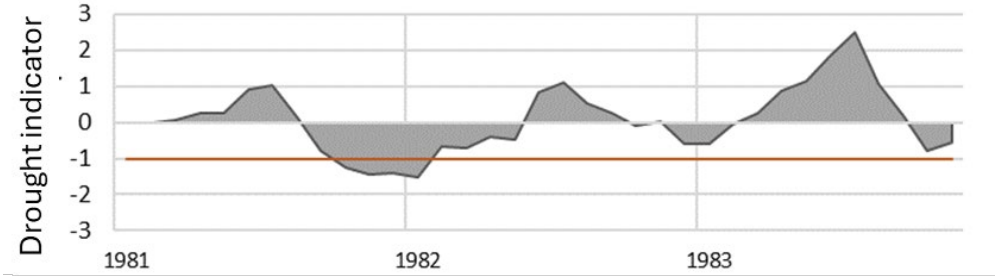


Figure 104. Example drought indicator time series (3-month scale, threshold = -1).

[9] This is an illustrative example and does not correspond to a real drought event in Costa Rica.

### 6.2.3 Definition of Regional Drought Events

The next step involves identifying drought events that occur simultaneously at several stations in the study region. For each month, stations with indicator values below the evaluation threshold (e.g., -1 for moderate and severe droughts) are identified. If the number of such stations exceeds a predefined percentage (e.g., 50%), a regional drought is declared.

By repeating these calculations for each simulation year, multiple regional droughts can be identified, each with an associated duration, severity, and intensity per station. Each regional drought becomes a distinct scenario, with an annual frequency of 1/N, where N is the number of simulation years. Figure 105 schematically illustrates how regional droughts are identified based on the threshold indicator value and the minimum number of qualifying stations. This approach can be applied to the entire study area or to subregions defined by other criteria, such as climate zones, productive zones, or administrative boundaries.

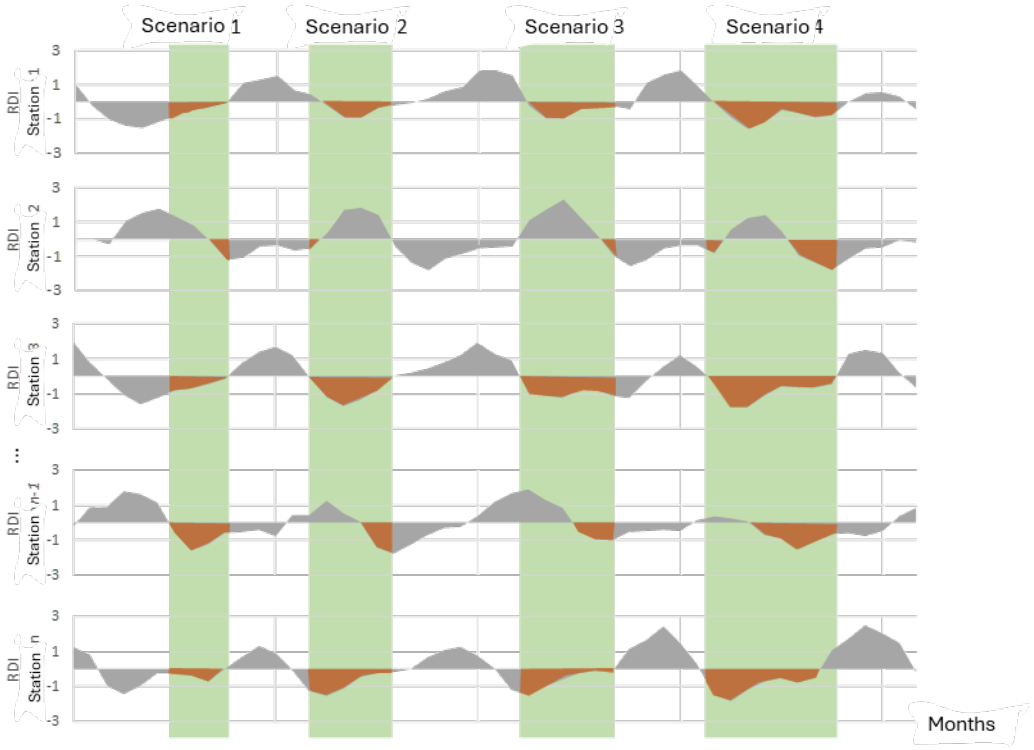


Figure 105. **Identification of regional droughts across all station time series in the study area**.

## 6.3 Pluvial and Fluvial Flood Hazard

Floods can occur in different forms depending on the origin of the triggering event. This section focuses on the assessment of pluvial flooding (caused by surface water accumulation) and fluvial flooding (caused by river overflow). The model for coastal flooding is presented in Section 6.4. The hazard modeling

approach implemented here follows a classic structure composed of meteorological forcing modeling (i.e., rainfall events), hydrological response modeling of the watersheds, and hydraulic modeling.

### 6.3.1 Rainfall Events (Heavy Rainfall)

From the precipitation series obtained at different stations across the territory, it is possible to extract synthetically generated heavy rainfall events with total values and spatial patterns that reflect historical rainfall characteristics. These events are generated by applying simple selection criteria to the simulated precipitation series. For example:

- A minimum number of stations recording a given rainfall (e.g., 70% of stations in a watershed must record precipitation for the event).
- A minimum threshold value for a significant event, meaning the recorded precipitation must exceed this value in the defined number of stations (e.g., precipitation greater than 10 mm in 24 hours).
- A mean threshold value for the average precipitation among stations exceeding the minimum threshold (e.g., average precipitation of at least 50 mm in 24 hours).

Applying these or similar criteria makes it possible to identify heavy rainfall events from the simulated daily series. The retrieved values are spatially interpolated using the Kriging method.

Simulated storms inherently have realistic precipitation patterns derived directly from individual series, which is an advantage as it removes the need for synthetic spatial patterns. Rainfall distribution varies significantly in magnitude and spatial pattern across the watershed. No two events are identical. Figure 106 illustrates stochastically generated rainfall events over an arbitrary watershed, showing total daily precipitation in a heavy rainfall scenario. Since rainfall does not fall uniformly over 24 hours, its intra-daily distribution is simulated using Huff curves (Huff, 1967).

Huff curves are a "design storm" methodology proposed by Huff (1967) to describe the temporal distribution of precipitation in probabilistic terms (Rao & Kao, 2006). Huff observed that most rainfall occurs in a small portion of an event's total duration, aligning with the IDF (Intensity – Duration – Frequency) curve concept where higher precipitation intensities occur over short periods. Rainfall events in each area are categorized into four quartiles, each representing the 25% segment of time during which most precipitation occurs (Figure 107).

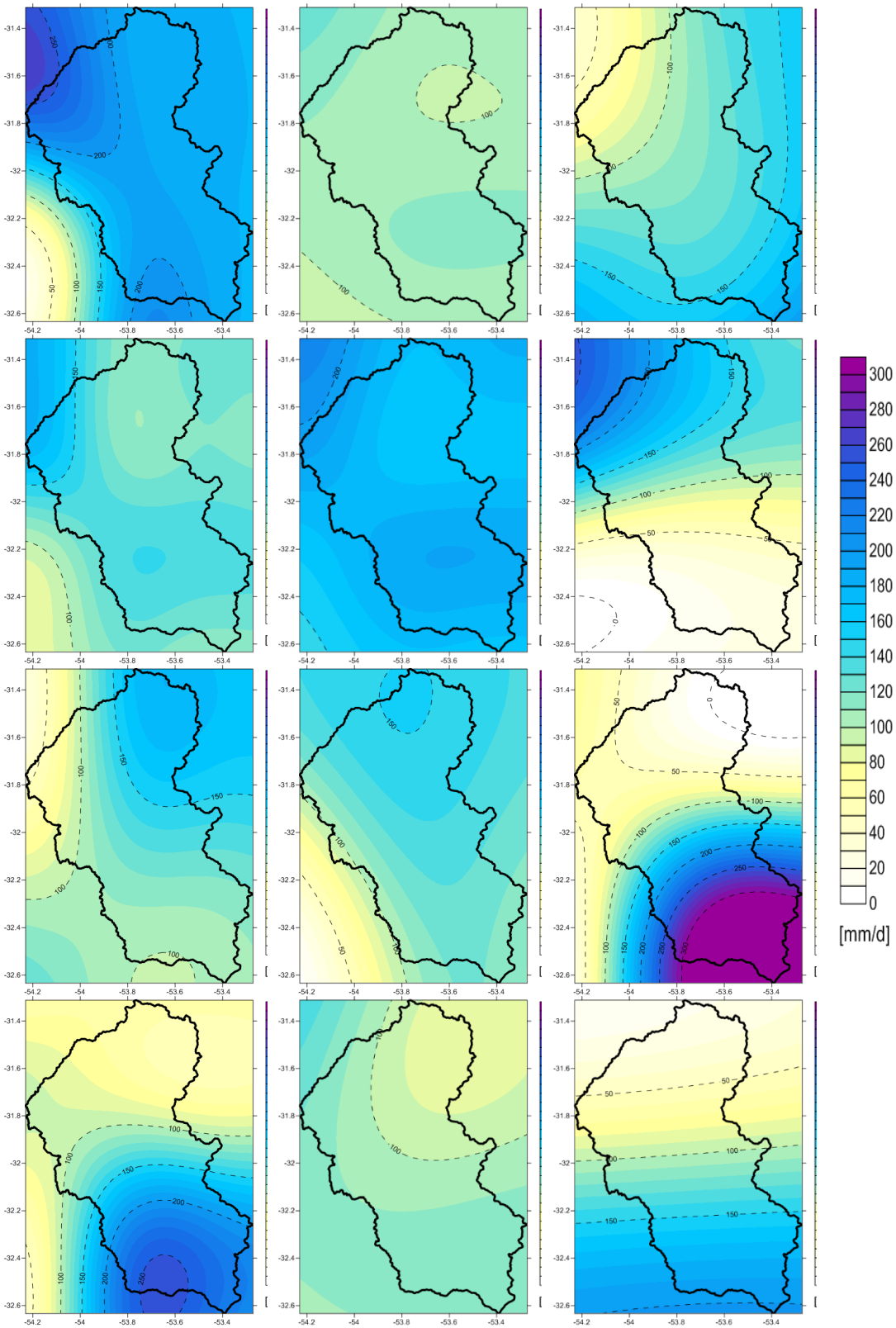


Figure 106. Illustration of stochastic precipitation events generated in an arbitrary watershed.

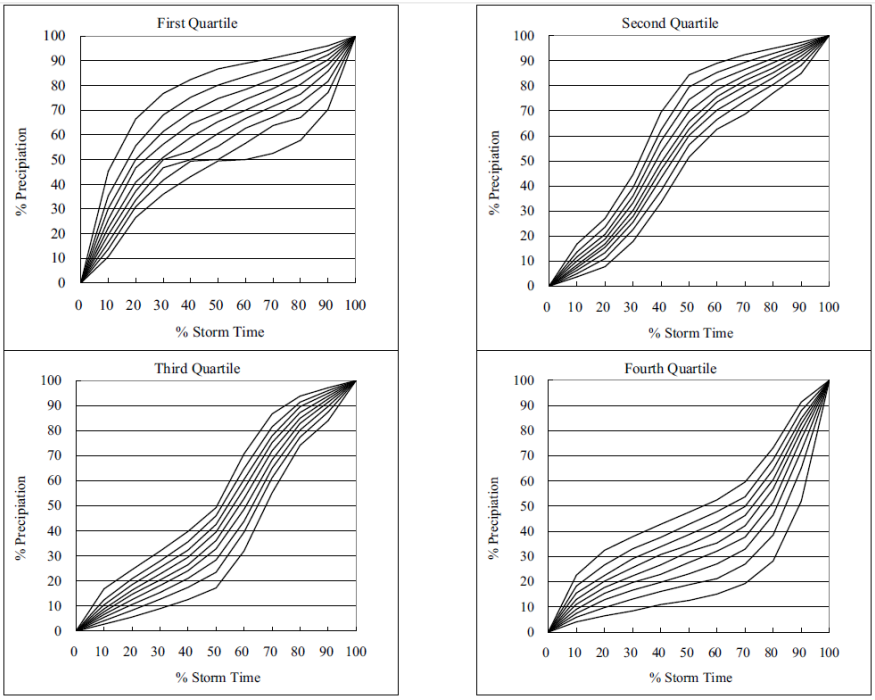


Figure 107. Example of Huff curves. Taken from Rao & Kao, 2006.

Huff curves, derived from intra-daily data (if available), are statistically built based on these quartiles. Once defined, the curves can be used to temporally distribute total daily rainfall into hourly values. The derivative of the Huff curve is the hyetograph, which expresses intensity over time (Figure 108). Huff curves are thus a powerful tool for synthesizing hyetographs from previously simulated daily data. As shown in Figure 109, rainfall events can be temporally distributed using Huff curves.

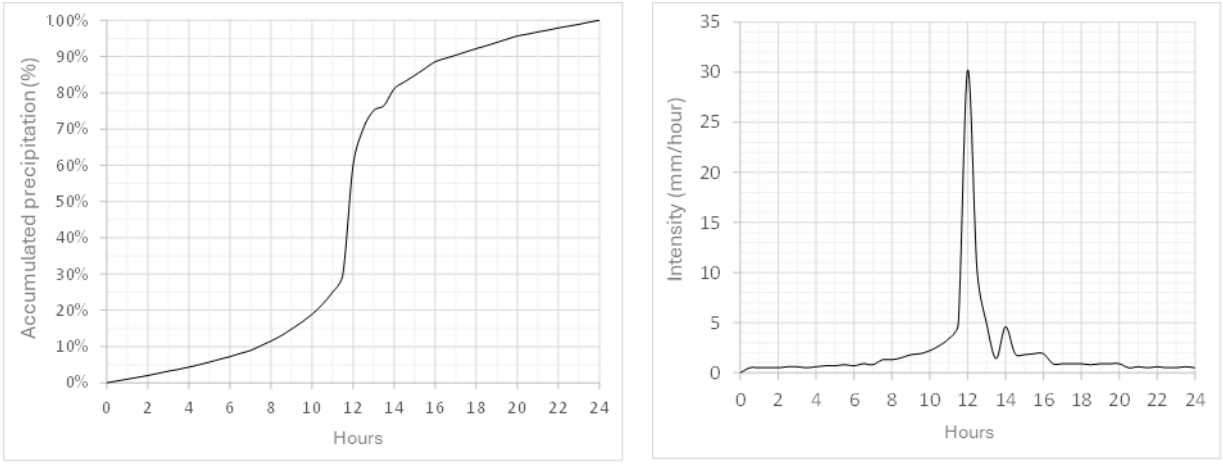


(a) (b)

Figure 108. (a) Huff curve. (b) Time derivative of the presented Huff curve.

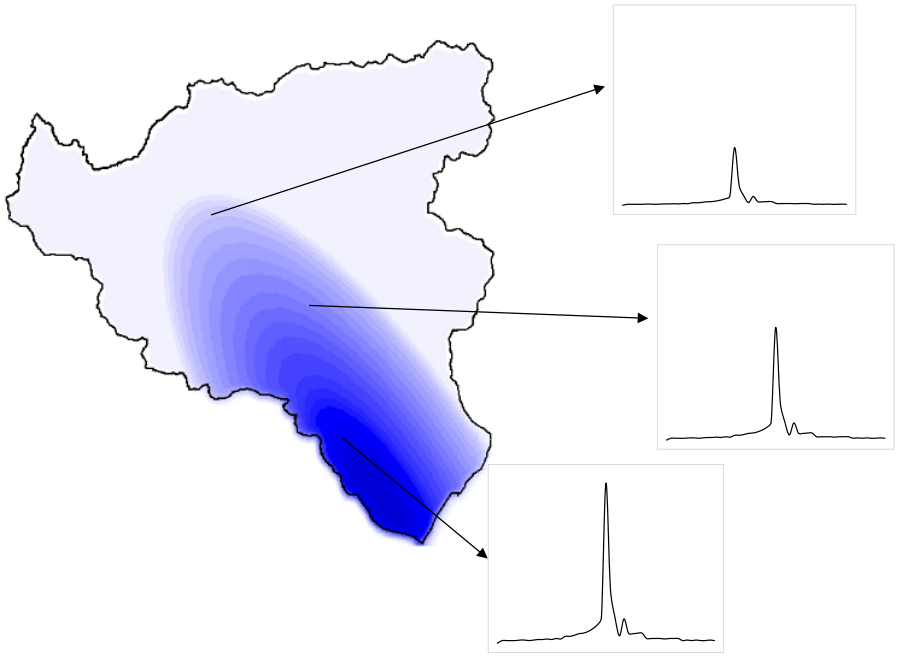

Figure 109. Ilustration of the temporal distribution of daily rainfall for a simulated rainstorm.

### 6.3.2 Estimating Runoff Volume

Once rainfall events are defined, input hydrographs for hydraulic modeling must be established. These are based on the effective precipitation volume that becomes surface runoff and reaches rivers and streams. *The Soil Conservation Service Curve Number (CN)* method is used to estimate runoff volume, a standard simplified infiltration model.

Effective precipitation corresponds to the remaining rainfall after subtracting infiltration, interception, and evapotranspiration processes. It is calculated as:

$$P_e = \frac{\left[P_m - \frac{508}{CN} + 5.08\right]^2}{P_m - \frac{2032}{CN} - 20.32} \qquad \text{Equation 2}$$

Where $P_e$ is the effective precipitation in cm, $P_m$ is the storm precipitation in cm, and $CN$ is the *curve number* based on land use, vegetation cover, and soil infiltration capacity. En la Table 37 lists *CN* values for different land covers and soil hydrologic groups (Chow et al., 1994). The application range for Equation 2, is:

$$P_m > \frac{508}{CN} + 5.08 \qquad \text{Equation 3}$$

Outside this range, effective precipitation is considered zero. It must also not exceed the total storm precipitation.

Table 37. *CN* values by land use and soil type[10]. (Soil Conservation Service, 1986)

| Land cover Type and Condition | A | B | C | D |
|---|---|---|---|---|
| Straight row crops - Good | 67 | 78 | 85 | 89 |
| Forest - Good | 30 | 55 | 70 | 77 |
| Grassland - Fair | 49 | 69 | 79 | 84 |
| Impervious surface | 100 | 100 | 100 | 100 |
| Residential district (1/8 acre) | 77 | 85 | 90 | 92 |
| Forest - Fair | 36 | 60 | 73 | 79 |
| Mixed forest and grassland - Good | 32 | 58 | 72 | 79 |
| Mixed forest and grassland - Fair | 43 | 65 | 76 | 82 |
| Residential district (1 acre) | 51 | 68 | 79 | 84 |
| Straight row cereals | 63 | 75 | 83 | 87 |
| Recently developed land | 77 | 86 | 91 | 94 |
| Urban district - Industrial | 81 | 88 | 91 | 93 |
| Paved streets with open gutters | 83 | 89 | 92 | 93 |
| Fallow (uncultivated) | 77 | 86 | 91 | 94 |
| Paved streets | 98 | 98 | 98 | 98 |
| Pasture | 30 | 58 | 71 | 78 |

### 6.3.3 Pluvial Flooding (Surface Water Accumulation)

The issue of pluvial flooding is modeled based on the potential for surface water accumulation, which is determined by the topography in terms of a topographic water accumulation potential, along with the infiltration rate at each point in the territory. The volume of water available for flooding is calculated as described in Section 6.3.2 (the infiltration model).

The topographic water accumulation potential is assessed by identifying areas of higher and lower susceptibility based on topographic features within a Digital Elevation Model (DEM), as illustrated in Figure 110.

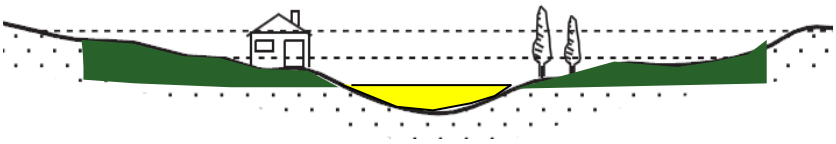

Figure 110. Illustration of areas with high (yellow), medium (green), or no (uncolored) accumulation potential.

The Topographic Accumulation Potential (TAP) is classified into three categories:

- High: Corresponds to topographic depressions.
- Medium: Corresponds to relatively flat sites.

[10] The soil types mentioned correspond to the Hydrologic Soil Groups defined by the United States Soil Conservation Service.

- Low: Corresponds to steep regions or hilltops.

For each node in the Digital Elevation Model (DEM), given its geographic location (X, Y), the accumulation potential is quantified by examining the four cardinal directions (north, south, east, and west). This search is bounded by the following parameters:

- $N_{max}$: Maximum horizontal distance within which the accumulation potential will be evaluated relative to a fixed location.
- *m*: Reference slope used to assess the accumulation potential of the site in relation to adjacent terrains.

Then, for each site (*X, Y*) in the DEM, a site (*K, L*) is sought such that the following condition holds:

$$Z_{K,L} \geq Z_{X,Y} + Z_{Lim} \quad \text{Equation 4}$$

where $Z_{Lim}$ is the required height difference between sites (*X, Y*) and (*K, L*) to obtain slope *m*.

If the site (*K, L*) exists, then site (*X, Y*) is classified as high accumulation, corresponding to a topographic depression. If this condition is not met, the mean topographic slope ($m_T$) between site (*X, Y*) and site (*K, L*) is calculated as:

$$m_T = \frac{Z_{X,Y} - Z_{K,L}}{D} \quad \text{Equation 5}$$

where *D* is the distance between sites (*X, Y*) and (*K, L*). If $|m_T| \leq m$, then site (*X, Y*) is classified as medium accumulation. Finally, if $|m_T| > m$, site (*X, Y*) is classified as low accumulation.

Figure 111 illustrates the identification of the accumulation potential along a terrain profile.

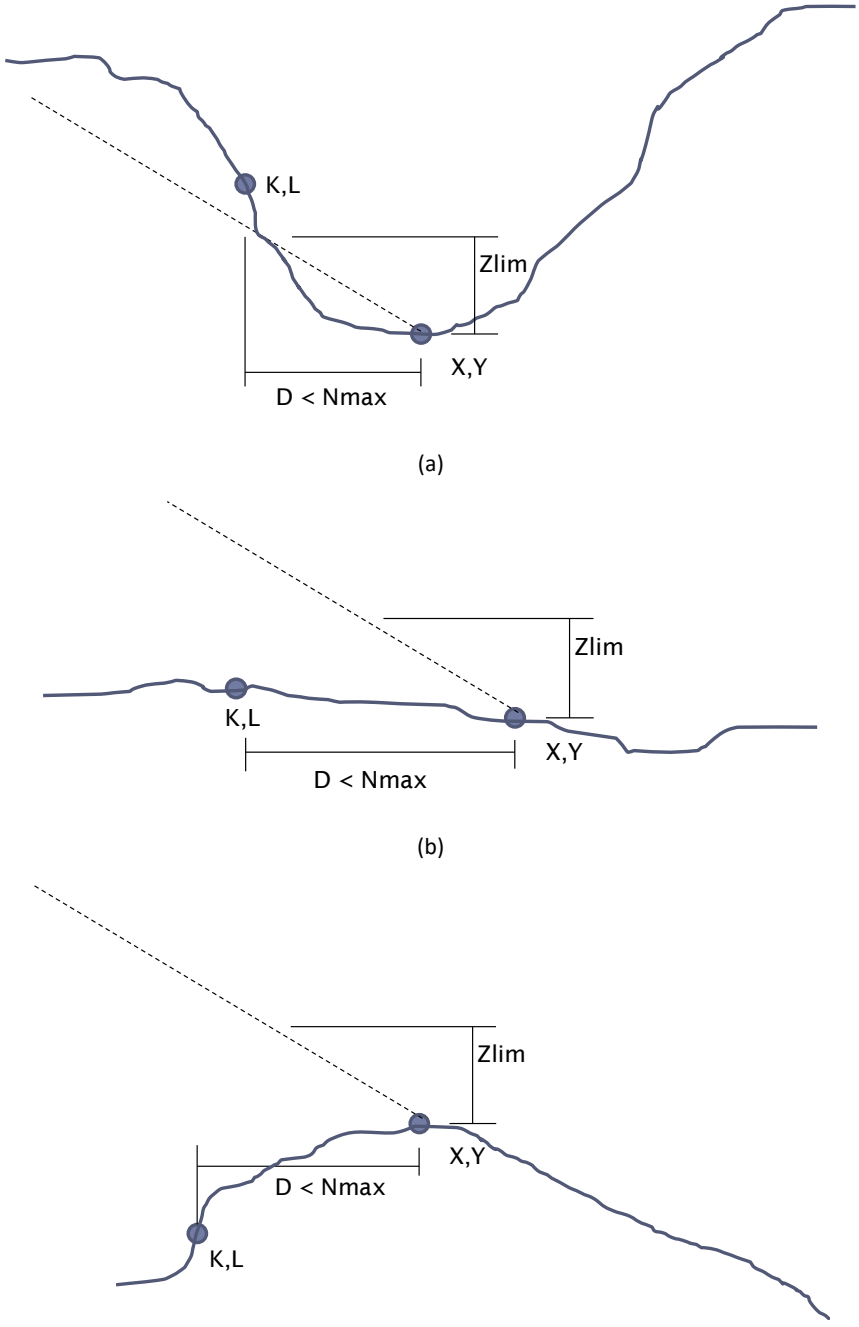


Figure 111. Illustration of TAP identification. a) Terrain with high accumulation. b) Terrain with medium accumulation. c) Terrain with low accumulation.

Once the Topographic Accumulation Potential (TAP) has been evaluated, the flood depth is calculated as a function of the effective precipitation (P_e), using the multipliers presented in Table 15.

Table 38. Multipliers of effective precipitation according to the Topographic Accumulation Potential (TAP)

| TAP | Multiplier of $P_e$ |
|---|---|
| High | 1.2 |
| Medium | 1.0 |
| Low | 0.0 |

### 6.3.4 Watershed Hydrological Response

Hydrographs are calculated using the Modified Clark model (Mod Clark; Kull & Feldman, 1998), a distributed hydrological response model that explicitly accounts for translation (movement of excess rainfall along the drainage system) and attenuation (discharge reduction due to water storage in the soil, surface, and channels) (Brunner & Bonner, 1994). Travel time variability from all watershed points to the outlet is incorporated.

The time it takes for a water droplet to reach the outlet is modeled with a travel time grid. For each cell:

$$t_{celda} = t_c \frac{d_{celda}}{d_{máx}} \quad \text{Equation 6}$$

Where $t_{cell}$ is the travel time from the cell, $t_c$ is the wathershed concentration time, $d_{cell}$ is the distance from cell to outlet, and $d_{máx}$ is the maximum distance from any cell to outlet. Various empirical formulas are jointly applied to determine $t_c$.

Each cell's runoff volume at each time step is routed using a linear reservoir model during the attenuation process. The continuity equation is:

$$\frac{dS}{dt} = I_t - O_t \quad \text{Equation 7}$$

Where $dS/dt$ is the change in storage over time, $I_t$ the inflow, and $O_t$ the outflow. In a linear reservoir, outflow is prooprtional to storage:

$$S = R \cdot O_t \quad \text{Equation 8}$$

Where $R$ is the reservoir coefficient. Combining and solving the equations using a finite difference approach yields:

$$O_t = C_A I_t + C_B O_{t-1} \quad \text{Equation 9}$$

where $C_A$ y $C_B$ are routing coefficients, which are calculated as follows:

$$C_A = \frac{\Delta t}{R + 0.5\Delta t} \quad \text{Equation 10}$$

$$C_B = 1 - C_A$$ Equation 11

The average outflow at time $t$ is:

$$\overline{O}_t = \frac{O_{t-1} + O_t}{2}$$ Equation 12

For each grid cell, the average outflow is calculated at every time step. The final hydrograph ($Q_t$) is the sum of all cell outflows:

$$Q_t = \sum_{i=1}^{Nceldas} \overline{O}_{i,t}$$ Equation 13

Figure 112 illustrates the Modified Clark rainfall-runoff model.

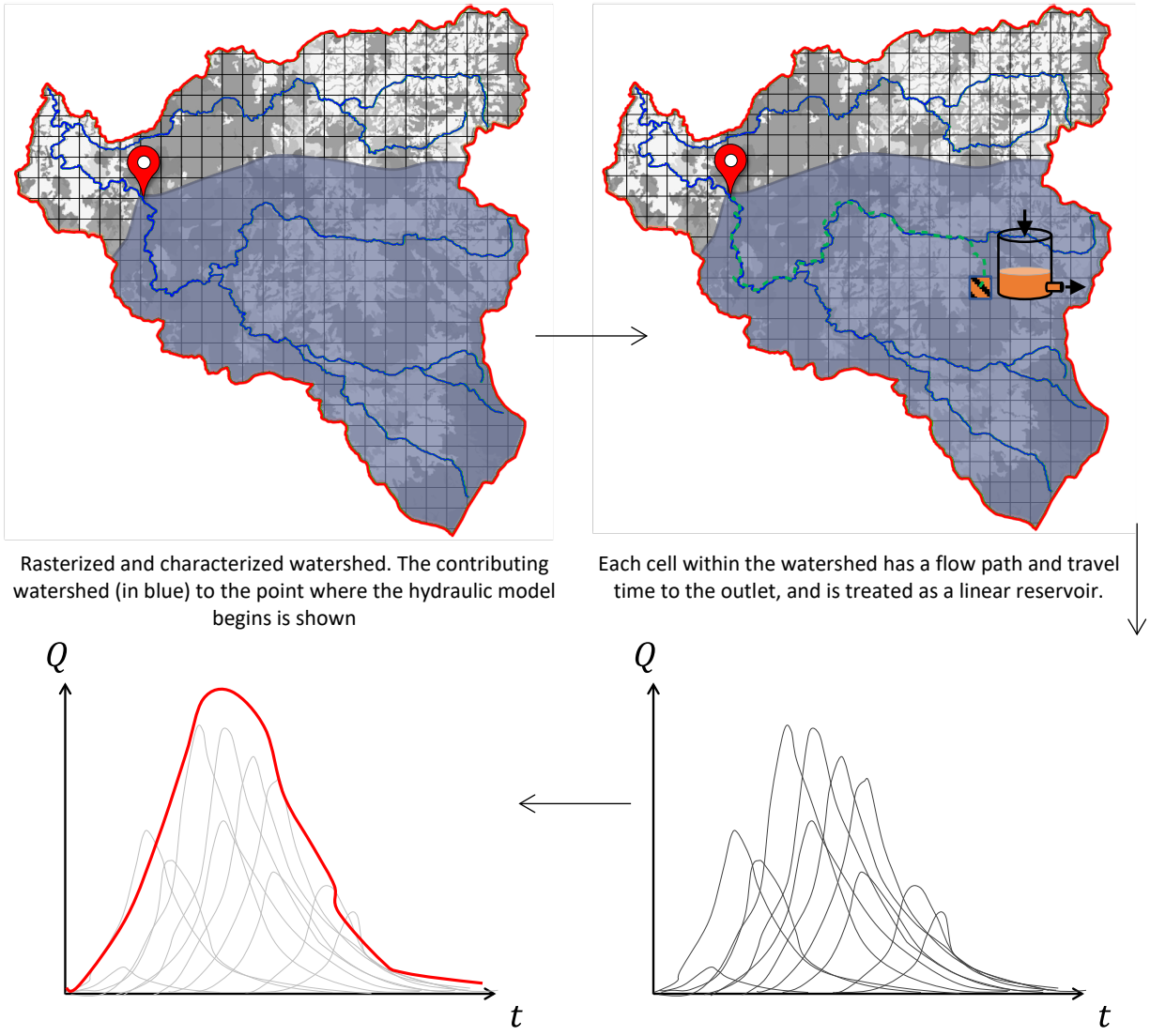


Rasterized and characterized watershed. The contributing watershed (in blue) to the point where the hydraulic model begins is shown

Each cell within the watershed has a flow path and travel time to the outlet, and is treated as a linear reservoir.

The sum of individual contributions forms the final simulated hydrograph.

Each cell thus generates a hydrograph at the outlet point of the contributing watershed.

Figure 112. Illustration of the modified Clark rainfall-runoff model.

### 6.3.5 Fluvial Flooding (River Overflow)

This section describes the hydraulic modeling that allows the routing of hydrographs calculated as watershed responses through river and stream channels.

#### *6.3.5.1 1D Model*

The goal of one-dimensional analysis is to solve water depth profiles along cross-sections of a river channel. It assumes unsteady, gradually varied, one-dimensional flow. The energy equation between two adjacent cross-sections, $ST_1$ and $ST_2$, is

$$Y_2 + Z_2 + \frac{\alpha_2 {V_2}^2}{2g} = Y_1 + Z_1 + \frac{\alpha_1 {V_1}^2}{2g} + h_e \quad \text{Equation 14}$$

Where $Y_1$ and $Y_2$ are water depth at sections $ST_1$ and $ST_2$ respectivelly, $Z_1$ and $Z_2$ are channel bed elevation at $ST_1$ and $ST_2$, $V_1$ and $V_2$ are average flow velocities (total discharge/total area), $\alpha_1$ and $\alpha_2$ are weighting coefficients, $g$ is gravity and $h_e$ is energy loss head. Energy loss head is defined as:

$$h_e = L\bar{S}_f + \mathrm{C}\left|\frac{\alpha_2 {V_2}^2}{2g} - \frac{\alpha_1 {V_1}^2}{2g}\right| \quad \text{Equation 15}$$

where $L$ is the weighted distance between cross-sections, $S_f$ is the representative friction slope and C is an expansion/contraction coefficient. Weighted distance and friction slope are:

$$L = \frac{L_{lob}\bar{Q}_{lob} + L_{ch}\bar{Q}_{ch} + L_{rob}\bar{Q}_{rob}}{\bar{Q}_{lob} + \bar{Q}_{ch} + \bar{Q}_{rob}} \quad \text{Equation 16}$$

$$S_f = \left(\frac{Q_1 + Q_2}{K_1 + K_2}\right)^2 \quad \text{Equation 17}$$

Where $L_{lob}$, $L_{ch}$ and $L_{rob}$ are distances along left overbank, main channel, and right overbank. $\overline{Q}_{lob}$, $\overline{Q}_{ch}$ and $\overline{Q}_{rob}$ are average discharges across those sections, $K_1$ and $K_2$ are conveyance values at cross-sections.

Conveyance and discharge per subdivision are:

$$Q = \mathrm{K}\sqrt{S_f} \quad \text{Equation 18}$$

$$K = \frac{1.486}{n} A R^{2/3} \quad \text{Equation 19}$$

where $K$ is conveyance, $n$ is the Manning's roughness coefficient, $A$ is the flow are, and $R$ the hydraulic radius.

#### 6.3.5.2 2D Model

The dynamic nature of floods and the movement of water into low-lying areas requires numerical models that incorporate two horizontal flow directions. The proposed method uses a two-dimensional model based on the conservation of momentum and continuity equations. Velocities are averaged over the vertical. The dynamic equations for momentum conservation are:

$$\frac{1}{g}\frac{\partial u}{\partial t} + \mathrm{u}\frac{\partial u}{\partial x} + \mathrm{v}\frac{\partial u}{\partial y} + \frac{n^2|u|u}{h^{4/3}} = -\frac{\partial h}{\partial x} - \frac{\partial z}{\partial x} \quad \text{Equation 20}$$

$$\frac{1}{g}\frac{\partial v}{\partial t} + \mathrm{u}\frac{\partial v}{\partial x} + \mathrm{v}\frac{\partial v}{\partial y} + \frac{n^2|v|v}{h^{4/3}} = -\frac{\partial h}{\partial y} - \frac{\partial z}{\partial y} \quad \text{Equation 21}$$

Where u and v are the velocity components $x$ and $y$ directions, $n$ eis Manning's roughness coefficient, $h$ is the free surface elevation relative to terrain and $t$ is time. The mass conservation (continuity) equation in two dimensions is:

$$\frac{\partial h}{\partial t} + \frac{\partial}{\partial x}\mathrm{uh} + \frac{\partial}{\partial y}\mathrm{vh} = 0 \qquad \text{Equation 22}$$

The floodplain area is divided into rectangular cells of length $\partial x$ and width $\partial y$. To calculate floodplain flows, the system of differential equations above is solved with appropriate initial and boundary conditions. Figure 110 shows an example of the 1D/2D hydraulic model conFiguretion for the Yaguarón River, Uruguay.

Figure 113. Example of the 1D/2D hydraulic model conFiguretion for the Yaguarón River, Uruguay.

## 6.4 Coastal Flood Hazard

Coastal flooding events are typically triggered by extreme meteorological phenomena capable of producing sea level surges along coastlines. Events such as hurricanes, although they do not directly impact Costa Rica's coasts[11], can generate storm surges that pose coastal flood risk. This study models coastal floods by considering hurricanes as the triggering phenomenon. Tsunamis are also considered in coastal flood evaluation, as described in Section 7.2.

[11] With the exception of Hurricane Otto in 2016.

Hurricane tracks consist of advisories issued every six hours indicating: date and time, geographic location of the cyclone's center, central pressure, and sustained wind speed over one minute at 10 meters above sea level. These advisories are typically issued by the U.S. National Hurricane Center for the entire North Atlantic basin. Figure 114 shows the track and advisories of Hurricane Otto (November 2016).

Figure 114. Track and advisories of Hurricane Otto

### 6.4.1 Hurricane Track Perturbation

For each hurricane track, a set of "*child*" tracks is generated using a two-dimensional Wiener process, whereby the historical track is artificially perturbed to create a new trajectory. This perturbation process is described in Equation 23:

$$\boldsymbol{x_s}(t_{k+1}) = \boldsymbol{x_s}(t_k) + \Delta \boldsymbol{X_{k,k+1}} + e \qquad \text{Equation 23}$$

Where $\boldsymbol{x_s}(t_k)$ is the position vector at time $t_k$, $\boldsymbol{x_s}(t_{k+1})$ is the position at $t_{k+1}$, $\Delta \boldsymbol{X_{k,k+1}}$ is the delta between $k$ and $k+1$, and $e$ is a normally distributed random variable with μ=0.0 and σ=0.5.

Simulated central pressures initially match those of the original hurricane and are then modified using the balance model proposed by Emanuel (2006), which considers atmospheric-oceanic parameters influencing a hurricane's lifecycle. This procedure allows artificial expansion of the hurricane catalog in the calculation region, enabling simulation of additional tracks not included in the original dataset. Typically, 100 child tracks are simulated per historical track.

Figure 112 illustrates perturbed tracks over a hypothetical territory.

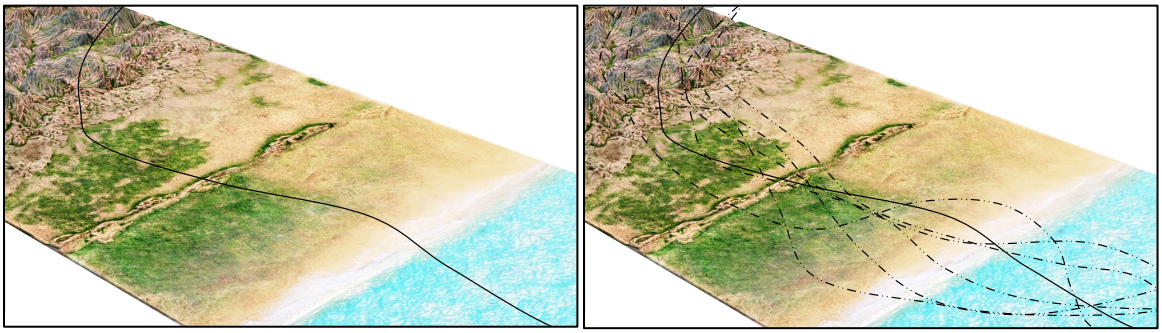

Figure 115 Illustration of trajectory perturbation over a hypothetical territory. From the original trajectory (left), a set of perturbed trajectories is generated (right)

### 6.4.2 Wind Field Modeling

Wind field modeling is crucial for evaluating storm surges, as wind shear is the main driver of sea level rise, especially at coastal zones located a moderate distance from the hurricane's center. Wind field modeling follows three steps (Vickery et al., 2009a):

1. Compute gradient wind speed from the hurricane's central pressure. This is the wind resulting from pressure gradient forces, initially neglecting surface friction and nonlinear effects.
2. Use a planetary boundary layer model to derive vertical wind speed profiles, factoring in surface roughness and average one-hour wind speed at 10 meters. Nonlinear friction effects are introduced as random perturbations.

The gradient wind speed ($v_G$) is calculated using Holland's model (1980):

$$v_G = \sqrt{\left(\frac{RMW}{r}\right)^B \cdot \frac{B \cdot \Delta P \cdot exp\left(-\left(\frac{RMW}{r}\right)^B\right)}{\rho} + \frac{r^2 f^2}{4}} - \frac{f \cdot r}{2} \qquad \text{Equation 24}$$

where $RMW$ is the radius to maximum winds, $r$ is the observation distance (i.e. the distance from the calculation site to the center of the storm), $\Delta P$ is the pressure gradient ($\Delta P = P_n - P_0$, where $P_n$ is the nominal atmospheric pressure, set at 1005 hPa), $\rho$ is air density, $f$ is the Coriolis parameter ($f = 2\Omega Sin\varphi$, where $\Omega$ is the Earth's angular rotation speed, and $\varphi$ is the latitude of the cyclone's eye, and $B$ is Holland's dimensionless parameter, a constant that defines the shape of the gradient wind profile and typically ranges between 0.7 and 2.2.

The radius of maximum winds ($RMW$) marks the point at which the gradient wind profile reaches its peak, measured from the center of the hurricane. Multiple approaches for calculating this parameter exist in the literature. In this study, the empirical equation proposed by Vickery & Whadera (2008) is applied.,

$$RMW = 3.015 - 6.291 \cdot 10^{-5}\Delta P + 0.0337\varphi \qquad \text{Equation 25}$$

To calculate Holland's parameter $B$, the formulation proposed by Vickery & Wadhera (2008) is used, as they found a sufficiently strong correlation between $B$ and a dimensionless parameter $A$ defined by them:

$$B = 1.732 - 2.237\sqrt{A}$$ Equation 26

$$A = \frac{RMW \cdot f}{\sqrt{2R_d T_s \cdot ln\left(1 + \frac{\Delta P}{P_0 \cdot e}\right)}}$$ Equation 27

where $R_d$ is the gas constant for air, $T_s$is the sea surface temperature (given in °K), and e is Euler's constant. For illustrative purposes, Figure 113 shows a wind field calculated for a stationary hurricane (i.e., with no forward motion), using the Holland model (1980) presented here. The resulting wind speed profile is symmetrical, leading to a wind field with circular contours. The calculated gradient wind corresponds to a sustained wind over a long period of time and is therefore associated with a one-hour duration.

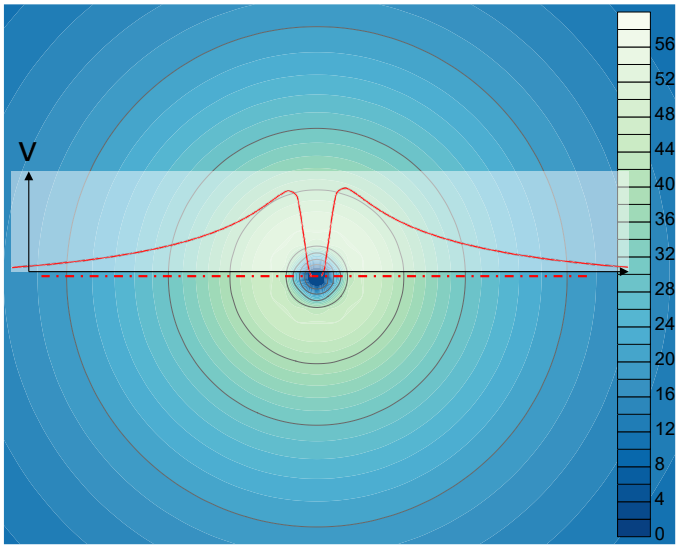


Figure 116. Gradient wind field of a stationary storm with a central pressure of 950 hPa. The wind speed profile shown is calculated using the Holland model (1980).

The gradient wind speed ($v_G$)) is adjusted to obtain the wind speed at ground level (actually at 10 meters above the surface) using a planetary boundary layer model. Vickery et al. (2009b) propose a model for the variation of the mean wind speed (over one hour), $u(z)$, as a function of the height above the surface, $z$, within the boundary layer, as follows:

$$u(z) = \frac{u_*}{k}\left[ln\left(\frac{z}{z_0}\right) - 0.4\left(\frac{z}{H^*}\right)^2\right]$$ Equation 28

where $k$ is the von Kármán constant ($k = 0.4$), $u_*$ is the friction velocity, $z_0$ is the aerodynamic roughness length, and $H^*$ is the height of the boundary layer, which can be modeled according to Vickery et al. (2009b) as follows:

$$H^* = 343.7 + \frac{0.26}{I}$$ Equation 29

where $I$ is the inertial stability, defined by Kepert (2001) as:

$$I = \sqrt{\left(f + \frac{2V_G}{r}\right)\left(f + \frac{V_G}{r} + \frac{\partial V_G}{\partial r}\right)}$$ Equation 30

Friction velocity $u_*$:

$$u_* = \sqrt{\frac{\tau}{\rho}}$$ Equation 31

where $\tau$ is the surface wind shear, defined as:

$$\tau = \rho \cdot C_d \cdot u^2$$ Equation 32

where $C_d$ is the drag coefficient and, $u$ is surface wind speed. The application of this boundary layer model results in logarithmic profiles of one-minute sustained wind speed variation with height above the surface. These profiles have been extensively validated against values recorded by drop sondes deployed over tropical cyclones during reconnaissance flights (see Vickery et al., 2009b for further details). Figure 117 shows three wind speed profiles calculated for different distances from the center of a cyclone with a central pressure of 930 hPa moving over open sea.

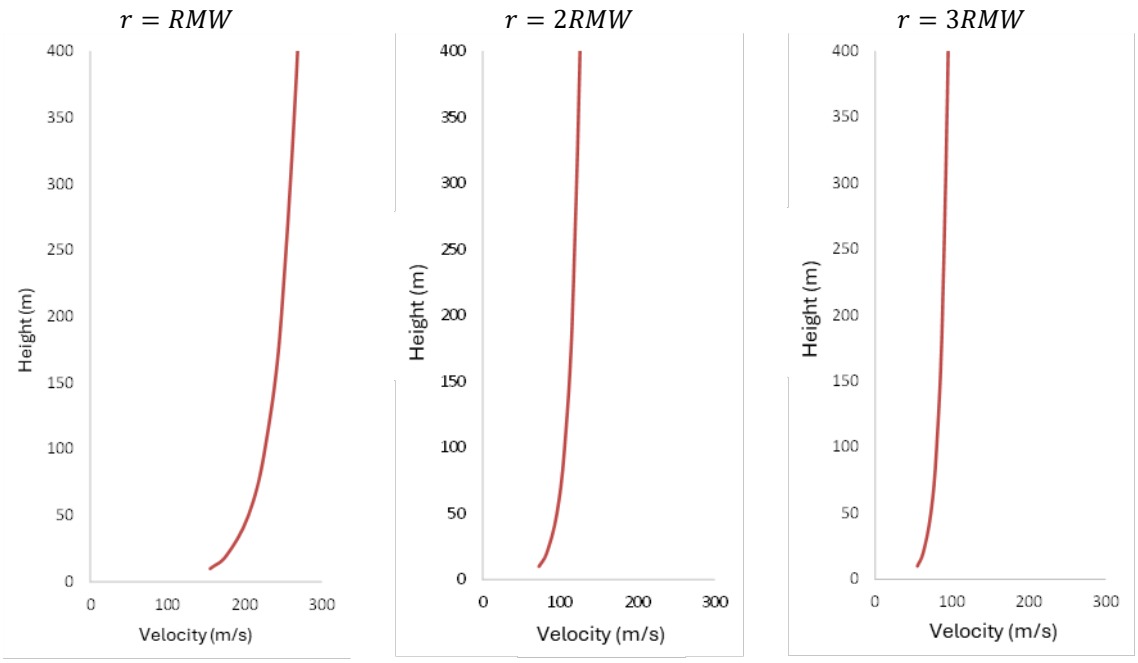


Figure 117. Logarithmic wind speed profiles calculated at different distances from the storm center for a hurricane with a central pressure of 930 hPa moving over open sea.

Surface roughness is associated with the size and density of obstacles to wind flow, which induce local turbulence and reduce surface wind speed. Surface roughness is directly incorporated into the boundary layer model through the parameters $z_0$ (aerodynamic roughness length) and $C_d$ (drag coefficient). Modifying these parameters affects the logarithmic wind profile, as illustrated in Figure 118.

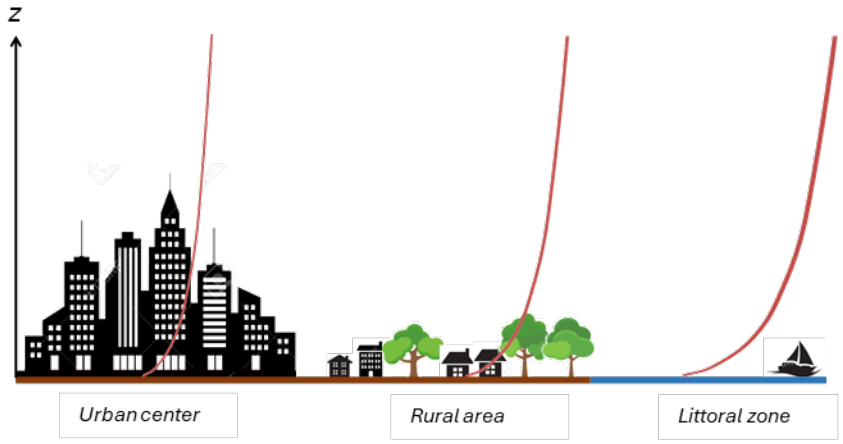


Figure 118. Illustration of the change induced in the logarithmic profile of the boundary layer model due to surface roughness.

Wind fields are defined geographically in terms of $v_{10}$. For each hurricane, multiple wind fields are simulated. At each grid point, probabilistic models are fitted, defining $v_{10}$ as a random variable.

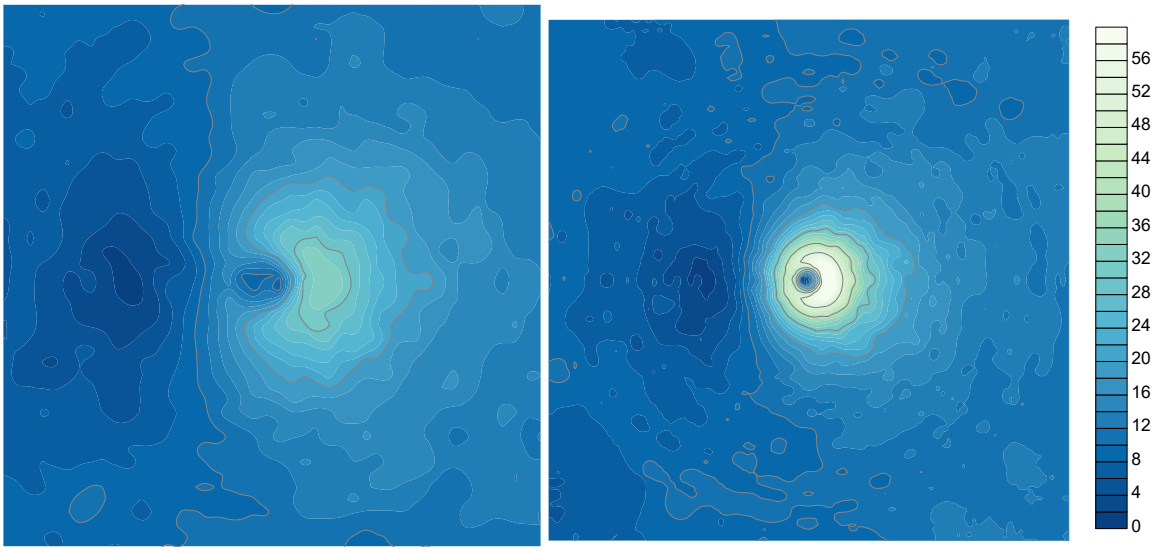


Figure 119. Examples of surface wind fields for hurricanes with a forward speed of 10 m/s moving northward and central pressures of 950 hPa (left) and 920 hPa (right).

### 6.4.3 Storm Surge Modeling

Storm surge is one of the most significant impacts of tropical cyclones on coastal zones. The rise in sea level is mainly caused by hurricane-induced wind shear, which pushes the ocean surface and generates an oceanic current that changes direction with depth due to Ekman spirals from the Coriolis effect. An additional contribution comes from the low atmospheric pressure at the storm center, which causes further sea level elevation. As the surge approaches the coast, local bathymetry amplifies the sea level rise, leading to flooding of extensive coastal areas. The total surge ($\eta$)) is the sum of the wind-induced surge ($\eta_C$) and the pressure-induced surge ($\eta_P$).

$$\eta = \eta_C + \eta_P \qquad \text{Equation 33}$$

The maximum wind-induced surge can be estimated using the model proposed by Tilburg and Garvine (2003), based on Ekman ocean circulation equations. The surge is computed at a specific coastal point, with the $x$ -direction aligned parallel to the continental shelf and the $y$ -direction perpendicular:

$$\eta_C = \int_0^L -\frac{fU_x}{g}\sqrt{\frac{\rho_a c_a U}{\rho \cdot c_b |U_x|}} + \frac{\rho_a c_a U_y U}{\rho g D(y)}\, dy \qquad \text{Equation 34}$$

Where $L$ is the width of the continental shelf, $\rho_a$ is air density, $c_a$ is the surface drag coefficient, $U$ is wind speed, $\rho$ is seawater density, $c_b$is seabed drag coefficient, $|U_x|$ is the component of wind parallel to the shelf, $U_y$is the perpendicular component, and $D(y)$ is the bathymetric profile.

The pressure-induced surge is modeled using the inverse barometric effect, where sea level rises approximately 1 cm for every 1 hPa drop in pressure:

$$\eta_P = \frac{\Delta P}{\rho \cdot g}$$ Equation 35

The pressure field associated with the cyclone is assumed symmetric and is defined as a function of central pressure and the radius to maximum winds.

$$P(r) = P_0 + (P_n - P_0)\, exp\left(-\frac{RMW}{r}\right)$$ Equation 36

Hydraulic modeling of tidal flooding along the coasts is commonly addressed through computational simulation, which—even in the two-dimensional case—requires very high computational costs as well as complex data preparation processes, such as continuous layers of topography and bathymetry or meshes generated over the terrain to be evaluated. For this reason, in this case, an approximate model has been implemented based on an algorithm that classifies cells as wet or dry, solving a simplified version of the two-dimensional flow equation in which the contribution of the inertia of the water volume in each terrain cell is neglected (see Gao et al., 2024):

$$\frac{\partial}{\partial x}\left(\eta + \frac{v^2}{2g}\right) = \frac{\tau_a - \tau_b}{\rho g d}$$ Equation 37

where $v$ is the flow velocity onshore, $\tau_a$ is the wind friction shear stress, $\tau_b$ is the bottom friction shear stress, and $d$ is the flood depth in the cell. Using a finite difference approach, the partial derivative shown can be simplified and evaluated discretely over a digital elevation model. Figure 120 illustrates the proposed iterative evaluation procedure for tidal flooding.

The proposed model has been compared with field observations as well as with simulations from hydrodynamic modeling systems, demonstrating a very good fit and high computational efficiency, making it the preferred solution for modeling multiple events within the catastrophic risk assessment framework.

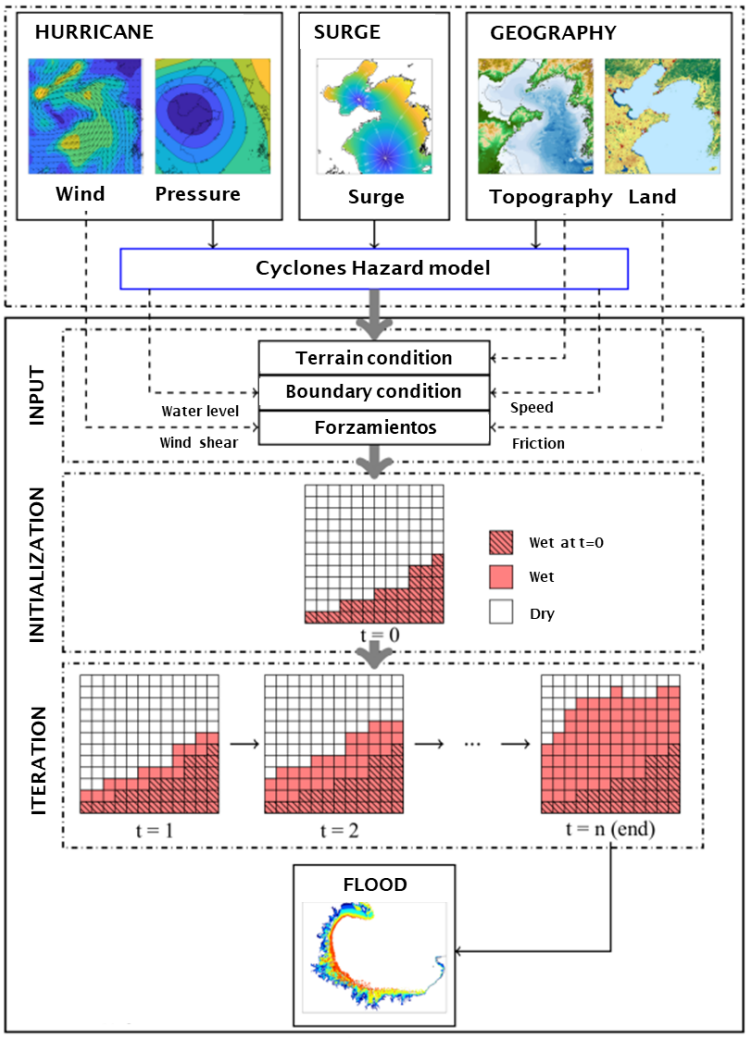


Figure 120. Conceptual framework of the tidal flooding model. Adapted from Gao et al., 2024.

# 7 PROBABILISTIC MODELING OF GEOLOGICAL HAZARDS

## 7.1 Earthquake

Due to existing uncertainties in aspects such as location, magnitude, and expected ground accelerations associated with future earthquakes, probabilistic methodologies are required to evaluate seismic hazard through numerical simulations of potential events. Although there is a shared conceptual framework for such evaluations, different choices can be made regarding geometric and seismicity models depending on the purpose of the analysis and the availability of information.

Generally, the probabilistic seismic hazard assessment (PSHA) follows four main steps: 1) Selection of the geometric model and tectonic zoning, 2) selection of the seismicity model and estimation of its parameters, selection of ground motion attenuation relationships and assignment to seismogenic sources and, 4) calculation of the seismic hazard.

### 7.1.1 Geometric Modeling

Based on existing studies of the tectonic environment of the study area, spatial domains are defined within which crustal ruptures may occur. These domains are typically represented by simple geometric shapes, such as oriented polygons, where earthquakes are assumed to occur. Each polygon defines a seismogenic source.

Each source is recursively subdivided into triangular sub-sources, as shown in Figure 121, while maintaining the same seismicity rate per unit area.

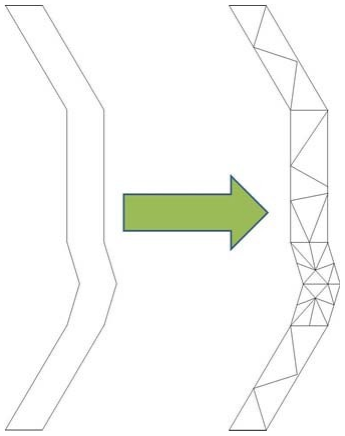

Figure 121. Subdivision of seismogenic sources into sub-sources

All relevant sources in the territory must be included in the modeling to capture all potential earthquake origins. As an example, the geometric model used in the ASLAC project (INGENIAR & ERN - Salgado et al., 2018) for Latin America and the Caribbean is shown.

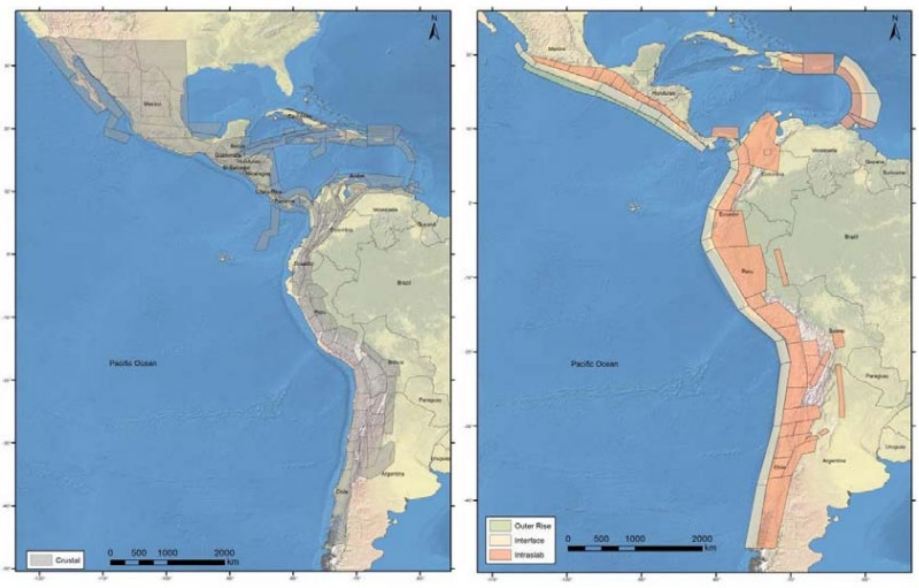


Figure 122. Geometric source model from the ASLAC project

### 7.1.2 Modeling seismicity

Seismicity modeling involves approximating the temporal occurrence of earthquakes for each source. Numerous seismicity models exist, with the main distinction being whether the process is stationary.

In seismic engineering, it is common to assume earthquakes follow a Poisson stochastic process. This assumption is valid in most cases, with few exceptions in specific regions.

Under the Poisson assumption, the modified Gutenberg-Richter model (Cornell and Van Marke) is often applied.

$$\lambda(M) = \lambda_0 \frac{e^{-\beta M} - e^{-\beta M_u}}{e^{-\beta M_0} - e^{-\beta M_u}}$$ Equation 38

Where $\lambda(M)$ is the annual recurrence rate for earthquakes with magnitude equal to or greater than $M_0$, $\lambda_0$ is the annual occurrence rate for magnitudes ≥ $M_0$ *(usually 4.0)*, $\beta$ is the exponential distribution parameter, and $M_u$ is the upper-bound magnitude.

The parameters $\lambda_0$ and $\beta$ are estimated using statistical analysis of the seismic catalog, after verifying data completeness and removing aftershocks. Using the maximum likelihood method:

$$\lambda_0 = \frac{N}{t}$$ Equation 39

$$\beta = \frac{N}{\sum_{i=1}^{N} M_i - M_0}$$ Equation 40

Here, $N$ is the number of events associated with the source and $t$ is the observation period.

### 7.1.3 Ground Motion Attenuation Modeling

Once the potential locations of earthquakes have been defined using the geometric model, and the activity rate of sources determined by the seismicity model, a strong ground motion attenuation model must be incorporated. This model accounts for the propagation of seismic waves through the Earth's crust and the associated energy loss from the rupture zone to the location of the exposed elements on the surface.

An attenuation model describes how a given intensity measure—such as peak ground acceleration (PGA) or spectral acceleration—varies as a function of earthquake magnitude and distance. Figure 123 presents an example of such a function. For a specific magnitude and distance, these models provide a probability distribution of acceleration.

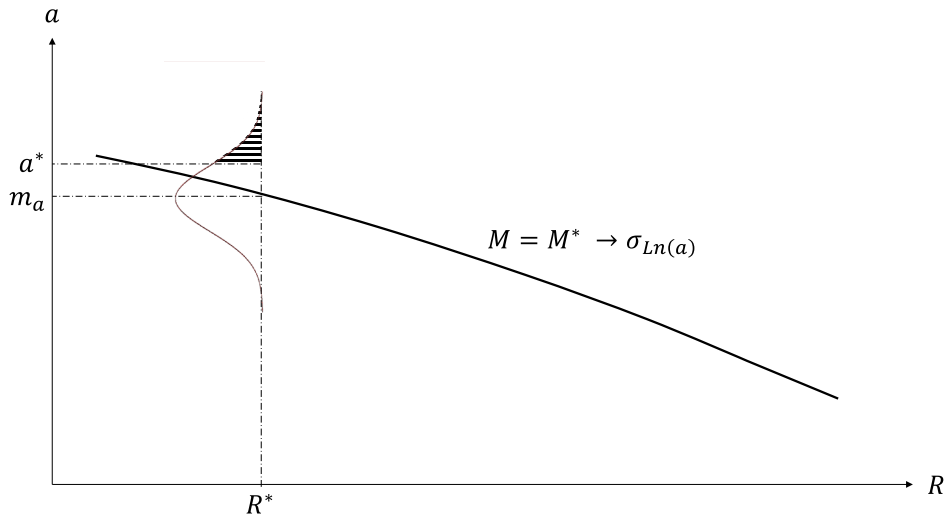


Figure 123. Example of a strong ground motion attenuation model.

The probability that ground motion exceeds a certain threshold $a^*$, given an event of magnitude $M^*$ at distance $R^*$, is calculated using:

$$P(a > a^* | M^*, R^*) = 1 - \Phi\left[\frac{Ln(a^*) - Ln(m_a)}{\sigma_{Ln(a)}}\right] \quad \text{Equation 41}$$

Where $\Phi(\cdot)$ is the standard normal distribution function, $m_a$ is the median ground acceleration, and $\sigma_{Ln(a)}$ is the standard deviation of the natural logarithm of acceleration.

There is a wide array of attenuation models in scientific literature. For this study, the selection of attenuation models will be based on those previously applied in recent seismic hazard assessments for Costa Rica, ensuring compatibility with local geological and tectonic characteristics.

### 7.1.4 Seismic Hazard Calculation

The hazard calculation is based on a spatial integration procedure that accounts for the various possible earthquake locations, with hypocenters defined at the centroids of the generated sub-sources. The annual

exceedance rate of an arbitrary intensity level $a*$, denoted as v(a*), is calculated using the following equation:

$$v(a^*) = \sum_{j=1}^{N} \sum_{i=1}^{n_j} \int_{M_0}^{M_u} -P(a > a^* | M, R) \cdot \frac{d\lambda(M)_{SF_{j,i}}}{dM} \qquad \text{Equation 42}$$

Here, *N* represents the number of sources in the model, and nj is the number of sub-elements into which source *j* has been divided. This equation is one of the many forms derived from the law of total probability. By applying these concepts, it is possible to determine exceedance rates for any intensity measure and generate standard hazard representations, such as uniform hazard maps or spectra.

## 7.2 Tsunami hazard

Tsunamis are gravity waves generated in the ocean when a triggering phenomenon causes the vertical displacement of a large water mass. These waves can travel thousands of kilometers and impact coastlines across multiple continents. There are different types of tsunamis, mainly classified by their triggering mechanism. In this study, only those associated with tectonic processes of the Earth's crust—commonly referred to as tectonic tsunamis—are considered.

Three key processes are involved in tsunami hazard: (i) generation, (ii) propagation, and (iii) run-up. Generation refers to the conditions under which vertical displacement of ocean water initiates gravity waves. Propagation describes how these waves travel across the ocean basin. Run-up involves the amplification of tsunami wave heights as they approach shallow coastal waters due to bathymetric effects

### 7.2.1 Generation

Modeling the generation mechanism of tectonic tsunamis requires considering two essential aspects: (i) the coupling between the elastic solid medium of the Earth's crust and the liquid medium of the ocean, and (ii) the relationship between vertical displacements of the ocean surface and the seabed.

#### *7.2.1.1 Earth-Ocean Coupling*

Tsunami generation is associated with the behavior of the water–seabed system, specifically how seismic waves influence the hydrodynamic waves that result. This can be approached through two different frameworks:

In a coupled system, seismic waves traveling through the crust influence the behavior of the overlying water column. This approach requires considering the variations in seabed shape within the tsunami propagation analysis.

In a decoupled system, there is no direct interaction between crustal deformation and water movement. Elastic deformations of the seabed due to seismic waves are considered negligible. When the coseismic seabed displacement is significant, it is commonly modeled as a rigid seabed with a shape matching the maximum elastic deformation induced by the earthquake.

These approaches have been evaluated by several authors using formulations based on Rayleigh wave theory. Ward (1980) and Okal (1988) extended the free spherical oscillation framework of Rayleigh to address tsunami generation and propagation in spherical coordinates.

#### *7.2.1.2 Seabed and Ocean Surface Displacement*

The standard assumption for determining the initial displacement of the ocean surface is that it matches the vertical displacement of the seabed. In this study, the seabed deformation resulting from crustal rupture is calculated using the formulation developed by Odaka (1985). Okada (1985), building on Volterra's dislocation theory, developed an analytical solution to compute displacement in an elastic medium due to a fault rupture. This formulation has been widely adopted for tsunami propagation modeling. The vertical deformation field ζ is calculated as follows:

$$\zeta = \left(-\frac{U_\phi}{2\pi}\left[\frac{3xdq}{R^5} + I_\phi \sin\delta\right] - \frac{U_\delta}{2\pi}\left[\frac{3dpq}{R^5} + I_\delta \sin\delta\cos\delta\right]\right)\Delta\Sigma \qquad \text{Equation 43}$$

Where $U_\phi$ is the strike-slip displacement, $U_\delta$ is the dip-slip displacement, $d$ is the source depth, $p$ and $q$ are functions of the dip angle, $I_\phi$ and $I_\delta$ are functions dependent on the site location and Lamé constants, and $\Delta\Sigma$ is the rupture area. Figure 124shows an example of a vertical seabed deformation field computed using Odaka's (1985) formulation for a Mw 7.0 earthquake with eastward strike and a focal depth of 5 km.

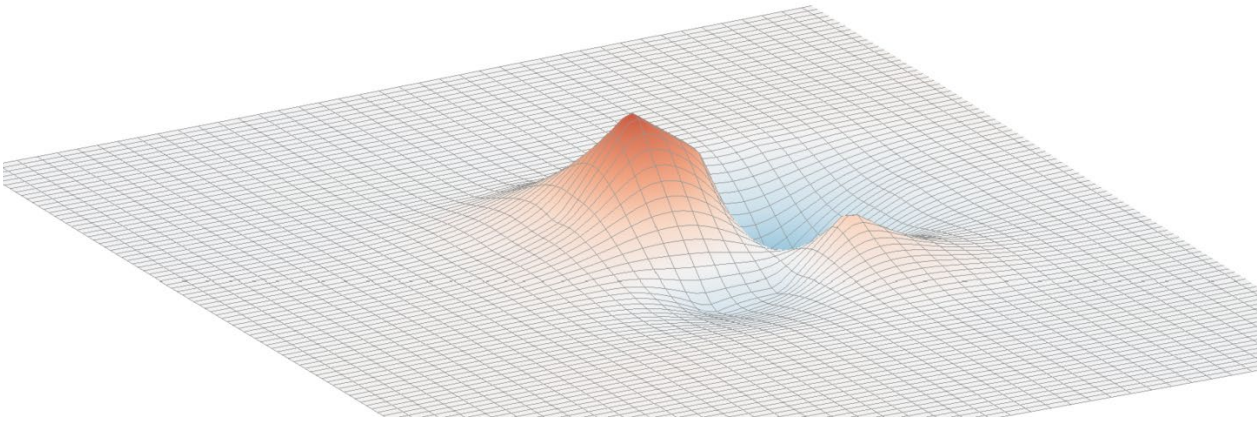

Figure 124. Vertical seabed deformation for a Mw 7.0 earthquake with eastward strike and 5 km depth.

### 7.2.2 Propagation

The propagation of tsunami waves across the ocean is generally modeled using shallow water wave theory. These are also known as gravity waves, since gravity acts as the restoring force in the medium. When gravity waves travel in a medium where the wavelength is much greater than the depth, the resulting vertical acceleration is negligible compared to gravity. This means the horizontal velocity of the water column is nearly constant from the seafloor to the surface—this is the defining characteristic of long waves or shallow-water waves.

In the case of tsunamis, ocean depths are typically around 5 km, while tsunami wavelengths can span several hundred kilometers. As a result, the long wave approximation is sufficiently valid to characterize tsunami energy propagation in the open ocean.

The mathematical development of shallow water wave theory is based on Stokes' formulation, which describes the one-dimensional motion of an inviscid fluid subject to constant gravitational force, bounded by a rigid bottom and a free surface. Although Stokes' equations have been known for over 150 years, no general analytical solution exists. Therefore, specialized formulations have been developed under simplifying assumptions for specific cases. For tsunami modeling, the relevant scenario involves long waves with small amplitudes, propagating in one direction in an incompressible medium with constant shallow depth.

Several mathematical models have been proposed under these conditions, including those by Boussinesq (1871), Korteweg and de Vries (1895), Kadomtsev and Petviashvili (1970), and Camassa and Holm (1993).

Using the theoretical framework of Korteweg and de Vries (1895), the dislocation model by Okada (1985), and nonlinear shallow water wave equations, Dutykh & Dias (2007) proposed an integral solution for the combined problem of tsunami generation and propagation. This formulation allows the calculation of water surface elevation, wave velocity, and seabed pressure at different times and locations, as a function of the seismic source geometry, average ocean depth, and a dislocation function that characterizes the coseismic seabed displacement.

$$\eta(x,y,t) = \frac{1}{(2\pi)^2} \iint_{\mathbb{R}^2} \frac{e^{i(kx+ly)}}{cosh(mH)} \int_0^t (1 - \omega \, sin\, \omega\tau) \bar{\zeta}(k,l,t-\tau) d\tau dk dl \qquad \text{Equation 44}$$

Where $k$ and $l$ are wave numbers in the $x$ and $y$ directions, $m = \sqrt{k^2 + l^2}$, $\omega = \sqrt{gm \tanh(mH)}$, $H$ is ocean depth, and $\bar{\zeta}$ is the combined Fourier-Laplace transform of the seabed deformation function. Figure 125 illustrates wave elevation propagation computed using the Dutykh & Dias (2007) model for the earthquake previously described in Figure 120.

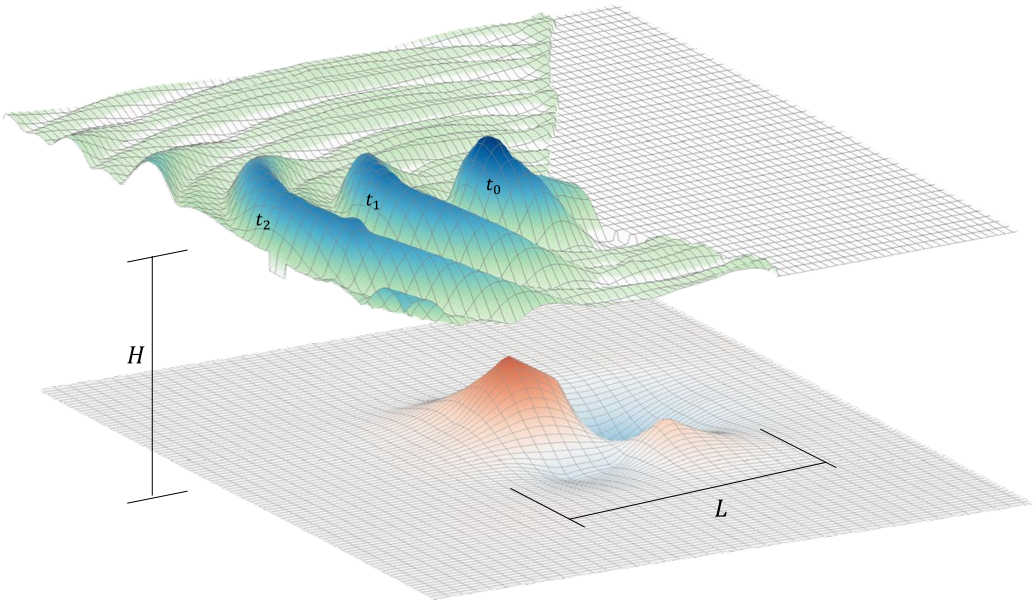


Figure 125. Simulation of tsunami wave elevation η at three time steps ($t_0$, $t_1$, $t_2$), for the earthquake in Figure 124, using the model by Dutykh & Dias (2007).

### 7.2.3 Run-Up

In deep ocean waters, tsunami wave amplitudes are low and practically imperceptible. However, as the waves approach the shore, their amplitude increases dramatically, resulting in large and destructive coastal waves. This amplification is due to the decreasing water depth near the coast.

In deep water, gravity waves travel at a speed equal to $\sqrt{gH}$, where $H$ is ocean depth and $g$ is gravitational acceleration. As long waves, their speed remains nearly constant in the deep ocean. As the tsunami wave enters shallower regions, the front slows down due to reduced depth, while the rear of the wave—still in deeper water—continues at a faster speed. This causes the wavelength to compress horizontally. Because of water's near-incompressibility, this compression results in a rapid increase in wave amplitude at the front, generating powerful surges upon landfall.

Several analytical models exist to solve the run-up problem. These are widely used to estimate coastal wave heights due to tsunamis and are based on the following assumptions:

- Wave breaking effects at the shoreline are neglected.
- Energy dissipation at the seabed is ignored.
- Total wave reflection at the shoreline is assumed; the shoreline remains fixed.
- The waves are treated as periodic gravity waves, neglecting the transient nature of tsunamis.
- The seabed slope is assumed to be constant.

Based on these premises, Madsen & Fuhrman (2007) proposed a method to estimate wave height at the shoreline and its onshore velocity:

$$\frac{R}{a_0} = 2\pi^{3/4}\left(\frac{a_0}{h_0}\right)^{-1/4}\xi^{-1/2} \qquad \text{Equation 45}$$

$$\frac{U}{\sqrt{g \cdot a_0}} = \frac{\sqrt{\pi}}{\xi}\left(\frac{R}{a_0}\right) \qquad \text{Equation 46}$$

Where $R$ is the run-up amplitude at the coast, $U$ is the onshore velocity, $a_0$ is the offshore wave amplitude, $h_0$ is the offshore water depth, and $\xi$ is the *surf parameter*, also known as the *Iribarren number*, defined by Iribarren & Nogales (1948) as,

$$\xi \equiv \frac{s}{\sqrt{\frac{h_0}{L}}} \qquad \text{Equation 47}$$

Where $L$ is the offshore tsunami wavelength and $s$ is the mean bathymetric slope. When $s$ is very small, the equations tend toward infinity. This means that extremely steep bathymetric profiles make the solution invalid, as wave amplitudes cannot increase indefinitely. This constraint, known as the breaking criterion, was described by Carrier and Greenspan (1958). Madsen and Fuhrman (2007) expressed it in terms of the Iribarren number:

$$\frac{R}{a_0} \leq \frac{R_{max}}{a_0} = \frac{1}{\pi}\xi^2 \qquad \text{Equation 48}$$

Where $R_{max}$ is the maximum amplitude the wave can reach under the conditions defined by $\xi$. Figure 126 shows the variation in wave run-up $R$ and onshore velocity $U$ with the Iribarren number, and how the breaking criterion defines the model's limit of validity.

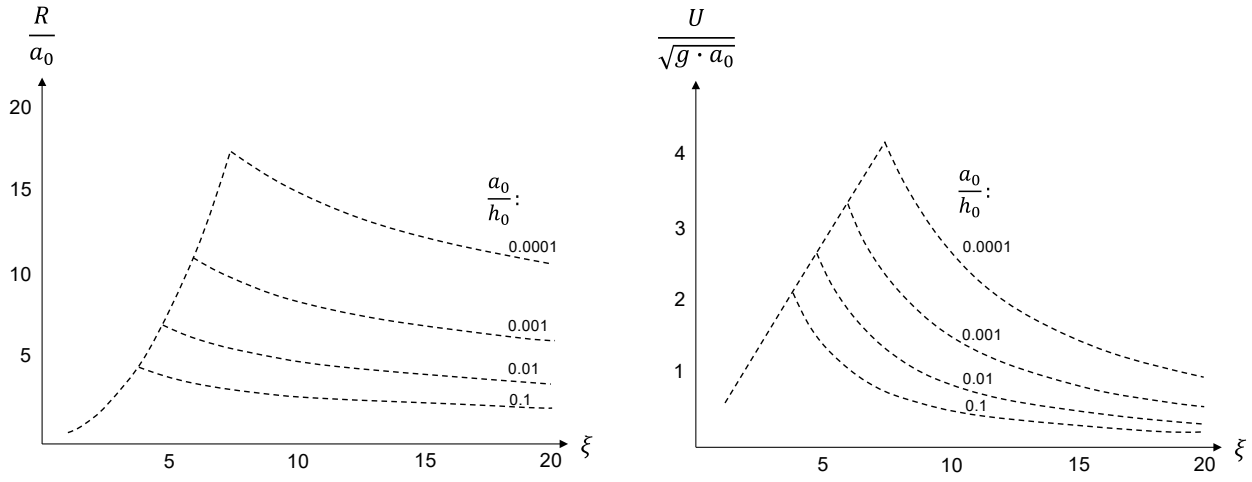


Figure 126. Variation of run-up amplitude $R$ and onshore velocity $U$ with the Iribarren number, including the breaking criterion as a limit of validity. Adapted from Madsen & Fuhrman (2007)

The hydraulic flow of wave amplitude will be modeled using the conceptual framework of the iterative wet and dry cell classification model presented in section 6.4.3, omitting the term related to surface wind shear, which does not apply in this context.

## 7.3 Volcanic Eruptions Hazard

### 7.3.1 Emission Source Location

In volcanic hazard modeling, it is essential to define the exact location from which material will be expelled into the atmosphere, in terms of both geographic position and opening probability. For most volcanoes, this definition is relatively straightforward, as they typically release material through the main crater. If the volcano under study has only one known crater and vent, and there is no evidence of magma intrusion elsewhere in the volcanic edifice, then the emission point will be that crater, with an opening probability equal to 1.

In cases where emission points other than the main crater are known, each of them could potentially release material during an eruption. In fact, material could be expelled from all points simultaneously in a single eruptive event. Quantifying the opening probability of each site can be a complex task, especially when limited information is available. What is important to acknowledge is that, during an eruptive episode, material may be emitted from one, several, or all of the identified emission points, meaning that their joint opening probabilities are greater than zero.

The above is valid as long as the emission points are clearly identified on the volcanic edifice. However, when the volcanic structure does not show clear evidence of the possible location of an emission point, it is possible to make inferences that lead to a spatial probability estimate of opening across the edifice. To quantify this spatial probability, the area is rasterized, and possible emission point locations are assigned based on existing geological evidence. This means that some locations will have a higher probability of becoming an emission point than others.

For each selected location, a kernel function is defined to describe the probability density of opening around that potential emission point. The procedure assigns the highest susceptibility values to the base points of the mesh (identified emission points) and generates a susceptibility grid using probability distribution surfaces. These are built by revolving normal probability density functions around the vertical axis and centering them on each base point. The result is a susceptibility mesh for the opening of emission points, as illustrated in Figure 127.

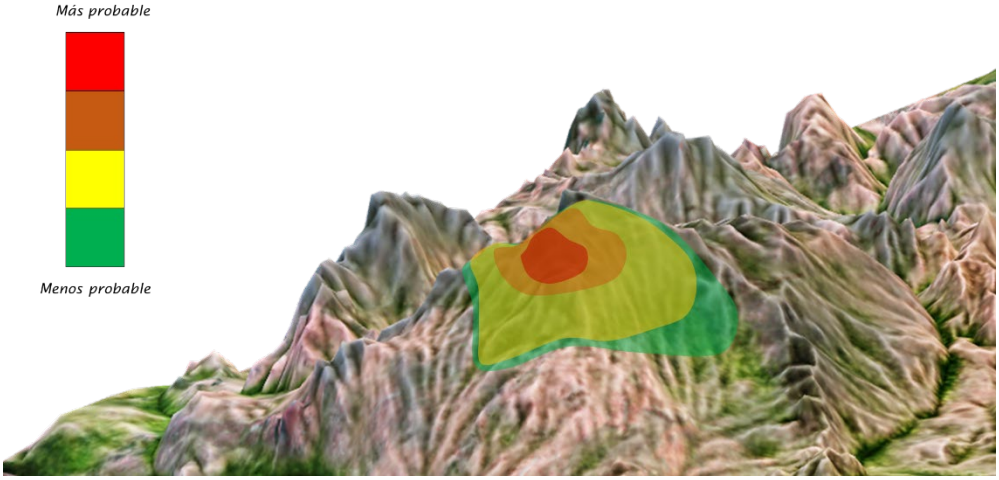


Figure 127. Illustration of the measurement of opening susceptibility on a volcanic edifice

### 7.3.2 Modeling of Wind-Transported Tephra Fallout

Pyroclastic fallout deposits result from the dispersal of volcanic material lofted into the eruption column and subsequently carried by atmospheric winds, followed by vertical settling due to gravity. Tephra fragments are classified by size, commonly using the $\phi$-scale in volcanology, which relates to the equivalent diameter of the particles (see Equation 49), and provides a standardized metric for categorizing particle sizes.

$$d = 2^{-\phi}$$ Equation 49

Tephra is classified into blocks or bombs, lapilli, coarse ash, and fine ash, as shown in Table 16. Blocks and bombs are larger than 64 mm in diameter ($\phi$ < –6). Blocks have irregular edges, indicating solid-state ejection, while bombs have rounded edges, indicating ejection in a molten state. Lapilli include fragments between 2 mm and 64 mm ($\phi$ between –6 and –1). Coarse ash ranges from 2 mm to 0.063 mm ($\phi$ from –1 to 4), and fine ash comprises particles smaller than 0.063 mm ($\phi$ > 4). Generally, blocks and bombs are not transported by wind and instead fall close to the vent along ballistic trajectories (see Section 7.3.3). Therefore, wind-transport modeling focuses on lapilli, coarse ash, and fine ash.

Table 39. Reference classification of tephra sizes (adapted from Mullineaux, 2013)

| Type | $\phi$ | $d = 2^{-\phi}$ | Size Reference |
|---|---|---|---|
| Blocks and Bombs | < -6 | > 64 mm |   |
| Lapilli | > -6 | < 64 mm |   |
| Coarse Ash | > -1 | < 2 mm |   |
| Fine Ash | > 4 | < 0.063 mm | 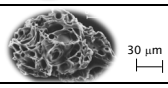  |

Observations of post-eruption tephra deposits reveal that larger fragments fall near the vent, while finer particles can travel great distances. The final location of a particle depends on its size, its initial position within the eruption column, and wind field characteristics. Windborne transport is typically modeled as an *advection-diffusion-sedimentation* process, the most widely accepted global approach for simulating tephra fallout. This model assumes the particle's final position is determined by wind advection, atmospheric turbulence, and gravitational settling, described by the following vector differential equation:

$$\frac{\partial C}{\partial t} = -\nabla uC + \nabla(k\nabla C) - \nabla u_s C + S_0 \qquad \text{Equation 50}$$

In this equation, *C(x, y, z, t)* represents the mass concentration of particles of a given size $\phi$ at a specific location and time. The vector $u_s$ is the three-dimensional wind velocity field, which drives horizontal transport. The tensor *k* denotes the atmospheric turbulent diffusivity, accounting for dispersion due to turbulent mixing. The vector $u_s$ is the terminal fall velocity of the particles, which points vertically downward and varies with particle size and air density. Finally, $S_0$ *(x, y, z, t)* is a source term describing the initial distribution of particles released into the atmosphere from the eruption column. The first term on the right-hand side ($-\nabla uC$) represents advective transport by the wind, the second term ($\nabla(k\nabla C)$) models turbulent diffusion, the third term ($-\nabla u_s C$) accounts for gravitational settling, and the last term ($S_0$) injects mass into the system. Since the behavior of each particle size class differs, Equation 50 must be solved independently for each $\phi$ value. Moreover, this modeling approach is valid only within the troposphere and should not be extended to simulate transport within the stratosphere.

To apply this model, an initial distribution of particle concentration in the eruption column must be specified, which varies by $\phi$. This work uses the formulation by Armienti et al. (1988):

$$M_\phi(z) = M_\phi \frac{A_\phi^2\left(1-\frac{z}{H}\right)e^{A_\phi\left(\frac{z}{H}-1\right)}}{H\left(1-\frac{1}{A_\phi}\right)e^{-A_\phi}} \qquad \text{Equation 51}$$

Where *H* is the column height, $M_\phi$ is the total mass for particle size $\phi$, and $A_\phi$ is a dimensionless parameter locating the maximum concentration height:

$$A_\phi = \frac{A}{v_{\phi 0}} \qquad \text{Equation 52}$$

Here, $A$ is a shape factor of the eruption column, which defines how concentrated the vertical distribution of tephra is; typical values range between 1 and 10 based on literature. The term $v_{\phi 0}$ refers to the terminal fall velocity of particles of size $\phi$ at sea level. This velocity is calculated based on Stokes' law and depends on the Reynolds number (see Bonadonna et al., 1998). The application of Equation 51 generates vertical mass distributions for each $\phi$ size class, as illustrated in Figure 128, showing that coarser particles tend to concentrate at lower altitudes, while finer particles are lofted higher.

.

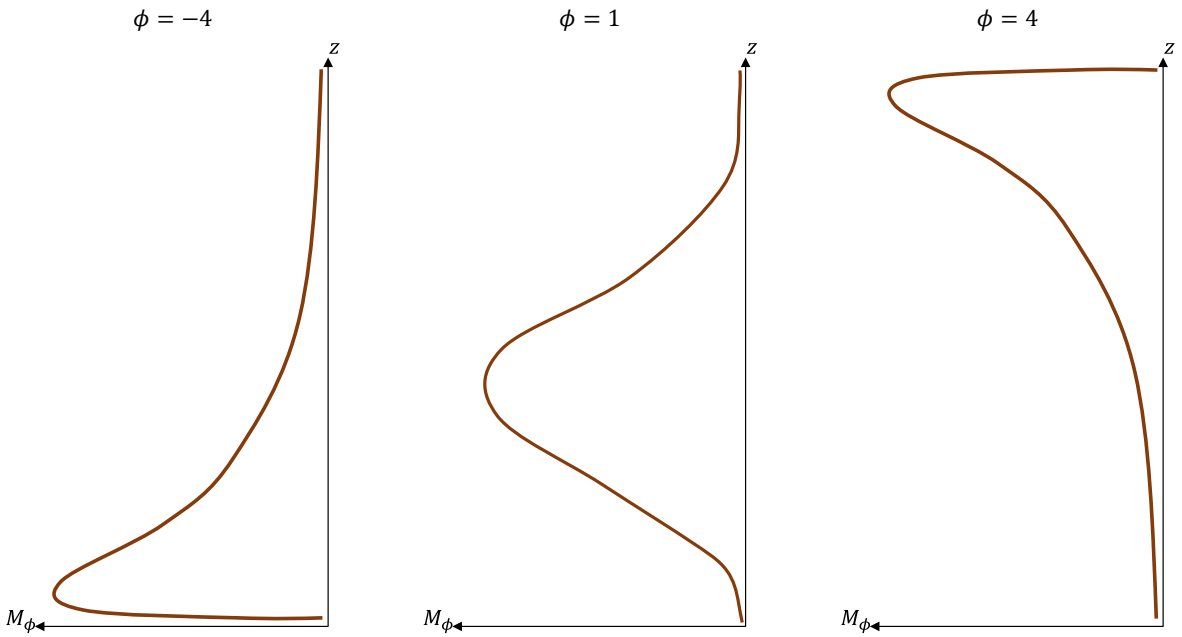


Figure 128. Variation in particle mass distribution by height for $\phi$ = –4, 1, and 4.

The total particle size distribution determines the masses $M_\phi$ to be transported by wind. Size distribution is modeled using a truncated normal distribution (Wood & Bursik, 1991) between $\phi_{min}$ and $\phi_{max}$, defined by a mean $\phi_m$ and standard deviation $\sigma_\phi$.

The model domain is divided into horizontal layers, allowing independent calculations for particle sizes and vertical positions. A disc of material of size $\phi_i$ at height $z_j$, with initial radius $r_0$ and mass $M_{\phi_i z_j}$, deforms horizontally with wind and vertically by gravity. The deposited mass is redistributed in an elongated, non-circular area defined by:

$$m_{\phi_i z_j} = M_{\phi_i z_j} f_{\phi_i z_j (x,y)} \qquad \text{Equation 53}$$

Where $m_{\phi_i z_j}$ is a bidimensional function $(x, y)$ of initial mass distribution of the dispersal disc ($M_{\phi_i z_j}$), and $f_{\phi_i z_j (x,y)}$ is a transformation function satisfying Equation 50. The function by Carslaw & Jaeger (1959), originally developed for heat conduction in solids, is valid for this purpose

$$f_{\phi_i z_j} = \frac{1}{2\pi r_0^2}\left[\mathrm{erf}\left(\frac{r_0 + r}{2\sqrt{k \cdot t_{fall}}}\right) + \mathrm{erf}\left(\frac{r_0 - r}{2\sqrt{k \cdot t_{fall}}}\right)\right] \cdot \mathrm{erf}\left(\frac{r_0}{2\sqrt{k \cdot t_{fall}}}\right) \qquad \text{Equation 54}$$

Where $r = \sqrt{x^2 + y^2}$, $k$ is the horizontal diffusivity[12], and $t_{fall} \cong z_j / v_{\phi_i}$ is the fall time. The Gaussian error function *erf* is used here. The spatial centroid of each layer is given by Folch & Felpeto (2005):

$$x_{\phi_i} = x_0 + \sum_{k=j}^{1} U_x(z_k) \frac{z_k - z_{k-1}}{v_{\phi_i}} \quad \text{Equation 55}$$

$$y_{\phi_i} = y_0 + \sum_{k=j}^{1} U_y(z_k) \frac{z_k - z_{k-1}}{v_{\phi_i}} \quad \text{Equation 56}$$

Where $x_{\phi_i}$, $y_{\phi_i}$ are the vent coordinates and $U_x(z)$, $U_y(z)$ are wind velocities at height $z$ in the two horizontal directions. The final deposited mass across the domain is calculated as:

$$m(x,y) = \sum_{i=\phi_{min}}^{\phi_{max}} \sum_{j=1}^{N_z} m_{\phi_i z_j} \quad \text{Equation 57}$$

The simulation outputs may be presented as deposited mass or, assuming particle density, as tephra thickness. This allows for the creation of isopach maps representing the spatial variation of tephra accumulation across the study region.

### 7.3.3 Modeling of Ballistic Projectiles

Ballistic projectiles are blocks or bombs ejected from the volcanic vent at an initial velocity $U_0$, too heavy to be suspended in air, and typically launched at a non-vertical angle ($\alpha_o$). This trajectory results in high-energy impacts at short distances from the crater. The trajectory is approximately parabolic due to aerodynamic drag acting on the projectile as it travels through the air, which slows it down. If air resistance were negligible, the motion would follow a purely parabolic path. Figure 129 (a) illustrates the initial conditions and trajectory of a ballistic projectile launched from a volcano.

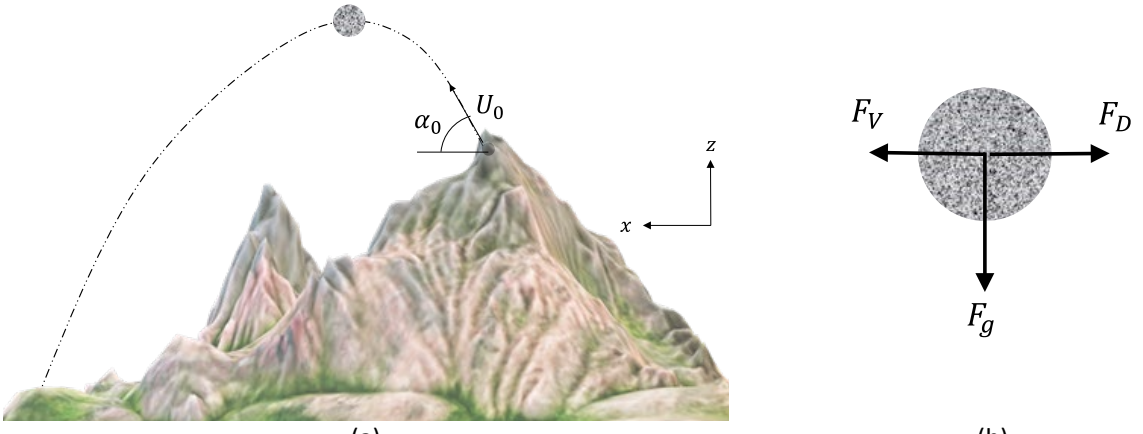


(a) (b)

Figure 129. (a) (a) Initial launch conditions and trajectory of a volcanic ballistic projectile. (b) Free body diagram showing acting forces.

[12] For simplicity, vertical diffusivity is considered negligible, and the horizontal diffusivity coefficients are assumed to be equal (i.e., $k = k_x = k_y$).

At any point during its flight, such as that depicted in Figure 129 (a), the projectile experiences three primary forces, as illustrated in Figure 129 (b): the initial thrust force ($(F_V)$ from the eruption, the drag force ($F_D$) acting opposite to motion and dependent on air density and drag coefficient, and the gravitational force ($F_g$) corresponding to the projectile's weight (adjusted for buoyancy, typically negligible). Other effects like the Magnus force from rotation are neglected here. These considerations lead to the following equations of motion (Mastin, 2001):

$$\frac{dV_x}{dt} = \frac{-V_x \cdot \rho_{aire} \cdot V \cdot A \cdot C_D}{2m} \quad \text{Equation 58}$$

$$\frac{dV_z}{dt} = \frac{-V_z \cdot \rho_{aire} \cdot V \cdot A \cdot C_D}{2m} - g\frac{\rho_b - \rho_{aire}}{\rho_b} \quad \text{Equation 59}$$

Where $V_x$ and $V_z$ are the projectile's velocities in the $x$ and $z$ directions, respectively. $V$ is the total velocity magnitude ($V = \sqrt{V_x^2 + V_z^2}$), $A$ is the cross-sectional area (i.e., exposed area perpendicular to direction of travel), $C_D$ is the drag coefficient, $m$ is the projectile's mass, and $\rho_b$ is the block's density.

The cross-sectional area and mass depend on the block's shape:

| | | |
|---|---|---|
| $A = D^2$ | For cubes with face perpendicular to the flow.<br>*D is the dimension of the cube* | Equation 60 |
| $A = \sqrt{3} \cdot D^2$ | For cubes with vertex facing the flow<br>*D is the dimension of the cube* | |
| $A = \frac{1}{4}\pi D^2$ | Para spheres<br>*D is the diameter of the sphere* | |
| $m = \rho_b D^3$ | For cubes | Equation 61 |
| $m = \frac{1}{6}\rho_b \pi D^3$ | For spheres | |

The drag coefficient $C_D$ is a function of the Reynolds number ($Re$) [13], which depends on air density, velocity, particle size, and air viscosity ($\eta$):

$$Re = \frac{\rho_{aire} \cdot V \cdot D}{\eta} \quad \text{Equation 62}$$

Depending on $Re$, $C_D$ varies (Mastin, 2001):

| | | |
|---|---|---|
| $C_D \cong \frac{24}{Re}$ | $Re < 10$ | Equation 63 |
| $C_D \cong \frac{18.5}{Re^{3/5}}$ | $Re < 10{,}000$ | |
| $C_D \cong 0.5$ | $Re < 30{,}000$ | |

[13] The Reynolds number is a dimensionless quantity that relates inertial forces to viscous forces in fluid dynamics.

For simplicity, air density and viscosity are considered constant, though in reality they vary with altitude. If needed, altitude-dependent formulations can be used (Mastin, 2001).

As noted by Hoerner (1965), these relationships are only valid when the Mach number ($Mc$) is less than approximately 0.5. For higher values, $C_D$ begins to increase, as shown in Figure 130, depending on block shape. The Mach number is calculated as:

$$Mc = \frac{V}{C}$$ Equation 64

Where *C* is the speed of sound in the medium, calculated as:

$$C = \sqrt{\gamma R T_{air}}$$ Equation 65

Where $\gamma$ is the ratio of specific heats at constant pressure and volume (≈1.4 for air), *R* is the specific gas constant, and $T_{air}$ is the ambient air temperature.

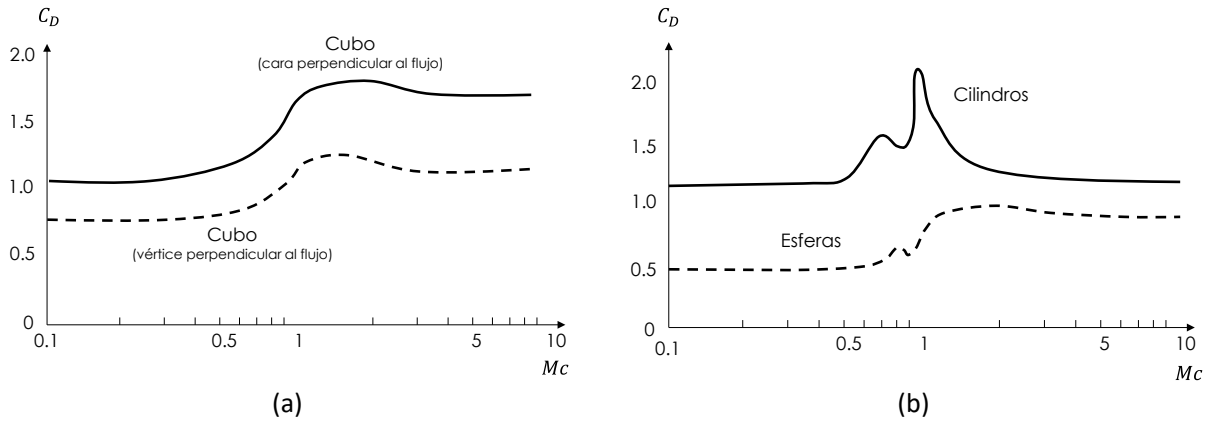


Figure 130. Variation of drag coefficient $C_D$ with Mach number for (a) cube with different orientations; (b) spheres and cylinders (adapted from Mastin, 2001)

The projectile's motion equations are numerically solved using a fourth-order Runge-Kutta method, yielding the final impact velocity $V$. The corresponding impact energy ($E_C$) is calculated as:

$$E_C = \frac{1}{2} m V^2$$ Equation 66

This impact energy represents the intensity of each simulated block. For each eruptive pulse, a predefined number of projectiles are launched with random angles and directions from the crater at speed $U_0$, and their impact positions and energies are determined accordingly.

### 7.3.4 Modeling of Pyroclastic Density Currents

Pyroclastic density currents (PDCs), or pyroclastic flows, result from the gravitational collapse of the denser portion of the eruption column or from the sudden collapse of a lava dome. The fragmented material

descends rapidly down the volcanic slopes with very high temperatures, exhibiting strong destructive potential. PDCs consist of hot, dry avalanches made up of gas and solid fragments of various sizes.

PDCs can be understood as comprising a *basal flow*, which is close to the surface and relatively shallow, consisting mainly of blocks, bombs, lapilli, and coarse ash, and *an overriding cloud*, composed of coarse and fine ash and gases.

#### *7.3.4.1 Concentrated Currents*

The main driving force behind the movement of a pyroclastic flow is gravity, particularly influencing the motion of the basal (concentrated) current. Therefore, it is crucial to use a digital elevation model (DEM) that accurately represents the volcano's topography. The DEM is a georeferenced raster dataset in which each cell corresponds to a topographic elevation. Figure 131 (a) illustrates an example of a DEM.

.

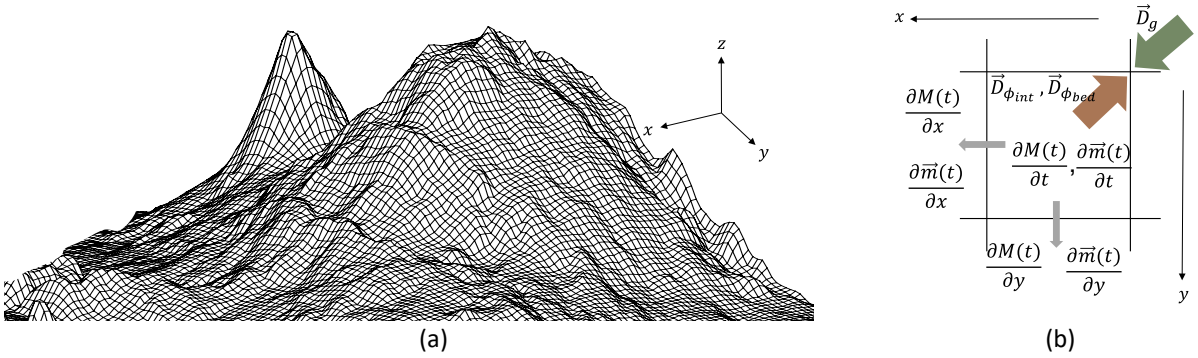


(a) (b)

Figure 131. (a) Illustration of a digital elevation model. (b) Flows and forcings considered in the two-dimensional model of basal flow transit, for a cell of the digital elevation model.

To simulate the motion of a basal flow over a DEM, one must understand the mass and momentum fluxes occurring in each cell through which the flow passes. A common simplification assumes that the flow thickness is small enough to neglect vertical ($z$-direction) variation in mass and momentum, reducing the problem to a two-dimensional surface flow. Figure 131(b) shows the relevant variables within a single DEM cell at a given time. Within this cell, both mass ($M$) and momentum ($\vec{m}$) change over time. We are interested in the rates of change of these quantities over time (i.e., $\partial M(t)/\partial t$ , $\partial \vec{m}(t)/\partial t$), as well as their spatial fluxes to neighboring cells in the $x$ and $y$ directions. The forces acting on the flow include gravity ($\vec{D}_g$), internal friction ($\vec{D}_{\phi_{int}}$), and basal friction with the terrain ($\vec{D}_{\phi_{bed}}$).

The two-dimensional gravity-driven flow can be modeled using the Saint-Venant equations (shallow water equations), widely applied in science and engineering. These partial differential equations describe the time and space evolution of conserved state variables (i.e., mass and momentum) based on external forcing (i.e., gravity). The system is expressed in vector form as (Patra et al., 2005):

$$\frac{\partial \vec{u}}{\partial t} + \frac{\partial \overrightarrow{F_u}}{\partial x} + \frac{\partial \overrightarrow{G_u}}{\partial y} = \overrightarrow{S_u} \qquad \text{Equation 67}$$

Where $\vec{u}, \overrightarrow{F_u}, \overrightarrow{G_u}$ are vectors of conserved state variables in time, $x$ -direction, and $y$-direction, respectively, and $\overrightarrow{S_u}$ is the source (forcing) vector. Assuming constant density, the vectors are defined as (Patra et al., 2005):

$$\vec{u} = \begin{pmatrix} h \\ hV_x \\ hV_y \end{pmatrix} \quad \text{Equation 68}$$

$$\overrightarrow{F_u} = \begin{pmatrix} hV_x \\ hV_x^2 + T_{xx} \\ hV_xV_y \end{pmatrix} \quad \text{Equation 69}$$

$$\overrightarrow{G_u} = \begin{pmatrix} hV_y \\ hV_xV_y \\ hV_y^2 + T_{yy} \end{pmatrix} \quad \text{Equation 70}$$

$$\overrightarrow{S_u} = \begin{pmatrix} 0 \\ g_x h - D_{x,\phi_{int}} - D_{x,\phi_{bed}} \\ g_y h - D_{y,\phi_{int}} - D_{y,\phi_{bed}} \end{pmatrix} \quad \text{Equation 71}$$

The vector $\vec{u}$ contains the state variables conserved over time: the flow mass represented by its thickness ($h$), and the momentum in both orthogonal directions ($hV_x$, $hV_y$). The vector $\overrightarrow{F_u}$ describes, in the x-direction, the fluxes of mass ($hV_x$), $x$-momentum ($hV_x^2 + T_{xx}$), and $y$-momentum ($hV_xV_y$), with $T_{xx}$ representing the normal stress in $x$ associated with the horizontal push caused by hydrostatic pressure, averaged along the vertical ($z$), exerted by the weight of the basal flow on the cell's mass. The vector $\overrightarrow{G_u}$describes the same processes as $\overrightarrow{F_u}$, but specific to the $y$ -direction. Finally, the source vector Su contains the forcing terms that drive the motion of the pyroclastic flow, i.e., gravitational forces ($g_x h$, $g_y h$), as well as those that oppose it: internal friction forces ($D_{x,\phi_{int}}$, $D_{y,\phi_{int}}$) and basal friction forces with the natural terrain ($D_{x,\phi_{bed}}$, $D_{y,\phi_{bed}}$). The terms $g_x$ and $g_y$ correspond to the gravitational acceleration components parallel to the topographic slope in each orthogonal direction.

Flow rheology is essential in modeling with this system. The *Mohr-Coulomb* rheological model, commonly used to describe pyroclastic flows, is adopted here. The equations are numerically solved using a finite difference scheme and a HLLC-type Riemann solver[14]. The outputs are spatial distributions of flow variables ($h, V_x, V_y$) for each time step. The time step is adjusted according to the initial flow velocity and DEM resolution to satisfy the Courant-Friedrichs-Lewy condition. The collapsed volume ($V_c$) is introduced as an initial column of material located at the volcano's summit, capable of collapsing in any direction. These initial conditions determine the flow path governed by the differential equation system. Varying the collapse direction allows simulation of flow spread in multiple directions (see Figure 132).

[14] Harten-Lax-van Leer-Contact

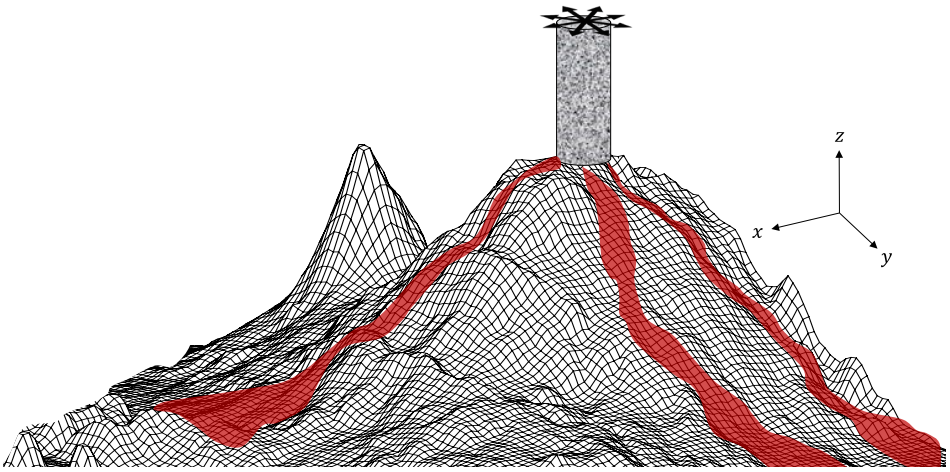


Figure 132. Illustration of the initial conditions of the pyroclastic flow transit model. The red patches illustrate the movement of the same collapsed volume in different directions. (Illustrative image, not to scale).

From the computed variables, the dynamic pressure of the basal flow is derived as the intensity measure for each pulse:

$$P_D = \frac{1}{2}\rho_s\sqrt{(V_x^2 + V_y^2)}$$ Equation 72

Since each event consists of *N* pulses, each with potential collapse depending on the eruption regime, the final intensity measure is taken as the maximum dynamic pressure from all collapsed pulses for each cell of the DEM:

$$P_D = max(P_{D1}, P_{D2}, \dots, P_{DN})$$ Equation 73

#### *7.3.4.2 Diluted Currents*

Above or adjacent to the basal flow travels a diluted pyroclastic density current, whose motion is also primarily gravity-driven but is significantly altered by the entrainment and mixing with ambient air. This interaction produces buoyant segments within the current, resulting in lower density and reduced dynamic pressure. Nonetheless, due to their high temperatures, diluted currents remain highly destructive and, because of their lower density, may extend farther than concentrated currents.

Although gravity is the primary driving force, the propagation of diluted currents is also governed by complex heat and mass transfer processes between the pyroclastic material and surrounding air. These phenomena are challenging to model and typically require intensive computational resources. To overcome this, we adopt a simplified yet widely accepted modeling approach known as the energy cone model (Sheridan & Malin, 1982), which estimates the travel extent of PDCs based on potential energy considerations.

The energy cone model allows for estimating the probable reach of pyroclastic flows in a given eruption scenario. In this model, the potential energy decreases with distance from the emission point as the

difference between the energy line and the ground elevation. The energy line is defined by its height from the cone's vertex and its slope angle. Figure 133 presents the primary variables of the model.

The susceptibility of a given location to PDC impact is then defined as a function of the energy head available at that location. The energy head $h$ is computed as:

$$h = H_0 + H_c - d\,tan(\alpha_c) - h_0$$

Equation 74

Where $H_0$ is the topographic elevation at the source, $H_c$ is the eruption column height, $d$ is the horizontal distance from the source to the analysis point, $\alpha_c$ is the cone's inclination angle, and $h_0$ is the topographic elevation of the analysis point. The energy cone thus delineates a probable impact region and is often subdivided into sectors to simulate different directions of flow propagation.

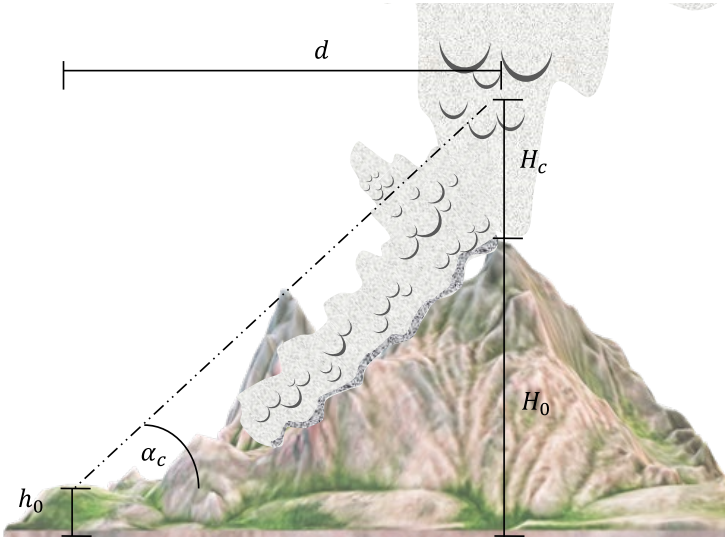


Figure 133. Illustration of the variables involved in the energy cone model.

To compute dynamic pressure, one must first estimate the flow velocity. This is done using the empirical relation proposed by Toyos et al. (2007), based on regression analysis of pyroclastic flow velocities from the Soufrière Hills (June 25, 1997) and Mount St. Helens (August 7, 1980) eruptions:

$$V = 0.38h^{0.68}$$

Equation 75

Finally, Dynamic pressure is obtained using:

$$PD = \frac{1}{2}\rho \cdot V^2$$

Equation 76

Where $\rho$ is the average density of the dilute current. For simplicity and conservatism, $\rho$ is assumed equal to the source crater density ($\rho = \rho_0$).

### 7.3.5 Modeling of Volcanic Mudo r Debris Flows (Lahars)

Lahars occur when erupted material reaches riverbeds and generates large debris flows. Since these flows follow river and stream channels, they can reach locations far from the eruption source. Generally, lahars can be understood as debris flows or torrential flows triggered by a volcanic event, meaning they transport volcanic ejecta.

"These types of flows can occur during (primary) or after (secondary) volcanic eruptions, through various mechanisms that enable the interaction of water with volcanic and non-volcanic materials. Water sources for lahars may include snow, ice, crater lakes, rainfall, river flows, or internal water reservoirs within the volcano." (SGC, 2015).

Two main mechanisms are identified for the primary lahar generation:

- *Mechanism 1*: As a consequence of pyroclastic flows contributing significant volumes of material into river or stream channels.
- *Mechanism 2*: As a result of an eruptive event depositing large amounts of tephra or pyroclastic flows within the volcano's watershed, followed by intense rainfall that generates runoff capable of eroding the freshly deposited surface material.

Lahar modeling is essentially the hydraulic routing of a biphasic flow with a high concentration of granular material of various sizes. These are neither dry avalanches nor pure fluid flows; thus, special rheological models are required to capture the phenomenon.

The key input for flow routing is a volume, discharge, or hydrograph specifying the inflow of material into the natural channel. For *Mechanism 1*, it is, first, necessary to model pyroclastic flows and identify those that can reach natural channels with sufficient volume and water mixing. To the base flow ($Q_{base}$) of the river, a flow component ($Q_{piro}$) is added, assumed to occur over a short time ($t_{piro}$), during which the total volume of pyroclastic flow reaching the channel is discharged, as shown in Figure 134. The time $t_{piro}$ is approximated as one-tenth of the watershed's time of concentration ($t_c$). Therefore, $Q_{piro}$ is simply the contributed volume ($V_{piro}$) divided by $t_{piro}$ (i.e., $Q_{piro} = V_{piro}/t_{piro}$).

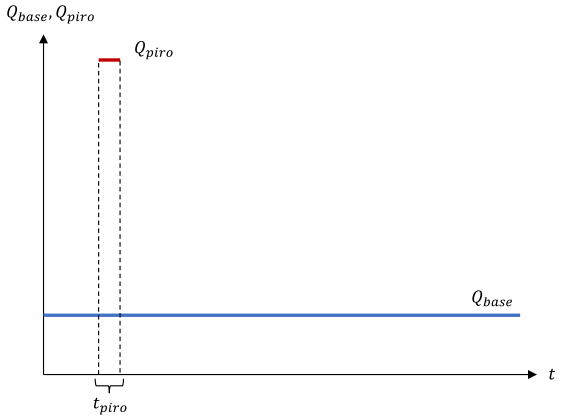


Figure 134. Inflow hydrograph for the hydraulic routing model under Generation Mechanism 1.

For *Mechanism 2*, the inflow volume must be determined from significant rainfall events following tephra fallout or pyroclastic deposition in the catchment. This requires modeling of volcanic products and rainfall conditions capable of triggering a lahar.

Hydraulic routing of lahars can be modeled with a two-dimensional approach based on the Saint-Venant equations, adapted for biphasic (solid-liquid) flows. The approach is essentially the same as for pyroclastic flows but extended to include both phases. Mass and momentum conservation for the solid and fluid phases are expressed as follows (Córdoba et al., 2015):

$$\frac{\partial \rho_s \varphi}{\partial t} + \nabla \cdot (\rho_s \varphi \vec{v}) = 0 \qquad \text{Equation 77}$$

$$\frac{\partial \rho_s \varphi \vec{v}}{\partial t} + \nabla \cdot (\rho_s \varphi \vec{v} \vec{v}) = \nabla \cdot T_s + f_s + \rho_s \varphi \vec{g} \qquad \text{Equation 78}$$

$$\frac{\partial \rho_f (1-\varphi)}{\partial t} + \nabla \cdot \left(\rho_f (1-\varphi) \vec{u}\right) = 0 \qquad \text{Equation 79}$$

$$\frac{\partial \rho_f (1-\varphi) \vec{u}}{\partial t} + \nabla \cdot \left(\rho_f (1-\varphi) \vec{u} \vec{u}\right) = \nabla \cdot T_f + f_f + \rho_f (1-\varphi) \vec{g} \qquad \text{Equation 80}$$

Where $\rho_s$ is the solid density, $\rho_f$ is the fluid density, $T_s$ and $T_f$ are the stress tensors of the solid and fluid phases, $f_s$ and $f_f$ are the interaction forces acting on each phase, $\vec{v}$ is the solid velocity, $\vec{u}$ is the fluid velocity, $\varphi$ is the volumetric fraction of solids (which may be assumed constant), and $\vec{g}$ is the gravitational force driving the flow.

Solving this system of equations provides estimates of the lahar's dynamic pressure, which serves as the intensity measure for lahar hazard modeling.

## 7.4 Landslide Hazard

Mass movement processes are defined as the downslope motion of a volume of rock or soil near the Earth's surface, driven mainly by gravity. These processes are a fundamental part of erosion, transporting material from high to low elevations, where it can be further mobilized by streams or rivers. Landslides occur continuously on all slopes—some very slowly, others abruptly, often with catastrophic outcomes. Any perceptible downslope movement of rock or soil, or a mixture of both, is generally referred to as a landslide. This study does not differentiate between landslide types, focusing instead on the probability of occurrence.

Landslide stability is governed by four fundamental aspects: (i) the loads acting on potential sliding masses, (ii) the role of water in modifying mechanical properties, (iii) geological structure and human interventions, and (iv) triggering events, particularly earthquakes and intense rainfall. This study focuses exclusively on rainfall-triggered landslides.

The first three aspects are collectively expressed as *susceptibility*—the intrinsic conditions favoring instability. The external trigger is treated as a separate input in the modeling framework detailed in Section

5. Landslide hazard is defined as the probability of failure ($P_L$), determined by the product of susceptibility ($P_S$) and the probability that a trigger exceeds a given threshold ($P(p \geq p_U)$):

$$P_L = P_S \cdot P(p \geq p_U) \quad \text{Equation 81}$$

Expanding this concept to a model where rainfall is represented as a set of mutually exclusive and collectively exhaustive events (e.g., storm events), annual landslide hazard rates ($v_L$) can be calculated by weighing the exceedance probabilities by the annual frequency ($F_j$) of each event:

$$v_L = P_S \left[ \sum_{j=1}^{Np} P(p_j \geq p_u) F_j \right] \quad \text{Equation 82}$$

### 7.4.1 Landslide Susceptibility

While limit equilibrium approaches are commonly used to model susceptibility, they are not feasible at national scales due to the lack of detailed geotechnical data. Instead, this study adopts an approach based on *propensity factors* known to influence slope stability.

Examples of such factors include loading conditions (e.g., number of dwellings, land cover, slope angle), geological structure (e.g., surface formations, proximity to faults or streams), and anthropogenic modifications (e.g., proximity to roads, socioeconomic status, distance to sewer infrastructure), as shown in Figure 135. These proxies help infer susceptibility without directly measuring geomechanical properties.

It is possible to define a function that relates all propensity factors—i.e., terrain conditions contributing to instability—to a measure of landslide susceptibility, expressed as the probability that a given location is unstable. Among the various available modeling approaches, Artificial Neural Networks (ANNs) have proven particularly effective for establishing these complex relationships.

ANNs require a historical landslide inventory for training and validation. Once trained, they provide a robust and detailed mechanism for modeling spatial landslide susceptibility.

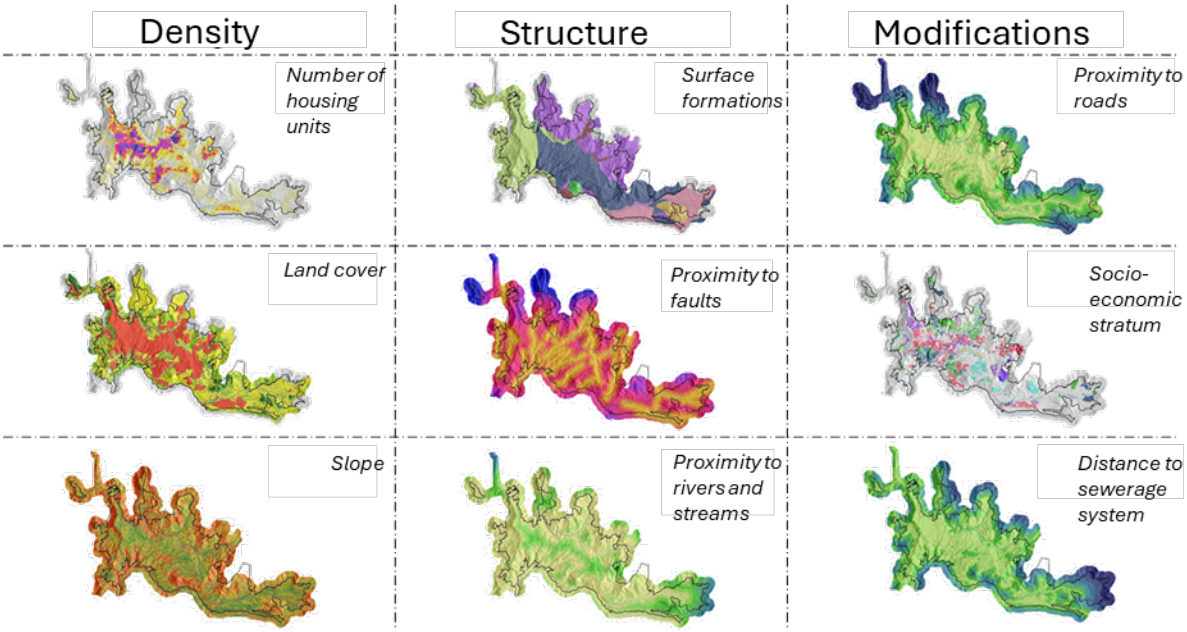


Figure 135. *Examples of propensity factors for the city of Manizales, Colombia.*

### 7.4.2 Rainfall-Landslide Thresholds

As previously discussed, landslide hazard at a specific location is calculated as a probability composed of susceptibility and the likelihood that a triggering event exceeds a defined threshold. This threshold is a key component of the model, as it defines the intensity of rainfall beyond which landslides are likely to occur.

Multiple types of rainfall–landslide thresholds exist in the literature. They can be broadly categorized into: (i) *Antecedent rainfall thresholds:* These define the probability of landsliding based on accumulated precipitation prior to the landslide event, using various accumulation windows. (ii) *Intensity–duration thresholds:* These use real-time rainfall characteristics, assessing the likelihood of landslides based on the intensity (precipitation per unit time) versus the storm duration. (iii) *Machine-learning-derived thresholds:* These are obtained using artificial neural networks or other AI approaches.

At this stage, it is not yet clear which threshold type—or combination thereof—will be used in this consultancy, as data availability is still under review.

### 7.4.3 Critical acceleration

To evaluate earthquake-induced landslide hazard, the methodology proposed by Newmark (1965) is employed. It uses a parameter known as *critical acceleration*, which represents the minimum ground acceleration required to trigger slope failure. This parameter depends on the static safety factor (*FS*) and the slope angle ($\alpha$), and is defined as:

$$A_C = (FS - 1) \cdot g \cdot \sin \alpha$$

Equation 83

Where $FS$ is the static safety factor, $g$ is gravitational acceleration, and $\alpha$ is the slope angle, approximated as the angle to the center of mass of the potential landslide.

Since earthquake ground acceleration is modeled as a random variable, the critical acceleration provides a basis to calculate the probability that a simulated seismic event will exceed this threshold, thus triggering a landslide. This probability of exceedance is illustrated in Figure 136.

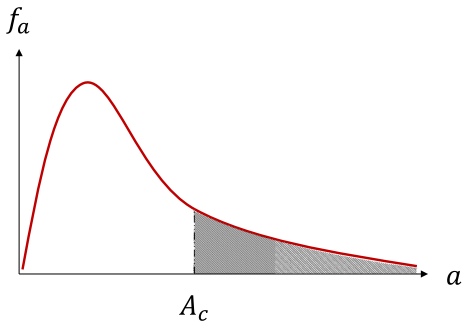


Figure 136. *Illustration of landslide probability calculation for a simulated seismic event*.

# 8 EXPOSURE MODELING

Exposure and vulnerability reflect the socioeconomic conditions in which hazardous events occur. The presence of exposed elements in areas susceptible to hazardous phenomena, along with their susceptibility to damage—shaped by social processes of vulnerability generation and accumulation—play a more decisive role in disaster occurrence than the hazard itself.

In general, an exposed element is any object, item, asset, or entity subject to damage or loss due to a hazard event. Exposed elements are essential in risk assessment, as they represent the targets over which modeled losses are quantified.

Exposed elements can be categorized according to the type of exposure, such as buildings, infrastructure, crops, and livestock. These categories differ in both their modeling requirements and their vulnerability to hazards.

In this study, the impact on buildings is measured in terms of direct damage to the structure, contents, and business interruption resulting from service disruption. Buildings are typically grouped into portfolios according to the entity responsible for the modeled losses, enabling simulation of impacts across large groups of exposed elements.

Infrastructure systems represent one of the most complex types of exposure to model. These systems consist of interconnected components forming nodes and arcs through which specific services flow. As a result, system components are interdependent. Damage includes both direct damage to individual elements and the resulting disruptions to service provision. This study focuses specifically on the direct damage to infrastructure system components.

In the case of agricultural production, the exposed element is typically a productive land unit. This unit encapsulates multiple aspects, including crop or production system type, production cycle, seasonal timing, soil type, and others. Impact is understood primarily as a reduction in crop yield or changes in pasture carrying capacity, leading to production loss. Unlike buildings or infrastructure, this loss represents an economic flow rather than a damaged asset.

Exposure is modeled through georeferenced data layers, where each element in the exposure portfolio has a spatial representation and a set of defining attributes. The minimum required information for characterizing exposed elements includes:

- Geographic location
- Replacement or compensation value, as applicable to the type of loss
- A vulnerability classification code

Depending on the assessment, additional information may be required to more accurately characterize each element and associate it with an appropriate vulnerability model. For example, building assessments may require data on the number of stories, use, age, structural system, and other attributes. It is worth noting that the information gathered covers all the aspects required to characterize the elements in relation to all the hazards included within the scope of this assessment.

## 8.1 Building Exposure

Information on the exposure of real estate assets in terms of replacement value represents a fundamental component in disaster risk assessment. Proper characterization is crucial for accurately estimating potential losses. The database of exposed elements can be defined at different levels of resolution, depending on the availability of information and the type of analysis to be conducted. In this context, cadastral data—providing location, socioeconomic strata, and appraised value—are commonly used in conjunction with housing census information, which includes details such as wall and roof materials, among others. In the absence of detailed information, approximate estimations may be necessary to represent the inventory of exposed assets.

For buildings, the minimum required information to be included in the exposure database consists of:

- *Identification*: A unique code identifying each building.
- *Location:* Georeferenced representation of each exposed element—using points, lines, or polygons—is essential to determine the hazard intensity affecting it.
- *Year of Construction:* Provides insight into construction criteria, materials, and techniques typical of the corresponding period.
- *Socioeconomic Stratum:* Indicates the quality of materials and construction, which is often linked to the socioeconomic level of the area.
- *Structural System:* Based on the above information, it is possible to assign a general layout of structural elements and construction material, referred to as the structural system. This determines the corresponding vulnerability curve used to assess the building's response to hazard.
- *Appraisal Value:* Represents the replacement value of the building, essential for estimating monetary losses in the event of a hazard.

Based on the information collected, all the above variables are derived to complete the exposure dataset as thoroughly as possible.

## 8.2 Infraestructure Exposure

This portfolio[15] is among the most challenging to characterize in terms of both exposure and vulnerability. As previously noted, infrastructure assets are organized as networks of interdependent components through which services or goods are delivered. These components are susceptible to damage from hazardous events, leading to both direct physical losses and disruptions to service provision and demand restoration.

[15] Set of assets

Depending on the sector and the type of infrastructure, the exposure model must capture the components relevant to each system. Table 40 provides a non-exhaustive list of typical components by sector.

Table 40. Typical Infrastructure Components by Sector

| Roads | Energy | Telecommunications | Transportation | Water and Sanitation |
|---|---|---|---|---|
| **Road Transportation**<br>• Roads and Highways<br>• Bridges<br>• Tunnels<br>• Traffic Management and Operations Centers<br>• Truck Terminals | **Power Generation**<br>• Thermoelectric Power Plants<br>• Hydroelectric Power Plants<br>• Alternative/Renewable Energy Power Plants<br>• Distributed Power Plants<br>• Other Generation Facilities<br>• Backup Generators<br>• Power Plant Substations<br>**Transmission**<br>• Transmission Lines and Towers<br>• Transmission Substations<br>• Converter Stations<br>• Regional Control Centers<br>**Distribution**<br>• Distribution Lines<br>• Distribution Substations<br>• Step-Down Transformers | **Landline Telephone Services**<br>• Switching Facilities<br>• Access Tandems<br>• Cabling<br>• Operator Stations<br>• Operator Data Centers<br>**Wireless Services**<br>• Cell Towers<br>• Base Transceiver Stations (BTS)<br>• Base Station Controller Sites<br>• Mobile Switching Offices<br>**Broadcasting Services**<br>• Television/Radio Network Headquarters<br>• Local Broadcasting Centers<br>• Data Centers<br>• Operations Centers | **River Transport**<br>• Locks and Canals<br>• Dams<br>• Docks<br>**Maritime Transport**<br>• Seaports (shallow-draft and deep-draft)<br>**Air Transport**<br>• Airports<br>• Runways and Airfields<br>• Heliports<br>• Air Traffic Control and Navigation Facilities<br>**Mass Transit**<br>• Subway Systems<br>• Bus Systems<br>• Tram and Ferry Systems | **Water Supply, Storage, and Treatment**<br>• Raw Water Storage Assets (reservoirs and tanks)<br>• Desalination Plants<br>• Water Treatment and Filtration Plants<br>• Finished Water Storage Assets (towers, water wells, and standpipes)<br>**Water Delivery**<br>• Water Tunnels<br>• Aqueducts<br>• Transmission Network<br>• Pumping Stations<br>• Pipeline Interconnections<br>• Distribution Network<br>• Service Pipes<br>• Monitoring and Control Stations<br>**Wastewater Collection**<br>• Sewer Intakes and Main Pipes (sanitary, stormwater, and combined)<br>**Treatment and Discharge**<br>• Effluent Storage (tanks, wells, ponds, and basins)<br>• Wastewater Treatment Plant<br>• Pumping and Discharge Facilities<br>• Monitoring and Control Stations |

## 8.3 Crop Exposure

Agricultural exposure will be quantified in terms of cultivated areas according to the main crops defined for this consultancy. The exposed elements will be cultivated land units, each with a specific location, crop type, and soil type. These units are generally modeled geographically as pixels with a resolution level appropriate to the scale of the study (Cardona et al., 2021).

For each exposed element or cultivated land unit, it is necessary to understand the crop characteristics at that location. The exposure model includes crop type, seasonality, planted area, and historical yields (tons produced per unit area).

The crop calendar determines its seasonality. This is important as it defines the duration of the various growth stages, from planting to maturity, as shown schematically in Figure 137 and Figure 138 for annual and perennial crops, respectively. It also indicates typical planting and harvest periods throughout the year. This information is essential for modeling crop vulnerability as a function of time.

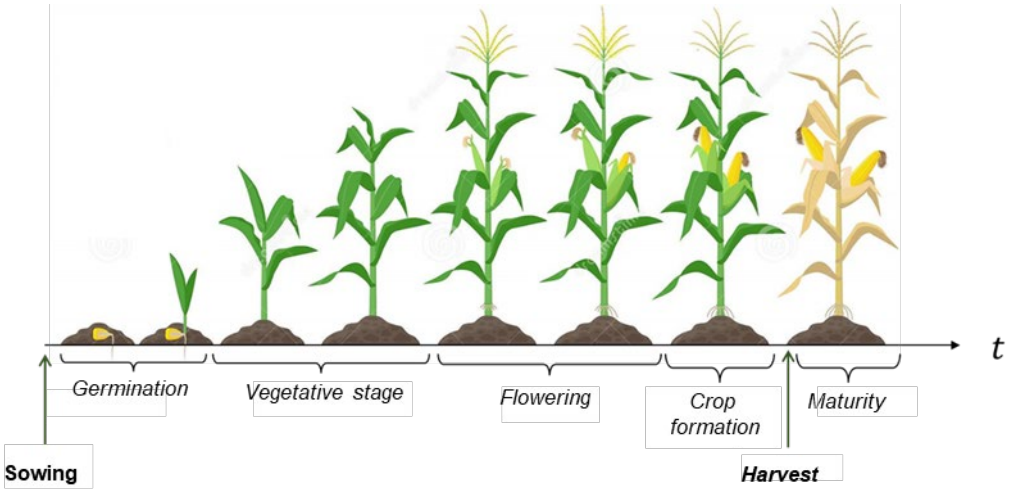


Figure 137. Illustration of phenological stages and their duration for an annual crop.

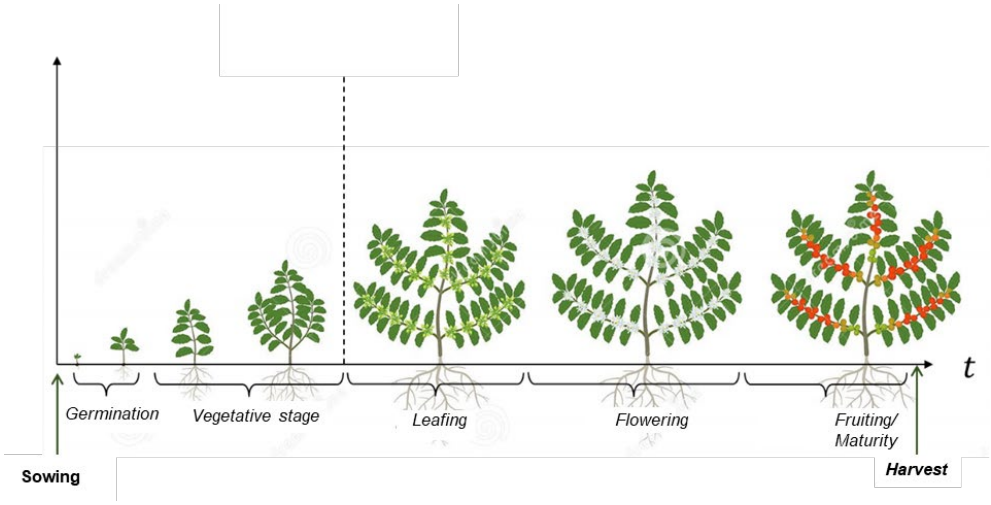


Figure 138. Illustration of phenological stages and their duration for a perennial crop.

Crop development is closely related to soil moisture in the root zone. Therefore, it is necessary to understand soil texture and characteristics that determine water retention capacity. The parameters required to estimate the soil's ability to store and retain water are shown in Figure 134. Depending on the soil water level, plant water availability is defined. After rainfall, excess water results in runoff and infiltration. This infiltrated water moves from saturation (no air content) to field capacity, the level at which soil retains water. As infiltration continues, plant-available water decreases until reaching the permanent wilting point, beyond which recovery is not possible. The available water range lies between field capacity and wilting point.

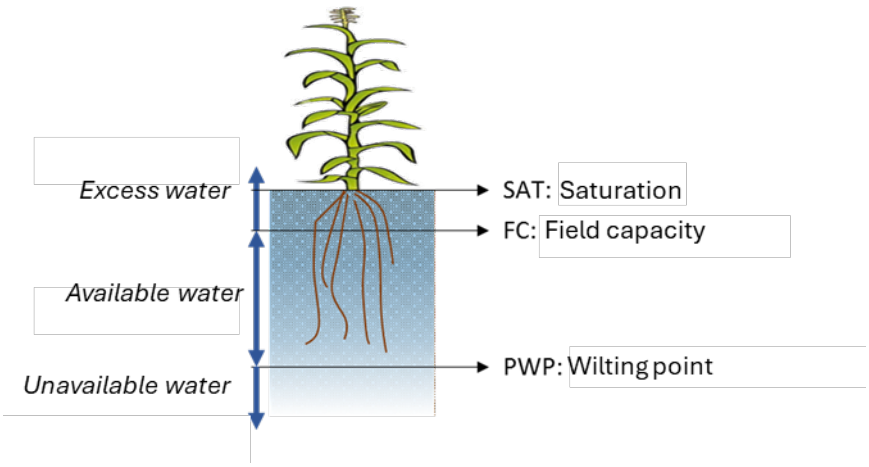


Figure 139. Illustration of water availability in the soil.

Water retention capacity strongly depends on soil texture. As a porous medium, soil's water storage capacity varies with the size of pores between particles. Texture is defined by the proportion of sand, silt, and clay. Sandy soils retain little water due to their coarse structure and macropores, while clay soils, made of fine particles and micropores, retain more water (Sheppard & Hoyle, 2018). Figure 140 illustrates the volumetric water content at field capacity by soil texture, ranging from coarse sands to fine clays.

As seen in Figure 140, field capacity increases with finer soil textures. However, plant-available water requires moisture levels above the wilting point. Wilting point also rises with finer textures, as more water is retained but less accessible to plants due to high retention forces in micropores, which is also tied to the soil's hydraulic conductivity.

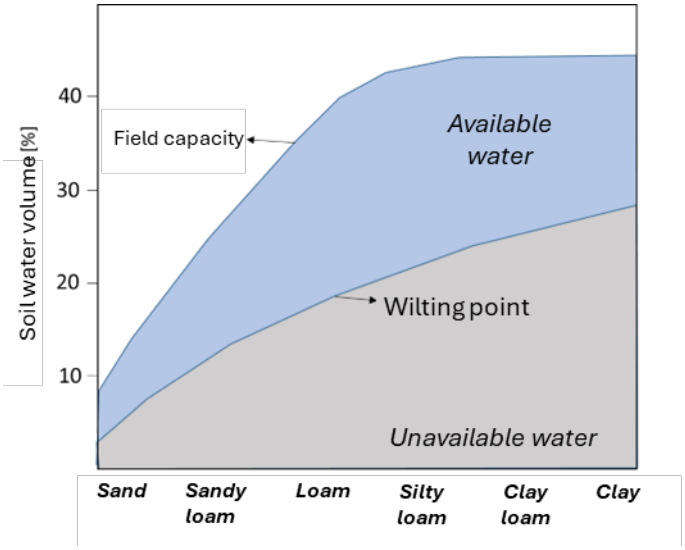


Figure 140. Water retention by soil type. Reproduced from Sheppard & Hoyle (2018).

Soil texture classification is based on the percentage of clay, silt, and sand. The U.S. Department of Agriculture (USDA) textural triangle summarizes these classes and is shown in Figure 141.

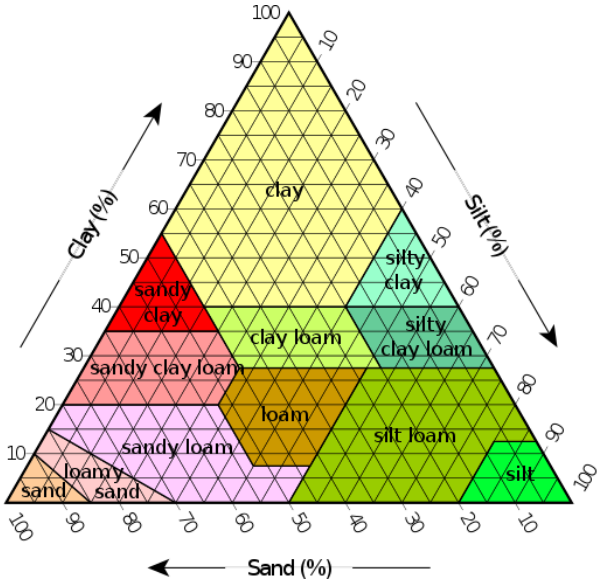


Figure 141. USDA soil textural triangle based on particle size.

## 8.4 Livestock Prduction Systems Exposure

Given the scope of this consultancy in regard to livestock systems (specifically grazing), a significant portion of the exposure model refers to pasturelands used for grazing. In this model —as detailed in Section 9.6— pasture is treated similarly to a crop, with its response to water and weather conditions used to determine yield in terms of dry matter. Accordingly, the information needed to characterize pasture is of the same type as required for agricultural products (see Section 8.3).

Additionally, data is required on grazing animal herds for each livestock production unit. The necessary information includes:

- Number of animals per hectare, broken down by sex and age group.
- Physiological status of the animals (e.g., pregnant females, nursing calves).
- Reference optimal weight for one livestock unit.
- Dry matter requirements per kilogram of body weight.

# 9 VULNERABILITY MODELING

The issue of vulnerability must be addressed differently for each type of hazard considered. This makes the study of vulnerability in exposed buildings, infrastructure, crops, and livestock highly complex, as it remains a highly active field of academic and research development.

## 9.1 Types of Physical Vulnerability Representation

The physical vulnerability of exposed elements can be mathematically represented in various ways, which are valid as long as the applied model sufficiently captures the complexity of the loss-generation process when exposed elements are impacted by a hazardous event. In addition, vulnerability models must be able to express the resulting loss in probabilistic terms, so that the conceptual risk assessment framework (see Section Section 5) can be properly applied.

### 9.1.1 Probabilistic Loss Model

In catastrophic risk modeling, losses are treated as random variables. This allows the inherent uncertainty in the amount of loss caused by any given hazard event to be explicitly considered in the calculations. Vulnerability is defined element by element within the exposure portfolio, meaning that the referenced loss is associated with a single exposed asset. Generally, loss is defined as a variable within the interval [0,1], that is, from zero to 100% of the element's exposed value (e.g., the replacement value of a building or the annual production value of a cultivated area). Therefore, in this context and throughout, when referring to vulnerability, it always corresponds to a relative loss in terms of damage severity—a fraction of the exposed value.

The most widely used model is the Beta distribution, originally proposed by Anne Kiremidjian and others in the development of the ATC-13 report and its companion commentary ATC-13-1 (ATC, 1985, 2002), which aimed to define probability models for earthquake-induced damage in California. Since then, the Beta distribution has become a global standard for modeling loss probability for all hazards and all types of exposed elements, due to its practical advantages:

- It describes a continuous random variable in the real interval [0,1].
- It is defined using only two parameters ($\alpha$ and $\beta$).
- It supports multiple distribution shapes depending on parameter values.

The probability density function ($f_P$) of the Beta distribution is given by:

$$f_p = \frac{\Gamma(\alpha+\beta)}{\Gamma(\alpha)\cdot\Gamma(\beta)}\cdot p^{\alpha-1}\cdot(1-p)^{\beta-1} \qquad \text{Equation 84}$$

where $\Gamma(\cdot)$ denotes the Gamma function. Because the Beta distribution is defined by two parameters, it requires two probability moments for characterization. As such, vulnerability models must provide at least two probability moments. It is common to define vulnerability models in terms of the expected value $E(p)$ and the variance $Var(p)$ of the loss. Using the method of moments, the parameters $\alpha$ and $\beta$ can be determined as follows:

$$\alpha = \frac{1 - (1 + C^2) \cdot E(p)}{C^2}$$ Equation 85

$$\beta = \frac{\alpha \cdot \left(1 - E(p)\right)}{E(p)}$$ Equation 86

where $C$ is the coefficient of variation (i.e., $C = \sqrt{Var(p)}/E(p)$).

The shape of the Beta distribution changes based on the values of these probability moments, as estimated from the vulnerability models. As previously noted, the flexibility of the Beta distribution to change shape within its defined interval is one of the reasons it is widely used in catastrophic risk modeling. Table 41 illustrates the expected shapes of the Beta distribution for various combinations of expected value and variance of the loss. The table includes a general description of what is expected from hazard events of different intensity levels[16], numerical examples of expected value and variance within [0,1], and a visual representation of the corresponding Beta distribution shape. It may be concluded that the Beta distribution suitably reflects the expected distribution of losses under different event scenarios.

[16] Table 18 describes linguistic intensity levels to illustrate the concept. However, in vulnerability modeling, the probability moments of loss are always indexed to physical measures of intensity.

Table 41. Illustration of Beta distribution variation for different hazard intensity levels.

| Description | Probability Moments | Beta Distribution |
|---|---|---|
| ***Very low intensity event:*** *Expected loss is low with low dispersion. That is, for very low intensity, losses are known to be small and with low variability.*<br>*Exponential decay distribution; most probability density is concentrated near zero loss, as expected for low-intensity events.* | $E(p)$ 0 1<br>$Var(p)$ 0 1 | 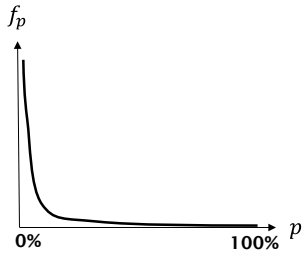 |
| ***Low intensity event:***<br>*Expected loss increases along with variance (i.e., loss becomes more uncertain).*<br>*Wider distribution, centered further to the right but still skewed toward low losses.* | $E(p)$ 0 1<br>$Var(p)$ 0 1 | 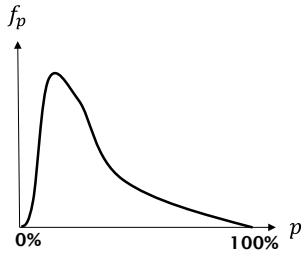 |
| ***Moderate intensity event:***<br>*Expected loss is significantly higher and variance reaches its maximum.*<br>*Symmetrical, bell-shaped distribution, as wide as possible, indicating maximum variability.* | $E(p)$ 0 1<br>$Var(p)$ 0 1 | 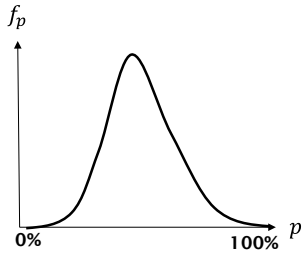 |
| ***High intensity event:***<br>*Expected loss continues to rise, but variance decreases as high damage levels become more certain.*<br>*Distribution becomes skewed to the right, concentrated in higher loss values, with some density still in lower losses.* | $E(p)$ 0 1<br>$Var(p)$ 0 1 | 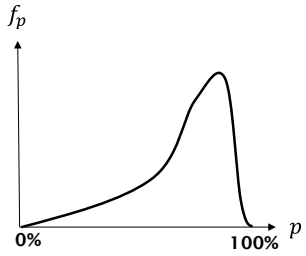 |
| ***Very high intensity event:***<br>*Expected loss is very high with low variance due to reduced uncertainty in damage severity.*<br>*Distribution resembles an exponential rise, indicating high certainty of extreme losses.* | $E(p)$ 0 1<br>$Var(p)$ 0 1 | 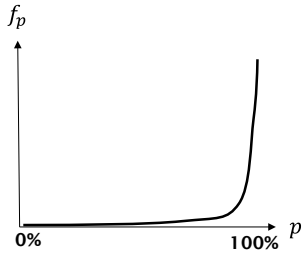 |

### 9.1.2 Vulnerability Functions

Vulnerability functions are mathematical representations of physical vulnerability, typically consisting of two distinct functions: one describing how the expected value of loss varies with hazard intensity, and another describing how the variance changes. Vulnerability functions are the preferred model for buildings and infrastructure elements in catastrophic risk assessments, as they accurately represent loss and require no preprocessing to be incorporated into the model.

The shapes of the expected value and variance functions are not entirely arbitrary. In general, they must follow the behavior illustrated in Table 41: the expected value function must be increasing, while the variance function should first increase and then decrease to appropriately reflect the variability expected with changing hazard intensity.

The most commonly used functional forms for describing vulnerability functions are those proposed in the ATC-13 report (ATC, 1985, 2002). These describe how the expected value and variance of loss change with any physical measure of intensity ($a$). For expected value, the function must increase, although its growth rate may vary with intensity:

$$E(p) = 1 - e^{ln\left(\frac{1}{2}\right)\cdot\left(\frac{a}{a_0}\right)^{\varepsilon}} \quad \text{Equation 87}$$

where $a_0$ is the intensity level at which the expected loss is 0.5, and $\varepsilon$ is an exponent controlling the slope of the curve near $a_0$.

There is limited empirical data available to determine the variance of loss. Following the behavior shown in Table 41, it is assumed that when expected loss is very low or very high, variance is also low. For intermediate values, the variance is harder to estimate empirically. A commonly used expression to model the variance of loss is:

$$Var(p) = Q \cdot \big(E(p)\big)^{r-1} \cdot \big(1 - E(p)\big)^{s-1} \quad \text{Equation 88}$$

where $Q$ and s are defined as:

$$Q = \frac{V_{max}}{{D_0}^{r-1}(1 - D_0)^{s-1}} \quad \text{Equation 89}$$

$$s = \frac{r-1}{D_0} - r + 2 \quad \text{Equation 90}$$

Here, $V_{max}$ is the maximum variance, $D_0$ is the damage level at which this maximum occurs, and $r$ is an exponent controlling the function shape (commonly $r = 3$). Figure 142 shows an example vulnerability function, highlighting the expected value and variance curves.

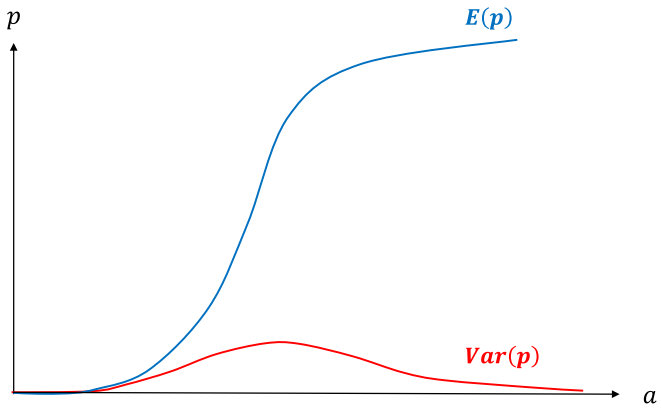


Figure 142. Illustration of a vulnerability function

Vulnerability functions are developed for types of exposed elements, based on a typology of construction types. This means that a single function may represent the behavior of multiple exposed elements that fall under the same typological category. This is reasonable given the probabilistic nature of the functions, which model the behavior of similar exposed assets. The typology or categorization of exposed elements is defined in the exposure model, typically based on the physical characteristics of the elements and the type of damage the hazard is expected to cause.

### 9.1.3 Binary vulnerability

In certain specific cases, it is necessary to define binary vulnerability models. These are used when vulnerability does not gradually change with intensity—either because the exposed element is highly vulnerable or because the hazard is so intense that it overwhelms resistance. In other words, this model is appropriate when vulnerability becomes saturated.

This model is defined by a threshold intensity ($a_T$) that, if exceeded, results in total loss (i.e., 100%) with a certain probability ($p_d$). The occurrence of total loss is modeled as a Bernoulli random variable with parameter $p_d$, resulting in the following expected value and variance of loss:

$$E(p) = \begin{cases} p_d & si\ a \geq a_T \\ 0 & si\ a < a_T \end{cases}$$ Equation 91

$$Var(p) = \begin{cases} p_d \cdot (1 - p_d) & si\ a \geq a_T \\ 0 & si\ a < a_T \end{cases}$$ Equation 92

### 9.1.4 Other Vulnerability Models

In general, any mathematical model capable of defining values for $E(p)$ and $Var(p)$ is valid for use in risk modeling. Some types of exposed elements, by their nature, cannot be modeled using vulnerability functions or binary models.

In this study, vulnerability for agricultural production under flood and drought hazards is handled using a specialized model. Crop vulnerability is modeled based on the yield calculation methodology developed

by the FAO (Food and Agriculture Organization of the United Nations). Vulnerability is defined as the yield loss that a crop experiences during a growing season affected by drought or waterlogging.

For livestock, vulnerability is quantified in terms of the ability of pasture or forage crops to provide sufficient caloric content to maintain livestock productivity. This is measured through the carrying capacity of the land and its variation due to simulated hazards.

### 9.1.5 Assignment of Vulnerability Model Types

To conduct risk modeling for the hazards and sectors considered in this study, different types of vulnerability models must be employed. Table 42 provides a summary of the model types used in each case.

Table 42. Types of vulnerability models by hazard-sector combination

| Exposure / Hazard | *Buildings* | *Infrastructure* | *Agriculture* | *Livestock* |
|---|---|---|---|---|
| ***Earthquake*** | Vulnerability Function | Vulnerability Function | | |
| ***River Flood*** | Vulnerability Function | Vulnerability Function | Specialized Model | Specialized Model |
| ***Coastal Flood*** | Vulnerability Function | | | |
| ***Drought*** | | | Specialized Model | Specialized Model |
| ***Volcanic Eruption*** | | Vulnerability Function / Binary Vulnerability | | |
| ***Landslides*** | | Binary Vulnerability | | |
| ***Tsunami*** | Vulnerability Function | | | |

The following sections detail the approach for developing the different vulnerability models listed in Table 41, except those corresponding to binary vulnerability, as no further elements are needed for their definition.

## 9.2 Building Vulnerability

### 9.2.1 Seismic Vulnerability

To assess the seismic vulnerability of a building, its lateral load capacity is considered typically condensed in its capacity curve. This curve is used to determine the structure's elastic and inelastic behavior under seismic demands, allowing for the derivation of a vulnerability function in terms of strong motion intensities. The equation employed in this case to estimate the expected value of loss takes the same form as Equation 87 in ATC-13 (ATC, 1985, 2002), but has been modified to be expressed in terms of interstory drift, as follows (Miranda, 1999; Ordaz, 2000)::

$$E[p|\gamma_i] = K_1 K_2 K_3 K_4 \left(1 - e^{\ln 0.5 \left(\frac{\gamma_i}{\gamma_0}\right)^{\varepsilon}}\right) \quad \text{Equation 93}$$

Where $\gamma_i$ is the máximum interstory drift, $\gamma_0$ and $\varepsilon$ are parameters defined according to the structural system, and $K - factors$ account for modifications to vulnerability due to plain irregularities ($K_1$) vertical irregularities ($K_2$), pounding with adjacent buildings ($K_3$), and previous unrepaired damage, short columns, among other factors ($K_4$).

The maximum interstory drift, $\gamma_i$, is determined from spectral acceleration using the following expression:

$$\gamma_i = \frac{\beta_1\beta_2\beta_3\beta_4(\eta N^{\rho})^2}{4\pi^2 N_h} \cdot Sa(T) \qquad \text{Equation 94}$$

Where $\beta_1$ is the ratio between the maximum lateral displacement at the top level of the structure and the spectral displacement, assuming a linear elastic behavior. This factor depends on the structural type and the number of stories. It is computed from the solution to the differential equation describing the behavior of a coupled system formed by a continuous shear beam and a flexural beam subjected to a height-dependent lateral load. The equation incorporates the mode of load application—given by the dimensionless parameter $\alpha$, and the contribution of shear and flexural deformations in the system. For instance, in a flexible building composed of concrete frames (without structural walls or bracing), shear deformations dominate, whereas in a structure with reinforced concrete walls, flexural deformations are predominant. Further details on how to estimate these parameters can be found in Miranda (1997), which presents results on the estimation of maximum lateral displacements using this approach.

$\beta_2$ represents the ratio between the maximum interstory drift and the global drift of the structure, defined as the maximum rooftop displacement divided by the total height. It depends on the contribution of shear and flexural deformations and the structural type. This factor reflects the tendency for lateral deformations during a strong earthquake not to distribute uniformly along the building height but rather to concentrate significantly in certain stories (see Miranda, 1997).

$\beta_3$ is the ratio between the maximum lateral displacement in the inelastic behavior model and that of the linear elastic model. This factor depends on the displacement ductility demand, the fundamental period of vibration of the structure, and the supporting soil type. It is determined using functions calibrated through statistical analyses of maximum lateral displacements of single-degree-of-freedom inelastic oscillators and their elastic counterparts, under hundreds of ground motion records from various soil types. For structures on soft soils, $\beta_3$ also depends on the ratio between the structure's fundamental period and the predominant period of the soil. For further details, see Miranda (1991, 1993, 1997). The global ductility demand of the structure is estimated based on spectral acceleration associated with the structure's vibration period, its lateral resistance, and the reduction factor of the applied loads. Structural lateral resistance depends on location and age, allowing classification according to the building codes in effect at the time of construction.

$\beta_4$ represents the ratio between the elastic and inelastic $\beta_2$ factors. This coefficient accounts for the different distribution of lateral loads along the height of the structure between the elastic and inelastic models. In the inelastic case, a strong concentration of force occurs. This factor depends on the number of stories and the level of inelastic deformation, measured in terms of displacement ductility demand. For more information, refer to Miranda (1997).

$\eta$ and $\rho$ are factors used to estimate the fundamental period of the structure based on the number of stories, $N$:

$$T = \eta N^{\rho}$$ Equation 95

These factors depend on the location, structural type, soil type, and year of construction. They reflect that the lateral stiffness of buildings in highly seismic areas tends to be greater than in those located in regions of lower seismicity. Additionally, they consider that structures built on soft soils are more flexible due to the foundation's flexibility. These parameters have been calibrated using analytical models, experimental results, and design considerations in accordance with construction codes.

- $h$ is the height of each story, which varies with structural type, geographic location, and construction date.
- $Sa(T)$ is the spectral acceleration, which depends on the fundamental period of vibration, the damping ratio of the structure, and the seismic hazard at the site.

To estimate all the parameters required to apply Equation 93, the structure's capacity curve is used. Also known as a pushover curve, it offers a reasonable approximation of the expected structural behavior in both the elastic and inelastic ranges under horizontal seismic loads. Methods for deriving these curves are detailed in ATC-13 (1985, 2002). The analysis considers variations in stiffness, structural period, and damping as interstory deformation increases.

Figure 143 illustrates a typical representation of a structural system's capacity curve. It is generally expressed in terms of base shear and the corresponding roof-level displacement.

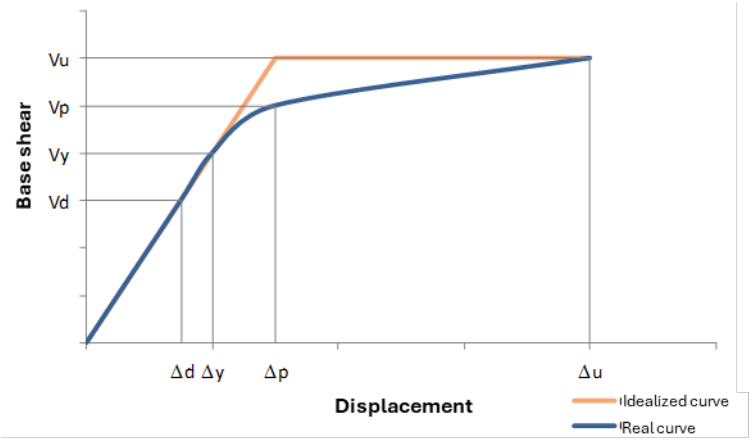


Figure 143. Illustration of a real and idealized capacity curve of a structural system

### 9.2.2 Vulnerability of Buildings to Flooding

In this study, building vulnerability is assessed based on the definition of archetypes. Archetypes are conceptual models of buildings that allow for the representation of the characteristics and conditions of their various components, from structural and construction elements to contents. Through this

representation, it becomes possible to combine specific loss functions for each building component to obtain an overall vulnerability function.

In general terms, it can be stated that the total loss resulting from the impact of flooding on an exposed element corresponds to the sum of the individual losses of all its components. Figure 144 schematically illustrates the types of content found in, for example, healthcare buildings.

Figure 144. Illustration of typical contents in a healthcare facility

Various archetypes will be defined to encompass different types of buildings according to their use sector and their typical structural and construction characteristics. An archetype is defined by its set of components. Each component has a defined condition within the archetype, characterized by its location (floor), local foundation, watertightness, protection (provided by other components), and type (thermal, mechanical, electrical, electromechanical, or construction-related). Each component also has an economic value that contributes to the building's total replacement value. Additionally, each component is associated with a damage function, which relates the flood depth at the component's relative location to the probability distribution of its potential loss.

The resulting vulnerability function is obtained by a weighted combination of all individual damage functions. These are adjusted vertically according to each component's position within the archetype and weighed by the individual value of each component. Figure 145 illustrates the construction of a vulnerability function based on archetypes.

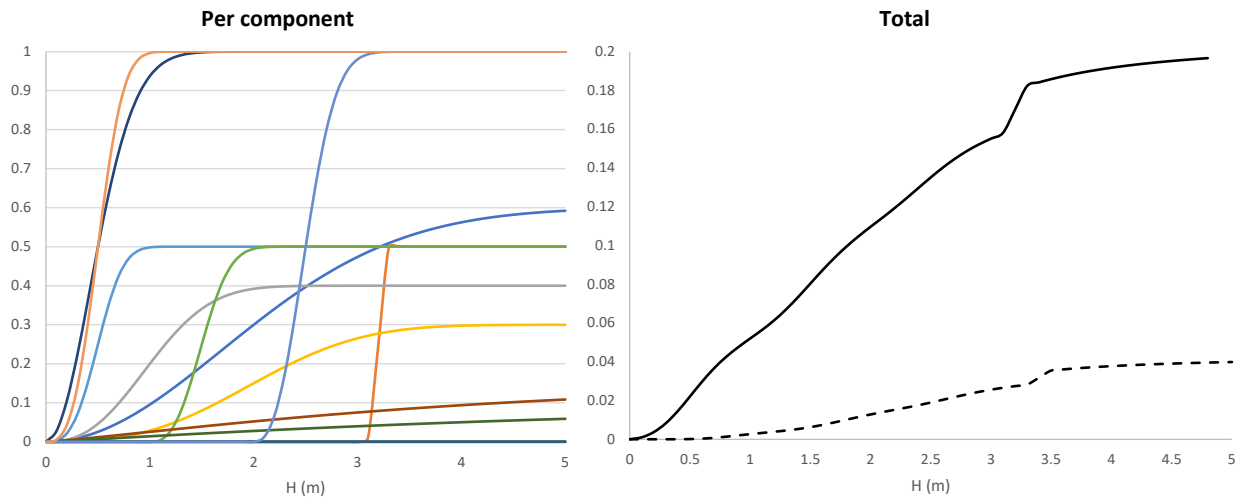


Figure 145. Illustration of a vulnerability function for a building archetype
*By component → Total*

## 9.3 Vulnerability of Infrastructure Elements

In the case of infrastructure elements, an archetype-based approach is also proposed for all hazards and all types of components. Infrastructure component archetypes are simplified representations of the various subcomponents that make up an infrastructure asset. These may include buildings, structures, machinery, electrical or electronic equipment, among others. These subcomponents collectively contribute to the functionality of the infrastructure asset, each exhibiting unique characteristics and responses to hazards depending on their position within the archetype. Consequently, each subcomponent is associated with distinct vulnerability functions that contribute to the overall vulnerability function of the archetype.

Assessing the condition of a component involves defining several characteristics such as elevation, type of foundation, water resistance, protection offered by other components, and component type. While this list is not exhaustive, it is considered sufficient to characterize the condition of any component within the archetype. Furthermore, all elements within the archetype have varying degrees of importance in the operation of the infrastructure. Although the use of cost as a criterion for assigning importance may be subject to debate, it is adopted here as a proxy indicator to evaluate the relative importance of each component in most archetypes.

The individual vulnerability functions for a given hazard are aggregated to produce a general vulnerability function for the archetype, with component value shares used as weighting factors. Figure 141 illustrates vulnerability functions for three thermal power generation plant archetypes, evaluated under different hazard scenarios.

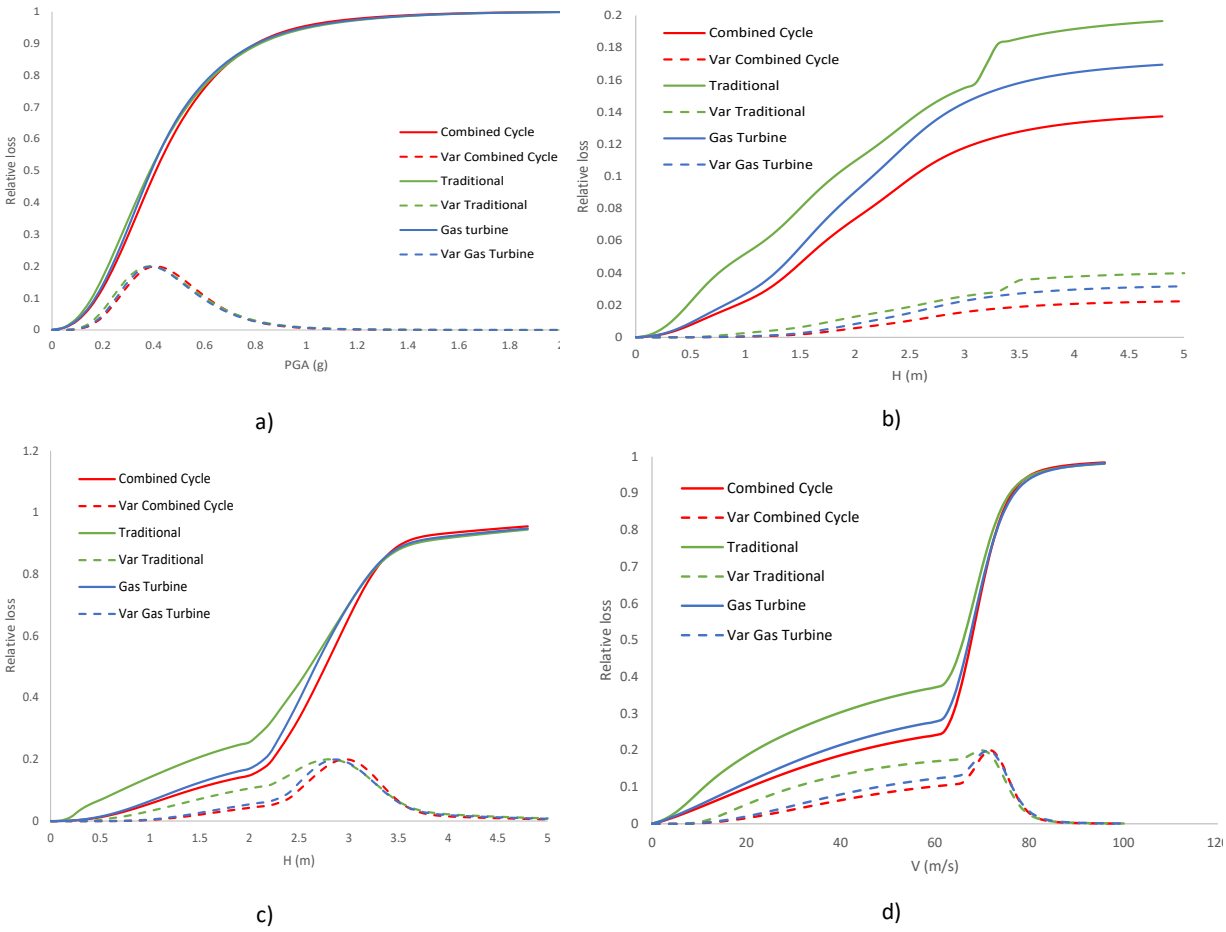


Figure 146. Vulnerability functions for three thermal power plant archetypes exposed to: a) earthquake, b) flood, c) tsunami, d) strong winds.

## 9.4 Vulnerability of Crops to Extreme Weather Events

This study applies the simulation-based approach proposed by Bernal et al. (2017). Crop yield modeling follows the conceptual framework developed by the FAO. Loss from a simulated hydrometeorological hazard is defined in terms of the yield reduction experienced by the crop. Since an agronomic crop response model is used, vulnerability curves or functions are not employed.

The crop response model has four main components: climate (in terms of temperature, precipitation, evaporative demand, and atmospheric carbon dioxide concentration), crops (development, growth, and yield processes), soil (water and salt balance), and management and administration (agricultural practices) (Steduto et al., 2012).

Temperature influences crop development, while precipitation plays a key role in determining the soil water balance within the root zone. Therefore, the main climate variables used in the model are daily maximum and minimum air temperatures, total daily precipitation, and atmospheric evaporative demand, expressed as evapotranspiration. Temperature and precipitation follow similar procedures. Evapotranspiration is calculated using the Penman-Monteith method (see Annex 1). Additionally,

atmospheric carbon dioxide ($CO_2$) concentration is included, as it affects crop expansion and stomatal conductance. Default annual $CO_2$ concentration values are taken from the Mauna Loa Observatory in Hawaii[17].

Crops are modeled through the biological, physical, and chemical processes that determine their yield. The model simulates crop growth and development throughout its specific growth cycle, including foliage expansion, root deepening, and biomass accumulation. All phenological stages (or growth stages) are considered: vegetative, flowering, yield formation, and maturation, with specific phenological patterns for herbaceous or forage crops.

Phenology refers to crop development stages and their duration, which may be defined in Growing Degree Days (GDD) or calendar days. Canopy Cover (CC) represents the amount of foliage, which is proportional to both the amount of water transpired and the amount of biomass produced. The root depth subcomponent models the process by which roots deepen at a constant relative rate during the growth phase until yield formation. The model may also include the effects of restrictive soil layers or shallow water tables that limit root growth.

Figure 147 shows the canopy cover and root depth development curves as a function of time. The top curve represents the evolution of canopy cover, determined by the Canopy Growth Coefficient (CGC) and Canopy Decline Coefficient (CDC). Canopy cover is expressed as the fraction of soil shaded by leaves or above-ground plant parts, with its maximum level ($CC_x$) being crop-specific. The second curve illustrates the effective root depth, from its minimum value ($Z_n$) at planting to its maximum value ($Z_x$) at physiological maturity. Together, these curves represent crop development and its interaction with soil and atmosphere.

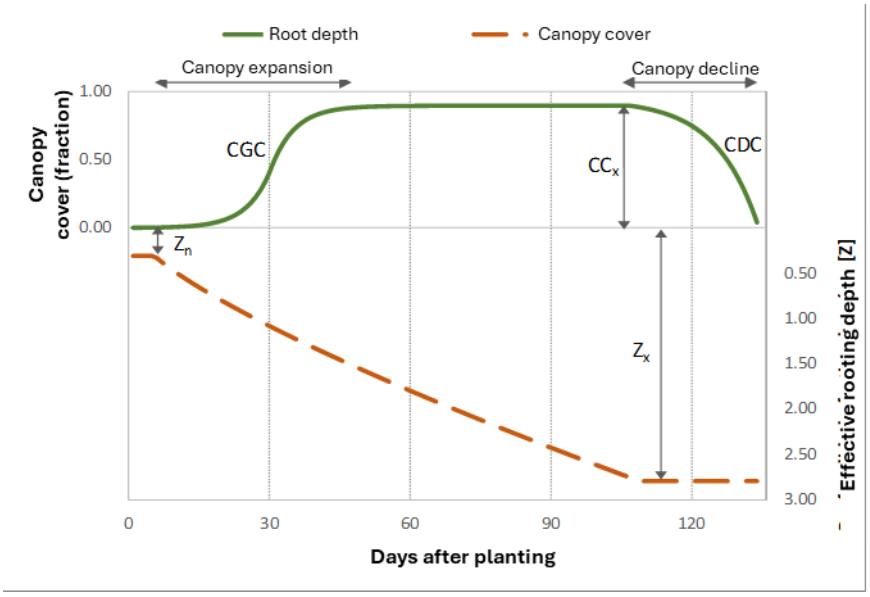


Figure 147. Time-based illustration of canopy cover and root depth development. Adapted from Steduto et al., 2012.

[17] www.esrl.noaa.gov/gmd/obop/mlo/

The model calculates crop transpiration separately from soil evaporation. The crop transpiration subcomponent determines water use by the plant when stomatal opening is not limited by stress. Soil evaporation accounts for water loss from moist soil surfaces not shaded by vegetation. Biomass production is defined as:

$$B = WP * \sum Tr$$ Equation 96

where $B$ is the accumulated biomass production, $Tr$ is the cumulative crop transpiration over the biomass production period, and $WP$ is the water productivity parameter, expressed as the amount of dry biomass (kilograms) produced per unit of area (m²) and transpired water (mm).

The model's robustness stems from the conservative nature of WP, which remains stable across a range of environments when normalized for evaporative demand.

Finally, a Harvest Index ($HI$) is used to estimate the yield $Y$ from the produced biomass $B$. This distinction between biomass and yield allows for separate evaluation of climatic effects on biomass production and harvest:

$$Y = HI * B$$ Equation 97

Figure 148 shows the time-based change of the Harvest Index ($HI$**)** for fruit or grain crops during the yield formation phase (from flowering to physiological maturity). $HI$ starts at zero, increases slowly at first, then accelerates and continues at a constant rate until reaching an upper level $HI_o$. This optimal harvest index is crop-specific, and data are typically available to determine it.

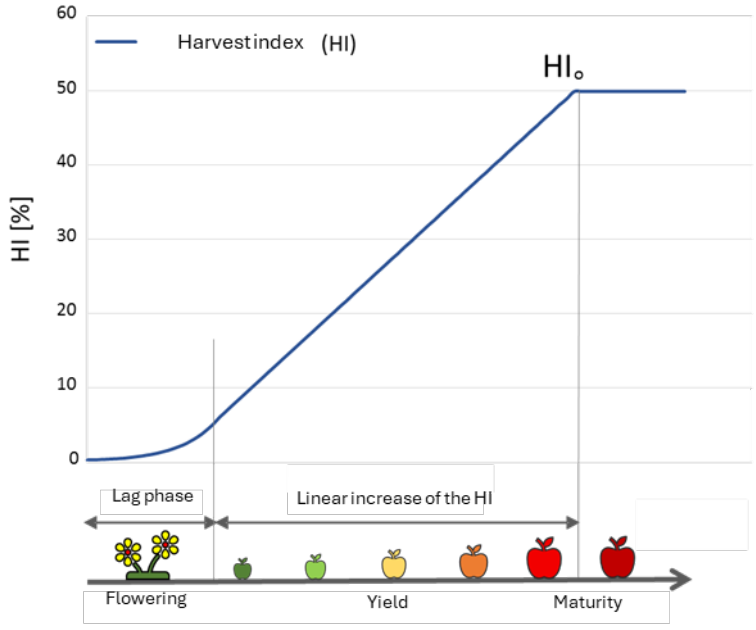


Figure 148. Time-based change in the harvest index (HI) for fruit or grain crops. Adapted from Steduto et al., 2012.

The soil is modeled as a vertical profile and includes the characteristics of the water table within the plant's root system. The root zone is expressed as a control volume where water balance is estimated. Soil may be subdivided into layers of variable depth, each with physical characteristics such as saturated water content, Field Capacity (FC), Permanent Wilting Point (PWP), and saturated hydraulic conductivity ($K_{sat}$). These values are used to calculate soil evaporation, internal drainage, deep percolation, surface runoff, and capillarity.

Figure 149 presents a simplified representation of the root zone model, where $D_r$ is root depletion and $W_r$ is the equivalent water depth. Total Available Water (TAW) is the amount of water retained in the root zone between FC (upper limit) and PWP (lower limit).

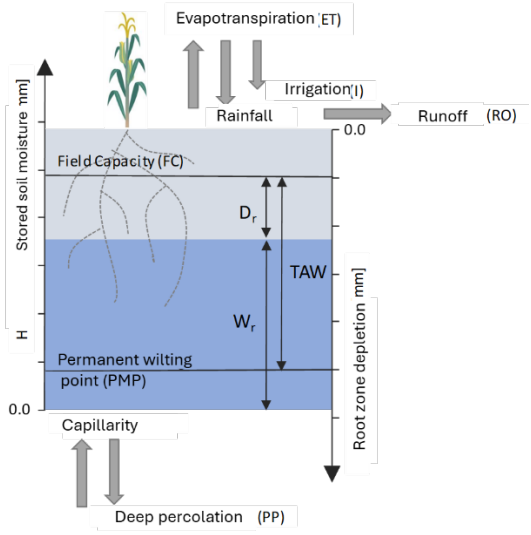


Figure 149. Control volume of the root zone. Adapted from Steduto et al., 2012.

Water balance within the root zone is computed on a daily basis throughout the crop's development. Water inflows considered in the model include rainfall, irrigation (if present), and capillary rise. Water outflows include runoff, evapotranspiration, and deep percolation.

In addition to the core components of crop development, the model incorporates stress coefficients ($K_s$), which are mathematical functions that modify parameters affected by adverse climatic conditions. As shown in Figure 150, $K_s$ values range from 0 (total stress) to 1 (no stress), and follow linear or convex functions.

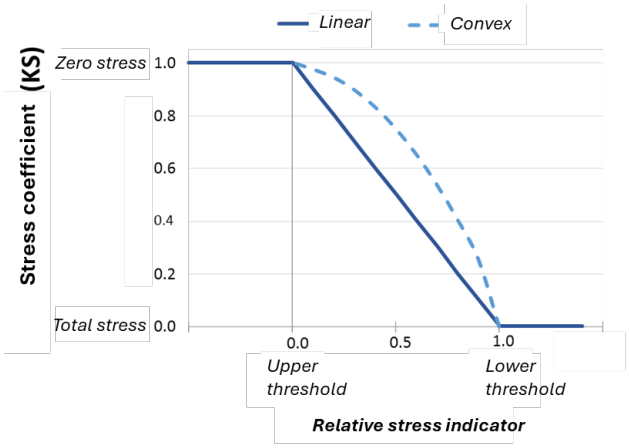


Figure 150. Stress coefficient function. Adapted from Steduto et al., 2012

The model simulates the effects of climatic events on five processes: canopy growth, stomatal conductance, early senescence, root deepening, and harvest index. These are shown as dotted lines in Figure 151, which provides an overview of the crop yield development scheme. A general summary of the calculation process is outlined below. All steps are computed using daily time intervals.

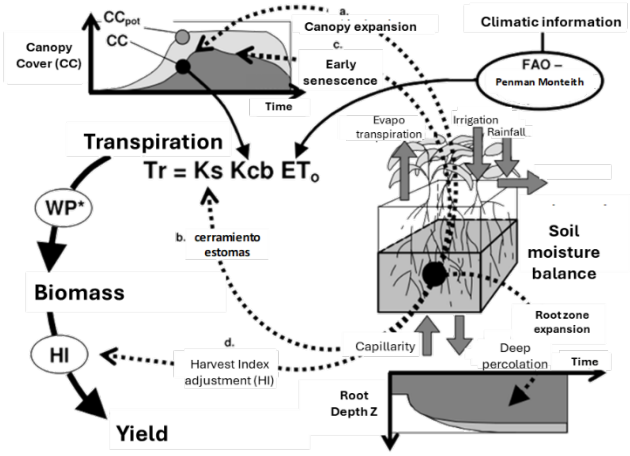


Figure 151. Schematic representation of the crop response model. Adapted from Raes et al., 2011

1. *Soil water balance*: Calculates the amount of water stored in the root zone by accounting for incoming and outgoing flows.
2. *Canopy expansion:* Simulates green canopy expansion by reducing the canopy growth coefficient using the stress coefficient for expansion $K_{s,exp,w}$, and modifying the canopy decline coefficient with the senescence stress coefficient $K_{s,sen}$.
3. *Transpiration:* Potential evaporation is calculated using a crop coefficient $K_{cb}$ and water stress coefficient $K_s$, as shown in the equation below:

$$Tr = K_s(K_{cb}CC^*)ETo \quad \text{Equation 98}$$

The crop transpiration coefficient $K_{cb}$ must be continuously adjusted based on simulated canopy cover to account for aging and senescence effects. The stress coefficient $K_s$ used here corresponds to stomatal stress $K_{s,sto}$, also ranging from 1 (no stress) to 0 (total stress).

- *Above-ground biomass:* The relationship between biomass produced and water consumed is known as water productivity ($WP$), which tends to be linear, as shown in Equation 99. To account for altered conditions, a normalized water productivity $WP^*$ is used, incorporating atmospheric $CO_2$ concentration and evaporative demand (Dirk Raes et al., 2011). Biomass accumulation is calculated on a daily basis as follows:

.

$$B = WP^* \sum_i \frac{Tr_i}{ETo_i} \quad \text{Equation 99}$$

Where $WP^*$ is multiplied by the ratio of daily crop transpiration to reference evapotranspiration $\frac{Tr_i}{ETo_i}$, accumulated over the crop development period.

4. *Yield:* As mentioned earlier, yield is calculated by multiplying above-ground biomass by a harvest index that depends on the crop type. To account for water stress, the harvest index must be adjusted from its reference value $HI_o$ (under optimal conditions) to the actual value using the stress coefficient:

$$Y = K_s * HI_o * B \quad \text{Equation 100}$$

Production loss is calculated as the difference between the expected yield under optimal conditions and the actual yield, multiplied by the productive area and the producer's cost of the agricultural product:

$$P = (Y_{op} - Y) \cdot A \cdot C \quad \text{Equation 101}$$

## 9.5 Vulnerability of Crops to Waterlogging

The methodology used to estimate crop response to excess water conditions (flooding, waterlogging, saturated soils) considers the phenological characteristics of plants that determine their biological response to oxygen deficiency in saturated soils. Generally, excessive soil moisture directly impacts the chemical and biological processes that occur in both the plant and the soil, with short- and long-term consequences for plant development. The first effect is the depletion of soil oxygen, preventing roots from obtaining the oxygen necessary for cell division, growth, and nutrient transport. This condition becomes critical as air temperature increases, exacerbating oxygen deficiency in waterlogged soils under high temperatures.

Crop susceptibility determines the biological response to oxygen deficiency; thus, flood-tolerant crops exhibit lower yield losses compared to those that lose their recovery capacity after prolonged exposure to

saturated soil conditions. In other words, crop susceptibility defines yield performance under excess soil moisture.

Vulnerability modeling is conducted using vulnerability curves, which relate yield loss to the accumulated surface water depth. These curves are based on the crop response model presented in Section 9.4. Vulnerability is defined in terms of the yield loss experienced by the crop during a prolonged period of soil saturation accompanied by surface water accumulation.

### 9.5.1 Crop Response to Saturated Soils

Water stress conditions due to excess moisture are represented by a stress coefficient ($K_{saer}$) and threshold indicators of stress. $K_{saer}$ is a modifier that quantifies the intensity of the effect caused by oxygen deficiency on crop-specific growth processes. As illustrated in Figure 152, $K_{saer}$ values range from 0 (total stress) to 1 (no stress), following a linear function. The thresholds for water stress are related to the volume of air relative to the total pore volume in the soil. The stress coefficient is zero when the soil is aerated, and it reaches one (maximum stress) when the soil is saturated due to flooding and no oxygen is available to the plant.

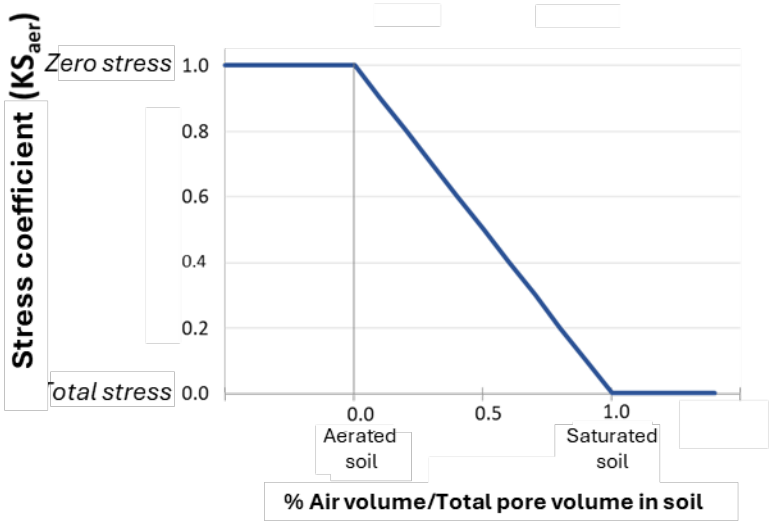


Figure 152. Function of the oxygen deficiency stress coefficient (K_saer) (Based on Steduto et al., 2012)

The coefficient $K_{saer}$ alters the calculated transpiration value, which also affects the total evapotranspiration and biomass production:

$$Tr = K_{saer}(K_{cb}CC^{*})ETo \qquad \text{Equation 102}$$

Crop susceptibility is specified by defining the upper threshold that indicates, for each crop type, the soil pore air volume considered healthy and non-restrictive for growth. Additionally, the number of consecutive days the soil remains saturated must be established to consider the air deficiency harmful to the plant.

## 9.6 Vulnerability of Livestock Production Systems

Vulnerability modeling for the livestock sector is based on the evaluation of the physiological characteristics of animals that determine their biological response to food intake. Feed availability is derived from the response of natural pastures (or other forage crops consumed directly and produced in the grazing area) to water availability, which may be reduced under drought conditions. The occurrence of frost or other weather phenomena also affects the amount of dry matter available to the animal. On the other hand, feed demand depends on the animal type, age, weight, physiological status, and environmental conditions (temperature and rainfall). Thus, animal susceptibility links feed demand and supply, and losses are determined based on the difference between the volume of feed animals stop consuming and the amount they should consume to reach optimal weight.

Vulnerability is defined in terms of the reduction in feed consumed by animals due to declines in the dry matter yield of natural pastures. Since a physiological model is applied to estimate feed intake reduction, no vulnerability curves or functions are used. The methodology proposed by this consulting group is currently the only one employing a model of this complexity for probabilistic risk assessment in the livestock sector.

### 9.6.1 Yield of Natural Pastures

Following the crop response model to water availability proposed by FAO and presented in Section 9.4, the yield of natural pastures is estimated under temperature stress conditions. Figure 153 outlines the calculation scheme for usable dry matter supply, derived from natural pasture biomass production. The process begins with defining climatic conditions (daily time series of precipitation and temperature) that determine frost events. Soil type and grass species—both of which vary depending on location within the country—are also defined. To adjust results to local conditions of climate and pasture production for animal feed, a reference yield value for the pasture must be included, ideally disaggregated by month or season, depending on data availability.

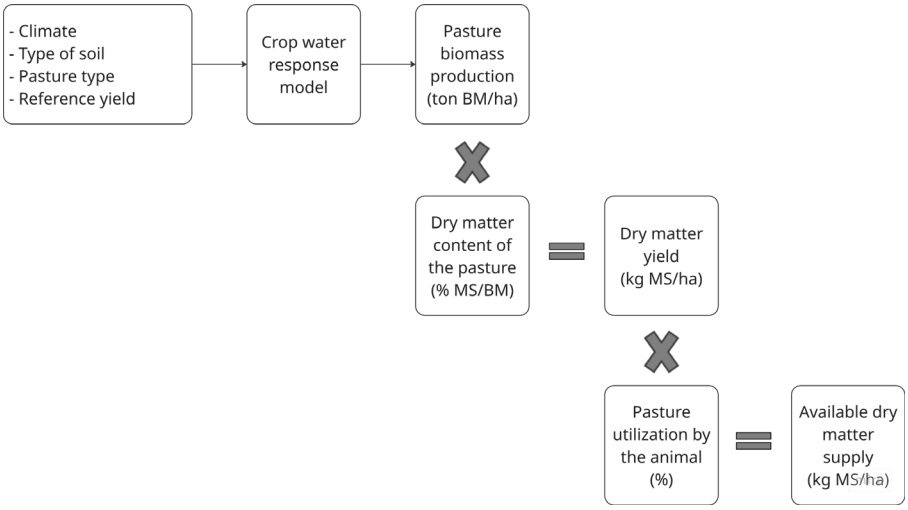


Figure 153. Scheme for calculating usable dry matter supply from pasture biomass

Using data on climate, grass species, and soil type, the pasture's response to water availability during a hazardous event can be estimated. The main outcome is the amount of biomass produced during the year in which the simulated event occurs.

Understanding that nutrients are concentrated in the dry matter of feed, it is necessary to know the dry matter content of the pasture to determine the total proportion of feed that is usable by animals. Finally, recognizing that not all available feed is actually consumed, a pasture utilization rate is defined—this is the proportion of offered feed that is effectively consumed. Factors affecting pasture utilization include accessibility, grazing method, seasonality, and forage loss (due to trampling, leaf death, defecation, etc.). In conclusion, biomass content and utilization rate define the amount of usable dry matter that contains the nutrients required to feed animals. This dry matter represents the available feed for a group of animals grazing in a defined area, according to the scale of analysis.

### 9.6.2 Grass Consumption as the Primary Feed Source for Livestock

The goal of livestock production is to raise healthy animals that can be used for meat, hide, or milk. Livestock production, therefore, seeks to feed animals so they reach a reference standard weight, depending on their species and physiological state, by the time they are sold or slaughtered. Grazing-based livestock production is limited by the voluntary intake of pasture, which must be estimated to determine the quantity of forage that should be made available to the animals.

The vulnerability model for the livestock sector used in this study calculates actual animal intake through two main components: the potential intake, which depends on the animal, and the relative intake, which depends on pasture availability.

The potential intake of pasture depends on the animal's characteristics (weight and physiological state) and is defined as the amount of feed it can consume under conditions of abundance and high quality. Intake increases with animal weight and higher energy requirements. Conversely, feed intake may decrease under thermal stress or illness. Potential intake can be modeled as.

$$I = j \cdot A \cdot Z(1.7 - Z) \cdot CF \cdot m \cdot p \cdot t \qquad \text{Equation 103}$$

where $j$ is a species-specific factor (e.g., 0.025 for cattle), $A$ is the animal's reference optimal weight (kg), $Z$ is the relative body size, and $CF$ is a correction factor based on the animal's condition at the time of analysis. $m, p, t$ are adjustment factors for lactation, weaning, and thermal stress, respectively.

The maximum limit for pasture consumption is defined by the animal's energy demand and physical feeding capacity, which, relatively speaking, depends on body size. A potential model is used to define the animal's growth curve:

$$N = A - (A - B)^{-kTA^{-0.27}} \qquad \text{Equation 104}$$

Where $N$ is the normal weight limit (kg), $A$ is the optimal reference weight (kg), $B$ is birth weight (kg), $T$ is age in months, and $k$ is a species-specific factor.

From the normal weight, relative body size $Z$ is defined as $N$ / $A$. The condition ratio RC refers to the ratio of the animal's current weight W to its normal weight at that age: $RC = W/N$. If $RC > 1$, the animal

exceeds the weight expected from the growth curve. In such cases, the potential feed intake is adjusted with the factor $CF$, as shown:

$$CF = RC(1.5 - RC)/0.5 \quad \text{Equation 105}$$

Animals tend to increase voluntary intake during lactation to compensate for the energy cost of milk production. This increase depends on time since parturition and the number of offspring, and is modeled as:

$$m = 1 + aM^b \exp\big(b(1 - M)\big)\, L \cdot D \quad \text{Equation 106}$$

where $M = T/c$, days in lactation, c = time to peak intake),, $L$ reflects the animal's condition at parturition, $D$ is the ratio of current to optimal milk production.

In the first weeks of life, an animal's intake of pasture depends more on rumen development than on weight. The proportion of pasture in the diet ($p$) is defined as:

$$p = (1 - P_{milk})/(1 + \exp(-a(T - X)) \quad \text{Equation 107}$$

Where $P_{milk}$ is the proportion of milk in the diet, $T$ is the number of days since birth, $X$ is a reference time (species-specific) and, $a$ is a species-specific coefficient.

During grazing, animals may suffer thermal stress, which affects their potential feed intake. In cold conditions, intake may increase by up to 1% per °C below the species-specific critical temperature. In hot conditions, intake may decrease by up to 2% per °C above the maximum reference temperature for cattle, and by 1% for other species. This effect is modeled in term $t$ of Equation 103.

Relative intake refers to the proportion of potential intake that an animal is expected to consume under restricted conditions, depending on pasture availability and quality. This intake is scaled between 0 and 1 and increases with easier access and higher-quality forage. Estimating relative intake is complex due to the high variability of plant species in natural grasslands and animals' selective feeding behavior—they preferentially consume higher-quality leaves, avoiding stems, dead, or trampled vegetation.

Pasture quality is related to its digestibility, defined as the time required for food to pass through the animal's digestive system. There is a positive correlation between digestibility and voluntary intake, expressed as:

$$pRQ = 1 - 1.7 * (\max\{\big(0.8 - \big(1 - P_{legume}\big)g\big) - D\big), 0.0\} \quad \text{Equation 108}$$

where $RQ$ is relative digestibility, $P_{legume}$ is the proportion of legumes in the pasture, $D$ is pasture digestibility and, $g$ is a photosynthesis-pathway coefficient (0 for C3 grasses, 0.16 for C4 grasses).

When forage availability is high, actual intake depends primarily on voluntary intake and pasture quality. If forage biomass drops below a certain threshold (e.g., ~3 tons of dry matter/ha for cattle), grazing becomes harder and more energy-consuming. The relative availability $F$ of pasture is linked to biomass $B$ as follows:

$$p\frac{dF}{dB} = 1 - F$$ Equation 109

$$pF = 1 - \exp(-aB)$$ Equation 110

Where $a$ is a constant rate dependent on pasture structure and animal type.

The model also includes the effect of selective intake. Animals do not consume all available forage but favor live over dead leaves, young over mature leaves, and leaves over stems. The selectivity index ($IS$) is defined based on forage availability $B$ (kg DM/ha) and its digestibility $D_{fd}$ (%):

$$IS = \max\{a.Ln(D_{fd} - b) + c + d.B + 1, 1\}$$ Equation 111

Where $a = -0.249$, $b = 23.7$, $c = 0.939$, $d = 8.3x10^{-5}$. This index is used to estimate the digestibility of selected forage ($D_{fs}$):

$$D_{fs} = IS.D_{fd}$$ Equation 112

The relative intake model does not account for limitations due to protein or mineral content, nor does it include the effect of water availability on digestibility.Actual intake ($C$) in kg of dry matter (DM) is the product of potential intake ($I$) and relative intake, which depends on forage availability $F$, relative quality $RQ$, and selectivity $IS$:

$$C = I * F * RQ * IS$$ Equation 113

Loss estimation in the livestock sector is based on the difference between actual livestock load and the carrying capacity of each grazing land unit. Carrying capacity is defined as the ratio of feed supply (pasture dry matter production) to feed demand (actual dry matter intake by animals). It is expressed in livestock units per hectare (LU/ha):

$$Carrying\ Capacity\ = \frac{Feed\ Supply}{Feed\ Demand} = \frac{DM\ Production}{Actual\ DM\ Intake\ per\ Animal}$$ Equation 114

Economic loss is calculated as the difference between the actual livestock load and the land's carrying capacity under simulated meteorological conditions, multiplied by the valuation of each animal according to the productive system:

$$Loss\ = (Livestock\ Load_{UTG} - Carrying\ Capacity_{UTG}) * Animal\ Valuation_{SP}$$ Equation 115

## 10 REFERENCES


Akaike, H. (1974). A new look at the statistical model identification. IEEE Transactions on Automatic Control, AC-19, 716–723

Adrián, J. & Chacón, E. (2019). Adaptación al cambio climático y gestión del riesgo de desastres en Costa Rica. San José, Costa Rica: UNA.

Aguilar, I., & Alvarado, G. E. (2014). Pérdidas humanas y económicas causadas por el vulcanismo en Costa Rica entre 1953 y 2005. Revista Geológica de América Central, 51, 93-128.

Alfaro, E. J. (2007). Ciclos secos y lluviosos en Centroamérica y sus relaciones con el Atlántico y el Pacífico Tropical. Tópicos Meteorológicos y Oceanográficos, 10(2), 76-84.

Allen, R. G., Pereira, L. S., Raes, D., & Smith, M. (1998). Crop evapotranspiration: Guidelines for computing crop requirements. Irrigation and Drainage Paper No. 56, FAO, (56), 300. https://doi.org/10.1016/j.eja.2010.12.001

Alonso-Henar, J., Montero, W., Martínez-Díaz, J. J., Álvarez-Gómez, J. A., & Zúñiga, F. R. (2013). The Aguacaliente fault, source of the Cartago 1910 destructive earthquake (Costa Rica). Terra Nova, 25(1), 60-67.

Alvarado Induni, G., Muller, C., Pacheco, J., Angarita, M., Sánchez, B., & Avard, G. (2020). El deslizamiento de las Torres del Irazú del 2020 (Costa Rica): antecedentes, colapso y situación actual. Technical Report.

Alvarado Rojas, M., Durán Vargas, D., Fallas Corrales, K., Hernández Araya, L. D., & Valverde Sánchez, R. (2006). Amenazas y vulnerabilidad: El caso de los ríos Reventado y Toyogres, Cartago. Reflexiones, 85(1-2), 331-349.

Alvarado, G. E. (2005). Costa Rica: Land of Volcanoes. San José, Costa Rica: Editorial Universidad de Costa Rica.

Alvarado, G. E. (2011). Los volcanes de Costa Rica. 3ª ed. San José, Costa Rica: EUNED.

Alvarado, G. E. (2021). Clasificación de la amenaza volcánica en Costa Rica. En CNE (Ed.), Amenaza volcánica en Costa Rica (pp. 10-29). San José, Costa Rica: CNE.

Alvarado, G. E., & Patiño, L. F. (2017). The history of volcanology in Costa Rica: From the Amerindian legends to the beginning of the twenty-first century. En:Geological Society, London, Special Publications, 442(1), 139-163.

Alvarado, G. E., & Schröder, W. (2011). Mapa geológico de Costa Rica y principales amenazas geológicas. Escala 1:400,000. San José: ICE.

Alvarado, G. E., Benito, B., Staller, A., Climent, Á., Camacho, E., Rojas, W., Marroquín, G., Molina, E., Talavera, J. E., Martínez-Cuevas, S., et al. (2017). The new Central American seismic hazard zonation: Mutual consensus based on up-to-date seismotectonic framework. Tectonophysics, 721, 462–476. https://doi.org/10.1016/j.tecto.2017.10.013

Alvarado, G. E., Brenes-André, J., Núnez, D., Borbon, J., Ramírez, M. A., Alpízar, Y., Núñez, S., Sibaja, J. P., & Esquivel, L. (2023). Actualización del análisis del peligro volcánico del Arenal, Costa Rica. Instituto Costarricense de Electricidad (ICE).

Alvarado, G. E., Brenes-André, J., Venegas, L., Alpízar, Y., Núñez, S., Sánchez, M., Abarca, K., Abarca, J., Báez, W. A., Sibaja, J. P., Esquivel, L., & Arcia, T. (2022). Análisis del peligro volcánico del Rincón de la Vieja, Costa Rica. Instituto Costarricense de Electricidad (ICE).

Alvarado, G. E., Campos-Durán, D., Brenes-André, J., Alpízar, Y., Núñez, S., Esquivel, L., Sibaja, J. P., & Fallas, B. (2021). Peligros volcánicos del Irazú, Costa Rica. Comisión Nacional de Prevención de Riesgos y Atención de Emergencias (CNE), Unidad de Investigación y Análisis del Riesgo.

Alvarado, G. E., Esquivel, L., Sánchez, B. E., & Alfaro, J. C. (2020). Actualización del peligro volcánico del Poás, Costa Rica. Comisión Nacional de Prevención de Riesgos y Atención de Emergencias (CNE), Unidad de Investigación y Análisis del Riesgo.

Alvarado, G. E., Esquivel, L., Sánchez, B. E., & Alfaro, J. C. (2020). Peligro volcánico del Turrialba, Costa Rica. Comisión Nacional de Prevención de Riesgos y Atención de Emergencias (CNE), Unidad de Investigación y Análisis del Riesgo.

Alvarado, G., Vega, A., Campos, N., & Chaves, I. (2014). El riesgo derivado de la amenaza volcánica en Costa Rica. San José, Costa Rica: CNE.

Andersen, E. Sparre. (1957). On the collective theory of risk in case of contagion between claims. Trans. XVth Int. Congress Actuaries. Vol. 2. No. 6. 1957.

Arroyo-Solórzano (2023). Riesgo sísmico ante terremotos potencialmente perjudiciales en la Gran Área Metropolitana de Costa Rica (GAM) (in English: Seismic risk assessment for potentially damaging earthquakes in the Metropolitan Area of Costa Rica (GAM)). Revista Geológica de América Central, 68, 2023, doi: 10.15517/rgac.2023.54878.

Arroyo-Solórzano, M., & Linkimer, L. (2021). Spatial variability of the b-value and seismic potential in Costa Rica. Tectonophysics. https://doi.org/10.1016/j.tecto.2021.228951

Astorga, Y. (2019). “En los últimos 5 años, Costa Rica enfrentó la sequía más severa de los últimos 75 años”. iAgua – Entrevista (2 oct 2019).

Avard, G., Mora, M., Bakkar, H., Alvarado, G. E., & col. (2021). Volcano hazard and surveillance in Costa Rica. Volcanica, 4(S1), 141-161.

Baker, S. (2020). Pasture recovery after bushfires. NSW DPI Pastures, Tamworth.

Banimahd, S. A., & Khalili, D. (2013). Factors Influencing Markov Chains Predictability Characteristics, Utilizing SPI, RDI, EDI and SPEI Drought Indices in Different Climatic Zones. Water Resources Management, 27(11), 3911–3928. https://doi.org/10.1007/s11269-013-0387-z

Barquero, J. (1977). El volcán Irazú y su actividad. Heredia, Costa Rica: Universidad Nacional.

Barquero, R. (Ed.). (2005). Los principales volcanes activos de Costa Rica. San José, Costa Rica: RSN-UCR/ICE.

Bernal. G., Cardona, O.D., Marulanda, M., Carreño, M. L. (2021). Dealing with Uncertainty using Fully Probabilistic Risk Assessment for Decision Making. Chapter 14 in: Eslamian, S., & Eslamian, F. (Eds): Handbook of Disaster Risk Reduction for Resilience. Springer.

Birkel Dostal, C. (2006). Sequía hidrológica en Costa Rica: ¿Se han vuelto más severas y frecuentes en los últimos años? Revista Reflexiones, 85(1-2), 31-45.

Bloemendaal, N., Haigh, I. D., de Moel, H., Muis, S., Haarsma, R., & Aerts, J. C. J. H. (2020). Generation of a global synthetic tropical cyclone hazard dataset using STORM. Scientific Data, 7(1), 1-12. [40]. https://doi.org/10.1038/s41597-020-0381-2, https://doi.org/10.1038/s41597-020-0381-2

Bonilla Vargas, A. (2014). Patrones de sequía en Centroamérica. www.gwpcentroamerica.org

Bonilla, A. (2014). Patrones de sequía en Centroamérica: impacto en la producción de maíz y frijol y uso del índice normalizado de precipitación. Ponencia, UICN/Universidad de Costa Rica.

Brenes, A., & Bonilla, A. (2012). La Niña 2010-2012. Estudio de caso Costa Rica. Global Assessment Report on Disaster Risk Reduction, GAR 2013. Corporación OSSO.

Brunner, G., & Bonner, V. (1994). Hydrologic Engineering Center - River Analysis System HEC-RAS (TP-147). Retrieved from http://www.hec.usace.army.mil/publications/Techni–alPapers/TP-147.pdf

Burbach, G. V., Frohlich, C., Pennington, W. D., & Matumoto, T. (1984). Seismicity and tectonics of the subducted Cocos plate. Journal of Geophysical Research, 89(B9), 7719-7735.

Calderón, A., & Silva, V. (2019). Probabilistic seismic vulnerability and loss assessment of the residential building stock in Costa Rica. Bulletin of Earthquake Engineering, 17(8), 1257-1284.

Campos-Durán, D., & Barrantes-Castillo, G. (2020). Evaluación de la vulnerabilidad asociada a la actividad del volcán Turrialba (2010-2017) en Santa Cruz de Turrialba. Revista Geológica de América Central, 63, 67-86.

CAPRA. (s.f.). Análisis probabilista de amenazas y riesgos naturales - Amenaza por deslizamientos en el distrito de Orosí.

Carbon Decisions International (CDI). (2015). Patrones y factores de cambio de la cobertura forestal natural de Costa Rica, 1987-2013. Informe preparado para el Gobierno de Costa Rica bajo el Fondo de Carbono del Fondo Cooperativo para el Carbono de los Bosques (FCPF).

Cardona, O., Ordaz, M., Mora, M., Salgado, M., Bernal, G., Zuloaga, D., González, D. (2013). Global Risk Assessment: A fully probabilistic seismic and tropical cyclone wind assessment. Bogotá: International Journal of Disaster Risk Reduction.

Cardona, O., Ordaz, M., Yamín, L., Arámbula, S., Marulanda, M., & Barbat, A. (2008). Probabilistic seismic risk assessment for comprehensive risk management modeling for innovative risk transfer and loss financing mechanisms. Beijing: 14 WCEE.

Cardona, O.D. (1986a). Análisis de vulnerabilidad y evaluación del riesgo sísmico. Seminario Nacional sobre Prevención y Manejo de Catástrofes Naturales, Asociación de Ingenieros Estructurales, octubre 1986, Medellín.

Cardona, O.D. (1986b). Estudios de vulnerabilidad y evaluación del riesgo sísmico: Planificación física y urbana en áreas propensas. Simposio International sobre Neotectónica y Riesgos Volcánicos, Revista CIAF No. 11, diciembre 1986, Bogotá.

Cardona, O.D. (1986c). Estudios de vulnerabilidad y evaluación del riesgo sísmico: Planificación física y urbana en áreas propensas. Asociación Colombiana de Ingeniería Sísmica. Reporte AIS-33. diciembre 1986, Bogotá.

Cardona, O.D. (1989). Enfoque metodológico para la evaluación de la amenaza, la vulnerabilidad y el riesgo sísmico. Sociedad Mexicana de Ingeniería Sísmica. No. 37, diciembre 1989, México, DOI: 10.18867/ris.37.304

Cardona, O.D. (1990). Términos de uso común en manejo de riesgos. Reporte AGID No. 13. 1er Simposio Andino de Geología Ambiental, 1ª Conferencia Colombiana de Geología Ambiental. Pag 587-593. Medellín. Cardona, O. D. (2001). Estimación holística del riesgo sísmico utilizando sistemas dinámicos complejos. Barcelona: Universidad Politécnica de Cataluña. CD: Premios de Investigación Social sobre protección civil, para tesis doctorales, 2002. Dirección General de Protección Civil, Ministerio del Interior, España.

Castellanos, E. J., et al. (2022). Brechas de adaptación al cambio climático en Centroamérica: desafíos para la resiliencia regional. Frontiers in Climate, 4, 934115.

Castillo, M., & Peraldo, G. (2000). Historia de la vulcanología en Costa Rica. En A. Ruiz & L. Camacho (Eds.), Memorias del Simposio en Geología Centroamericana (pp. 15-28). San José: UCR.

Castro-Vincenzi, J. (2024, 19 de abril). Costa Rica amidst climate change: Navigating the economic perils and opportunities. ReVista: Harvard Review of Latin America.

CATIE, Centro Agronómico Tropical de Investigación y Enseñanza. (2018a). Prácticas efectivas para la reducción de impactos por eventos climáticos: Cultivo de caña de azúcar en Costa Rica. Recuperado el 13 de marzo de 2024, de https://www.mag.go.cr/bibliotecavirtual/F01-8327.pdf

CATIE, Centro Agronómico Tropical de Investigación y Enseñanza. (2018b). Prácticas efectivas para la reducción de impactos por eventos climáticos en el cultivo de café en Costa Rica. Recuperado el 13 de marzo de 2024, de https://www.mag.go.cr/bibliotecavirtual/F01-8206.pdf

CATIE, Centro Agronómico Tropical de Investigación y Enseñanza. (2018c). Ficha técnica para sistemas productivos con ganado bovino. Recuperado el 13 de marzo de 2024, de https://www.mag.go.cr/bibliotecavirtual/L01-8412.pdf

CATIE, Centro Agronómico Tropical de Investigación y Enseñanza. (2018d). Acciones para fortalecer la adaptación y mitigación del cambio climático en el sector cafetalero de Costa Rica.

Centro Internacional de Métodos Numéricos en Ingeniería (CIMNE); ITEC S.A.S.; INGENIAR LTDA.; EAI S.A.; International Strategy for Disaster Reduction (ISDR). (2013). Global Assessment Report on Disaster Risk Reduction, GAR 2013. Modelación probabilista de riesgos naturales en el nivel global: el modelo global del riesgo. Modelos globales de terremoto y ciclón y evaluación de riesgo de desastres de los países para las amenazas de terremoto, ciclón e inundaciones.

CEPAL. (2010). La economía del cambio climático en Centroamérica: Reporte Técnico 2010. Comisión Económica para América Latina y el Caribe (CEPAL), México.

Chacón Soto, V. (2023, 21 de junio). Científicos alertan aumento en nivel del mar en todas las zonas costeras del país. Semanario Universidad.

Chen, C., I. Noble, J. Hellman, Murillo, M., Chawla, N. (2015). University of Notre Dame Global Adaptation Index: Country Index Technical Report. USA: University of Notre Dame. Disponible en: https://gain.nd.edu/our-work/country-index/

Chen, W., Moriya, K., Sakai, T., Koyama, L., & Cao, C. (2014). Monitoring of post-fire forest recovery under different restoration modes based on time series Landsat data. European Journal of Remote Sensing, 47(1), 153-168.

Chow, V. T., Maidment, D. R., Mays, L. W., & Saldarriaga, J. G. (1994). Hidrología aplicada (No. 551.48 C4H5).

CIMNE, ITEC S.A.S., INGENIAR LTDA., EAI S.A. (2012) Probabilistic modelling of natural risks at the global level: Global Risk Model. Background paper for the GAR13.

CNE – Comisión Nacional de Emergencias (2015). Política Nacional de Gestión del Riesgo 2016-2030. San José, Costa Rica: CNE.

CNE – Comisión Nacional de Emergencias (2020). Clasificación de la amenaza volcánica y evaluación de la red de monitoreo (Informe técnico). San José, Costa Rica: CNE-OVSICORI-RSN.

CNE. (2023). CNE brinda monitoreo y vigilancia. El Observador CR.

Colegio Federado de Ingenieros y de Arquitectos de Costa Rica (CFIA). (2010). Código Sísmico de Costa Rica 2010 (4.ª ed.). Cartago: Editorial Tecnológica de Costa Rica.

Comisión Nacional de Emergencia. (2014). PLAN GENERAL DE LA EMERGENCIA POR SEQUIA.

Comisión Nacional de Emergencias (CNE). (2016). Política Nacional de Gestión del Riesgo 2016-2030. San José, Costa Rica.

Comisión Nacional de Prevención de Riesgos y Atención de Emergencias. (s.f.). Deslizamientos, inundaciones, sismos. Costa Rica.

Contraloría General de la República (CGR). (2017). Presión sobre la hacienda pública en un contexto de variabilidad y cambio climático: Desafíos para mejorar las condiciones presentes y reducir los impactos futuros. San José, Costa Rica: CGR.

Copernicus Climate Change Service. (2017). ERA5: Fifth generation of ECMWF atmospheric reanalyses of the global climate. Copernicus Climate Change Service Climate Data Store (CDS). Retrieved from https://cds.climate.copernicus.eu/cdsapp#!/home

Corrales, L. (2017). Cambio climático: Impactos y desafíos para Costa Rica. San José, Costa Rica: Programa Estado de la Nación.

Coto-Cedeño, W. I. (2018). Ash clouds, fields of sand: Volcanic activity in Costa Rica and its impact on the agriculture sector, 1950–2017. Revista Geográfica de América Central, 62(1), 98-127.

Cramér, H. (1930) On the Mathematical Theory of Risk, Skandia Jubilee Volume, Stockholm.Cruz, M. G., Alexander, M. E., & Wakimoto, R. H. (2003). Assessing canopy fuel stratum characteristics in crown fire prone fuel types of western North America. International Journal of Wildland Fire, 12(1), 39-50.

Cruz Roja Costarricense. (2024a). Informe de Situación #1: Lluvias Intensas - November 2024.

Cruz Roja Costarricense. (2024b). Informe de Situación #2: OPERACIÓN: Lluvias Intensas - November 2024.

DeMets, C., Gordon, R. G., Argus, D. F., & Stein, S. (2010). Geologically current plate motions. Geophysical Journal International, 181(1), 1-80.

Dirección de Cambio Climático, & Ministerio de Ambiente y Energía. (2022). Plan Nacional de Adaptación al Cambio Climático 2022-2026.

Embrecths, P., Klüppelberg, C., Mikosch, T. 2012. Modelling Extremal Events for Insurance and Finance. Springer-Verlag. Berlin

ERN (Equipo Regional de Evaluación de Riesgos) (2014). Escenario de riesgo volcánico en San José, Costa Rica (Informe ERN-CAPRA-R5-T2.16). México: BID.

Escoto Castillo, Ana, Sánchez Peña, Landy, & Gachuz Delgado, Sheila. (2017). Trayectorias Socioeconómicas Compartidas (SSP): nuevas maneras de comprender el cambio climático y social. Estudios demográficos y urbanos, 32(3), 669-693. https://doi.org/10.24201/edu.v32i3.1684

Escoto, Ana & Sanchez, Landy & Gachuz, Sheila. (2017). Trayectorias Socioeconómicas Compartidas (SSP): nuevas maneras de comprender el cambio climático y social. Estudios demográficos y urbanos. 96. 669-693. 10.24201/edu.v32i3.1684

Evaluación de Riesgos Naturales - América Latina - Consultores en Riesgos y Desastres [ERN-CAPRA]. (s.f.). Análisis probabilista de amenazas y riesgos naturales - Revisión de eventos históricos importantes (Informe Técnico ERN-CAPRA-T2-1, Tomo II).

Evaluación de Riesgos Naturales ERN – América Latina. (2009). Modelación Probabilista de Amenazas Naturales. Informe ERN-CAPRA-T2-3. http://www.ecapra.org.

FAO, & UNESCO. (2025). Mapa Mundial de Suelos de FAO/UNESCO | Portal de Suelos de la FAO | Organización de las Naciones Unidas para la Alimentación y la Agricultura. Retrieved March

10, 2025, from https://www.fao.org/soils-portal/soil-survey/mapas-historicos-de-suelos-y-bases-de-datos/mapa-mundial-de-suelos-de-faounesco/es/

FAO. (2010). Wildland fire management terminology (Updated July 2010).

FAO. (2014). Impacto del fenómeno de El Niño 2014 en la seguridad alimentaria de Mesoamérica. Organización de las Naciones Unidas para la Alimentación y la Agricultura, Panamá.

FAO. (2020). Harmonized World Soil Database. Recuperado de http://www.fao.org/soils-portal/datahub/soil-maps-and-databases/harmonized-world-soil-database-v12/en

Fernández, W., Amador, J., & Campos, M. (2006). Impacts and Adaptation to Climate Change and Extreme Events in Central America. San José, Costa Rica: Centro de Investigaciones Geofísicas, UCR.

Freitas Guimarães, L., Nieto-Torres, A., Bonadonna, C., & Frischknecht, C. (2021). A new inclusive volcanic risk ranking, Part 2: Application to Latin America. Frontiers in Earth Science, 9, 757742.

Gao, X., Shuiqing, L., Dongxue, M., Yahao, L., Po, H. (2024) Development of a novel storm surge inundation model framework for efficient prediction. Geosci. Model Dev., 17, 5497–5509, 2024

Global Programme on Risk Assessment and Management for Adaptation to Climate Change. Coautores: Mechler, R. (lead author, IIASA); Schindler, S. (GIZ); Hanke, N. (GIZ); Högl, M. (GIZ); Siebert, M. (GIZ). Evaluación de riesgos relacionados con el clima. Una metodología de 6 pasos. Disponible en: https://www.adaptationcommunity.net/climate-risk-assessment-management/

Global Water Partnership (GWP). (2020). Hacia políticas de gestión de la sequía en Centroamérica. GWP Centroamérica – CCAD, Nota informativa.

González, R., Anzúles, A. S., Vera, A. Z., & Riera, L. B. (1994). Manual de pastos tropicales para la Amazonía ecuatoriana. Francisco de Orellana, Ecuador. INIAP, 32-35.

Gornitz, V. (1995). Sea-level rise: A review of recent past and near-future trends. Earth Surface Processes and Landforms, 20(1), 7-20.

Gutiérrez R., H. J. (2001). Vulnerabilidad de las coberturas vegetales de Colombia, aproximación a un modelo para la evaluación de la vulnerabilidad de las coberturas vegetales de Colombia ante un posible cambio climático utilizando SIG. Bogotá, Colombia: IDEAM. - p.v.: i.

Gutiérrez, J. A. (2012). Seismic Risk Prevention in Costa Rica: A Successful 39 Year Experience. En 15th World Conference on Earthquake Engineering (15WCEE), Lisboa, Portugal. (Paper No. 567).

GWPCAM, G. W. P. C. A. (2014). Sequía 2014: Un escenario que se puede prevenir. www.gwpcentroamerica.org

Hidalgo Leiva, D., Linkimer, L., Arroyo, I., Arroyo-Solórzano, M., Piedra, R., Climent, A., Díaz, V., Esquivel, L., Alvarado, G., Castillo, R., Carranza-Morales, M., Cerdas-Guntanis, L., Escalante-Meza, J., Lobo-Aguilar, S., Rodríguez, M., & Rojas, W. (2022). The 2022 seismic hazard model for Costa Rica. Bulletin of the Seismological Society of America. https://doi.org/10.1785/0120220119

Hidalgo, H. G., & Alfaro, E. J. (2012). Some physical and socio-economic aspects of climate change in Central America. Revista de Climatología, 12, 1-12.

Hidalgo, H. G., & Alfaro, E. J. (2015). Skill of CMIP5 climate models in reproducing 20th century basic climate features in Central America. International Journal of Climatology, 35, 3397-3411.

Hidalgo-Leiva, D. A., Linkimer, L., Arroyo, I. G., Arroyo, M., Piedra, R., Climent, Á., … & Alvarado, G. E. (2023). The 2022 Seismic Hazard Model for Costa Rica. Bulletin of the Seismological Society of America, 113(1), 23-41.

IKI, Iniciativa Climática Internacional (2023). NAMA Café Costa Rica | IKI Centroamérica & Caribe. Retrieved March 13, 2025, from https://iki-cac.org/hub-innovacion-clima-biodiversidad/acciones-climaticas-innovadoras/sistemas-alimentarios-y

Imbach, P., et al. (2017). Climate change, ecosystems and smallholders: A socio-ecological assessment in the tropics. Climatic Change, 141(1), 123-137.

INGENIAR (2014). Global Risk Model v2 for the Global Assessment Report (GAR-15) on disaster Risk Reduction. UNDRR

Instituto de Innovación y Transferencia de Tecnología Agropecuaria (INTA). (2015). Manual de definición de clases y especificaciones cartográficas de la Leyenda CLC-CR, para la generación de mapas de uso y cobertura de la tierra de Costa Rica. MAG, INTA, FITTACORI, SUNII.

Instituto Meteorológico Nacional (IMN) & Ministerio de Ambiente y Energía (MINAE). (2000). Primera Comunicación Nacional a la Convención Marco de las Naciones Unidas sobre Cambio Climático. San José, Costa Rica: MINAE.

Instituto Meteorológico Nacional (IMN) & Ministerio de Ambiente y Energía (MINAET). (2008). El clima de Costa Rica: Su variabilidad y cambio climático. San José, Costa Rica: MINAET.

Instituto Meteorológico Nacional (IMN) & Ministerio de Ambiente y Energía (MINAET). (2009). Segunda Comunicación Nacional a la Convención Marco de las Naciones Unidas sobre el Cambio Climático. San José, Costa Rica: MINAET.

Instituto Meteorológico Nacional (IMN) & Ministerio de Ambiente y Energía (MINAET). (2011). Análisis del riesgo actual del sector hídrico de Costa Rica ante el cambio climático. San José, Costa Rica: IMN-MINAET/PNUD.

Instituto Nacional de Estadística y Censos (INEC). (2015). VI Censo Nacional Agropecuario: Resultados generales (1ª ed.). INEC. ISBN: 978-9968-683-96-8. https://inec.cr/estadisticas-fuentes/censos/censo-agropecuario-2014

Instituto Nacional de Estadística y Censos (INEC). (2024). Encuesta Nacional Agropecuaria: Resultados generales de la actividad agrícola y forestal (Edición 2023) [Informe anual, recurso electrónico]. INEC. ISSN: 2215-552X. https://inec.cr/estadisticas-fuentes/encuestas/encuesta-nacional-agropecuaria?filtertext=2023&page=2

inta, Instituto Nacional de Innovación y Transferencia en Tecnología Agropecuaria, & sector AGRO ALIMENTARIO. (2022). Medidas de adaptación al Cambio Climático, Sistemas Pecuarios, Guía Técnica.

Intergovernmental Panel on Climate Change (IPCC). (2022). Climate Change 2022: Impacts, Adaptation and Vulnerability. Contribution of Working Group II to the Sixth Assessment Report of the IPCC (Chap. 12: Central and South America). Cambridge: Cambridge University Press.

International Federation of Red Cross and Red Crescent Societies (IFRC). (2023). Early Action Protocol Summary: Costa Rica | Floods caused by Tropical Cyclones.

INVU – Instituto Nacional de Vivienda y Urbanismo (2017). Guía para la integración de la gestión del riesgo en el ordenamiento territorial. San José, Costa Rica: INVU.

IPCC. (2014). Cambio Climático 2014: Impactos, adaptación y vulnerabilidad – Resumen para Responsables de Políticas. Quinto Informe de Evaluación del IPCC, Ginebra.

IPCC. (2021). AR6 Climate Change 2021: The Physical Science Basis.

IPCC. (2022). Climate Change 2022: Impacts, Adaptation and Vulnerability – Summary for Policymakers. Sexto Informe de Evaluación del IPCC, Ginebra.

JPL NASA, J. P. L. (2019, August 8). NASA Gauges Plant Stress in Costa Rican Drought. https://www.jpl.nasa.gov/news/nasa-gauges-plant-stress-in-costa-rican-drought/

Kirgman, J.F.C. (1992). Poisson Processes. Clarendon Press

Knapp, K. R., M. C. Kruk, D. H. Levinson, H. J. Diamond, and C. J. Neumann, 2010: The International Best Track Archive for Climate Stewardship (IBTrACS): Unifying tropical cyclone best track data. Bulletin of the American Meteorological Society, 91, 363-376. doi:10.1175/2009BAMS2755.1

Kolarsky, R. A., Mann, P., & Montero, W. (1995). Forearc deformation related to the subduction of the Cocos Ridge, southeastern Costa Rica. En P. Mann (Ed.), Geologic and Tectonic Development of the Caribbean Plate in Southern Central America (Geological Society of America Special Paper 295, pp. 215-242).

Kull, D. W., & Feldman, A. D. (1998). Evolution of Clark's unit graph method to spatially distributed runoff. Journal of Hydrologic engineering, 3(1), 9-19.

La Ruta del Clima. (2021). Una Ley Marco de Cambio Climático para Costa Rica: Estructuras básicas y ejemplos. San José, Costa Rica: La Ruta del Clima.

LaFemina, P., Dixon, T., Malservisi, R., & otros. (2009). Fore-arc motion and Cocos Ridge collision in Central America. Geochemistry, Geophysics, Geosystems, 10(5), Q05S14.

Linkimer, L., & Alvarado, G. E. (2014). Sismicidad histórica de Costa Rica (1821–2013). San José, Costa Rica: Red Sismológica Nacional (UCR-ICE).

Linkimer, L., Arroyo, I. G., Alvarado, G. E., Arroyo, M., & Bakkar, H. (2018). The National Seismological Network of Costa Rica (RSN): An Overview and Recent Developments. Seismological Research Letters, 89(2A), 392-401.

Linkimer, L., Böse, M., Clinton, J., & otros. (2021). Preliminary Results of an Earthquake Early Warning System in Costa Rica. Frontiers in Earth Science, 9, 700843.

Lizano Araya, M. A., Lizano Rodríguez, O. G., & Alfaro Herrera, E. J. (2023). Escenarios de inundación ante el aumento del nivel del mar por Cambio Climático, para las Playas del Coco, Tamarindo y Sámara, Costa Rica. Entorno Geográfico, (25), 1-24.

Lizano, O. G. (2013). Erosión en las playas de Costa Rica, incluyendo la Isla del Coco. InterSedes, 14(27), 6-27.

Lizano, O. G. (2014). Algunos impactos costeros en Costa Rica debido al calentamiento global. Ambientico, (246), 23-28.

Lizano, O. G. (2014b). La dinámica oceanográfica al frente del Humedal Nacional Térraba-Sierpe (HNTS) y su relación con la muerte del manglar. Revista de Biología Tropical, 62(4).

Lizano, O. G., & Gutiérrez, A. (2011). Erosión en las costas de Costa Rica, un problema de todos. En Torno a la Prevención, 7, 14-16.

Løvholt F., Glimsdal, S., Harbitz, C., Horspool, N., Smebye, H., Del bono, A., Nadim, F. (2014). Global tsunami hazard and exposure due to large co-seismic slip. International Journal of Disaster Risk Reduction, Volume 10, Part B, December 2014, Pages 406–418. doi:10.1016/j.ijdrr.2014.04.003.

Lücke, O. H., & Arroyo, I. G. (2015). Density structure and geometry of the Costa Rican subduction zone: Evidence from 3-D local earthquake tomography. Solid Earth, 6(4), 1169-1198.

Lundberg, F. (1903) Approximerad Framställning av Sannolikehets-funktionen. Återförsäkering av Kollektivrisker (Producción aproximada de la función de probabilidad. Reaseguro de Riesgos Colectivos), Almqvist & Wiksell, Uppsala.Mace, G. M., M. Barrett, N. D. Burgess, S. E. Cornell, R. Freeman, M. Grooten, & A. Purvis. (2018). Aiming Higher to Bend the Curve of Biodiversity Loss, Nature Sustainability, 1, 448–451.

MAG, Ministerio de Agricultura y Ganadería (2013). NAMA-AGRICOLA Acción de Mitigación Nacionalmente Apropiada en el sector Agrícola de Costa Rica.

MAG, Ministerio de Agricultura y Ganadería (2016). NAMA Ganadería - Ganadería bovina en Costa Rica. www.fb.com/namaganaderia

Marshall, J. S., Anderson, R. S., & Mendoza, J. (2000). Strike-slip faulting along the North Panama Deformed Belt and uplift of the Talamanca Range (Costa Rica–Panamá). Geology, 28(10), 907-910.

Marulanda, M., Cardona, O., Mora, M., & Barbat, A. (2014). Design and implementation of a voluntary collective earthquake insurance policy to cover low-income homeowners in a developing country. Barcelona: Natural Hazards Journal.

Melson, W. G., & Sáenz, R. (1968). The 1968 eruption of Volcán Arenal, Costa Rica: Preliminary summary of field and laboratory studies. Washington, DC: Smithsonian Institution.

MINAE – Ministerio de Ambiente y Energía (2018). Plan Nacional de Adaptación al Cambio Climático 2018-2030. San José, Costa Rica: Dirección de Cambio Climático.

Ministerio de Ambiente y Energía (MINAE). (2015). Estrategia Nacional REDD+ Costa Rica. MINAE. Recuperado el 7 de marzo de 2024, de https://www.forestcarbonpartnership.org/sites/fcp/files/2015/October/8-Costa%20Rica%20Borrador%20de%20la%20Estrategia%20Nacional%20REDD+Spanish%20v%2030%20Sept.pdf

Ministerio de Ambiente y Energía (MINAE). (2018). Política Nacional de Adaptación al Cambio Climático 2018-2030. San José, Costa Rica.

Ministerio de Ambiente y Energía (MINAE). (2018). Política Nacional de Adaptación al Cambio Climático 2018-2030. San José, Costa Rica: MINAE.

Ministerio de Ambiente y Energía (MINAE). (2022). Plan Nacional de Adaptación al Cambio Climático 2022-2026. San José, Costa Rica.

Ministerio de Ambiente y Energía (MINAE). (2022). Plan Nacional de Adaptación al Cambio Climático de Costa Rica 2022-2026. San José, Costa Rica: MINAE (Dirección de Cambio Climático).

Ministerio de Ambiente, Energía y Telecomunicaciones (MINAET). (2009). Estrategia Nacional de Cambio Climático. San José, Costa Rica: MINAET.

Montero, W. (1989). Los terremotos en la historia de Costa Rica (1821-1930). San José, Costa Rica: Editorial Universidad de Costa Rica.

Montero, W. (1994). Neotectonics and related stress distribution in a subduction collision zone—Costa Rica. En S. K. Seth & W. D. Means (Eds.), Geology of an Evolving Arc: 75th Anniversary of the Central American Geological Society (Geological Society of America Special Paper 295, pp. 115-140).

Montero, W., Denyer, P., Barquero, R., Alvarado, G. E., & Cowan, H. (1998). Map and database of Quaternary faults and folds in Costa Rica and its offshore regions. U.S. Geological Survey Open-File Report 98-481.

Mora, M. M. (2024). Historia y desarrollo de la vulcanología en Costa Rica desde las publicaciones periódicas de finales del siglo XIX al XXI. Revista Geológica de América Central, 64, 15-32.

Mora, M., Bakkar, H., Alvarado, G. E., & col. (2022). Volcanic monitoring and hazard assessment in Costa Rica. En W. Torres & G. Soto (Eds.), Volcano Observatories in Latin America (pp. 33-50). San José: UNA Press.

Morales, M. (2018). Brechas de conocimiento en adaptación al cambio climático: Informe de diagnóstico Costa Rica. Red Regional de Cambio Climático y Toma de Decisiones – Proyecto LatinoAdapta (UNESCO-UNITWIN). San José, Costa Rica.

Morales, R., & Liao, A. (1999). Amenazas volcánicas en Costa Rica: una estrategia de prevención. Revista Costarricense de Salud Pública, 8(15), 53-63.

Nicholls, R. J., & Cazenave, A. (2010). Sea-Level Rise and Its Impact on Coastal Zones. Science, 328(5985), 1517-1520.

NORSAR et. al. Proyecto regional RESIS II – Evaluación de la Amenaza sísmica en Centroamérica. 2008.

OACG, O. del A. y C. G. (2025). Observatorio de Sequía. https://oacg.fcs.ucr.ac.cr/index.php/observatorio-de-sequia-una

Observatorio Vulcanológico y Sismológico de Costa Rica, OVSICORI-UNA. (2022). Informe anual de sismicidad 2021. Heredia, Costa Rica: Universidad Nacional.

Ordaz M., Martinelli F., Aguilar A., Arboleda J., Meletti C. and D'Amico V. (2015). CRISIS 2015, Program for computing seismic hazard. Instituto de Ingeniería. Universidad Nacional Autónoma de México. México City, México.

Orozco Montoya, R. A., & Brenes Maykall, A. (2023). Evolución del riesgo en el territorio nacional: implicaciones y desafíos para la política pública. Consejo Nacional de Rectores.

OVSICORI-UNA (2016). Informe de actividad del volcán Turrialba, 2014-2016. Heredia, Costa Rica: OVSICORI, Universidad Nacional.

OVSICORI-UNA (2017). Reporte especial: Erupción freática del volcán Poás (Abril 2017). Heredia: Universidad Nacional.

OVSICORI-UNA (2019). Boletín de vigilancia volcánica: Rincón de la Vieja 2011-2019. Heredia: Universidad Nacional.

Peraldo, G., & Montero, W. (1994). Los temblores del período colonial en Costa Rica, 1538–1821. Cartago, Costa Rica: Editorial Tecnológica.

Pérez Arrieta, N. (2013). Análisis de vulnerabilidad ante sismos y deslizamientos del sector de Jucó de Orosi de Paraíso de Cartago. Universidad Central.

Pesaresi, M.; Politis, P. (2023): GHS-BUILT-H R2023A - GHS building height, derived from AW3D30, SRTM30, and Sentinel2 composite (2018). European Commission, Joint Research Centre (JRC) PID: http://data.europa.eu/89h/85005901-3a49-48dd-9d19-6261354f56fe, doi:10.2905/85005901-3A49-48DD-9D19-6261354F56FE

Peters, J., & Easton, D. (1996). Runoff Simulation Using Radar Rainfall Data. Water Resources Bulletin, 32(4), 753–760.

Poleo, D., Solano, E., & Stolz, W. (2014). La Oscilación Madden-Julian y las precipitaciones extremas en Costa Rica. Tópicos Meteorológicos y Oceanográficos, 13. Instituto Meteorológico Nacional, Costa Rica.

Pounds, J. A., Bustamante, M. R., Coloma, L. A., Consuegra, J. A., Fogden, M. P. L., Foster, P. N., … & Young, B. E. (2006). Widespread amphibian extinctions from epidemic disease driven by global warming. Nature, 439(7073), 161-167.

Programa Estado de la Nación. (2022). Vigésimo Octavo Informe Estado de la Nación en Desarrollo Humano Sostenible. San José, Costa Rica.

Protti, M., González, V., Newman, A., & otros. (2014). Nicoya earthquake rupture anticipated by geodetic measurement of the locked plate interface. Nature Geoscience, 7(2), 117-121.

Protti, M., Güendel, F., & McNally, K. (1995). Correlation between the age of the subducting Cocos Plate and the geometry of the Wadati–Benioff zone under Nicaragua and Costa Rica. En P. Mann (Ed.), Geologic and Tectonic Development of the Caribbean Plate in Southern Central America (GSA Special Paper 295, pp. 309-326).

Quesada-Hernández, L. E., Hidalgo, H. G., & Alfaro, E. J. (2020). Asociación entre algunos índices de sequía e impactos socio-productivos en el Pacífico Norte de Costa Rica. Revista de Ciencias Ambientales (Costa Rica), 54(1), 29-48.

Quesada-Hernández, L. E., Hidalgo, H. G., Alfaro, E. J., Quesada-Hernández, L. E., Hidalgo, H. G., & Alfaro, E. J. (2020). Asociación entre algunos índices de sequía e impactos socio-productivos en el Pacífico Norte de Costa Rica. Revista de Ciencias Ambientales, 54(1), 16–32. https://doi.org/10.15359/RCA.54-1.2

Quesada-Román, A. (2020). Landslides and floods zonation using geomorphological analyses in a dynamic catchment of Costa Rica. Journal Title, Volume(Issue), pages.

Quesada-Román, A., Hidalgo, H. G., & Alfaro, E. J. (2024). Assessing the impact of tropical cyclones on economic sectors in Costa Rica, Central America. Tropical Cyclone Research and Review, 13, 196-207.

Raes, D., Steduto, P., Hsiao, T. C., & Fereres, E. (2011). FAO cropwater productivity model to simulate yield response to water AquaCrop. In Reference Manual of AQUACROP (p. 56).

Reguero, B. G., Losada, I. J., Díaz-Simal, P., Méndez, F. J., & Beck, M. W. (2015). Effects of Climate Change on Exposure to Coastal Flooding in Latin America and the Caribbean. PLOS ONE, 10(7), e0133409.

República de Costa Rica (2006). Ley No. 8488: Ley Nacional de Emergencias y Prevención del Riesgo. La Gaceta, N°8 (11-01-2006).

República de Costa Rica. (2005). Ley Nacional de Emergencias y Prevención del Riesgo, Ley Nº 8488. La Gaceta Nº11 (11-1-2006). San José, Costa Rica: Asamblea Legislativa.

Retana, J. A. (2012). Eventos hidrometeorológicos extremos lluviosos en Costa Rica desde la perspectiva de la adaptación al cambio en el clima. Tropical Journal of Environmental Sciences.

Retana, J. A., Molina, M. J., Calvo, M., & Sanabria, N. (s.f.). Descripción de riesgo ante eventos hidrometeorológicos extremos en los cantones de Bagaces, Tilarán, Abangares y los distritos de Lepanto, Cóbano y Paquera. Instituto Meteorológico Nacional.

Rodríguez, J. (2018). Análisis de la Gestión de los Eventos de Sequía ante el Cambio Climático en los Sectores Agropecuario e Hídrico del Cantón de Hojancha, Guanacaste, Costa Rica.

Rodríguez, L. (2019). Costa Rica enfrentó 134 conflictos por el agua en una década. Semanario Universidad – Universidad de Costa Rica (27 mar 2019).

Rosenzweig, C., A. Iglesias, X. B. Yang, P. R. Epstein, & E. Chivian. (2001). Climate Change and Extreme Weather Events – Implications for Food Production, Plant Diseases, and Pests, Global Change and Human Health, 2(2), 90–104.

Ruiz Cubillo, P., & Soto, G. (2014). Preparación del mapa de susceptibilidad a deslizamientos utilizando imágenes LiDAR en los Cerros de Escazú, cantones Aserrí, Desamparados, Alajuelita, Santa Ana y Escazú, Costa Rica. https://doi.org/10.13140/RG.2.2.33311.76967

Salazar, M., Alvarado, G. E., Madrigal, J., & Monestel, Y. (2019). Deslizamientos históricos importantes en el volcán Barva (Costa Rica) y su transformación en flujos de escombros volcánicos. Revista Geológica de América Central, 61, 107-119. doi: 10.15517/rgac.v61i0.40090

Salgado, D. (2009). Inundaciones y gestión del riesgo de desastres. Retos para su reducción y mitigación.

Salgado, M. A., Zuloaga-Romero, D., Cardona, O. D. (2013). Evaluación probabilista del riesgo sísmico en Bogotá y Manizales con y sin la influencia de la Caldas Tear. Revista de Ingeniería, Facultad de Ingeniería, Universidad de los Andes, No. 38. Bogotá Junio. http://www.scielo.org.co/scielo.php?script=sci_arttext&pid=S0121-49932013000100002

Salgado-Gálvez, M., Ordaz, M., Singh, K., Cardona, O., Reinoso, E., Aguado, A., Zuloaga Romero, D., Garnica, B., & Bernal, G. (2018). Homogeneous and continuous probabilistic seismic hazard model for Latin America and the Caribbean. Presentado en la 16th European Conference on Earthquake Engineering, Thessaloniki, Grecia, junio de 2018.

Sánchez, F. (2015). HEC-HMS Manual elemental.

Schmidt, V., Moya, A., Climent, A-, Rojas, W. & Boschini, I. (2005). Microzonificación sísmica de San José, Costa Rica. (In English: Seismic Mizcrozonation of San José, Costa Rica). Universidad de Costa Rica

Schwarz, G. (1978). Estimating the Dimension of a Model. Annals of Statistics, 6: 461–464.

Sequeira-Arguedas, J. M. (2021). Geología, geomorfología y ocurrencia de deslizamientos en la cuenca alta del Río Virilla, Costa Rica. Universidad de Costa Rica.

Sheffield, J., Goteti, G., & Wood, E. F. (2006). Development of a 50-year high-resolution global dataset of meteorological forcings for land surface modeling. Journal of Climate, 19(13), 3088–3111. https://doi.org/10.1175/JCLI3790.1

Sheppard, J., & Hoyle, F. (2018). Water availability. Recuperado de http://soilquality.org.au/factsheets/water-availability

Sistema Nacional de Información Territorial (SNIT). (2024). Serie de mapas de cobertura y usos de la tierra de Costa Rica - REDD (MC) (Ediciones 2021, 2019, 2017, 2015, 2013) [Capas ráster]. SNIT.

Recuperado el 7 de marzo de 2024, de https://www.snitcr.go.cr/ico_servicios_ogc_info?k=bm9kbzo6ODY=&nombre=Secretar%C3%ADa%20REDD+

Sistema Nacional de Monitoreo de la Cobertura y Uso de la Tierra y Ecosistemas (SIMOCUTE). (2019, junio). Diagnóstico de mapeo sobre cobertura y uso de la tierra y ecosistemas. SIMOCUTE. Recuperado el 13 de marzo de 2024, de https://simocute.go.cr/assets/documents/Diagn%C3%B3stico_de_Mapeo_sobre_Cobertura_y_Uso_de_la_Tierra_y_Ecosistemas.pdf

Small, C., & Naumann, T. (2001). The global distribution of human population and recent volcanism. Environmental Hazards, 3(3-4), 93-109.

Smithsonian GVP – Global Volcanism Program (2013). Costa Rica: Holocene volcanoes and historical eruptions. Smithsonian Institution.

SNIT, S. N. de I. T. (2025). Instituto Geográfico Nacional Costa Rica. Retrieved March 10, 2025, from https://www.snitcr.go.cr/ico_servicios_ogc_info?k=bm9kbzo6NTA=&nombre=INTA

Soil Conservation Service. (1971). National engineering handbook, Section 4: Hydrology USDA, Springfield, VA.

Soil Conservation Service. (1986). Urban hydrology for small watersheds, Technical Release 55. USDA, Springfield, VA.

Soto Zúñiga, B. (2013). Las condiciones de sequía y estrategias de gestión en Costa Rica. Informe técnico nacional, Instituto Meteorológico Nacional – Programa NDMP, San José.

Soto Zúñiga, B. (2013). Las condiciones de sequía y estrategias de gestión en Costa Rica. Recuperado de https://www.droughtmanagement.info/literature/UNW-DPC_NDMP_Country_Report_Costarica_2013.pdf

Soto, B. (2013). Las condiciones de sequía y estrategias de gestión en Costa Rica. http://elpais.cr/frontend/noticia_detalle/1/75950

Stine, C. M., & Banks, N. G. (1991). Costa Rica Volcano Profile (USGS Open-File Report 91-591). Reston, VA: United States Geological Survey.

Suppasri, A.,Mas, E., Charvet, I., Gunasekera, R., Imai, K., Fukutani, Y., Abe, Y., Imamura F. (2013). Building damage characteristics based on surveyed data and fragility curves of the 2011 Great East Japan tsunami. Nat Hazards (2013) 66:319–341. DOI 10.1007/s11069-012-0487-8

Umaña González, P., & Blanco Picado, P. (2016). Deslizamientos en San José. UCR Ciencia + Tecnología.

UNDRR – United Nations Office for Disaster Risk Reduction (2015). Implementing the Sendai Framework: Lessons from Costa Rica. Global Platform 2017 Publications. Geneva: UN.

UNDRR (2022). Costa Rica: Voluntary national report for the midterm review of the Sendai Framework. Geneva: United Nations.

UNISDR. (2015). Marco de Sendai para la Reducción del Riesgo de Desastres 2015-2030. Naciones Unidas, Ginebra.

United Nations Development Programme (UNDP). (2021). Scaling up Climate Ambition on Land Use and Agriculture (SCALA) in Costa Rica [sitio web]. Recuperado de https://www.adaptation-undp.org/projects/scala-costa-rica

United Nations Office for Disaster Risk Reduction (UNDRR). (2022). Costa Rica is making firm progress in its knowledge of systemic risk. Recuperado de UNDRR.org (08-04-2022).

United Nations Office for Disaster Risk Reduction (UNDRR). Terminology. https://www.undrr.org/terminology/hazard

United Nations Office for the Coordination of Humanitarian Affairs (UNOCHA). (2015). Sequía en el Corredor Seco Centroamericano – Informe de situación. Naciones Unidas, Nueva York.

US Army Corps of Engineers. (2000). Hydrologic Modeling System HEC-HMS, Technical Reference Manual. Hydrologic Engineering Center.

Vallejos Vásquez, S., Esquivel Valverde, L., & Hidalgo Madrigal, M. (2012). Histórico de desastres en Costa Rica (Febrero 1723 - Setiembre 2012). Comisión Nacional de Prevención de Riesgos y Atención de Emergencias.

Van der Ploeg et al. (2010). The TEEB Valuation Database: overview of structure, data and results. En Foundation for Sustainable Development. Wageningen, the Netherlands.

Van der Zee, A., et al. (2012). Estudio de caracterización del Corredor Seco Centroamericano (Países CA-4) – Tomo I. CCAD/SICA – OCHA, San José.

Villalobos, J. (2015). Percepción del riesgo volcánico y conocimiento de planes de emergencia en comunidades cercanas al volcán Poás. Revista Geográfica de América Central, 54, 143-158.

Villalobos-Sequeira, J., Centeno-Morales, J., Cordero-Cordero, S., Anchia-Leitón, D., & González-Varela, M. (2024). Assessing the social vulnerability to floods in Pandora Oeste, Limón, Costa Rica, Central America. REDER, 8(2), 228-240.

Watson, F., Guzmán-Arias, I., & Villagra-Mendoza, K. (2022). Case Study: analysis of flood adaptation measures through the simulation of an event in the Matina Limón river, Costa Rica. Tecnología en Marcha, 35(4), 28-44.

Waylen, P., Caviedes, C., & Quesada, M. (1996). Interannual variability of monthly precipitation in Costa Rica. International Journal of Climatology, 16(2), 173-193.

Wilks, D. S. Department of E. & A. S. C. U. (2006). Statistical methods in the atmospheric sciences. In International Geophysics Series (Vol. 59). https://doi.org/10.1002/met.16

World Bank. (2010). Disaster Risk Management in Latin America and the Caribbean Region: GFDRR Country Notes - Costa Rica.

World Bank. (2021). Climate Risk Country Profile: Costa Rica. Washington, DC: The World Bank Group.

World Food Programme (WFP). (2015). Análisis inicial del impacto de la sequía en la seguridad alimentaria en Guatemala, El Salvador y Honduras. WFP – UNOCHA (Informe en línea).

World Meteorological Organization (WMO). (2023). Estado del Clima en América Latina y el Caribe 2023. Organización Meteorológica Mundial, Ginebra.

Zeballos, A., Ramírez-Cortés, F., Ishizawa, O., & Pita, G. (2016). Análisis de los resultados de la evaluación del riesgo sísmico y las funciones de vulnerabilidad de la red del Instituto Costarricense de Acueductos y Alcantarillados. Washington, DC: Global Facility for Disaster Reduction and Recovery (GFDRR) – Banco Mundial.

## A. 1 CALCULATION OF REFERENCE EVAPOTRANSPIRATION

The calculation of the potential evapotranspiration series follows the methodology described in the manual *Crop Evapotranspiration: Guidelines for Computing Crop Water Requirements* (Allen et al., 1998). This section provides a general overview of the procedure for applying the FAO Penman-Monteith method. For more detailed information, refer to FAO Irrigation and Drainage Paper No. 56.

Reference evapotranspiration is understood as the atmospheric potential for evaporation. It is calculated for a uniform vegetated surface under non-limiting water conditions. The reference surface is a hypothetical crop with an assumed height of 0.12 m, a fixed surface resistance of 70 s/m, and an albedo of 0.23 (Allen et al., 1998). It is independent of crop type, growth stage, or management. Because soil water is not limited, soil properties do not influence the outcome. These standardized conditions allow comparison across different locations or weather stations to assess atmospheric evaporative demand, since ETo varies only with climatic conditions.

### A. 1.1 FAO Penman-Monteith Method

The Penman-Monteith method quantifies the simultaneous processes of evaporation (water vaporizing from surfaces such as soil or wet vegetation) and transpiration (vaporization of water from within plant tissues). Required parameters include solar radiation, air temperature, humidity, wind speed (affecting evaporation), vapor flux, and aerodynamic resistance (associated with transpiration):

$$ET_0 = \frac{0.408\Delta(R_n - G) + \gamma \frac{900}{T+273} u_2 (e_s - e_a)}{\Delta + \gamma(1 + 0.34u_2)} \qquad \text{Equation A. 1}$$

where

$ET_0$ reference evapotranspiration [mm/day]

$R_n$ net radiation at the crop surface [MJ/m$^2$/day] (Equation A. 24)

$G$ soil heat flux density [MJ/m$^2$/day]

$\gamma$ psychrometric constant [kPa/°C] (Equation A. 3)

$T$ mean daily air temperature [°C]

$u_2$ wind speed at 2 meters height [m/s]

$(e_s - e_a)$ vapor pressure deficit [kPA] (Equation A. 5) y (Equation A. 12)

$\Delta$ slope of the vapor pressure curve [kPa/°C] (Equation A. 6)

The coefficient 0.408 converts net radiation from MJ/m²/day to an equivalent evaporation in mm/day.

Applying the Penman-Monteith method requires meteorological data that may not always be available. Missing parameters are estimated using expert judgment, regional climatological data, and FAO-recommended calculation procedures (Raes, 2009). For this study, climate parameters such as radiation, atmospheric pressure, wind speed, and specific humidity were sourced from the Princeton University database (Sheffield et al., 2006).

## A. 1.2 Atmospheric Parameters

### A. 1.2.1 Atmospheric Pressure (*P*)

Atmospheric pressure is the force exerted by the weight of the atmosphere. It can be estimated from elevation above sea level:

$$P = 101.3\left(\frac{293 - 0.0065z}{293}\right)^{5.26} \quad \text{Equation A. 2}$$

where

$P$ atmospheric pressure [kPa]

$z$ elevation above sea level [m]

If atmospheric pressure is measured directly at monitoring stations, the recorded value is used—ensuring the unit is correctly converted to kilopascals (kPa).

### A. 1.2.2 Psychrometric Constant $\gamma$

Psychrometric constant defined as:

$$\gamma = \frac{c_p P}{\varepsilon \lambda} = 0.664742x10^{-3}P \quad \text{Equation A. 3}$$

where

$\gamma$ = psychrometric constant [kPa/°C]

$P$ = atmospheric pressure [kPa]

$\lambda$ = latent heat of vaporization, 2.45 MJ/kg a 20°C

$c_p$ = specific heat at constant pressure, 1.013x10$^{-3}$ MJ/kg°C

$\varepsilon$ = ratio of molecular weight of water vapor to dry air (0.622).

## A. 1.3 Air Temperature

Air temperature is essential for calculating reference evapotranspiration. Mean daily air temperature ($T_{mean}$) is used in the Penman-Monteith equation to estimate the slope of the saturation vapor pressure curve (Δ) and the influence of air density (Pa). Values are taken from meteorological stations or databases such as the one provided by Princeton University. In this study, modeled temperature series were used directly in the Penman-Monteith equation for the probabilistic risk analysis.

## A. 1.4 Air Humidity

### A. 1.4.1 Saturation Vapor Pressure ($e_s$)

The saturation vapor pressure at a given temperature *T* is:

$$e°(T) = 0.6108 * \exp\left(\frac{17.27T}{T + 237.3}\right)$$ Equation A. 4

where

$e°(T)$ = saturation vapor pressure at air temperature *T* [kPa]

$T$ = air temperature [°C]

The mean saturation vapor pressure is calculated using daily maximum and minimum temperatures:

$$e_s = \frac{e°(Tmax) + e°(Tmin)}{2}$$ Equation A. 5

where

$e_s$ = mean saturation vapor pressure [kPa]

$Tmax$ = daily maximum air temperature [°C]

$Tmin$ = daily minimum air temperature [°C]

This approach is recommended over using mean temperature, as the non-linearity of the vapor pressure–temperature relationship could lead to underestimation of the parameter.

### A. 1.4.2 Slope of Saturation Vapor Pressure (Δ)

The slope of saturation vapor pressure for a given temperature *T*:

$$\Delta = \frac{4098 * \left[0.6108 * \exp\left(\frac{17.27T}{T + 237.3}\right)\right]}{(T + 237.3)^2}$$ Equation A. 6

where

Δ = slope of the vapor pressure curve [kPa/°C]

T = mean air temperature [°C]

### A. 1.4.3 Actual Vapor Pressure ($e_a$)

As per FAO guidelines, actual vapor pressure can be derived from dew point temperature, psychrometric data, or relative humidity, depending on data availability:

- $e_a$ from dew point temperature (Tdew)

$$e_a = e°(Tdew) = 0.6108 * \exp\left(\frac{17.27Tdew}{Tdew + 237.3}\right)$$ Equation A. 7

- $e_a$ from máximum and minimum relative humidity (RHmax, RHmin)

$$e_a = \frac{e°(T_{\min})RH_{max} + e°(T_{\max})RH_{min}}{2}$$ Equation A. 8

- $e_a$ from máximum temperatura and mínimum RH

$$e_a = e°(T_{\max})RH_{min}$$ Equation A. 9

- $e_a$ from average relative humidity

This study uses Princeton's database (Sheffield et al., 2006), which includes mean specific humidity.

From specific humidity, relative humidity is calculated as:

$$\mathrm{RH} = 0.263\ P\ shum\ \left[\exp\left(\frac{17.67(T - To)}{T - 29.65}\right)\right]^{-1}$$ Equation A. 10

where

RH = relative humidity [-]

P = atmospheric pressure [Pa]

$shum$ = specific humidity [-]

$T$ = mean air temperature [Kelvin]

$To$ = reference temperature, 273.16 K

Alternatively:

$$\mathrm{RH} = \frac{P\ shum}{0.622\ e_s}$$ Equation A. 11

where $e_s$ is the mean saturation vapor pressure [kPa].

Finally, actual vapor pressure is calculated from RH and mean temperature:

$$e_a = e°(T_{mean})RH_{mean}$$ Equation A. 12

where $e_a$ is the actual vapor pressure [kPa] and RH is the relative humidity expressed as a fraction. If RH is given as a percentage, it must be converted to a fraction before being used in the equation.

## A. 1.5 Radiation

Net radiation can be calculated using parameters such as extraterrestrial radiation, solar radiation, clear-sky radiation, and longwave radiation, based on calibrated constants and functions. It can also be calculated from radiation measurements recorded at specialized stations or included in radar-based climate databases. The following describes the options for calculating net radiation.

### A. 1.5.1 Extraterrestrial Radiation

Extraterrestrial radiation is calculated based on latitude and day of the year, using the following function:

$$R_a = \frac{24 * 60}{\pi} G_{sc} d_r [\omega_s \sin(\varphi) \sin(\delta) + \cos(\varphi) \cos(\delta) \cos(\omega_s)] \quad \text{Equation A. 13}$$

where

$R_a$ = extraterrestrial radiation [MJ/m$^2$d]

$G_{sc}$ = solar constant = 0,082 MJ/m$^2$min

$d_r$ = inverse relative Earth–Sun distance [-] (Equation A. 14)

$\omega_s$ = sunset hour angle [rad]

$\varphi$ = latitude [rad] (Equation A. 16)

$\delta$ = solar declination [rad] (Equation A. 15)

The inverse relative Earth–Sun distance and solar declination are calculated as:

$$d_r = 1 + 0.033 * \cos\left(\frac{2\pi}{365} J\right) \quad \text{Equation A. 14}$$

$$\delta = 0.409 * sen\left(\frac{2\pi}{365} J - 1.39\right) \quad \text{Equation A. 15}$$

Where $J$ is the day of the year (1 = January 1st, 365 = December 31st).

The sunset hour angle ($\omega_s$) is given by:

$$\omega_s = \arccos[-\tan(\varphi) \tan(\delta)] \quad \text{Equation A. 16}$$

### A. 1.5.2 Maximum Sunshine Duration (N)

Maximum sunshine duration N, is given by:

$$N = \frac{24}{\pi}\omega_s$$ Equation A. 17

Where $\omega_s$ is the sunset hour angle from Equation A.16. The number of maximum daylight hours is used to estimate solar radiation.

### A. 1.5.3 Solar or Shortwave Radiation

Solar radiation values can be obtained from direct measurements or calculated using the Ångström formula, which relates extraterrestrial radiation ($R_a$) to actual sunshine duration ($n$) and maximum sunshine duration ($N$):

$$R_s = \left(a_s + b_s \frac{n}{N}\right) R_a$$ Equation A. 18

where

$R_s$ = solar or shortwave radiation [MJ/m$^2$d]

$n$ = actual sunshine duration [hours]

$N$ = maximum possible sunshine duration [hours] (Equation A. 20)

$R_a$ = extraterrestrial radiation [MJ/m$^2$d] (Equation A. 13)

$a_s$ = regression constant representing the fraction of extraterrestrial radiation reaching the Earth on very cloudy days (n = 0), typically $a_s$ = 0.25

$a_s + b_s$ = fraction of extraterrestrial radiation reaching Earth on clear days (n = N), typically $b_s$ = 0.50

Net shortwave radiation (incoming solar radiation minus reflected) is calculated as:

$$R_{ns} = (1 - \alpha)R_s$$ Equation A. 19

Where $\alpha$ is the albedo or reflectivity coefficient of the crop. For the standard reference crop, $\alpha$ = 0.23..

- Available Measurements

In the Princeton climate variable database, daily solar radiation data is available. The parameter corresponding to shortwave radiation is dswrf (downward shortwave radiation), equivalent to $R_s$ calculated from Equation A. 19. To calculate net shortwave radiation, the reflected component must be subtracted, using:

$$R_{ns} = dswrf * (1 - \alpha)$$ Equation A. 20

Where *dswrf* is the measured shortwave radiation in MJ/m²/day.

### A. 1.5.4 Net Longwave Radiation

Net longwave radiation can be obtained from measurements or estimated using the Stefan–Boltzmann law, corrected in this methodology to account for humidity and cloud cover effects:

$$R_{nl} = \sigma \left[\frac{T_{max,K}^4 + T_{min,K}^4}{2}\right] \left(0.34 - 0.14\sqrt{e_a}\right) \left(1.35\frac{R_s}{R_{so}} - 0.35\right)$$ Equation A. 21

where

$R_{nl}$ = net longwave radiation [MJ/m$^2$d]

σ = Stefan–Boltzmann constant = 4.903 x 10-9 MJ/K$^4$m$^2$día

$T_{max,K}$ = daily maximum absolute temperature [K]

$T_{min,K}$ = daily minimum absolute temperature [K]

$e_a$ = actual vapor pressure [kPa],

$R_s/R_{so}$ = relative shortwave radiation (values ≤ 1.0)

$R_s$ = measured or calculated solar radiation [MJ/m$^2$d]

$R_{so}$ = clear-sky radiation [MJ/m$^2$d] (Equation A. 22)

Clear-sky solar ($R_{so}$) radiation is calculated as::

$$R_{so} = \left(0.75 + 2x10^{-5}z\right)R_a$$ Equation A. 22

where z is the station elevation or point of interest above sea level [m].

- Available Measurements

The Princeton climate database includes daily longwave radiation measurements. The parameter corresponding to longwave radiation is *dlwrf* (downward longwave radiation), representing incoming atmospheric longwave radiation.

To compute net longwave radiation ($R_{nl}$), the amount of longwave energy emitted back to the atmosphere is estimated using the Stefan–Boltzmann equation:

$$R_{nl} = dlwrf - \left(\varepsilon_o \sigma {T_{media,K}}^4 + (1 - \varepsilon_o) * dlwrf\right)$$ Equation A. 23

where

$dlwrf$ = measured longwave radiation [MJ/m$^2$d]

$\varepsilon_o$ = emissivity, 0.98 for vegetation

σ = Stefan–Boltzmann constant = 4.903 x 10-9 MJ/K$^4$m$^2$día

$T_{media,K}$ = daily mean temperature [K]

The term $\left(\varepsilon_o \sigma {T_{media,K}}^4 + (1-\varepsilon_o) * dlwrf\right)$ represents longwave radiation reflected to the atmosphere.

### A. 1.5.5 Net Radiation

Net radiation ($R_n$) is calculated as the difference between net shortwave radiation ($R_{ns}$) and net longwave radiation ($R_{nl}$):

$$R_n = R_{ns} - R_{nl} \qquad \text{Equation A. 24}$$

Values for $R_{ns}$ and $R_{nl}$ can be obtained using theoretical functions (Equation A. 19 y Equation A. 21) or measures (Equation A. 20 and Equation A. 23).

## A. 1.6 Wind Speed

Wind speed must be included in the evapotranspiration calculation and is expressed as the daily average. Measurement stations must specify the height of measurement, as wind speed increases with height due to surface friction. Wind speed used in the Penman–Monteith equation must be standardized to 2 meters height. If measured at a different height, the following correction is applied:

$$u_2 = u_z \frac{4.87}{\ln(67.8z - 5.42)} \qquad \text{Equation A. 25}$$

where

$u_2$ = wind speed at 2 m above surface [m/s]

$u_z$ = measured wind speed at height z [m/s]

$z$ = measurement height above surface [m]

If no wind speed measurements are available, FAO Paper No. 56 recommends the following default values:

Light wind $u_2 = 0.5\ m/s$

Light to moderat: $u_2 = 2\ m/s$

Moderate to strong: $u_2 = 4\ m/s$

Strong wind: $u_2 = 5.5\ m/s$

## A. 1.7 Climate Variables from the Princeton Database

When using data from databases, it must be verified that the variables align with Penman–Monteith input parameters.

- *Radiation:*

Radiation values are provided in watts per square meter ($W/m^2$) and must be converted to megajoules per square meter ($MJ/m^2$) for use in the Penman–Monteith equation. Note that the database contains incoming shortwave or longwave radiation, not net radiation.

- *Relative Humidity:*

The database provides specific humidity. It must be converted using Equation A.10 or A.11 to obtain relative humidity.

No corrections are made for wind speed or atmospheric pressure.

The procedure for computing reference evapotranspiration from historical climate variables (other than temperature) accounts for their temporal variability. Specifically, for each point with available data between 1981 and 2010, a multi-year average is calculated for 10-day periods (decadal averages). This yields 36 average values per year, capturing the seasonal behavior of each variable. For instance, warm air in summer can hold more water vapor than cold air in winter. The daily ETo value is based on the decadal average for the corresponding calendar date.

These decadal averages for non-temperature variables are used in both historical and simulated evapotranspiration series. No stochastic modeling or simulation is applied to radiation, humidity, wind speed, or pressure, as this would require complex meteorological models beyond the scope of this project.